DECADAL SCALE CLIMATE VARIABILITY DURING THE LAST MILLENNIUM AS RECORDED BY THE BONA CHURCHILL AND QUELCCAYA ICE CORES

DISSERTATION

Presented in Partial Fulfillment of the Requirements

for the Degree Doctor of Philosophy

in the Graduate School of The Ohio State University

By

David Urmann, M.S.
Geological Science Graduate Program

* * * * *

The Ohio State University
2009

Dissertation Committee:
Professor Lonnie Thompson, Advisor
Professor Gary McKenzie
Professor Doug Alsdorf
Professor Cornelis Vanderveen
Professor Greg Wiles

ABSTRACT

This thesis outlines the development of the timescales, the calibration of the ice-climate relationships, and the possible linkages between the Quelccaya Summit Ice Core and the Bona Churchill Ice Core, with different modes of decadal and interannual climate variability during the last 1,000 years. The Bona Churchill Ice Core (BC1), drilled to bedrock in the spring of 2002 in the Wrangell-St. Elias Mountains of southeast Alaska (61^{o} 24$^{'}$ N, 141^{o} 42$^{'}$W, 4420 meters), is one of the only annually dateable records of extended historical duration to ever be recovered from the northeastern side of the Pacific Basin. The Quelccaya Summit Ice Core (168.8m) was obtained during the most recent drilling project at Quelccaya (13º 56’S, 70º 50’W, 5670 meters), which took place in the summer of 2003 and is the longest of the three ice cores obtained. Dr. Thompson has led glacial studies in the region since 1976. These include a major drilling project in 1983; the mapping of the retreat of the Quelccaya Ice Cap using surface and aerial photos; documentary photography of the retreat of the Kori Qalis glacier; and setting up and recording data from automated weather stations.

The timescale for BC1 is well constrained during the last 1,000 years by annual layering, the identification of the 1963 β- peak, the 1912 eruption of Katmai, and the 1783 eruption of Laki. Additionally, this study pinpoints the period A.D. 760 to 777 (according to the BC1 timeline) as the likely timing of the White River Ash, an important regional chronostratigraphic marker. It should be noted that the timeline before A.D. 1000 is only an approximation that is based entirely upon a simple time-depth model and the assumptions that are inherent to the model. The time-depth model suggests that the bottom of the ice core corresponds to A.D. 265.

The timescale for the 2003 Quelccaya Summit Core is based upon multiple lines of evidence, including annual layer counting based on peaks in dust, a well-defined annual cycle in δ^{18}O, the identification of ash layers in the ice core corresponding to historic volcanic eruptions, and comparisons of the Quelccaya core with other regional ice cores. Counting of annual layers was possible from A.D. 615 to 2003. By using a time-depth model, the timeline can be extended to A.D. 315, which corresponds with the end of the core. A comparison with the 2003 Coropuna Core (15° 31′S, 72 °39′W) that was obtained from the western cordillera of the Peruvian Andes shows that individual years can be identified and matched peak for peak for the last 200 years. This serves as a valid cross-check on the derived timeline and shows that the isotope profiles are not unique to either ice core, but are rather preserved systematically across this entire region of the Andes. Comparisons of the isotopic profiles from the 2003 to the 1983 Quelccaya ice cores over the last 500 years show that despite the differences in sampling methods, both records are nearly identical. This attests to the stability of the derived δ^{18}O profiles through time and as a verification of the original 1983 timescale developed by Dr. Thompson.

The records of δ^{18}O and dust from BC1 can be related to long-term shifts in atmospheric circulation, which are expressed by the two primary modes of Northern Hemisphere circulation: the Aleutian Low (AL) and the Arctic Oscillation (AO). This thesis shows that the strongest climate signal in both δ^{18}O and dust is that produced by the history of northerly flow (associated with weak AL and negative AO), versus southerly flow over the drill site. Comparisons with other regional records suggest that the longer-term trends in the records of both δ^{18}O and dust, upon which the AO modulated peaks and troughs are superimposed, may reflect gradual changes in the strength or position of the AL through time. It is observed that large dust events and more negative values of δ^{18}O occur when the AL is weak and the AO is negative as a result of an anomalous northerly flow over the drill site that likely results in the emplacement of a dustier, colder, and more continental air mass. In general, the AO acts to modulate the strength of the correlation between δ^{18}O and dust with the AL, so that when the AO is negative (positive), a stronger (weaker) correlation is observed with the AL. The record from BC1 provides an important record of past AO variability at a time when more

investigators are just beginning to take an in-depth look at the effects of this feature on the climate in Alaska.

The relationships identified between $\delta^{18}O$ and dust with both the AO and AL suggests that the temperature response recorded by BC1 is indefinable, because more negative values of $\delta^{18}O$ are associated with a weaker AL and/or a negative AO and more positive values of $\delta^{18}O$ are associated with a stronger AL and/or a positive AO. Historical records show that a weaker (stronger) AL is associated with cooler (warmer) conditions and a negative (positive) AO is associated with warmer (cooler) conditions. This ambiguous relationship could explain why the record of BC1 $\delta^{18}O$ shows no response to modern warming. During the last 25 years the AL has gotten stronger and the AO has been more positive, suggesting at least cooler temperatures in the upper atmosphere due to the influence of the AO and warmer temperatures at the surface due to the influence of a stronger AL. These results are consistent with the accumulation record from BC1 and with historical records, which show trends toward increasing precipitation and temperature. These trends might be expected given an overall increase in the regional lapse rate and increased moisture flux into the region, which is typically associated with a strong AL.

The analysis of the 2003 Quelccaya core identifies a strong correlation between Quelccaya $\delta^{18}O$ and NINO 4 Sea Surface Temperatures (SSTs) ($r=0.646$, $p<0.001$, 1856-2003). The Pierson correlation coefficient between Jan-Dec NINO 4 SST and Quelccaya $\delta^{18}O$ during the period 1856 to 1882 is 0.75 (as opposed to 0.65 for the modern period of record from 1882 to 2000), indicating that a strong relationship between $\delta^{18}O$ and SST persisted even during the Little Ice Age (LIA) despite a substantially different background climate. Previous studies of the 1983 Quelccaya $\delta^{18}O$ and of the record of NINO 4 SSTs show that decadal rather than interannual variability is dominant in both records. ENSO events can be observed in the 2003 Quelccaya $\delta^{18}O$ superimposed on the lower-frequency decadal variability, but they are not the dominant feature. This occurs as Quelccaya $\delta^{18}O$ is most strongly correlated with SST in the easternmost margin of the Pacific Warm Pool (PWP), and in general SST anomalies in this region are more persistent and evolve on slower timescales than those in the eastern Pacific. Previous studies indicate that increased convection in the eastern portion of the warm pool results in weaker trade winds in the Atlantic and warmer SST in the northern tropical Atlantic. Establishing a connection between decadal variability in the Pacific and Atlantic is of key importance, as the Atlantic is the primary moisture source area for Quelccaya.

One of the primary purposes of this thesis was to reconstruct a multi-ice core history of El Niño events using the records from BC and Quelccaya, but the results of this analysis were of limited use because of the weak overall relationship between BC and ENSO events. The lack of connection between the ice core variables from Peru and Alaska during both the last 100 years and the last 1,000 years might result from the BC record of $\delta^{18}O$ being more strongly related to fluctuations in the AO than in the AL. However, it might result from the fact that the Quelccaya $\delta^{18}O$ record reflects decadal NINO 4 variability and seems for the most part disconnected from the lower-frequency regime shifts associated with the PDO, which primarily reflects North Pacific variability.

Although it was not feasible to reconstruct a multi-ice core history of El Niño from the records from Quelccaya and Bona Churchill, the concept of constructing a history of El Niño events from the Quelccaya core is promising. As proof of concept, this thesis finds strong linkages between the time series of $\delta^{18}O$ from Quelccaya with reconstructions of El Niño events based on historical records during the last 500 years and with a reconstruction of the Palmer Drought Severity Index (PDSI) for the southwestern U.S., a region with a strong and dependable ENSO teleconnection. Additionally, a strong relationship is noted between modern corals growing near Palmyra Island (162ºW, 6ºN) with Quelccaya $\delta^{18}O$. This is of particular interest, as the strongest correlations between Quelccaya $\delta^{18}O$ and Pacific SSTs occur in this same region. However, despite the fact that modern coral records exhibit a match with the Quelccaya, the relationship is not as clear when older fossil coral records from the same location are examined. The Quelccaya record offers a great deal of promise for future reconstructions of ENSO variability but needs to be paired with other proxy records that exhibit a strong ENSO signal.

ACKNOWLEDGMENTS

I wish to thank my advisor, Lonnie Thompson, for intellectual support, in-depth discussions on climate variability, and enthusiasm throughout the course of my studies. I would like to thank the research staff in the Byrd Polar Ice Core Paleoclimatology Group: Ellen Mosley-Thompson, Henry H. Brecher, Mary Davis, Ping-Nan Lin, and Victor Zagorodnov. Without their efforts to retrieve and perform the sampling and analysis of the ice cores discussed herein, this work would not be possible.

I would like to thank Gary McKenzie for his support, our lively conversations, and moral encouragement during this process. I extend my gratitude to Doug Alsdorf and Cornelis Vanderveen for their input and review of this thesis during the developmental process. I thank Greg Wiles for the discussions we have had on climate variability in Alaska and for the invaluable feedback given during the review process of my thesis. Last but not least, I would like to thank my research colleagues, Aron Buffen, Natalie Kehrwald, Sangsuk Lee, and Y. C. Fang, for making my years at Ohio State more interesting and for providing feedback on my thoughts and ideas, which led to the completion of this thesis.

VITA

September 6, 1974………Born – Salt Lake City, UT, USA

1997……………………..B.S., Utah State University

1998-2001………………Range Technician (Field Work), Salt Lake District BLM

1999……………………..Field Work: Grand Staircase National Monument, Utah

2001-2003………………Graduate Teaching Assistant, The Ohio State University

2003……………………..Field Work: Quelccaya Ice Core Expedition

2004……………………..M.S. Geology, The Ohio State University

2007……………………..Forest Technician (Field Work), Uinta National Forest

2005-Present…………….Graduate Research Assistant, The Ohio State University

PUBLICATIONS

1. Urmann, D., ENSO and PDO variability in ice core and lake level records over the past century, master’s thesis, The Ohio State University, 196, 2004.

2. Urmann, D., *Trail Guide to Grand Staircase Escalante National Monument*, Layton, UT: Gibbs Smith, 1999.

FIELD OF STUDY

Major Field: Geological Sciences

TABLE OF CONTENTS

Page
Abstract ii
Acknowledgments vi
Vita vii
List of Tables xii
List of Figures xvi

Chapters:

1. Introduction to Pacific Climate Variability 1

    1.1 The ENSO Phenomena 1
        1.1.1 Introduction 1
        1.1.2 A brief history of the study of ENSO 2
        1.1.3 ENSO components and progression: the SO, SSTs, and Walker Circulation 6
        1.1.4 Defining ENSO events 8
    1.2 The history of ENSO variability for the past 1,000 years 8
    1.3 The response of ENSO to climate change 12
    1.4 Interannual climate variability in the North Pacific 14
        1.4.1 The Aleutian Low 14
        1.4.2 The Pacific North American pattern 19
        1.4.3 Pacific Decadal Oscillation (PDO) 20
        1.4.4 Siberian High—East Asian winter monsoon 26
        1.4.5 Arctic Oscillation and the North Atlantic Oscillation 27
    1.5 Climate Regimes—A unifying concept 28

2. The Bona Churchill Ice Core 30

    2.1 Abstract 30
    2.2 Introduction and background 32

    - 2.2.1 The Bona Churchill Ice Cores: field work lab analysis 32
    - 2.2.2 The Bona Churchill Ice Cores: laboratory analysis 34
    - 2.2.3 Climatology of the St. Elias Region, Alaska 37
    - 2.2.4 Reconstructions of Alaska climate change 40
  - 2.3 Timeline verification and development 46
    - 2.3.1 Identifying annual and seasonal markers in BC1 46
    - 2.3.2 The 1963 peak in β- and ^{3}H 51
    - 2.3.3 Volcanic events as time horizons... 52
    - 2.3.4 The White River ash 54
  - 2.4 Defining annual and seasonal cycles in BC1 59
    - 2.4.1 Development of a seasonal composite.. 59
    - 2.4.2 Timing of the seasonal peak in dust.. 74
    - 2.4.3 Seasonal divisions 76
  - 2.5 Comparisons and reproducibility of results 80
    - 2.5.1 Short and long cores: the first 10 meters 80
    - 2.5.2 The two long cores: a 114 m comparison 81
    - 2.5.3 The development of the accumulation record...................................... 84
  - 2.6 Calibration, time series, and seasonal composites 85
    - 2.6.1 Introduction.. 85
    - 2.6.2 Regional precipitation and temperature data sets 86
    - 2.6.3 Calibration of accumulation.. 88
    - 2.6.4 Calibration of the d-excess record 93
    - 2.6.5 Calibration of δ^{18}O and dust 97
    - 2.6.6 Nitrate overview.. 107
    - 2.6.7 Calcium overview: time series and seasonal cycle 108
    - 2.6.8 Magnesium overview: time series and seasonal cycle........................ 109
    - 2.6.9 Chloride overview... 109
    - 2.6.10 Sodium overview: time series and seasonal cycle 110
    - 2.6.11 Sulfate overview: time series and seasonal cycle 110
    - 2.6.12 Ammonium overview: time series and seasonal cycle 111
    - 2.6.13 Potassium overview 111
  - 2.7 Discussion and results.. 111
    - 2.7.1 Introduction: interactions between the AO/AL.................................. 112
    - 2.7.2 The 1960s dust event: evidence of the AL/AO connection 112
    - 2.7.3 A regime shift in the 1920s: evidence of an AO-modulated signal.... 117
    - 2.7.4 Dust and δ^{18}O: paleothermometers or records of AO/AL variability? 119
    - 2.7.5 Conditions associated with pre-1960 dust events in BC1................... 121
  - 2.8 Conclusions... 129

3. Results from the 2003 Quelccaya Summit Core 133

  - 3.1 Abstract 133
  - 3.2 Introduction and background 134
    - 3.2.1 Quelccaya drilling projects from 1976 to 2003 134
    - 3.2.2 Analysis and sampling of the 2003 ice core 136
  - 3.2.3 Quelccaya geography... 137

  3.2.4 General climatology of the Altiplano and Quelccaya 137
  3.2.5 Recent warming in the Andes 138
3.3 Timeline verification and development 139
  3.3.1 Seasonal cycles 139
  3.3.2 Layer counting 139
  3.3.3 Volcanic events as time horizons 141
  3.3.4 Comparison with the Coropuna Ice Core 141
3.4 Record development 142
  3.4.1 Accumulation 142
3.5 Calibration and time series summaries 143
  3.5.1 Calibration of $\delta^{18}O$ 143
  3.5.2 Accumulation and dust: calibration and time series overview 151
3.6 Discussion 152
  3.6.1 Quelccaya $\delta^{18}O$: A record of decadal or interannual variability? 152
3.7 Conclusions 155

4. Ice Core-Based ENSO Reconstructions 156

4.1 Introduction 156
4.2 ENSO and $\delta^{18}O$: results from the 1983 Quelccaya Ice Core 156
4.3 A Quelccaya-based ENSO reconstruction 157
4.3.1 An automated method for defining ENSO 158
4.3.2. Hand selection as a means for defining ENSO events 161
4.3.3 Discussion: hand counts versus the automated reconstruction 165
4.4 A multiple ice core-based ENSO reconstruction 169
  4.4.1 An ENSO reconstruction: the ice core-based approach 171
  4.4.2 An ENSO reconstruction: the ice core-climate approach 173
  4.4.3 Creating an ice core-tree ring index composite ENSO index 176
4.5 Conclusions 177

5. Ice Cores, Tree Rings, and Corals 180

5.1 Introduction 180
5.2 Comparison of records from BC and Quelccaya 180
5.3 Relationships between Quelccaya $\delta^{18}O$ and Pacific coral records 188
5.4 Tree rings and ice cores 196
  5.4.1 Introduction 196
  5.4.2 Comparisons of tree ring and ice core data sets 204
5.5 Conclusions 211

6. Conclusions and Review 215

6.1 The Bona Churchill Ice Core 215
  6.1.1 Climate-ice relationship 215
  6.1.2 Timescale and seasonal patterns of BC1 216
  6.1.3 The record of BC1 from A.D. 1000 to 2000 218

6.2 The Quelccaya Ice Core 219
    6.2.1 Climate-ice relationship 219
    6.2.2 Timeline 221
6.3 ENSO reconstructions and ice core comparisons 221
    6.3.1 An ice core-based ENSO reconstruction 221
    6.3.2 Quelccaya-Bona Churchill comparisons 222
    6.3.3 Tree ring and corals 222

Appendix A: Alaskan weather data 224

A.1 Gulkana 224

A.2 Chitina 224

A.3 McCarthy 3 SW 225

A.4 McCarthy 1 NE 225

A.5 Kennecott 225

A.6 Paxson 225

A.7 NCEP/NCAR data sets 226

A.8 Construction of composite records 226

    A.8.1 The Alaskan Short Composites 226

    A.8.2 The Alaskan Long Composite (ALC) 228

Bibliography 239

LIST OF TABLES

Table Page

1.1 Proxy ENSO records for 1,000 years 9

2.1 Error estimates for the derived BC1 timescale 50

2.2 List of volcanic events and relationship to BC1 51

2.3 Relationship between BC1 (Table 2.3A) and Alaska weather station data (Table 2.3B) with indices of Pacific Climate Variability 87

2.4 Radiosonde data from Yakutat (1958 to 2006) smoothed with a 5-year moving average and correlations with weather station data, teleconnection indices, and ice core time series 90

2.5 Correlation analysis: spring-based - BC d-excess and $\delta^{18}O$ (5-year averages) 102

2.6 Number of BC1 ice core variables recording specific events 123

2.7 Different modes of the AL and AO and example years in which they occurred...... 116

3.1 Errors associated with the timescale of the 2003 Quelccaya Core 140

4.1 El Niño years that are clearly identified by both the time series of O18 and of accumulation, using the hand count method 162

4.2 All of the reconstructed El Niño years derived from the process of hand selection described in Section 4.3.2. 163

4.3 Correlations between ice core variables and ENSO indices 171

4.4 List of El Niño years, per *Quinn* (1987). This list only includes years defined by *Quinn* (1987) as strong, strong +, or very strong 173

4.5 Ice core response to El Niño years as defined by *Quinn* (1987). 174

5.1 Number of $\delta^{18}O$ events from BC matching minima and maxima in the record of Quelccaya $\delta^{18}O$ 185

5.2 Number of d-excess events from BC matching minima and maxima in the record of Quelccaya $\delta^{18}O$ 186

5.3 Summary of precipitation reconstructions for the southwestern U.S. 199

5.4 Reproduction of the results of *Grissino and Mayer* (2002) that depict years with greatest and least flow on the Rio Grande, as reconstructed from tree ring data in the region 200

5.5 Summary of drought years in the PNW from multiple tree ring based studies since A.D. 1500.. 202

5.6 Summary of North Pacific Regime shifts. Reproduced from *Verdon and Franks* (2006) 210

A.1 A list of stations that were used in the reconstruction of the ALC. Also reported are the r values for the correlation between the composite time series and individual stations. 229

A.2 Compares timing of known eruptions and those identified in BC1, Dye 3, and GRIP from 1795 to 1980. Shown are (A) years of known eruptions, and in cases where the eruption was only identified in BC1, the BC1 timeline was used; (B) the VEI; (C) checked if the event is indicated in BC1 Sulfate (the magnitude of the event in the ice core records is indicated as small or large by "x- or x+"); (D) checked if the event is indicated in BC1 Sulfate; (E) checked if the event was found in Dye 3 record; (F) checked if the event is indicated in GRIP record; (F) name of volcano, if known; (G) uncertainty with the date, if any.. 231

A.3 Compares timing of known eruptions and those identified in BC1, Dye 3, and GRIP from 1648 to 1795. Shown are (A) years of known eruptions, and in cases where the eruption was only identified in BC1, the BC1 timeline was used; (B) the VEI; (C) checked if the event is indicated in BC1 Sulfate (the magnitude of the event in the ice core records is indicated as small or large by "x- or x+"); (D) checked if the event is indicated in BC1 Sulfate; (E) checked if the event was found in Dye 3 record; (F) checked if the event is indicated in GRIP record; (F) name of volcano, if known; (G) uncertainty with the date, if any.. 233

A.4 Compares timing of known eruptions and those identified in BC1, Dye 3, and GRIP from 1648 to 1450. Shown are (A) years of known eruptions, and in cases where the eruption was only identified in BC1, the BC1 timeline was used; (B) the VEI; (C) checked if the event is indicated in BC1 Sulfate (the magnitude of the event in the ice core records is indicated as small or large by "x- or x+"); (D) checked if the event is indicated in BC1 Sulfate; (E) checked if the event was found in Dye 3 record; (F) checked if the event is indicated in GRIP record; (F) name of volcano, if known; (G) uncertainty with the date, if any.. 235

A.5 Compares timing of known eruptions and those identified in BC1, Dye 3, and GRIP from A.D. 1000 to 1450. Shown are (A) years of known eruptions, and in cases where the eruption was only identified in BC1, the BC1 timeline was used; (B) the VEI; (C) checked if the event is indicated in BC1 Sulfate (the magnitude of the event in the ice core records is indicated as small or large by “x- or x+”); (D) checked if the event is indicated in BC1 Sulfate; (E) checked if the event was found in Dye 3 record; (F) checked if the event is indicated in GRIP record; (F) name of volcano, if known; (G) uncertainty with the date, if any... 237

LIST OF FIGURES

Figure Page

1.1 Position of the polar and subtropical jet streams during a Positive PNA 3

1.2 Position of the Polar Jet Stream during a Negative PNA 4

1.3 Map of NINO 1+2, NINO 3, NINO 3, NINO 3.4, NINO 4, and Puerto Chicama, Peru 7

1.4 ENSO indices 1950 to 1960. Plot of the monthly SOI and SST anomalies at NINO 3.4 and Purto Chicama. Values of the SOI have been standardized and inverted for ease of comparison with SST anomalies 11

1.5 The average number of El Niño events per a decade using a 50-year window (recalculated at yearly intervals) based on data from *Quinn* (1987)................................ 15

1.6 The primary impact on study areas during a strong AL 16

1.7 Surface Pressure (A) and SST (B) anomalies associated with positive PDO Index... 22

2.1 Detailed maps of drilling location (B and C), surrounding weather stations (A), volcanoes (B), mountain ranges (A). 33

2.2 Complete β- profile of BC1 with depth plotted against decays per unit time. The 1963 β- peak is labeled as "A".. 35

2.3 Comparison of BC1 and BC2 at the 1963 β- showing the similarities of the two profiles. Depth in meters is plotted at the top of each graph. (Note the depth scale is not the same for each graph.) Graph A shows (1) δ18O and (2) β- disintegrations per hour for BC1. Graph B shows (1) δ18O and (2) β- disintegrations per hour for BC2. The point labeled "A" in both graphs is time equivalent. 36

2.4 Detailed profiles of ^{3}H, dust, K+, and δ18O from 1962 to 1964 and interpreted seasonal cycles in BC1. Dotted lines correspond with annual peaks in ^{3}H. The point A corresponds with the 1963 β- peak. Depth is plotted in meters at the top and the bottom of the graph. Note: Potassium is shown as it exhibits a different profile than dust and the other ice core parameters. 37

2.5 Average monthly precipitation at Chitna, Gulkana and McCarthy in mm of precipitation. Note that precipitation is at its lowest in April and that a secondary low occurs in November. Data were obtained from the Western Regional Climate Center ... 39

2.6 Mean temperatures in Alaska since 1949. Note rapid increase after 1976 PDO shift.45

2.7 Detail of Katmai Eruption in BC1 with (A) Sulfate (B) Chloride (C) Fluoride (D) Dust and (E) $\delta^{18}O$. The depth scale for A-E is given at the bottom of figure, and the timeline is given at the bottom of A. Note that Sulfate levels are up to 10x higher than background in 1912 and parts of 1913.. 47

2.8 Detail of Tambora and Unknown (1810) volcanic event in BC1 with (A) Sulfate (B) Chloride (C) Fluoride (D) Dust and (E) δ18O. The depth scale for A-E is given at the bottom of figure, and the timeline is given at the bottom of A. Note that Sulfate levels are up to 5x higher than background in 1815-1816 and 3x higher in 1810-1811.................. 48

2.9 The 39 dust peaks identified in BC1 between 2001 and 1963. Each peak that was counted is labeled in consecutive order between 1 and 39 in the shaded row just below the peaks. Depth is plotted at 5m intervals so as not to be confused. This graph is shown to verify the annual nature of the peaks in dust. 49

2.10 Regression plot of BC1 $\delta^{18}O$ and BC1 dust. In general, a strong correlation is observed between $\delta^{18}O$ and dust, but a group of years between A.D. 760 and 777 are seen as outliers to this general relationship. This could occur as background dust levels increased during this period in association with the eruption of the White River Ash. ... 55

2.11 Time series of $\delta^{18}O$ and dust from BC1 from A.D. 500 to 2001. The high dust concentrations (denoted with arrow) occurring between A.D. 760 and 777 could be associated with White River Ash 56

2.12 Photos of Ash at A.D. 760 to 770 (416 m) in BC1 that could be reworked White River Ash. The portion of the core between 416 and 417m where this material is found has the highest dust concentration besides the bottom of the core. The volcanic shards are quite small, and the ice core itself is not as transparent and has almost grayish milky coloring here, as compared to the rest of the core 57

2.13 Correlation plot of 20-year averages of BC1 mean dust (pink) and ratio of Q1/Q3 of dust. Q1 refers to the 1st quartile of samples within a year and Q3 to the third quartile. In general, the ratio Q1/Q3 has a strong relationship to the average annual dust, but a group of years between A.D. 760 and 777 are seen as outliers to this general relationship. This occurs because the actual dust peak (Q1) is not changed, but the background dust level is higher (Q3). The general relationship is that higher average dust is associated with larger dust peaks or higher Q1 values (where Q3 is relatively constant). The increase in background levels of dust is unusual and could be the result of reworking of the White River Ash in the environment. 58

2.14 Illustrates the process of the construction of seasonal composites. (A) The original unprocessed ice core data are shown in detail for the year 2001. Depths correspond with top of each sample. (B) The transformed depths are shown with values between 0 and 1. (C) The .05 ST increments are shown, and which sample corresponds with each arrow can be seen. 61

2.15 Seasonal composites of each ice core variable. Each is shown for a 2-year interval. Age increases with depth to the right. The "T" in the circle with the attached dashed line marks the location of the ^{3}H peak, based on 3 years of data discussed in Section 2.3.2, and * marks the location of a possible winter peak in Na^+, Cl^- and Mg^{2+}. 62

2.16 d-excess profile and events in BC1 63

2.17 Dust profile and events in BC1 64

2.18 δO^{18} profile and events in BC1 65

2.19 Nitrate profile and events in BC1 66

2.20 Calcium profile and events in BC1 67

2.21 Magnesium profile and events in BC1 68

2.22 Chloride profile and events in BC1 69

2.23 Sodium profile and events in BC1 70

2.24 Sulfate profile and events in BC1 71

2.25 Ammonium profile and events in BC1 72

2.26 Potassium profile and events in BC1 73

2.27 Number of weather stations reporting peaks in ^3H in each month between 1962 and 1966. Based on weather station data collected under GNIP from Adak, Bethel, and Palmer in Alaska and Ottawa, Canada 74

2.28 Spring- and fall-based years in BC1. All values are standardized between 0 and 1 for ease of comparison 77

2.29 Ice Core δO^{18} and possible subdivision of the ice core year. Values of $\delta^{18}O$ were standardized between 0 and 1 79

2.30 Ice core δO^{18} and subdivision of the ice core year with Q3 and Q1 defined.......... 80

2.31 Comparison of short cores and long cores from BC. Points B and C are labeled for BC1 and then shown with arrows for the other ice cores 82

2.32 Depth-adjusted comparison of the shallow and long cores from BC 83

2.33 Difference in meters between BC1 and BC2 at time-equivalent horizons recognizable in both BC1 and BC2 84

2.34 The 500-year record of BC accumulation (5-year average) and the timing of large BC dust events. The large dust events are shown with arrows and labeled A-E. Note that all long-term variability has been removed from the time series.......... 86

2.35 Alaska Long Precipitation Record and BC1 Accumulation Time Series where both time series are plotted as z-scores.......... 91

2.36 BC1 accumulation time series and NCEP/NCAR Lapse Rate for BC (A) and Yakutat 200 mb and 700 mb Radiosonde data (B).......... 92

2.37 BC1 d-excess and Aleutian Low time series, 5-year averages 1902-1993.......... 94

2.38 Correlation plot of AL pressure anomalies (grouped by strength) and BC1 d-excess. 95

2.39 Time series (5-year averages) of d-excess and Godthab DJF temperatures.......... 96

2.40 % Missing d-excess samples in BC1 by year 98

2.41 Dotted lines represent the occurrence of a negative AO and weaker-than-normal AL. BC1 values are winter-based years 99

2.42 Mean 850 mb geopotential height during the 15 years from 1950-2000 with most negative values of $BC1_{q1}$ $\delta^{18}O$ 100

2.43 Mean 850 mb Geopotential Height during the 15 years from 1950-2000 with most positive values of $BC1_{q1}$ $\delta^{18}O$ 103

2.44 Surface temperature anomalies associated with the 10 most depleted (A) and the 10 most enriched (B) years since 1950 in $BC1_{q1}$ $\delta^{18}O$ 105

2.45 Correlation field between annual values of $BC1_{q1}$ $\delta^{18}O$ and DJF 200 mb geopotential height.. 106

2.46 Different flow pressure fields associated with the AO and the AL 113

2.47 Wind anomalies at 300 mb associated with weak AL and negative AO 114

2.48 DJF 300 mb Mean Vector Winds for the 5 years with the highest dust concentrations since 1950 115

2.49 Shows step changes in values of d-excess, $\delta^{18}O$, and accumulation, along with changing relationship to Icelandic Low (an AO proxy) 118

2.50 BC1 d-excess and accumulation (5-year averages) time series 119

2.51 5-year average z-scores of dust and summer temperatures from *Szeicz and MacDonald* (1995).. 124

2.52 Comparison of BC1 δ18O with last 500 years from PrCol Mt. Logan, modified from *Fisher* (2004) 127

2.53 Record of δ18O and dust. Shows gradual increase in (decrease) δ18O (dust) from A.D. 270 to A.D. 1200-1400. Followed by higher (lower) periods during the time periods A.D. 1400 to 1750 and lower(higher) values since A.D. 1750. * = White River Ash? , A= large isotope excursion 131

3.1 Location of the Quelccaya drill site. 135

3.2 Quelccaya δ^{18}O and NIÑO 4: SSTs time series in the NINO 4 region in the tropical Pacific Basin and the Quelccaya δ^{18}O record show a strong relationship for the entire 142-year record. ($r=0.646$, $p<0.001$) [y-axis representing normalized values] 145

3.3 Quelccaya δ^{18}O and Pacific SSTs. Correlation field map of Quelccaya δ^{18}O and SST for the period 1945-2003. Correlations are derived from SST and δ^{18}O values that were smoothed with a 5-year centered average 146

3.4 Reason for difference between hand count and automated 147

3.5 δ^{18}O events as defined by a 30-year centered average from A.D. 800 to 2000 150

3.6 Dust events as defined by a 30-year centered average from A.D. 800 to 2000 153

4.1 Comparison of the use of different sliding windows in the determination of ENSO events using the automated method. The y-axis is the number of events in A and the ratio of El Niño to La Niña events in B 159

4.2 Compares different cutoff points using different levels of the standard deviation... 160

4.3 Example of hand selection of ENSO events 164

4.4 Shows the effect of splitting annual dust peak on calculated values 165

4.5 Comparison of hand and automated counts 166

4.6 Illustration of differences between hand and auto count 167

4.7 El Niño events during the last 100 years and ice core time series 170

4.8 Comparison between El Niño events as defined by *Quinn* (1992) and ice core data (A.D. 2000 to 1750). 172

4.9 Comparison between El Niño events as defined by *Quinn* (1992) and ice core data (A.D. 1500 to 1750). 175

4.10 Shows multirecord index 178

4.11 Arrow labeled 2- point to dominant decadal variability observed in NINO 4 SST. Box labeled 1 shows negative regime in the PDO when values are generally low over several decades.. 179

5.1 Comparison of (A) BC δ18 and Quelccaya δ18O (B) calculated from 20-year averages from A.D. 1000 to 2000. (C) Shows a 50-year sliding correlation window, which was recalculated annually. 182

5.2 Comparison of (A) d-excess and Quelccaya δ18O (B) calculated from 20-year averages from A.D. 1000 to 2000. (C) Shows a 50-year sliding correlation window that was recalculated annually 184

5.3 Ice core variables, PDO, and ENSO events during the last 100 years. Positive PDO regimes are shaded, and El Niño events are indicated by arrows in each time series. (A) Shows Quelccaya δ18O, (B) BC d-excess, (C) BC δ18O, and (D) BC Accumulation. All of the time series are plotted as standardized values between -1 and 1 as described in the text. ENSO events are defined as periods when both the SOI and NINO 3.4 exceed more than 1 std, for more than 6 months in a year... 189

5.4 Comparison between Quelccaya δ18O and coral record from Guam by *Asami* (2005). Dashed line represents annual values δ18O, and the dark line is the 5-year average. Up-pointing arrows are cool events as reconstructed by corals from Guam before 1870, and down-pointing arrows are warm events as reconstructed by corals from Guam before 1870 (*Asami*, 2005) 191

5.5 Comparison between δ18O and *Cobb* (2001) SB17 coral record from A.D. 1152 to 1217. Both records are presented as 5-year averages for easy comparison (see text). Arrows are drawn to show a possible lead and lag relationship between the two records. 193

5.6 Comparison between δ18O and *Cobb* (2001) Spl 14 coral record from A.D. 1320 to 1462. Both records are presented as 5-year averages for easy comparison (see text). Arrows are drawn to show a possible lead and lag relationship between the two records. 194

5.7 Comparison between δ^{18}O and *Cobb* (2001) SB17 coral record from A.D. 1637 to 1700. Both records are presented as 5-year averages for easy comparison (see text). Arrows are drawn to show a possible lead and lag relationship between the two records. 194

5.8 A comparison between δ^{18}O and *Cobb* (2001). Modern coral record from A.D. 1889 to 1995 shows that both records are strongly related, as peaks are easily matched in both records. Both records are presented as 5-year averages for easy comparison (see text). 195

5.9 Compares the reconstructed SW PDSI and drought events to the response in the ice core records from Quelccaya and Bona Churchill from A.D. 1000 to 2000. Dashed lines represent the largest drought events in the record of SW PDSI. (A) Quelccaya δ^{18}O, (B) BC1 δ^{18}O, (C) BC d-excess, (D) BC accumulation, (E) SW droughts during the MWP from Table 5.8 are shown as "*", (F) SW PDSI Reconstruction. Drought events from the SW PDSI reconstruction that match with Quelccaya δ^{18}O are indicated underneath (A) as either "+" matching, "-" not matching or "?" difficult to define. All time series are shown as 5-year averages and are scaled between -1 and 1 for easy comparison 206

5.10 Drought events during the MWP (A.D. 1200 to 1300) and during the last 150 years depicted as dashed lines and shown overlaid on the time series of the year averages of SW PDSI and Quelccaya δ^{18}O. Drought events shown as dashed lines occur at 1213–1221, 1246–1258, and 1272–1297, as identified by *Grissino-Mayer* (2002) and in 1855-1865, 1889-1896, 1931-1940, and 1950, as identified by *Herweijer* (2007)................. 208

5.11 Compares the reconstructed PNW PDSI and drought events to the response in the ice core records from Quelccaya and Bona Churchill from A.D. 1600 to 2000. Dashed lines represent the largest drought events in the record of PNW PDSI, as derived from Table 5.3. (A) Quelccaya δ^{18}O, (B) BC1 δ^{18}O, (C) BC d-excess, (D) BC accumulation, (E) PNW PDSI Reconstruction. The box labeled "a" is one of the larger drought events during the last four centuries, and it is depicted for easy comparison with the ice core records. Time series are shown as 5-year averages and are scaled between -1 and 1. ... 209

5.12 Cold and warm temperature regimes, as identified by *Ware* (2000), compared (A) Quelccaya δ^{18}O, (B) BC1 δ^{18}O, (C) BC d-excess, (D) BC accumulation from A.D. 1600 to 2000, and (E) cold and warm regimes of *Ware* (2000). *Ware* (2000) identified cold and warm regimes based on reconstructed temperatures from tree ring at different locations along the coast of the western United States (see Section 5.4.2.3). Warm regimes are depicted with shaded boxes that overlie the rest of the time series. Time series are shown as 5-year averages and are scaled between -1 and 1. 212

5.13 Comparison of positive and negative PDO regimes as identified by *Verdon and Franks* (2006) with (A) Quelccaya δ^{18}O, (B) BC1 δ^{18}O, (C) BC d-excess, (D) BC accumulation from A.D. 1600 to 2000, and (E) positive and negative PDO regimes identified by *Verdon and Franks* (2006). Periods with a positive PDO are depicted with shaded boxes that overlie the rest of the time series. Time series are shown as 5-year averages and are scaled between -1 and 1 213

CHAPTER 1

INTRODUCTION TO PACIFIC CLIMATE VARIABILITY

This thesis primarily focuses on investigating how different modes of interannual to decadal climate variability are recorded in the ice cores from Quelccaya and Bona Churchill (BC). This chapter examines the paleoclimatic history and climatic impacts of El Niño Southern Oscillation (ENSO), the Pacific Decadal Oscillation (PDO), the Aleutian Low (AL), the PNA (Pacific North American) pattern, the Siberian High (SH), the North Atlantic Oscillation (NAO), and the Arctic Oscillation (AO). The specific regional climatic effects of these different modes of climate variability are examined further. The concept of "climate regimes" is discussed as it provides a conceptual basis by which to link synoptic scale phenomena that occur at timescales of days to weeks with the physical variability observed in the ice core that is only resolvable at seasonal or greater timescales.

1.1 The ENSO phenomena

1.1.1 Introduction

ENSO is widely recognized as the largest contributor of interannual climatic variability on the planet. ENSO events originate from changes in atmospheric and oceanic variability in the tropical Pacific, but they alter climate on a global scale. The ENSO phenomena consist of both atmospheric and oceanic components. “EN,” the first two letters of ENSO, refers to the “El Niño component” and is associated with predictable changes in the pattern of Sea Surface Temperatures (SST) in the equatorial Pacific and along the western coast of South America. The second two letters of ENSO refer to the Southern Oscillation (SO), which is a pattern of contrasting and alternating atmospheric pressure between Tahiti (French Polynesia) and Darwin (Australia). ENSO is often called a “coupled ocean-atmosphere phenomena” because the induced changes in

SST are intimately linked with changes in the atmosphere. ENSO events recur on average every 3 to 7 years, and although they occur semi-periodically, the occurrence of individual events is difficult to predict.

The far-reaching climatic effects of ENSO that occur outside the tropics are known as teleconnections. ENSO teleconnections in North America result from changes in the average positions of the subtropical and polar jet streams that are induced by changes in the Walker Circulation (*Hoerling and Kumar*, 2000). ENSO-induced changes in the average position of the jet stream result in anomalous patterns of both precipitation and temperature across North America (Fig. 1.1 and 1.2). Generally, the effects of La Niña are similar to those of El Niño, but opposite in sign. ENSO-driven shifts in North American jet stream patterns are best expressed by changes in the PNA pattern and also by the attendant changes in the strength and position of the AL.

1.1.2 A brief history of the study of ENSO

The local fishermen of Peru were familiar with the periodic warming of Peru's coastal waters long before the Spaniards arrived. The Peruvians named this phenomenon La Corriente El Niño (child of Christ) or El Niño. In 1895, at an international Geographical Society Conference in Lima, Federico Pezet remarked, "That this hot current has caused the great rainfalls in the rainless regions of Peru appears a fact" (*Nash*, 2002). It is clear that by the 1890s the idea of the El Niño event as an important modifier of local climate was in place. Gilbert Walker was the first to describe the SO in detail and published two landmark papers, in 1923 and 1924, outlining his findings.

It wasn't until the 1960s that researchers began to recognize that El Niño events, which at the time were primarily thought to be of only regional significance, might affect climate on a global scale. *Bjerknes* (1969) demonstrated that changes in the distribution of SSTs in the Pacific were related to changes in the intensity of the Walker Circulation and that changes in one would induce changes in the other. The work of Bjerknes effectively linked the atmospheric component and the SST temperature component of ENSO as a coupled atmosphere-ocean phenomenon; thus, our modern concept of ENSO was established.

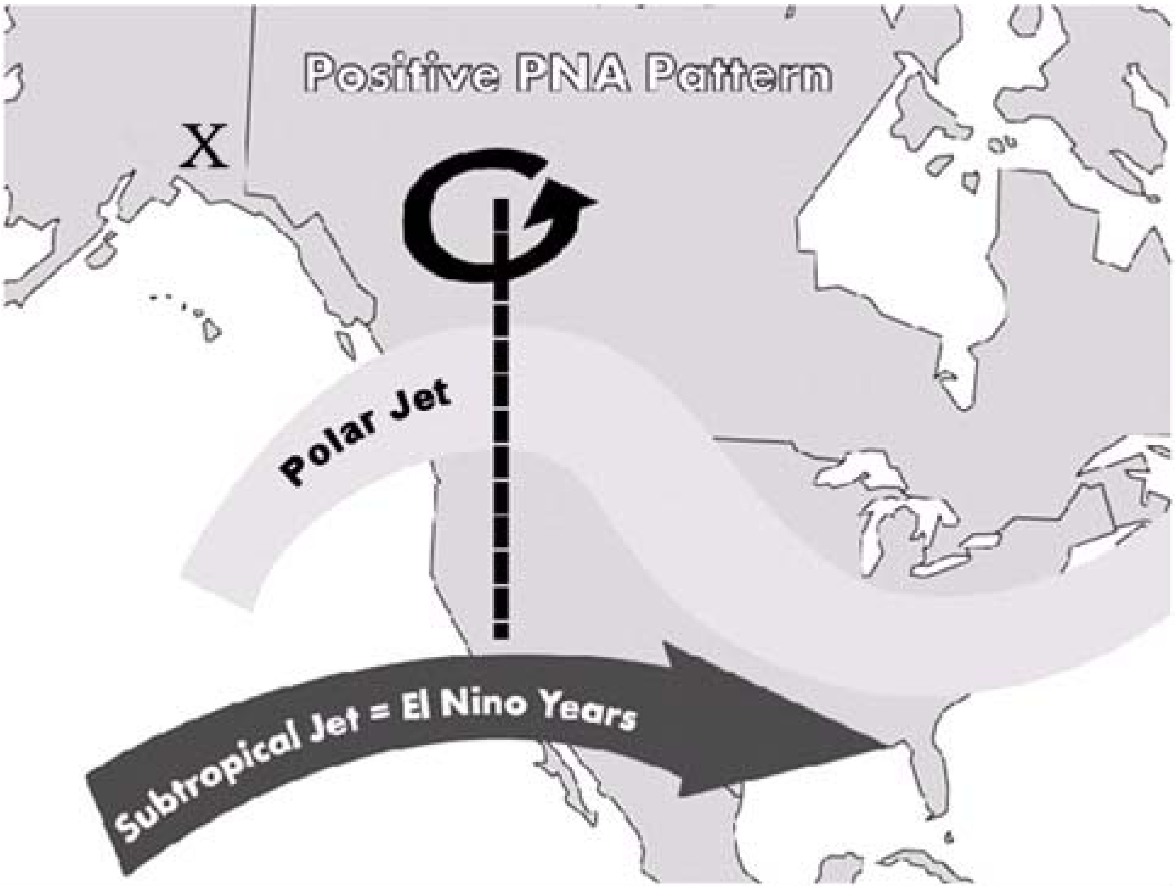

Figure 1.1 Position of the polar and subtropical jet streams during a positive PNA pattern. This pattern occurs more frequently during El Niño years. Small changes in the orientation of the axis are common in all years and often result in large changes in precipitation patterns in the western United States, but temperature anomalies remain similar. The black line represents the axis of the western ridge, and "X" marks the location of Bona Churchill.

Figure 1.2 Position of the Polar Jet Stream during a negative PNA pattern. Negative PNA patterns occur more frequently during La Niña years, but do not occur exclusively during La Niña years. "X" marks the location of the Bona Churchill drill site.

Bjerknes (1969) linked fluctuations in the strength of the trade winds to SSTs in the Pacific by proposing that stronger trade winds (La Niña conditions) result in upwelling of cold water along the South American coast and pile warm water up in the western Pacific, while weaker trade winds (El Niño conditions) result in a disruption of upwelling and an enlargement of the West Pacific Warm Pool (WPWP). Bjerknes proposed that the winds themselves were generated by the differences in SST, so that the two processes mutually reinforce each other, but what Bjerknes's work leaves unclear is whether changes in SST drive atmospheric circulation patterns or vice versa.

Klaus Wyrtki (1975) proposed that the collapse of the trade winds started much farther west than the coast of Peru. This is in opposition to Bjerknes, who believed that a weakening of the trades occurred first in the east (shutting off upwelling along the coast of Peru). Wyrtki's proposal was based on new evidence showing that the elevation of the sea surface was up to a foot higher on the western side of the Pacific (warm side) during a La Niña. Once the trade winds in the western Pacific stopped blowing, the warm water could travel back to the east in a narrow channel along the equator as a Kelvin wave. Wyrtki's work explains how temperatures along the coast of Peru could warm even before the trade winds had diminished in strength.

Global climate models have been used to investigate potential changes in future ENSO variability resulting from global warming. Unfortunately, predictions based on these models are of limited use, as different models indicate a wide range of possible responses. On the plus side, the development of these models has highlighted a number of issues regarding the underlying physical processes that determine how ENSO variability might respond to global warming or cooling. For example, the modeling results of *Clement* (1996) suggest physical controls of oceanic processes, whereby a warming of the Pacific basin would result in an increase of SSTs only in the western Pacific, resulting in a more “La Niña-like” SST gradient across the Pacific. The physical processes suggested by *Clement’s* (1996) results are supported by historical observations of SST during the last 100 years, which indicate that the western Pacific has warmed by 0.2° C, while warming in the eastern tropical Pacific has been virtually absent (*Latif et al.,* 1997). This example shows how model results could provide an underlying physical mechanism to support one's interpretation of historical or proxy data.

1.1.3 ENSO components and progression: the SO, SSTs, and Walker Circulation

The Southern Oscillation Index (SOI) is a measure of the standardized differences between the pressure at Tahiti (Eastern Pacific) and the pressure at Darwin (Western Pacific). This pressure field oscillates through time with changes in the SO correlating strongly with the distribution of sea surface temperatures in the tropical Pacific. Large positive values of the SOI, associated with La Niña conditions, indicate a tighter pressure gradient across the Pacific, a stronger South American High, and an intensification of trade winds. Negative values of the SOI are associated with El Niño conditions, a weaker pressure gradient across the Pacific, a weaker South American High, and weaker trade winds. Records of the SOI are available from the 1870s to the present, but the earlier records are of poorer quality and often have missing data points.

The Walker Circulation refers to a pattern of west to east circulation along the equator. The rising limb of this circulation is centered near Indonesia, and the falling limb is located in the eastern Pacific along the coast of South America. The rising limb occurs in the region where SSTs are highest and is associated with a region of maximum convection in the Pacific. The descending limb is associated with subsidence, stability, and little rainfall. The position of the rising limb shifts eastward (westward) during El Niño (La Niña) events, producing changes in patterns of rainfall distribution in the tropics.

NINO 1, 2, 3, 3.4, and 4 are different indices of SST temperatures used to document changes in SSTs both along the coast of South America and in the equatorial Pacific. Niño 1 and 2 give information about coastal SSTs, and Niño 3, 3.4, and 4 give information about areas progressively westward (Fig. 1.3). SSTs along the coast of Peru have been recorded at Puerto Chicama since 1925 and are very similar to records from the NINO 1 and 2 records.

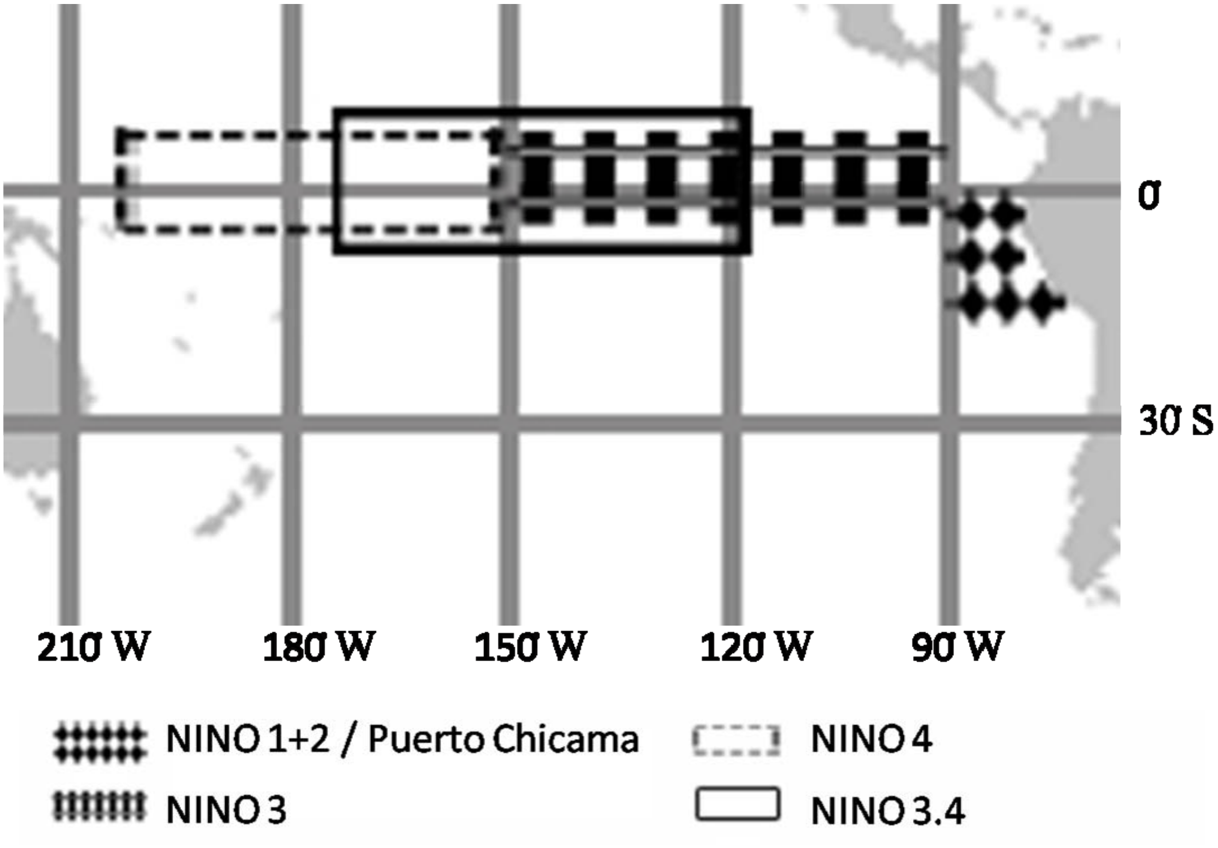

Figure 1.3 Boxes show the location of NINO 1+2, NINO 3, NINO 3.4, NINO 4, and Puerto Chicama (Peru). NINO indices are calculated by averaging the SST within each box.

Rasmusson and Carpenter (1982) attempted to define the normal sequence of events during an El Niño based on a composite of six different events. These events all occurred when the PDO was negative; therefore, the defined sequence may not be representative of the broader population of El Niño events. Despite this attempt to define a typical progression, it must be stressed that El Niño events are often variable and not always predictable. A case in point is the extreme El Niño event that developed during 1982-1983. Despite the magnitude of the 1983 event, weather forecasters completely missed forecasting its development. Interestingly, Rasmusson's and Carpenter's paper, in which the "typical" El Niño event was described, had just been published, and their description of the '"typical" El Niño event describes the initial phase of an El Niño as warming along coastal Peru. However, the 1982 event began with warming in the central

Pacific. This demonstrates the problem of relying on generalizations made from the relatively short historical record. In fact, El Niño events that have occurred since 1983 have all started with warming in the central Pacific rather than warming along the South American coast. This is evident in the time series of monthly NINO 3.4 and Puerto Chicama SST, which show Puerto Chicama SST leading changes in the other indices before 1983.

1.1.4 Defining ENSO events

No consensus or standard definition exists to define the required criteria for a year to be classified as either an El Niño or a La Niña year. As part of the research for my master's thesis (*Urmann,* 2003), several different methods for defining the occurrence of ENSO events were investigated, and it was observed that while individual lists of El Niño years may vary slightly, the larger events are obvious in all of them (*Urmann*, 2003). The side-by-side plot of the different Niño indices shows that before 1982, changes in Puerto Chicama SSTs lead those observed in NINO 3 and 3.4. However, this situation is reversed after 1982 (*Wang*, 1995)

1.2 The history of ENSO variability for the past 1,000 years

Previous reconstructions of past ENSO variability have been based upon historical records, ice core data, global climate models, and the variations in annual growth rings of both fossil corals and trees. Several studies of decadal and centennial climate variability in regions where ENSO has strong modern teleconnections suggest that a more El Niño-like state may have existed during the LIA, and more La Niña-like conditions may have prevailed during the MWP. Table 1.1 reviews and highlights the findings of past studies as well as the limitations with which they can be applied.

Proxy Record	**Location**	**Author**	**Results (with respect to El Niño)**
Moisture-sensitive conifers	New Mexico	*D'Arrigo and Jacoby* (1992)	→Decadal changes in precipitation →Highest: 1906-1930 →Lowest: 1566-1595 and 1870-1894
Tree ring network	Western United States	*Lough* (1992)	→Changes in NA ENSO teleconnection: →Low # of events 1851-1900
Historical record of Quinn	Coastal regions of Peru, Ecuador, and Chile	*Quinn* (1987) *Diaz and Pulwarty* (1992)	→Peaks in frequency 1680-1770 and 1820-1930 →Several periods with very low reoccurrence intervals mark the record
Historical record of Quinn	Nile River levels, Egypt	*Quinn* (1992)	→More frequent during LIA than MWP →Large El Niño in A.D. 1200
Multiple proxy records: historical, tree ring, and ice core	Peru; Western United States	*Michaelsen and Thompson* (1992)	→No significant change in ENSO activity from LIA to present →Higher activity: early 1700s and 1900s →Lower activity: early 1800s
Corals	Galapagos	*Dunbar* (1994)	Greater ENSO activity in 1600s and 1800s
Corals	Palmyra: Central Tropical Pacific	*Cobb* (2003)	→Peak in ENSO activity 1650-1680, similar to 1997 →Decrease during MWP
Climate model	N/A	*Mann* (2005)	→Increase in LIA →Decrease in MWP

Table 1.1 Proxy ENSO records for 1,000 years.

This review of the current literature reveals no clear consensus on the relationship between ENSO variability and the climatic shifts associated with either the LIA or the MWP (Table 1.1). Several reasons account for this lack of consensus. One reason is that only a small number of high-resolution records are available from the tropics. For example, although several LIA fossil corals have been examined, only one fossil coral from the MWP is available, and this solitary record provides the foundation for several theories pertaining to ENSO behavior during the MWP. Another reason for the lack of consensus is that a large proportion of proxy-based ENSO reconstructions are from regions outside the tropics. As such, they can be viewed only as reconstructions of region-specific teleconnections rather than of ENSO itself. A final reason is that even high-quality annually resolvable paleoclimatic records often have a degree of uncertainty in the dating. This uncertainty makes comparing reconstructed records of individual ENSO events nearly impossible, as an error in dating as small as one year can invalidate the entire comparison.

Studies of the growth rings of fossil coral have provided interesting "snapshots" of ENSO variability through time. For instance, fossil corals from the Palymra Island (162° W, 6° N) indicate a peak in ENSO intensity from 1650 to 1680. Notably, the magnitude of events during this period appears similar to the large 1997 event (*Cobb et al.,* 2003). Additionally, fossil coral records from the Galapagos indicate that greater than present variability in SST occurred during the 1600s and 1800s and suggest that the 1982-1983 El Niño was the strongest event to occur since 1586 (*Dunbar et al.,* 1994).

Instrumental records of El Niño events extend back to the 1850s and increase in reliability through time. Instrumental records have been extended using historical accounts of the regional effects of El Niños and their related global teleconnections. For instance, *Quinn* (1987) and *Ortlieb* (2000) use the documented local effects of El Niño to reconstruct a history of events from 1500 to 1900 using records of rainfall, shipwrecks, fishing logs, drought, and flooding events in Chile and Peru. The record of Quinn suggests that El Niño frequency was at its lowest in 1650 and highest at 1890 (Fig. 1.4.).

However, it is difficult to draw meaningful conclusions from the trends because the use of reconstructions based on documentary evidence is limited by the changing availability of records through time and by the qualitative, rather than quantitative, nature of these records.

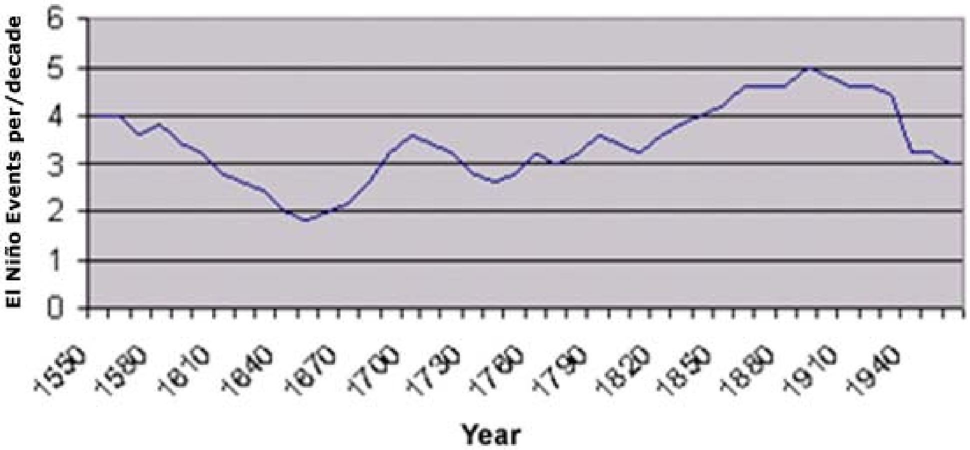

Figure 1.4 The average number of El Niño events in a 10-year period (recalculated at yearly intervals). The record of El Niño is based on data from Quinn (1987).

Several studies have used tree ring data from the western United States to reconstruct the North American ENSO teleconnection (*Lough*, 1992; *D'Arrigo and Jacoby*, 1992; *Stahle*, 1998; *D'Arrigo*, 2006). A tree ring study by *Stahle et al.* (1998) used tree ring data from the southwestern United States and from Indonesia to reconstruct the SOI from 1706 to 1977. Several features of importance stand out in the reconstruction. First off, the reconstructed SOI exhibits a period of low variance centered around 1840 and shows an increase in the level of variance after 1879. Second, the number of cold events, and to a lesser degree warm events, increases after 1879. In fact, the entire record from 1706 to 1977 shows an evolution toward more La Niña-like conditions. Whether this is the result of a change in ENSO or simply representative of a change in the southwestern United States, teleconnections is difficult to determine. A study by *D'Arrigo* (2006) makes use of a similar, but expanded and updated, tree ring data set as used in the study by *Stahle* (1998) to reconstruct ENSO variability during the last 600 years. The study focuses on solar modulation of ENSO variability and finds evidence for increased ENSO variability associated with the Spörer (A.D. 1450) and Dalton (A.D.1800) minima, but not with the Maunder Minima (A.D.1700).

A study by *Cook* (2004) of tree rings from the southwestern United States shows that drier conditions prevailed during the period A.D. 900 to 1300 and that wetter conditions persisted from 1300 to the present. A 400-year reconstruction of precipitation from teak chronologies in Thailand, where El Niño events are associated with drought, indicated the occurrence of two long and persistent decadal scale droughts centered at 1705 and 1740 (*Buckley et al.,* 2007). Additionally, a study by *Verschunn* (2000) of lake levels in equatorial east Africa found that lake levels peaked from 1650 to 1750 and were at a minimum during the period A.D. 1000 to 1200. These conditions respectively suggest El Niño and La Niña-like conditions.

Some recent evidence suggests that one might be in error to link more El Niño-like conditions in the Pacific with the occurrence of more frequent and/or stronger El Niño events. Historical observations of SST indicate that a more “La Niña like” state has evolved during the past 100 years (*Latif et al.,* 1997), even as the frequency of El Niño events has increased. This apparent contradiction exemplifies how crucial it is to define what is meant by the terms “El Niño-like” or “La Niña-like.” Using these terms may be appropriate to describe long-term climatic shifts, but their relationship to actual changes in ENSO variability is not well documented.

1.3 The response of ENSO to climate change

No clear consensus exists as to how the effects of either climatic or solar variability affect the behavior of ENSO, but several possibilities exist. The first is that ENSO operates independently of global climatic variations. A second would be that an “ocean thermostat” exists whereby tropical cooling has the effect of producing a more El Niño-like state. The third is the opposite in that tropical cooling (warming) would result in less (more) El Niño events. The study of *Stahle* (1998) suggests that more La Niña-like conditions have evolved in the Pacific between the end of the LIA and the present in response to warming. Furthermore, existing coral data seem to suggest the possibility of an Ocean Thermostat, but this needs to be confirmed by the examination of additional fossil coral specimens from the MWP.

A recent study by *Mann* (2005) using a simplified Zeibak-Cane model investigated the response of ENSO to solar and volcanic forcing. The part of the study dealing with solar forcing is of particular interest, as changes due to solar forcing can be regarded as analogous to changes due to greenhouse warming. *Mann* (2005) argues for an "ocean thermostat (per *Clement et al.,* 1996)" whereby warming of the Pacific basin is distributed so that the east cools and the west warms, creating a more La Niña-like state. This result is evident in the model output as NINO 3.4 temperatures are inversely correlated with solar forcing. This ocean thermostat hypothesis agrees with observed SST trends in the tropical Pacific that were mentioned previously and with paleoclimate data, cited by *Mann* (2005), of ENSO conditions during the Medieval Warm Period and Little Ice Age.

Several modeling studies along with observational data have pointed toward changes in tropical circulation patterns that may alter the strength and frequency of ENSO events and ENSO-related teleconnections. A study of satellite data by *Fu* (2006) shows that Hadley Cells have increased in width during the last 20 years of the 21st century, possibly in response to warming global temperatures. One theory for the cause is proposed by *Held* (2006), who suggests that the width of the Hadley circulation is determined by the latitude where baroclinic eddies begin to occur. *Held* (2006) proposes that warming surface temperatures cause a poleward shift in the latitude of baroclinic eddy formation as a result of increased static stability in the subtropics. This occurs as warming results in higher atmospheric moisture content in the tropical atmosphere. Modeled results by *Dargan* (2007) simulate the increased width in the Hadley circulation in agreement with the proposed mechanisms of *Held* (2006) and with the observational studies of *Fu* (2006).

One result of the increasing width of the Hadley Circulation, which is shown by several climate models and recent instrumental evidence, is a drying in the southwestern United States (*Seager et al.* 2007). The weakening of the Walker Circulation (*Held*, 2006) in response to global warming suggests more El Niño-like conditions in the Pacific. Modeling results of *Vecchi and Soden* (2007) show that an eastward shift in precipitation occurs along with a weakening of the Walker Circulation, and this also indicates a shift toward a more El Niño-like base state.

More La Niña-like conditions or “Mega La Niña events” have been suggested as a cause for previous large-scale drought episodes in the American Southwest, such as those that occurred during the MWP (*Cook et al.,* 2004). This recent research suggests that two distinct phenomena may be responsible for droughts in the Southwest. First off, as suggested by previous studies, droughts may be associated with individual La Niña events or the development of a La Niña-like base state. Alternatively, drought conditions may develop because of a more El Niño like base state in a warmer global climate as a result of changes in the width of the Hadley Circulation.

1.4 Interannual climate variability in the North Pacific

1.4.1 The Aleutian Low

The Aleutian Low (AL) is a semi-permanent area of low pressure that is typically centered over the Aleutian Islands. The AL is the dominant feature of circulation (Fig. 1.5 and 1.6) in the North Pacific (NP), and in the upper troposphere it is associated with a larger feature known as the East Asian Trough. The AL has a strong influence on the climate of North America during the winter. However, during the summer the AL weakens and the general storm track moves northward. Traveling cyclones generally develop to the northeast of Japan and reach a maximum intensity in the region of the AL. *Zhu* (2006) defines the Low as not a climatological low but merely as a low “on average” produced by the perpetual progression of cyclones through the region. The timing of the maximum intensity as well as the trajectory of the average cyclone defines the mean climatological AL.

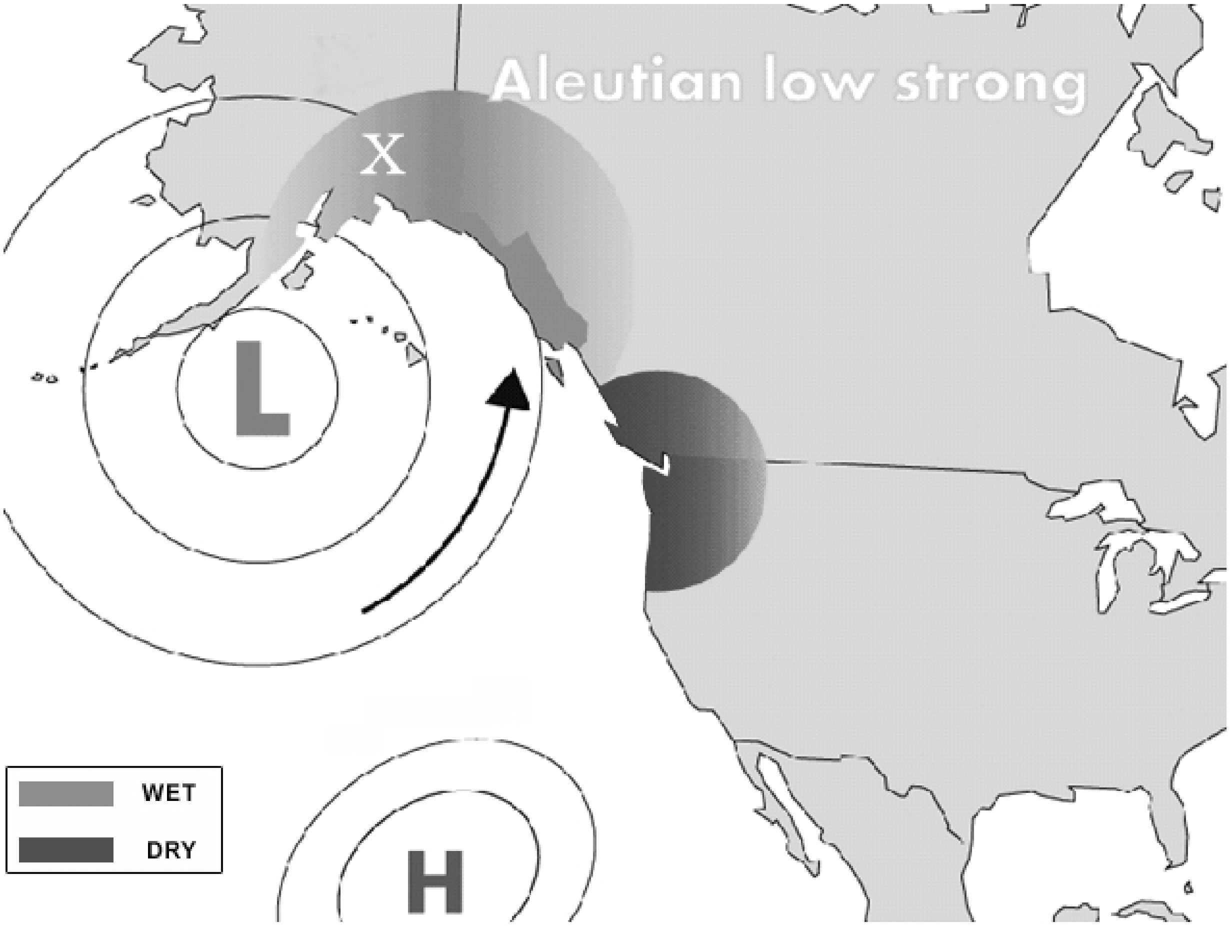

Figure 1.5 Impacts associated with a strong Aleutian Low. Temperatures at the Bona Churchill drill site are warmer than usual when the Aleutian Low is strong. The arrow in the figure highlights the stronger circulation from the tropical Pacific to the drill site, which is marked with an "X."

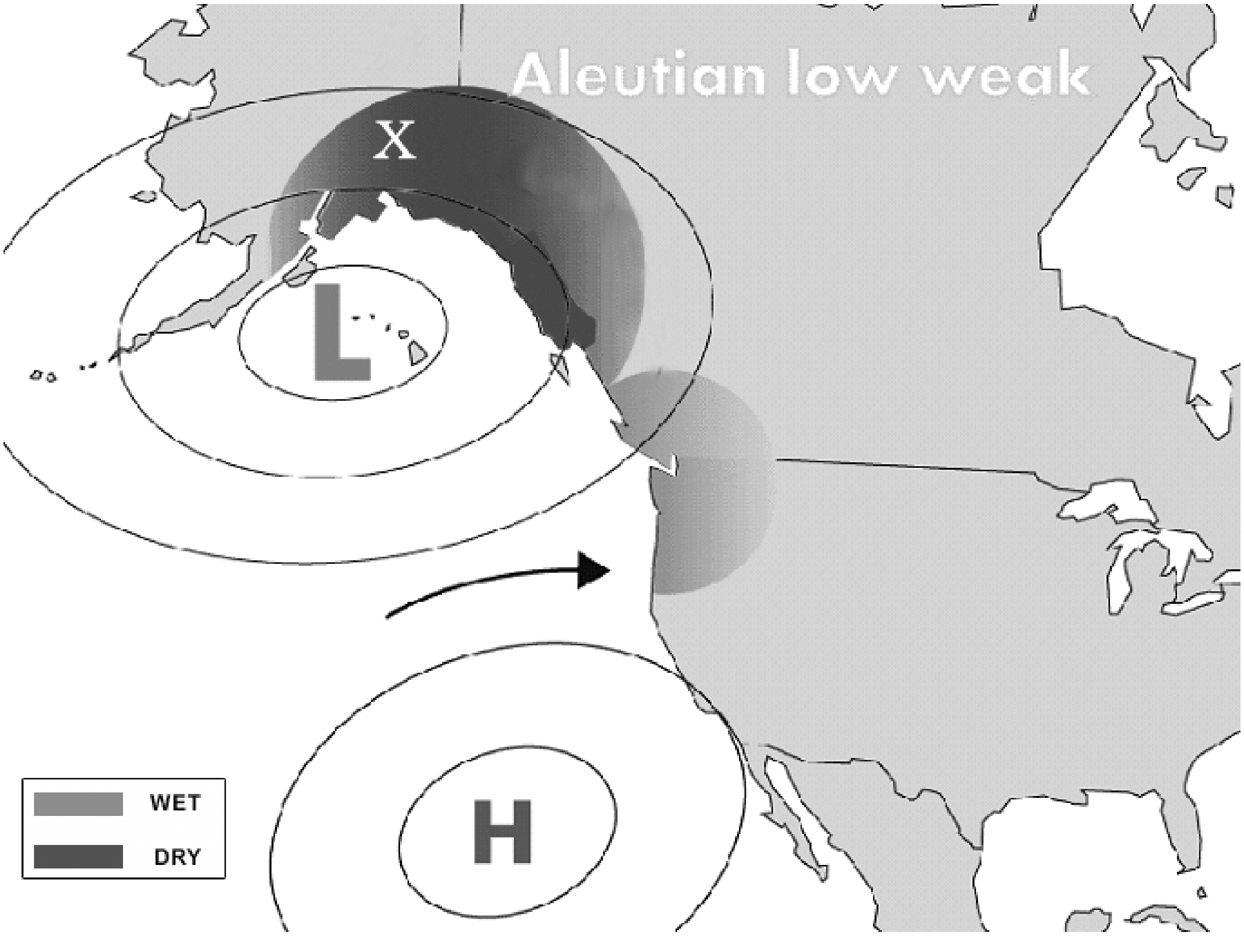

Figure 1.6 Impacts associated with a weak Aleutian Low. Temperatures at the Bona Churchill drill site are cooler than usual when the Aleutian Low is strong. The arrow in the figure highlights the weakened and more zonal circulation, which accompanies a weak Aleutian Low.

Several studies have shown that the strength of the AL is modulated by ENSO events so that El Niño events intensify the AL and La Niña events weaken the low (*Hoerling and Kumar*, 2002). Changes in the strength of the AL due to ENSO events are caused by the redistribution of areas of maximum convection along the equator that result in the development of circulation anomalies in the Northern Hemisphere. The amplitude of the anomalies generated during the winter is much greater than those generated during the summer due to the seasonal withdrawal of the jet stream to the north and a general decrease in circulation strength (*Diaz et al.,* 2001).

During years in which the AL is weak (strong), most cyclones reach a maximum intensity west (east) of the dateline (*Zhu*, 2006). Wind flow patterns in the mid troposphere during years in which the AL is strong are characterized by a more zonal flow west of 160° W and a more meridional component only near the North American coast.Weak years are characterized by more variability due to weaker steering winds and a maximum meridional wind component west of 160° W (*Zhu*, 2006). In the upper troposphere during strong years, one finds a broad trough across the North Pacific, and an intensified zonally stretched jet traverses most of the Pacific. Weaker years exhibit a narrowed trough restricted to the western Pacific and a ridging pattern in the eastern Pacific (*Zhu*, 2006). Several studies have found that when the AL is shifted to the east it is more intense (*Overland*, 1999; *Zhu et al.,* 2006).

The strength of the AL varies seasonally but also undergoes significant decadal variability. A study by *Overland et al.* (1999) on January and February anomalies of the strength of the AL showed that 37% of the monthly variance was across periods longer than five years. Long-term shifts in the strength of the AL occurred in 1925, 1931, 1939, 1947, 1959, 1968, 1977, and 1989 (*Overland et al.,* 1999). Monthly values of Aleutian Low pressure and the location of the Aleutian Low for the period 1899-1995 were obtained from http://atmos.msrc.sunysb.edu/coa/index.shtml. Monthly values of the Aleutian Low index are area-weighted and do not represent the central pressure of the low.

1.4.1.1 Late Holocene reconstructions of the Aleutian Low

The record of ^{18}O in sedimentary calcite from Jelly Bean Lake in Alaska provides a high-resolution record (5 to 30 years) of North Pacific circulation for the last 7,500 years (*Anderson et al.,* 2005). This record shows that periods of intensification occurred during the interval from 4500 to 3000 years B.P. and during the period centered between 1200 and 300 years B.C. (*Anderson et al.,* 2005). *Anderson* (2005) suggests that the dominant direction of onshore flow in relationship to the orientation of the coastal ranges may play an important role in fractionation processes driving changes in the record of δ^{18}O from Jelly Bean Lake. When the AL is strong, a southerly flow directs moisture into the coastal ranges, resulting in increased rainout along the coastal side of the mountains and in the emplacement of a more depleted air mass in the interior of Alaska. This flow contrasts to that occurring with a weaker AL; this results in a more zonal flow and a more westerly trajectory that is able to move parallel to the coastal mountains and hence undergoes less fractionation as the moisture mass moves inland.

Records of the productivity of Pacific fisheries have also been related to long-term shifts in the strength of the Aleutian Low. A study by *Finney* (2002) examined δ^{15}N measurements in lake sediment cores from Kodiak Island, Alaska to reconstruct salmon abundance during the past 2,000 years. Carcass remains from salmon contribute a significant amount of nutrients to lake ecosystems in this region compared to other sources, and the record of sedimentary δ^{15}N can be used as a reliable indicator of past salmon productivity. The reconstructed record of Salmon productivity constructed by *Finney* (2002) shows that productivity began a gradual increase around A.D. 100 and continued gradually increasing until A.D. 1200. Overall higher levels of productivity persisted between A.D. 1200 and 1900. The gradual increase in productivity seen in the earlier part of the record might have occurred due to intensification and eastward migration of the AL during this period (*Anderson*, 2005).

Comparisons of *Finney's* (2002) reconstruction of salmon productivity with *Baumgartner's* (1992) reconstructions of anchovy and sardine productivity off the coast of California suggest that an inverse relationship exists between these records so that when salmon productivity is high, anchovy and sardine productivity is low. Furthermore, the records of Alaskan salmon productivity are also inversely related to records of fish remains from Saanich Inlet, British Columbia (*Tunicliffe et al.,* 2001). The independent response by different records in different regions suggests that long-term changes in fishery productivity may be driven by coherent patterns of basin-wide climate change.

The record of $\delta^{18}O$ from the Mt. Logan ice core has been related to large-scale shifts between mixed (strong AL) and pure zonal (weak AL) flow regimes (*Fisher et al.,* 2004). *Fisher* (2004) identifies two important regime shifts, one at A.D. 800 and another at 1840 that may mark abrupt transitions between zonal and mixed-flow regimes. *Fisher* (2004) suggests that the period before each shift was dominated by zonal flow and colder conditions, and the period after the shift was dominated by mixed flow and warmer conditions. Although the transitions from zonal to mixed regimes occurred abruptly in the time series of Mt. Logan $\delta^{18}O$, the transitions from mixed back to zonal occurred gradually following each regime shift.

The Mt. Logan record and the record from Jelly Bean Lake both indicate that an abrupt transition in circulation took place at A.D. 800. This is in contrast to the records of fishery productivities from Alaska and California, which suggest that the transition from a weak to strong AL was a gradual process that began at approximately A.D. 100 and culminated by A.D. 1200. In fact, the most significant transition in the records of fishery productivities occurs at A.D. 1200 and coincides with the termination of the MWP.

1.4.2 The Pacific North American pattern

The PNA describes the primary patterns of atmospheric flow across the United States and Canada. A positive PNA pattern is characterized by the development of a strong AL, increased meridional flow over North America, a reinforced Canadian high, and the development of a deeper than normal trough over the eastern United States (Fig. 1.1). A negative PNA pattern is characterized by a weakening of the AL and Canadian high, which results in more zonal flow across the United States, the development of a weak trough over the Pacific, and a weak ridge over the western United States (Fig. 1.2). *Yarnal and Diaz* (1986) showed that small changes in the position or shape of the PNA pattern might result in large changes in precipitation patterns along the west coast of the

United States. Temperature patterns are, in general, more uniform and resistant to small changes or perturbations of the PNA pattern (*Yarnal and Diaz,* 1986).

Changes in the PNA pattern represent the primary North American ENSO teleconnections (*Yarnal and Diaz,* 1986). During warm (cool) phases of both ENSO and the PDO, the PNA tends to be positive (negative). Positive and negative PNA patterns are not unique to either El Niño or La Niña events, and roughly 50% of positive and negative events occur during years when ENSO is not a significant factor. However, positive (negative) PNA patterns are twice as likely to develop during warm (cold) events (*Yarnal and Diaz,* 1986). Positive PNA patterns occurred in 54% of the El Niño months and 24% of the non-El Niño winter months (*Yarnal and Diaz,* 1986). The reverse PNA was found by *Yarnal and Diaz* (1986) to occur in 50% of La Niña winter months versus 25% of non-La Niña winter months. Because the AL is one of the centers of action used to define the PNA pattern, a strong correlation exists ($r=0.89$ and $p < 0.05$, 1949-1995) between the strength of the AL and the PNA index. This suggests that a proxy reconstruction of the AL index from ice core data would also serve as a reconstruction of the PNA index.

1.4.3 Pacific Decadal Oscillation (PDO)

The PDO, like ENSO, is an oscillatory mode of SST variability, but it is centered over the North Pacific and operates over periods of decades rather than the shorter timeframes associated with ENSO. Positive (negative) phases of the PDO favor high (low) salmon production in Alaska and off the coast of California, Oregon, and Washington (*Mantua*, 2002). During positive (negative) phases of the PDO, SSTs are warmer (cooler) than normal along the west coast of North America and in the Gulf of Alaska (Fig. 1.7) (*Hare and Mantua*, 2000). The PDO generates a characteristic atmospheric pressure anomaly so that during a positive (negative) PDO a low-pressure (high-pressure) anomaly is centered over the North Pacific and a high-pressure (low-pressure) anomaly is centered over the western United States (*Mantua*, 2002). These atmospheric anomalies are primarily expressed during October through March. The atmospheric anomalies associated with the positive (negative) phases of the PDO can be associated with positive (negative) PNA patterns (*Mantua*, 2002).

The PDO operates on a much longer timescale than ENSO, with positive and negative phases persisting on the order of 20-30 years. Prior shifts in the mode of the PDO occurred in 1924-1925 and in 1946-1947 (*Mantua,* 2002). The PDO index is defined as the principal component of SST anomalies in the Pacific pole-ward of 20º N. Global SST anomalies were removed from each month of data in order to remove long-term global trends and to isolate the North Pacific. The index of the PDO (1900-2002) used in this study was obtained from JIASO: http://www.jisao.washington.edu/pdo/.

ENSO and the PDO both force similar atmospheric anomalies over North America, but although both modes of variability force changes in the PNA pattern, ENSO events also force changes in the strength and amount of moisture that is transported from the tropics by the subtropical jet stream. In general, the Southwest is wetter during positive phases of the PDO, but this may be due to the positive amplification of ENSO events that results from a positive PDO rather than due to the effects of the PDO that are independent of ENSO. Separating the effects of the PDO from those of ENSO can be difficult, given the similar climate response of these variables.

1.4.3.1 Tropical--extratropical interactions (PDO vs. IPO variability)

The Inter-decadal Pacific Oscillation (IPO) refers to coherent changes in SST that occur across the entire Pacific Basin (Fig. 1.7). A study by *Chavez et al.* (2003) showed that basin-wide changes in SST caused similar variations in sardine populations off the coasts of Peru, Chile, Japan, and California on decadal timescales (*Chavez*, 2003). Shifts in the ratio of the number of sardines to anchovies occurred in approximately 1925, 1950, and 1975, and most recently in the mid-1990s (*Chavez*, 2003). A second line of evidence for IPO variability comes from the studies of corals by *Linsley* (2000) in the South Pacific. Proxy records of temperature from corals in the South Pacific (21º 30’ S, 159º 30’ W) show that "several of the largest decadal changes observed during the last 100

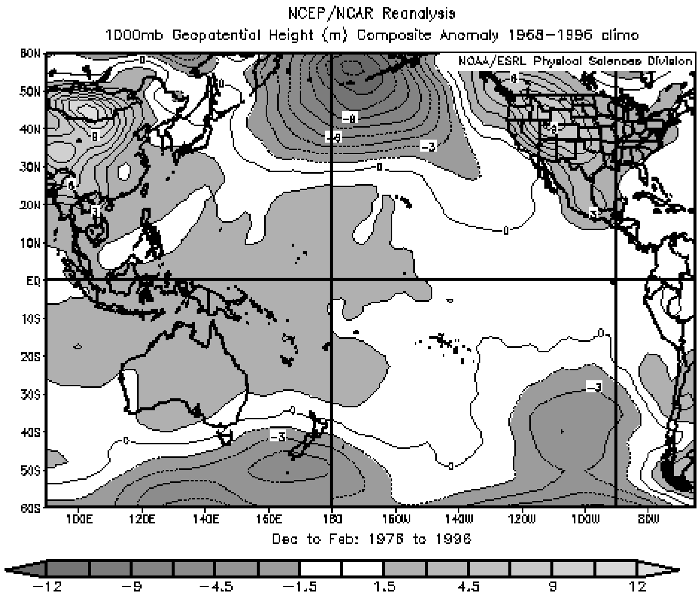

A. Surface Pressure Anomalies in mb with PDO+

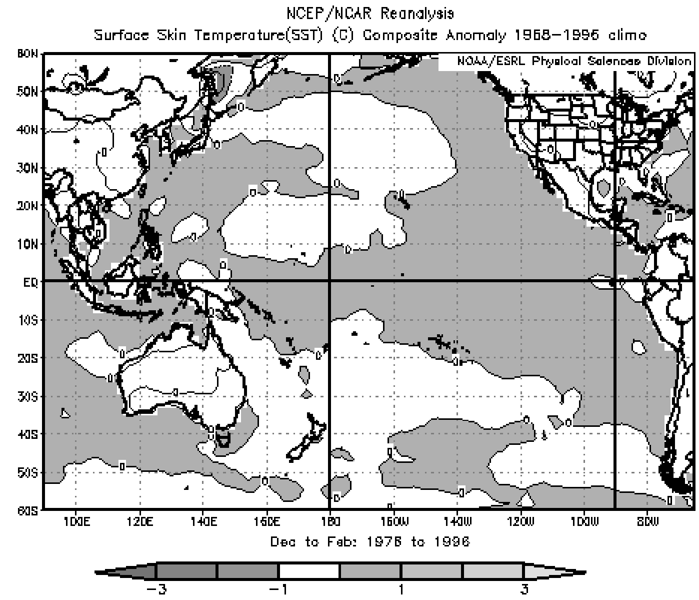

B. SST Anomalies in C° with PDO+

Figure 1.7 Surface Pressure (A) and SST (B) anomalies associated with a positive PDO Index. The effects of a negative PDO pattern are similar, but opposite in sign.

years are in phase in the North and South Pacific gyres." A more recent study by *Linsley* (2004) using an approximately 300-year record of SSTs from fossil corals growing in the South Pacific and North American tree ring-based reconstructions of PDO variability. It shows that PDO variability has been more consistently in phase with IPO variability since 1880 and that before 1880, little relationship existed between these two variables. *Linsley* (2004) also found that this shift in 1880 was related to amplitude of the IPO signal so that larger amplitude fluctuations took place after 1880 and smaller fluctuations before 1880.

Despite the evidence from corals and biological proxies for IPO variability, the relationship between tropical and North Pacific variability that occurs at both decadal and interannual timescales remains unclear and will require a longer record of both modes of variability. Three possible drivers of PDO variability were reviewed by *Nakamura* (1997):

1. The PDO is a result of tropical forcing.
2. The PDO is a result of extratropical forcing.
3. The PDO is a result of both tropical and extratropical forcing. In particular, the North Pacific subtropical gyre is most influenced by the tropics, and the subpolar gyre, of the North Pacific, is influenced by conditions outside of the tropics.

Decadal variations in SSTs in the North Pacific are most prominent along both the subarctic and subtropical fronts (*Nakamura et al.,* 1997). The subarctic front marks the boundary where cool water from the subpolar gyre interacts with warm water from the Kuroshio Extension. The subtropical front is located to the north of Hawaii and trends in a northeast-southwest direction.

SST variability along the subtropical front is related to tropical SST variability, but variability along the subarctic front is not (*Nakamura et al.,* 1997 Changes in the strength of the Pacific high are tied to variability along the subtropical front, and changes in the AL are associated with changes along the subpolar front (*Nakamura et al.,* 1997). It might be argued that tropical SST variability is linked to SST variability in the North Pacific via atmospheric teleconnections. *Nakamura* (1997) argues that at least some of the variability seen in this region is independent of the tropics. One line of reasoning is that cooling along the subarctic front occurred two years earlier, in 1974, than the subsequent tropical warming, in 1976, that was supposed to have forced the cooling in the first place. The relationship between the subtropical front and PDO variability allows room for ENSO variations to be reflected in the PDO index. *McCabe and Dettinger* (2002) suggest that the PDO in some sense is a measure of how ENSO events influence the evolution of North Pacific (NP) SSTs.

1.4.3.2 PDO variability during the last millennium

A number of studies relying both on coral and tree ring data have attempted to reconstruct past regime shifts in the PDO index. Although numerous studies have reconstructed past regime shifts, the study by *Verdon and Franks* (2006) that examines North Pacific climate variability since A.D. 1600 does an excellent job of identifying common regime shifts prevalent in studies by *Biondi* (2001), *D'Arrigo* (2001), *Gedalof and Smith* (2001), *MacDonald and Case* (2005), and *Linsley* (2000). Regime shifts that stand out in the study *Verdon and Franks* (2006) occurred in 1661, 1680, 1696, 1717, 1725, 1760, 1776, 1790, 1805, 1825, 1924, 1942, and 1975. Using this time series of regime shifts and reconstructions by *D'Arrigo* (2005) and by *Mann* (2000) of ENSO, *Verdon and Franks* (2006) concluded that the influence of the PDO on the ratio of El Niño to La Niña events is consistent during the last 400 years.

Gedalof and Mantua (2002) used five independently reconstructed PDO indices, some of which have been previously mentioned, in order to find the leading mode of variability between these different reconstructions during the period 1840 to 1990. The first principal component of this analysis is well correlated with the PDO index (r=0.64) during the period of record, and the reconstruction identifies key regime shifts in 1977, 1947, and 1905, but misses the 1925 shift (*Gedalof and Mantua,* 2002). The intercorrelations between the different proxy indices are strongest since 1975 and weaker during the period 1825 to 1875, suggesting variations in the strength of the signal across the Pacific.

A study by *Wilson* (2006) used a network of tree ring data from the Gulf of Alaska (GOA) to identify regime shifts in the North Pacific during the last 1,300 years.

This record captures known historical shifts in the 1970s, 1940s, and 1920s and shows that similar shifts occur frequently in the longer record as well. However, several prolonged periods, from A.D. 970 to 1070, A.D. 1150 to 1250, and A.D. 1450 to 1650, stand out because of an absence of shifts during these time periods. Another study, by *Biondi* (2001), used a network of tree ring records from Baja and southern California that were sensitive to changes in winter precipitation to reconstruct the PDO since 1661. This reconstruction shows that decadal variability has persisted since 1661 and has not undergone a substantial change in character. However, variability during the last 100 years appears to occur at a somewhat lower frequency than in the earlier part of the record. Other interesting features are a contraction in the amplitude of the signal centered at 1800 and significant shifts in the mode of the reconstructed index, which took place at 1750, 1905, and 1947.

MacDonald and Case (2005) used tree ring data from precipitation-sensitive species in Alberta and California to reconstruct the PDO from A.D. 993 to 1996. This study finds that the 50- to 70-year PDO frequency has been strong during the last 200 years and only sporadically strong before that. Periods with a strong 50- to 70-year periodicity include A.D. 1300 to 1500 and A.D. 1000 to 1200, while the period A.D. 1600 to 1800 is marked by absence of variability at this amplitude. Another significant feature of this record is the occurrence of a persistently negative PDO from A.D. 900 to 1300. This period in which the PDO is persistently negative overlaps with a period in which tree reconstructions show that the western United States was in a persistent drought (*Cook*, 2004). Higher than average values are observed between A.D. 1450 and 1550, and lower than average values are observed from A.D. 1600 to 1800. Comparisons of this reconstruction with previous tree ring-based reconstructions show that a strong correlation exists (r=0.57) with the correlation by *Biondi* (2001).

Gedalof and Smith (2001) used tree ring records from Oregon and Alaska to reconstruct PDO variability from A.D. 1600 to 2000. It is noted that an absence of regime shifts occurs between A.D. 1840 and 1923. Significant shifts, some of which were equal in magnitude to the 1976 shift, occurred in A.D. 1662, 1680, 1696, 1712, 1734, 1758, 1798, 1816, 1840, 1923, 1946, and 1977. Interdecadal variability is dominant between

A.D. 1662 and 1840. Interannual variability is dominant from A.D. 1840 to 1930, and the authors suggest a possible shift back to an interdecadal mode in 1976.

D'Arrigo (2001) used tree rings from the Gulf of Alaska, the Pacific Northwest, and sites in Mexico to reconstruct PDO variability for the past 300 years. The analysis by *D'Arrigo* (2001) argues that tree ring components from the southwestern United States (precipitation sensitive), as well as records from Alaska (temperature sensitive), are required to create a realistic reconstruction of the PDO index, because using two different sites allows region-specific climate variability to be eliminated from the equation. Additionally, the PDO may exhibit both high- and low-latitude bands of variability so that records from both these bands are required for a reconstruction. The reconstruction itself suggests lower-amplitude PDO after the mid 1800s.

Linsley (2000) compared coral records from the South Pacific (Rarotonga; 21° S, 160° W) with 15 circum-Pacific tree ring indicators, as presented by Evans et al. (2001b). A comparison of these records shows similar symmetry about the equator, suggesting that the PDV has a tropical source and that variability is propagated by a fast-acting mechanism such as the atmosphere. Coral and tree ring records show increasing decadal coherency in the 20th century and weaker coherency between A.D. 1820 and 1880.

Minobe (1997) examined historical records of Pacific and Indian SST along with data from 65 tree ring sites in the United States and Canada to reconstruct Pacific climate variability. This study identified regime shifts in A.D. 1890 and 1920, in addition to the later shifts that occurred in 1947 and 1976. It is interesting to note that the 1890 shift is not as clearly indicated in the proxy reconstructions just discussed. The 50- to 70-year period in the PDO is seen in the tree record from 1800 to 1900 and in the instrumental record from 1900 to the present so that this mode of variability has been present since 1800.

1.4.4 Siberian High--East Asian winter monsoon

Patterns of upper-level air flow across Asia are important predictors for winter cyclone development in the Pacific. The Siberian High (SH) is a semi-permanent area of high pressure that is centered over northern Mongolia and is strongest during the winter when ground temperatures are coldest (*Panagiotopoulos et al.,* 2005). A strong SH and deep AL are associated with a more active East Asian Winter Monsoon (EAWM). Indices of the EAWM are strongly correlated with the strength of the mid-latitude jet stream as it exits Asia and with surface temperatures in Japan, Korea, and eastern China (*Chang*, 2005). At the surface, the AL is a closed low-pressure cell that approximately straddles the dateline, but at the 500mb level it is a low-pressure trough that is centered further east, approximately over the Sea of Oshtok (*Jhun and Lee*, 2004). Cyclonic circulation around this trough coupled with anticyclonic circulation around the SH bring cold polar air southward into Asia. The strength of this cold air flow is directly related to the strength of the EAWM. Studies also indicate that a stronger EAWM is associated with stronger-than-normal convention over the western Pacific (*D'Arrigo et al.,* 2005). Tree ring reconstructions of the SH by *D'Arrigo* (2005) indicate that the weakening of the SH since the 1970s is the most significant feature in the entire record from A.D. 1599 to 1980.

1.4.5 Arctic Oscillation and the North Atlantic Oscillation

The Arctic Oscillation (AO) measures changes in the distribution of atmospheric mass from high to low latitudes. When the AO is in a positive mode (the reverse occurs during the negative mode), the circumpolar vortex is strong; the jet stream in the mid latitudes exhibits a more zonal trajectory; and outbreaks of polar air into the mid latitudes are less frequent (*Thompson and Wallace,* 2001). Although the NAO is calculated differently from the AO, both of these time series are virtually identical. A preference to the AO is given in this thesis when reporting observed correlations, as it is calculated using a global rather than an Atlantic-based data set.

Changes in the strength of the AO are closely linked to the strength of the primary NH centers of action. *Rossby* (1939) first identified a correlation between the strength of the AL with the mean pressure difference between 35° N and 55° N. A stronger (weaker) AL is associated with the negative (positive) phase of the AO. Studies of the SH by *Jhun and Lee* (2004) show that it is more closely correlated with the AO than other teleconnections indices and that the strength of this correlation increases at decadal timescales. The degree to which the AO, AL, and SH exhibit independent variability and the amount that is shared is the subject of debate, as is the question regarding whether these relationships have changed through time. For instance, a recent study by *Castanheira* (2003) found that a significant negative correlation only exists between North Pacific and Atlantic pressure fields when the polar vortex is strong.

1.4.5.1 Reconstructions of the NAO/AO

Numerous studies have examined potential proxies for reconstructing NAO variability, but resultant time series often correlate poorly. *Cook and D'Arrigo* (2001) performed a multivariable/multiproxy reconstruction of the NAO from A.D. 1400 to the present. This shows that the persistently positive phase exhibited by the NAO during the latter half of the 20th century is out of the ordinary but not unique. One feature that stands out from this reconstruction and others like it is the lack of any persistent or low-frequency trends. However, an examination of a longer record of the reconstructed Icelandic SLP and of the Siberian High based on Greenland ice cores by *Meeker and Mayewski* (2002) shows that before A.D. 1400, both of these centers of action were weaker.

1.5 Climate Regimes--A unifying concept

Climate regimes are defined as "persistent anomalies" in large-scale atmospheric flow patterns (*Dole and Gordon,* 1983). Seasonal anomalies and interseasonal variability are largely the result of the frequency at which a particular climate regime appears or persists. For instance, the largest difference in precipitation frequency (days/season) in the western United States is found between the positive PNA and negative PNA patterns (*Robertson and Ghil,* 1999). Defining the specific responses within a region to the persistence of a given climate regime allows a means of connecting and verifying relationships between records at different localities. For instance, during a positive PNA pattern, conditions are likely to be warm in both Alaska and the Pacific Northwest. Alaska is wetter than normal and the Pacific Northwest is drier than normal. If these types of conditions were documented in the records from both Alaska and the Pacific Northwest, it would more likely be in response to the development of a positive PNA pattern than local variability.

Forcing the atmosphere by changes in SSTs (El Niño or PDO), anthropogenic-induced changes in the composition of the atmosphere, solar variations, and so on may result in variations in the probability density function (PDF) of specific climate regimes (*Robertson and Ghil,* 1999). External forcing may result in the prevalence of a single climate regime during a particular season, and the associated climate anomalies throughout the affected region could be explained in terms of the dominance of a specific climate regime. Any particular season may be influenced by one or more climate regimes. Most climate regimes persist for only a few days to a few weeks (*Robertson and Ghil,* 1999), and half of the time the atmosphere is in a transitional state between climate regimes. Climatic regimes can be thought of as end members of different continuums, with each end member representing some idealized atmospheric flow pattern.

CHAPTER 2
THE BONA CHURCHILL ICE CORE

2.1 Abstract

The Bona Churchill Ice Core (BC1), drilled to bedrock in the spring of 2002 in the Wrangell-St. Elias Mountains of southeast Alaska (61° 24' N, 141° 42'W; 4420 meters), is one of the only annually dateable records of extended historical duration to ever be recovered from the northeastern side of the Pacific Basin. The results presented in this chapter discuss the development of the timescale, the calibration of the ice-climate relationship, and the possible extension of the ice-climate relationship during the last 1,000 years.

The timescale for BC1 is well constrained during the last 1,000 years, and annual layering is present throughout this portion of BC1. In addition to the clear presence of annual layers, the dating of BC1 is well constrained by the identification of the 1963 β-peak, the 1912 eruption of Katmai, and the 1783 eruption of Laki in the ice core. Additionally, this study pinpoints the period A.D. 760 to 777 (according to the BC1 timeline) as the likely timing of the White River Ash. The White River Ash is an important regional chronostratigraphic marker that radiocarbon dates show was deposited between A.D. 694 and 936.

The strongest climate signal exhibited by the records of $\delta^{18}O$ and dust can be considered to be the history of northerly flow (associated with weak Aleutian Low [AL] and negative Arctic Oscillation [AO]) versus southerly flow over the drill site. The analysis of the ice-climate relationship shows that the records of $\delta^{18}O$ and dust from BC1 can be related to long-term shifts in atmospheric circulation as expressed by the AL and the AO, the two primary modes of Northern Hemisphere circulation. These results show that the correlation between $\delta^{18}O$ and dust with the AL is strongest when the AO is negative. The AO acts to modulate the strength of the correlation between $\delta^{18}O$ and dust with the AL so that during periods when the AO is negative, a stronger correlation is

observed with the AL. In general, different combinations of the AO and AL result in an onshore flow from the Pacific, but circulation is substantially different and offshore flow occurs when the AO is negative and the AL is weak.

Large dust events and more negative values of $\delta^{18}O$ occur in BC1 when the AL is weak and the AO is negative, as this is associated with the occurrence of an anomalous northerly flow over the drill site that likely results in the emplacement of a dustier, colder, and more continental air mass. Large and abrupt dust events that coincide with more negative isotopic values occurred at A.D. 890, 998, 1040, 1100, 1273, 1322, 1360, 1515, 1700, 1750, 1835, and in 1966. Historical records show that the 1966 event was coincident with record cold temperatures in Alaska, a negative AO, and a weaker-than-normal AL.

High concentrations of dust and low values of $\delta^{18}O$ characterize both the MWP and LIA, and this simultaneous occurrence is strong evidence that the term time series of both $\delta^{18}O$ and dust over the last 1,000 years are not records of temperature. This thesis suggests that the influence of a negative AO and weak AL is the primary signal in BC1, and as a result one of the most striking features of the time series of both $\delta^{18}O$ and dust are the large-scale events that are shared in both records. Most of the peaks and troughs in the time series of $\delta^{18}O$ are not associated with dust events, but almost all of the significant dust events correspond with troughs in $\delta^{18}O$. This makes sense, as the record of dust events only records times when the AO is negative and the AL weak and hence only encapsulates a small percentage of modern variability.

The lack of any low-frequency AO signal, with the exception of the event at A.D. 1400, may suggest that the longer-term shifts in the record $\delta^{18}O$ and background dust concentrations are indeed reflective of AL variability. This conclusion is supported by comparisons of the record of BC1 $\delta^{18}O$ and reconstructions of salmon productivity constructed by *Finney* (2002), which show that productivity began a gradual increase around A.D. 100 and continued to gradually increase until A.D. 1200. Overall higher levels of productivity persisted between A.D. 1200 and 1900. This general trend corresponds well with BC1 $\delta^{18}O$ where it is observed that values of $\delta^{18}O$ increase gradually in the early part of the record and are less negative in general after A.D. 1200.

2.2 Introduction and background

2.2.1 The Bona Churchill Ice Cores: field work lab analysis

The Bona Churchill Ice Cores were recovered from the saddle (61^{o} 24$^{'}$ N, 141^{o} 42$^{'}$W; 4420 meters), separating Mount Churchill (61°25′N, 141°42′W. 4,766 meters) and Mount Bona (61°23′N, 141°44′W. 5,005 meters) between April 30th and June 10th, 2002 by a team of research scientists led by Dr. Lonnie Thompson from the Byrd Polar Research Institute (BPRC) of The Ohio State University (Fig. 2.1). Bona Churchill Core 1 (hereafter referred to as BC1) drilled to bedrock measures 460m in length and is the longest core ever recovered from a mountain glacier. Borehole measurements at 10m and 460m of -23.1° C and -6°C, respectively, indicate that the Bona-Churchill col supports a cold based glacier. The two summits separating the col, Mt. Bona and Churchill, lie in the northern half of the St. Elias Range in southeastern Alaska (Fig. 2.1C). The St. Elias range runs along a northwest-southeast axis approximately 100km from the coast and is characterized by the imposing elevations of its numerous peaks, including St. Elias (5490m) and Mt. Logan (6051m) and one of the world's largest mountain glacier systems.

In total, 623 meters of ice were recovered by the Bona Churchill ice core drilling team. The upper 180 meters of BC1 were drilled with an electro-mechanical drill, and the remainder was drilled using a thermo-alcohol electric drill. Drilling of BC1 ended when repeated attempts were made with different drilling techniques to extend the core without success. Large pebbles and visibly dirty ice were recovered from samples corresponding to the bottom of the ice core. This is in contrast to the rest of the ice core, which exhibits no visible dust layers. The final depth is similar to the depth calculated from radar sounding measurements, which indicated that 460m is the approximate depth of the ice.

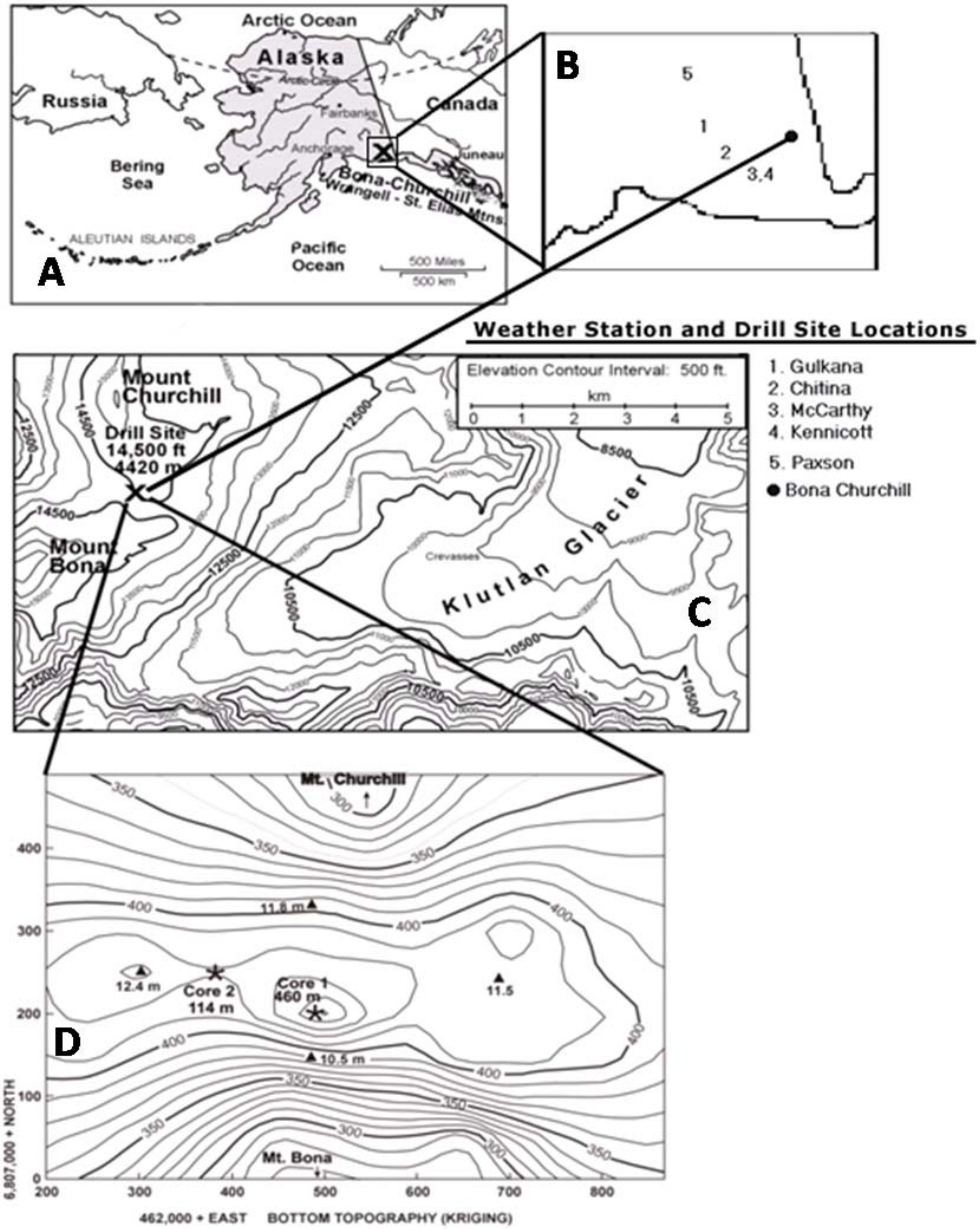

Figure 2.1 Detailed maps of drilling location surrounding weather stations (A) overview, (B) drill site in relationship to surrounding weather stations, (C) Bona Churchill saddle, and (D) Detail of drill site and locations of drilling points.

In addition to BC1, a secondary core of 114 meters in length (hereafter referred to as BC2) and four additional shallow cores (referenced as BCS-1, BCS-2, BCS-3, and BCS-4), of 10 to 12m in length were drilled in a diamond-shaped configuration across the col (Fig. 2.1D). The length of these cores is as follows: BCS1 was 12.3m in depth, BCS-2 was 11.66m, BCS-3 was 11.38, and BCS-4 was 11.14m. The shorter ice cores were obtained in order to characterize the spatial distribution of snow accumulation. All of these cores were transported in a frozen state to the cold room facilities at the BPRC for further analysis.

2.2.2 The Bona Churchill Ice Cores: laboratory analysis

Analysis and sampling of the concentrations of particulates and major ions for BC1-2 and BCS 1-4 were completed at BPRC by Mary Davis and Tracy Mashiotta. The values of $\delta^{18}O$ for BC1 and BC2 and values of d-excess for BC1 were measured by Ping-Nan Lin. The ion and isotope profiles of BC1 are based on measurements from 12,161 individual samples. Each sample was removed from the ice core using a mechanical saw in a clean low-temperature environment. The outermost 5 mm was removed from each sample in order to avoid the possibility of external contamination. A portion of each sample was then removed, and the stable isotopic ratios of oxygen and hydrogen were determined with a Finnigan-MAT mass spectrometer. The remaining portion of the sample was cleaned in a Class 100 Clean Room using purified deionized water before concentrations of microparticles were determined in 16 size ranges using a model TAII Coulter Counter. Concentrations of major ions SO_4^{2-}, $Ca^{2+,}$ NO_3^-, NH_4^+, Na^+, Cl^-, Mg^{2+}, K^+ and F^- were measured using a Dionex ICS -2500 ion chromatographs with Dionex AS 40 auto sampler, as outlined in *Thompson et al.* (2002).

The 1963 β- peak was identified in BC1 by constructing a β- profile of the top 100 m of the ice core. This profile consists of 119 samples that were taken at an average interval of approximately 84 cms and measured with a Tennelec Alpha/Beta counting system (Fig. 2.2). Higher-resolution sampling was performed across the interval surrounding the 1963 peak in both BC1 and BC2 (Fig. 2.3). Three separate β- pulses, each associated with individual annual dust peaks, are apparent in BC1. Following the

1963 peak, annual spikes in Beta activity are observed in BC1 occurring in conjunction with peaks in dust and diminishing in magnitude in subsequent years.

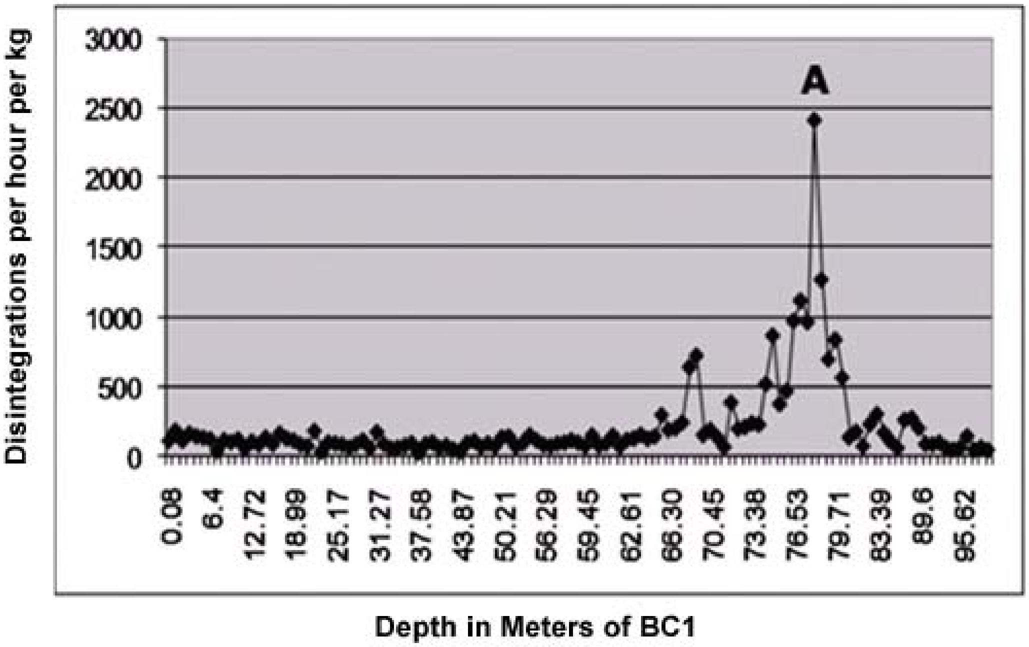

Figure 2.2 Complete β- profile of BC1 with depth plotted against decays per unit time. The 1963 β- peak is labeled as "A".

A detailed profile of ^{3}H was constructed from 29 samples collected across a segment of ice representing the 3 years of accumulation between 1962 and 1964 so that the seasonal cycle of ^{3}H in the ice core could be defined and compared with the seasonal cycles exhibited by the other ice core parameters. The ^{3}H profile for BC1, presented in Figure 2.4, is based on 29 samples, which averaged 17 cm in length and were taken from just above and below the 1963 β- peak. Fourteen of the samples were taken at an average interval of 12 centimeters between 77.33-78.89 meters so that the area encompassing the two dust spikes on either side of the 1963 beta spike could be covered at the highest resolution. The remaining 15 samples were cut from the ice adjacent to where the higher-resolution sampling ended. The increased sampling allowed us to view a larger stratigraphic section than we could have otherwise without increasing the total number of samples. Measurements of ^{3}H were made by Uli Siegenthaler using a gas proportional counter. The current detection limit in an underground laboratory is 0.32 TU (*Siegenthaler et al.,* 1975).

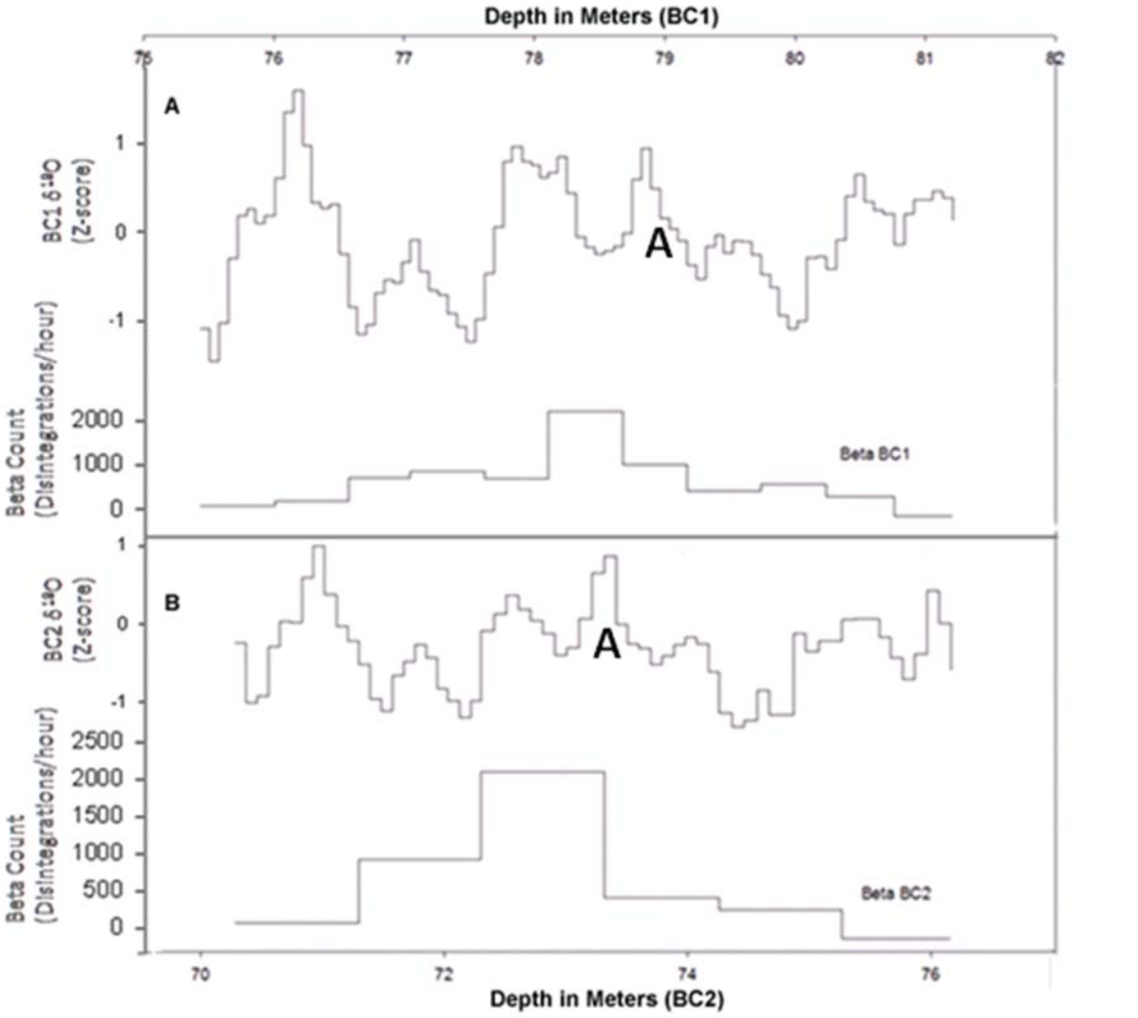

Figure 2.3 Comparison of BC1 and BC2 at the 1963 β- showing the similarities of the two profiles. Depth in meters is plotted at the top of each graph. (Note that the depth scale is not the same for each graph.) Graph (A) shows (1) δ^{18}O and (2) β- disintegrations per hour for BC1. Graph B shows (1) δ^{18}O and (2) β- disintegrations per hour for BC2. The point labeled “A” in both graphs is time equivalent.

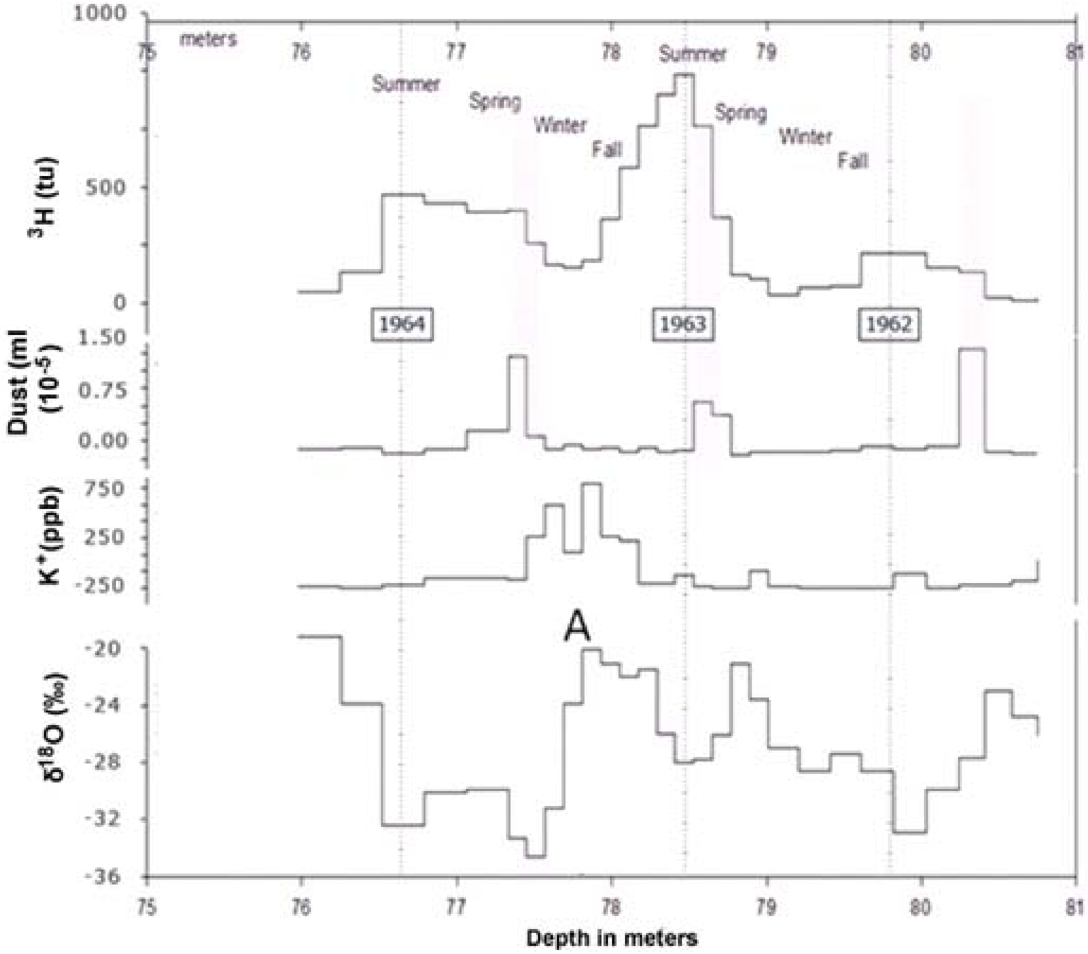

Figure 2.4 Detailed profiles of ^{3}H, dust, K+, and δ^{18}O from 1962 to 1964 and interpreted seasonal cycles in BC1. Dotted lines correspond with annual peaks in ^{3}H. The point A corresponds with the 1963 β- peak. Depth is plotted in meters at the top and the bottom of the graph. Note: Potassium is shown as it exhibits a different profile than dust and the other ice core parameters.

2.2.3 Climatology of the St. Elias Region, Alaska

Winter climate in the region is influenced by a number of different circulation patterns that result from the interaction of different modes of climate variability, which include the AL, the AO, ENSO, and the PDO. A study by *Mock et al.* (1998) identified 13 major different circulation patterns that affected the climate between Alaska and Siberia and determined that subtle shifts in circulation patterns can dramatically alter surface climate. In general, during winters when the AL is weak, flow is more zonal across the region, the air mass is drier and colder, and storms take a southerly track into the Pacific Northwest (*Rogers*, 1981). When the AL is strong, storms are steered northward toward the Wrangell Mountains and a warmer, more marine air mass (*Rogers*, 1981). Recent studies of surface air temperatures based on surface air temperatures from 14 weather stations across Alaska found a significant correlation with both the SOI and PDO between 1954 and 2000 (*Papineau,* 2001).

Much of the correlation between the SOI and temperature might itself be attributed to the PDO, as the mode of the PDO is not only associated with a stronger AL, but also with changes in the ratio of El Niño to La Niña events (*Renwick and Wallace,* 1996). ENSO has been shown to be most strongly correlated with the strength of the AL, as opposed to its position (*Rogers*, 1981). Several studies have shown that the climate of Alaska is impacted more by the position of the AL than by its strength (*Rodionov*, 2005). This finding is highlighted by a study by *Luchin* (2002), which found that the AL during warm winters was not only about 3-6-hPa deeper than normal, but also shifted 3°-6° north and 10°-20° west of its long-term mean position. The westward movement of the low favors a circulation pattern that brings a warm flow from mid latitudes of the Pacific into Alaska.

The role of the AO on climate in Alaska hasn't received a great deal of attention and has just begun to be investigated. In general, the findings of *Thompson and Wallace* (1998) suggest that when the AO is positive (negative), circulation is more zonal (meridional), temperatures are colder (warmer), and the storm track is further north (south) than usual. A recent study by *Bond and Harrison* (2006) found that much of the signal from the SOI occurred during years when the AO was negative. The study by *Bond and Harrison* (2006) found that the effects of ENSO are weaker when the AO is positive and enhanced when the AO is negative. Note: These findings are very similar to what is observed in the record of BC1, in that the AO modulates the signal of the AL in the ice core record (Section 1.4.1).

Weather station data from McCarthy, Kennecott, Chitina, Gulkana, and Paxson (station summaries in Appendix A) were examined to identify climatic patterns in the valleys surrounding the St. Elias Range. Analysis of the weather station data showed that peak mean temperatures occur during July and minimums occur during January. Peak precipitation occurs between June and September, depending on the station, with a secondary smaller precipitation peak occurring in December (Fig. 2.5). Precipitation minima occur in November and April, with April generally being the most dry month of the year. The average summer peak in precipitation, from all six weather stations, is roughly 3.5 times as large as the winter peak. However, the annual variations in summer precipitation exhibit much less year-to-year variability than winter precipitation, and as a result, winter variability may have a stronger climate signal in the ice core record than might otherwise be expected assuming that precipitation patterns at McCarthy reflect those at the drill site (*Urmann*, 2003).

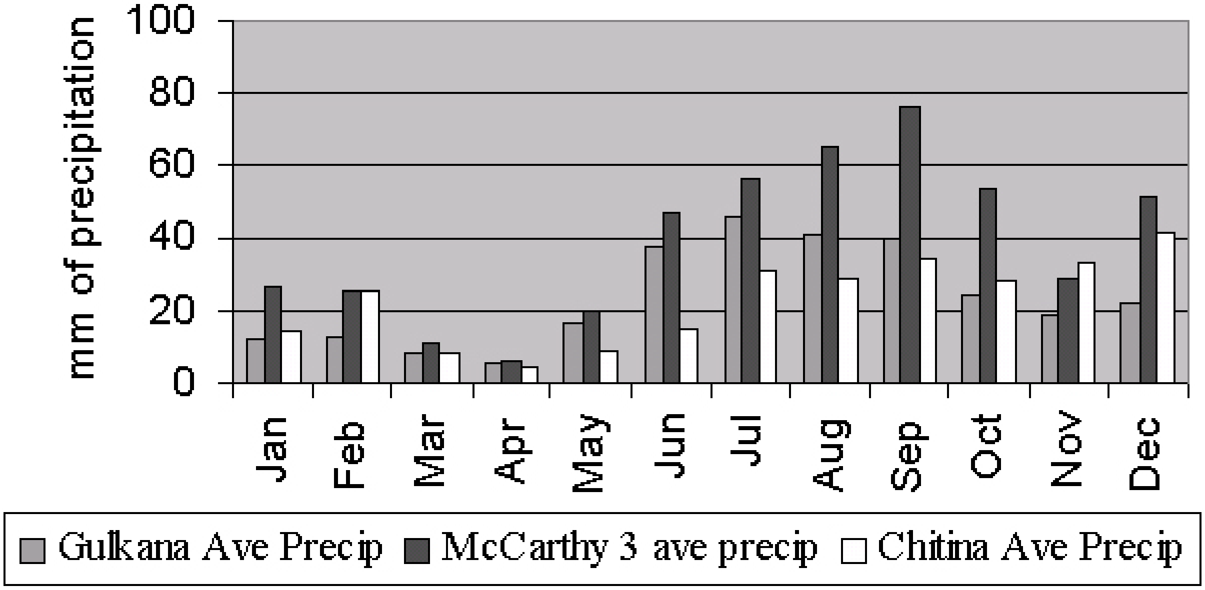

Figure 2.5 Average monthly precipitation at Chitna, Gulkana, and McCarthy in mm of precipitation. Note that precipitation is at its lowest in April and that a secondary low occurs in November. Data were obtained from the Western Regional Climate Center.

Direct relationships between ice core data and meteorological records are complicated by both elevation and geographical factors. The St. Elias Mountains lie inland from the coast and are subject to the rain shadow effect created by the Chugach

Mountains. This is exemplified by a comparison of the records from coastal weather stations, which in the case of Valdez and Cordova record up to 280 centimeters of precipitation a year. By comparison, an inland weather station, such as Gulkana, receives on average 25 centimeters of precipitation a year. Elevation also plays an important role but one that is not as quantifiable, because existing station data all come from valley locations that are subject to strong wintertime inversions.

2.2.4 Reconstructions of Alaska climate change

2.2.4.1 Overview

The Holocene climatic history of Alaska can be broadly separated into two different phases. The first was a period of early Holocene warmth (Climatic Optimum), which occurred between 8 and 5ka. This warmth was followed by Neoglacial cooling, which began between 5ka and 2ka. Neoglacial cooling was briefly interrupted by the Medieval Warm Period (MWP) years, which occurred between A.D. 800 and 1200, but continued during the Little Ice Age (LIA), which lasted from 1200 to 1900. Significant warming has occurred in the last 100 years, which likely equals or exceeds in magnitude the warming that occurred during the MWP and the earlier Climatic Optimum. Glacial expansions during the LIA exceeded prior Neoglacial advances, and the LIA likely represents the coldest period since the last ice age. The LIA and MWP were first recognized in European climate records, but attempts to place these events in a more global context has proven difficult, as these events likely occurred at different times and with varying intensity in different regions (*Luckman*, 2000). For instance, the dates just given correspond best with records from Alaska, but records from Greenland and Europe suggest a later time period for the termination of the MWP.

2.2.4.2 The onset of the Neoglacial

Conflicting evidence makes it difficult to determine the exact timing of the start of the Neoglacial in Alaska. A study by *Calkin et al.* (2001) shows that a period of early Holocene warmth was followed by Neoglacial cooling starting between about 4k BP and 3.5k BP. However, several recently developed lines of evidence point to a late start for the Neoglacial in this region. For instance, a study by *Lamoureux and Cockburn* (2005) of two lakes from White Pass, British Columbia showed that glacial-derived sedimentation didn't begin until 2ka. These results are consistent with pollen records from British Columbia and southeastern Alaska, which indicate an increase in Western Hemlock starting 2-3k BP. The arrival of pollen from this "far-traveled" exotic species could be attributed to a sustained strengthening of the AL (*Spooner et al.,* 2003). *Spooner et al.* (2003) speculate that this strengthening of the AL is coincident with the onset of more frequent El Niño events during the late Holocene, as indicated by several other studies.

2.2.4.3 The Medieval Warm Period (MWP)

Evidence from Jelly Bean Lake and the Mt. Logan core suggest that a rapid intensification of the AL at A.D. 800 marks the start of the MWP (*Anderson et al.,* 2005; *Fisher et al.,* 2004). The rapid intensification of the AL at A.D. 800 is followed in the Mt. Logan core by a gradual increase toward more positive values of $\delta^{18}O$ from A.D. 800 to 1840 that represents a weakening of the AL. A similar trend is seen in the Jelly Bean Lake record, but the reversal occurs around A.D. 1700, and according to *Anderson* (2005) it is coincident with the start of the LIA. Both of these records indicate a gradual transition out of the MWP and into the LIA, but it appears that the results of *Andrews* (2005) and *Fisher* (2004) are mutually inconsistent, as *Fisher* (2004) suggests that warming associated with the MWP coincided with the strengthening of the AL, while *Anderson* (2005) on the other hand suggests an intensification of the AL at 1700 resulted from LIA cooling.

Several lines of evidence indicate a shift from warmer to colder temperatures in Alaska at A.D. 1200 that mark the end of MWP. Studies of glacially overrun trees and fossil stumps indicate that a significant glacial advance occurred in the Wrangell Mountains as early as A.D. 1100-1200 and was generally coincident with advances that began in the coastal regions of Alaska and British Columbia by A.D. 1200 (*Calkin et al.,* 2001; *Luckman*, 2001). Tree ring records from the Canadian Rockies indicate that the period 1190-1250 was colder than normal and further support the A.D. 1200 date as an important transitional period (*Luckman*, 2001).

Further evidence for a climatic transition at A.D. 1200 comes from records of fishery productivity from both Alaska and California. A study by *Finney et al.* (2002)

reconstructing salmon abundance based on $\delta^{15}N$ from lake sediment cores recovered from Kodiak Island, Alaska show that salmon abundance peaked at approximately A.D. 1200 (see Section 1.4.1.1, on Aleutian Low). Records of anchovy and sardine productivity from the Santa Barbara Basin indicate a decrease in productivity coincident with the increase in salmon productivity in Alaska (*Baumgartner et al.,* 1992).

2.2.4.4 The LIA

Three separate intervals of cooling have been associated with the LIA in Alaska between A.D. 1200 and 1900. The timing of glacial advances has been constrained by the study and precise dating of glacially overrun trees and fossil stumps. The first period of glacial advance began as early as A.D. 1100-1200 in the Wrangell Mountains and was generally coincident with advances that began in the coastal regions of Alaska and British Columbia by A.D. 1200 (*Calkin et al.,* 2001; *Luckman*, 2001; *Wiles*, 2002). The second and third periods of advance are centered at 1650 and 1850, respectively (*Calkin et al.,* 2001). The second advance, although centered at 1650, extended to at least A.D. 1700 in the Wrangell Mountains (*Wiles et al.,* 2002). Some glaciers in the Wrangell Mountains recorded their final stage of advance as late as the turn of the century (*Wiles et al.,* 2002).

Records of varves from Hector Lake (51° 34'N, 116° 20'W), in the Canadian Rockies, where higher sedimentation rates can be linked with glacial advances, were used by *Leonard* (1997) to reconstruct a 4450-year record of glacial activity. The record of varved sediments shows that low sediment accumulation occurred from the late A.D. 1300s to the 1550s and that high sedimentation, associated with advancing ice, occurred at A.D. 1200 and from A.D. 1600 onward. The timing of the changes in the sedimentation generally agrees with the record of Alaskan glacial advances.

Tree ring records in the Canadian Rockies provide a regional record of estimated summertime temperatures during the past 1,000 years (*Luckman*, 2001). A record reconstructing summer temperatures back to A.D. 1073 from spruce growing near the Athabasca glacier in the Canadian Rockies shows that 8 of the 10 coldest years in the entire record occurred during the 19th century. Other cold periods in Luckman's reconstruction include A.D. 1190-1250, 1280-1340, 1440-1500, and the 1690s.

A network of trees in the St.Elias-Wrangell Mountain was used by *Davi et al.* (2003) to reconstruct warm season temperatures (July-September) back to A.D. 1593.

This reconstruction shows two prominent cool periods as well as modern warming. The cool periods are centered in the late 1600s to early 1700s and in the late 1700s to early 1800s. The coldest year in the record of *Davi et al.* (2003) occurs in A.D. 1810 and coincides with a massive volcanic eruption previously identified in the literature as occurring in A.D. 1809 (*Dai et al.,* 1991). Other years that were exceptionally cold include A.D. 1601, 1641, 1695, 1783, 1816, and 1831. A more recent study by *Wilson et al.* (2006) used tree rings from the GOA to reconstruct January to September temperature for that region for the past 1300 years. This study indicates that the coldest temperatures occurred between A.D. 1560-1570, 1690-1710, and 1830-1870, and in contrast a period of prolonged warmth is evident in the tree ring records between A.D. 1720 and 1820.

Other regional and hemispheric tree ring studies show results that share commonalities with the temperature reconstructions of *Davi et al.* (2003) for the Wrangell Mountains and those of *Wilson et al.* (2006) for the GOA. For instance, *D'Arrigo et al.* (2001) made use of 20 tree-ring width records from sites between 45° N and 70° N to reconstruct temperatures from A.D. 1671 to 1993. Although it is similar to that presented by *Davi et al.* (2003) for the Wrangell region, a primary difference is that the Northern Hemisphere record indicates that the cold period in the 1800s lasted longer (nearly the entire century) than the cold period seen in the Wrangell reconstruction, which is limited to the early part of the century. A study by *Szeicz and MacDonald* (1995) reconstructed summer temperature from White Spruce in the Mackenzie and Franklin Mountains of northwestern Canada. The results from this study are very similar to those of *Davi et al.* (2003) and may suggest that the periods with the lowest temperatures occurred just after A.D. 1700 and just after 1800.

A detailed study of $\delta^{15}N$ at Karluk Lake over the past 300 years by *Finney et al.* (2000) shows periods of decreased salmon abundance centered at approximately 1740 and at 1810. These two periods correspond well with tree ring records from the Wrangell region, reconstructed by *Davi et al.* (2003), which show that these were the two coldest periods in the last 300 years. However, as decreased salmon productivity is associated with a weaker-than-normal low, this study suggests that although the last 300 years has been generally characterized by a stronger-than-normal AL, the coldest periods within this timeframe were characterized by a weak low.

A study by *Overpeck et al.* (1997), which compiled previous studies examining numerous proxy records of Arctic climate since A.D. 1600, identified several commonalities. The first is the start of present warming at approximately A.D. 1840. The second is that the coldest LIA temperatures occurred in most records during the first part of the 19th century. Overpeck notes that before A.D. 1800, records of Arctic climate change are less coherent and exhibit more regional independence.

In summary, numerous proxy and historical records are available that document high-latitude climate change since A.D. 1600 Although many of these records demonstrate regional differences in temperature patterns and timing of temperature changes, it is useful to review the common elements that stand out. For instance, two common periods of cooling are identified in numerous records. The first occurs just after A.D. 1700 and the second just after A.D. 1800. Additionally, the timing of the present warming starts as early as A.D. 1840 in some records, but it does not show up in others until the 1920s.

2.2.4.5 Recent climate change in Alaska

A number of lines of evidence indicate that significant regional warming has occurred in Alaska during the last 30 years (Fig. 2.6). For instance, a study by *Springer* (1999) indicates that the number of days without snowfall in the summer at Barrow, Alaska has increased from 80 days in the 1950s to more than 100 days in the 1990s. Additionally,, research by *Sturm* (2001) using photo comparisons indicates that the abundance of shrubs has increased in areas previously occupied by tundra between 1950 and 2000. Furthermore, data from *NSDIC* (1998) indicates that five of the earliest thaws on the Tanna River in Alaska, where records have been kept for 82 years, occurred during the 1990s. Finally, evidence from *Osterkamp* (1998) indicates that melting permafrost in Alaska is resulting in ground subsidence. The proxy evidence just mentioned supports data from meteorological stations in Alaska, which show an average increase in temperature of 1° C/decade for the last three decades (*Arendt et al.,* 2002).

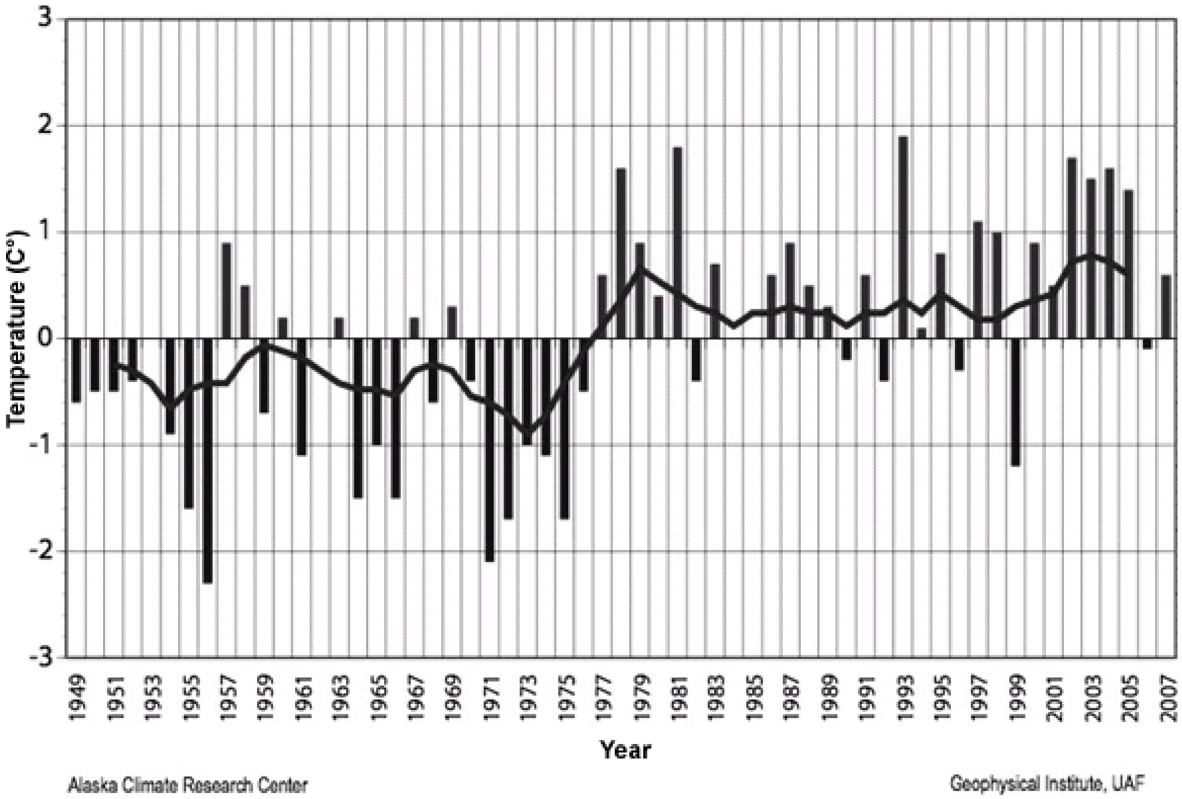

Figure 2.6 Mean temperatures in Alaska since 1949. Note rapid increase after 1976 PDO shift. *Image reproduced from climate.gi.alaska.edu.*

Studies of Alaska's glaciers by *Calkin and Wiles* (2001) indicate that many of Alaska's glaciers reached LIA maxima between A.D. 1850 and 1900 and have since retreated. A survey of glaciers across Alaska by *Molnia* (2008) shows that out of 700 named glaciers in Alaska, almost 99% are retreating. This is despite the fact that precipitation across the state has increased by up to 30% in the last century (*Molina*, 2008). A study by *Arendt et al.* (2002) of more than 50 glaciers across Alaska showed that the average glacier had experienced thinning at a rate of 0.52 m per year during the period 1950-1990 and that during the period 1990-2001 this rate had more than tripled to 1.8 m per year.

2.3 Timeline verification and development

The timescale for BC1 is based upon multiple lines of evidence, including the identification of radioactivity in the ice core from open air nuclear testing in the 1950s and 1960s, peaks in SO_4^{2-} and F^- that correspond with historic volcanic eruptions, and annual layering. Annual layers are clearly resolvable throughout the last 1,000 years of the record (estimated errors are given in Table 2.1). Beyond this, the timeline has been based on a simple depth model that is calculated using only the observed thinning rates during the last 1,000 years. Counting of individual layers is straightforward given the presence of a well-defined seasonal cycle coupled with a high rate of accumulation. Annual layers within the top 100 years average 1.2 m in thickness, while annual layers at the bottom of the ice core, which according to the depth model correspond to the years A.D. 365 to 265, are on average 4.88 cm thick. The accuracy of the layer count is verified by the excellent match between the timing of known historic volcanic eruptions and the occurrence of SO_4^{2-}/F^- peaks in BC1 (Fig. 2.7 and 2.8 and Tables A.2 to A.5 in Appendix A) and by the identification of peaks in ^3H and ß- in 1963 (Fig. 2.3 and 2.4).

2.3.1 Identifying annual and seasonal markers in BC1

Annual peaks in dust, calcium, nitrate, and magnesium are resolvable throughout the ice core and have been used to develop the timeline presented in this thesis. Multiple lines of evidence support the conclusion that these peaks are annual in nature. The strongest evidence comes from the upper portion of the core, where identification of the peaks of ^3H and ß- in the ice core allow an independent measure of age. A count of dust peaks from the surface of the core to the 1963 ß- horizon reveals 39 dust peaks (Fig. 2.9). The number of dust peaks is equal to the number of years present between the top of the ice core and 1963. The odds of this happening by chance alone, if one assumes that dust peaks are not annual, are essentially zero.

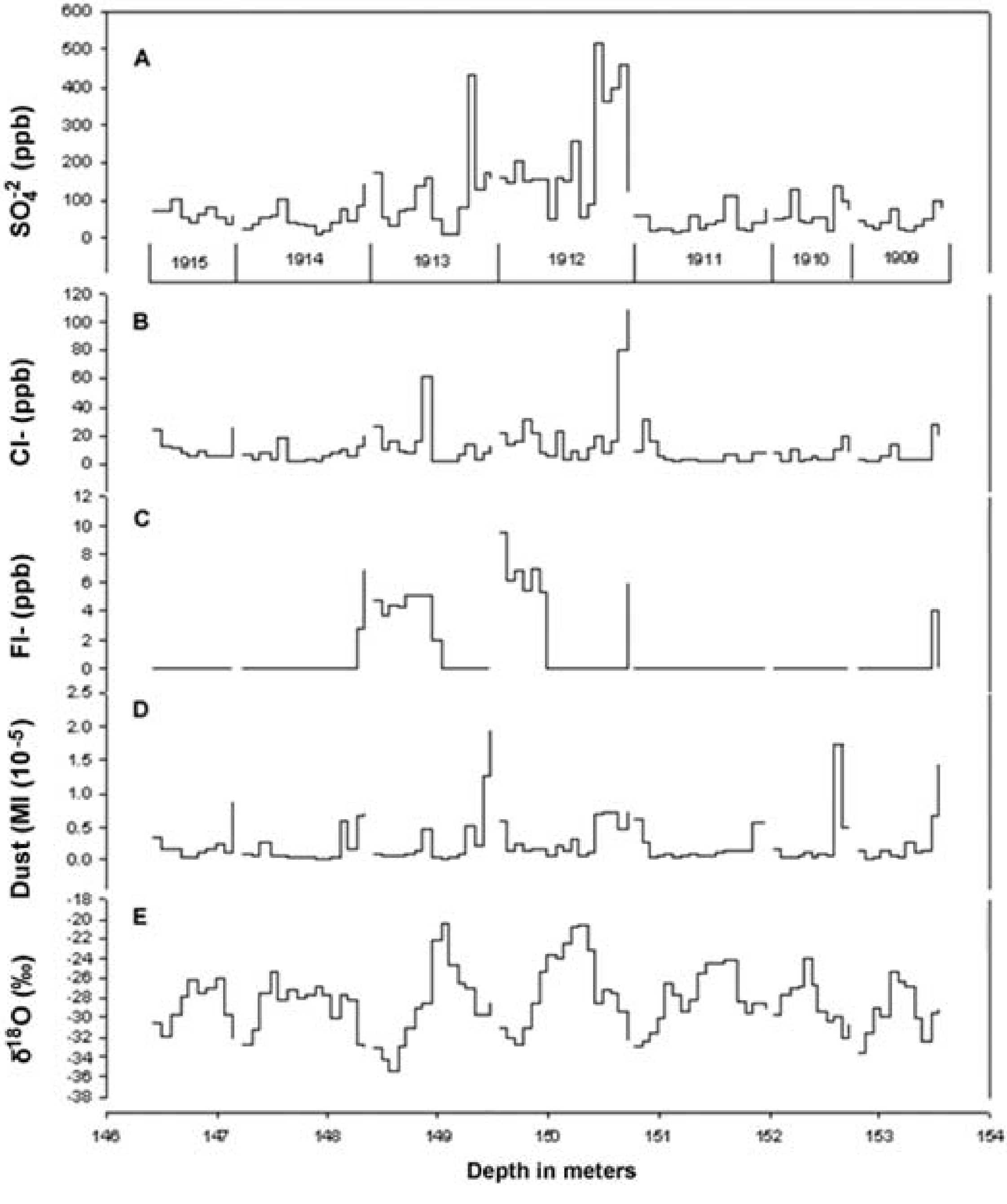

Figure 2.7 Detail of Katmai Eruption in BC1 with (A) Sulfate (B) Chloride (C) Fluoride (D) Dust and (E) $\delta^{18}O$. The depth scale for A-E is given at the bottom of the figure, and the timeline is given at the bottom of A. Note that sulfate levels are up to 10x higher than background in 1912 and parts of 1913. Gaps in the time series represent annual breaks inserted when developing the timeline.

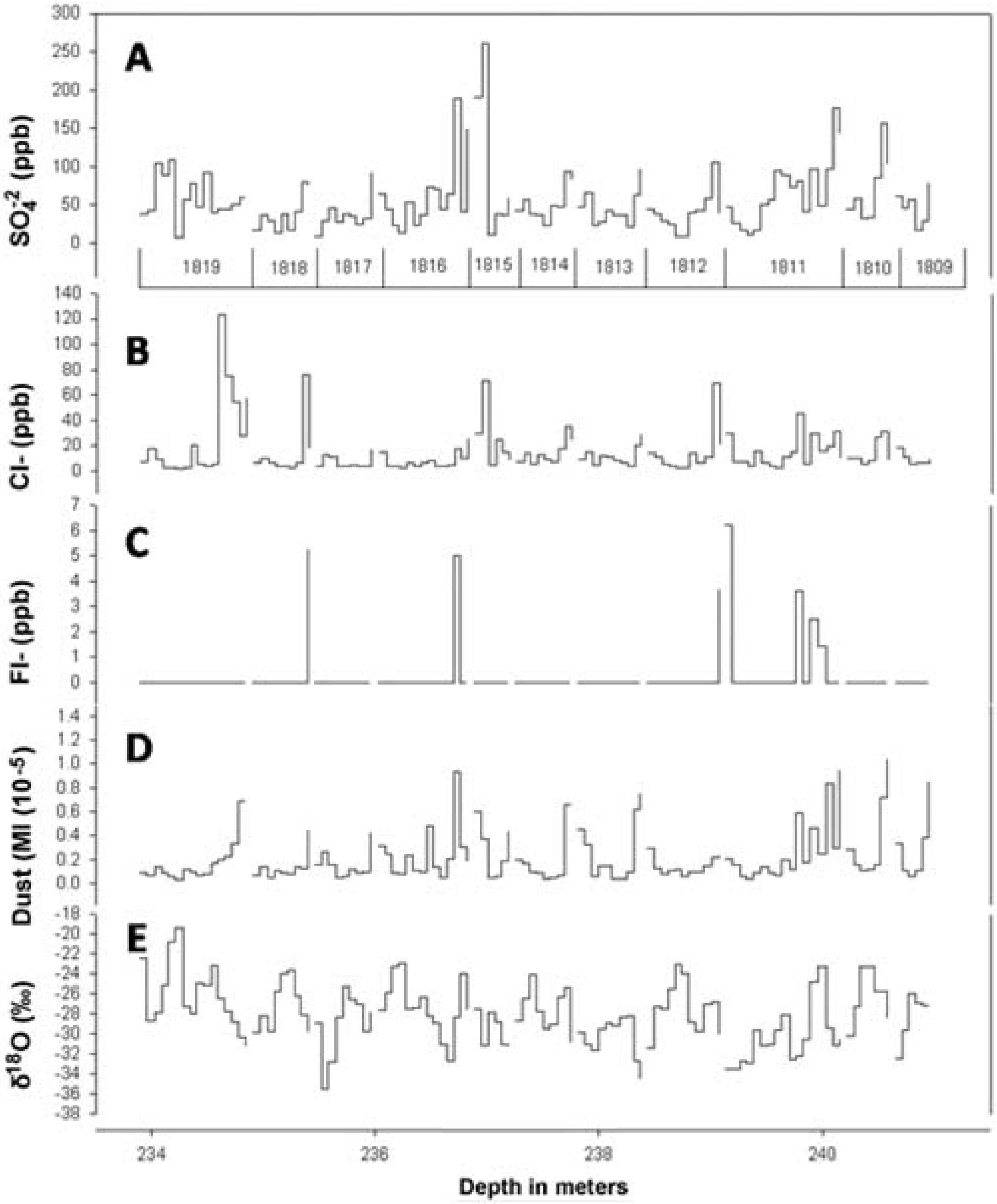

Figure 2.8 Detail of Tambora and unknown (1810) volcanic event in BC1 with (A) Sulfate (B) Chloride (C) Fluoride (D) Dust and (E) δ^{18}O. The depth scale for A-E is given at the bottom of the figure, and the timeline is given at the bottom of (A). Note that sulfate levels are up to 5x higher than background in 1815-1816 and 3x higher in 1810-1811. Gaps in the time series represent annual breaks inserted when developing the timeline.

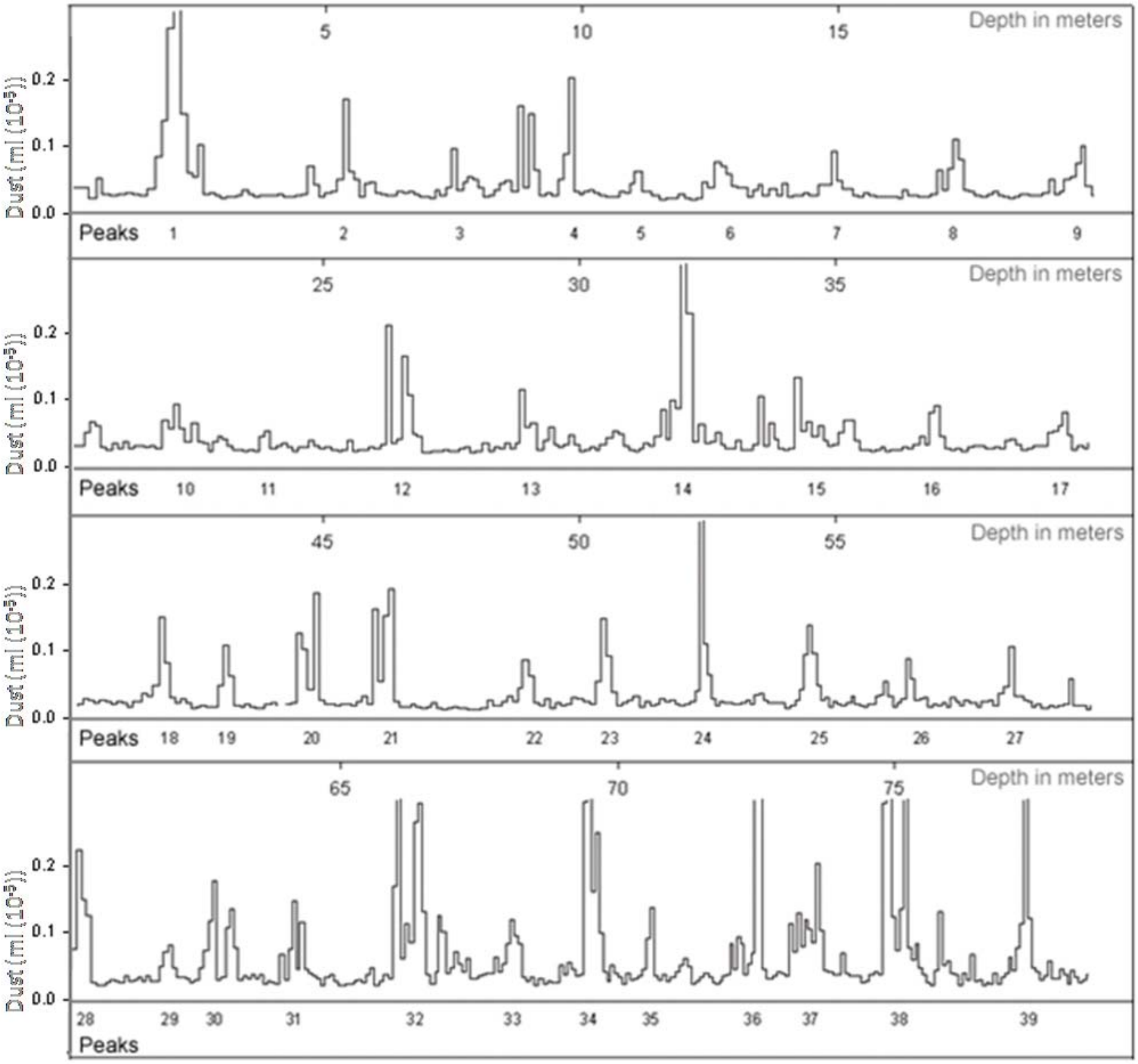

Figure 2.9 The 39 dust peaks identified in BC1 between 2001 and 1963. Each peak that was counted is labeled in consecutive order between 1 and 39 in rows labeled peaks. Depth is plotted at 5 m intervals so as not to be confused. This graph is shown to verify the annual nature of the peaks in dust.

Estimated range of error associated with the derived timescale for BC1	
Derived Age	Estimated Error
2000-1850	+/- 1 year
1850-1700	+/- 2 years
1700-1000	+/- 10 years
1000-750	+/- 25 years (assuming that thinning model is appropriate)
500-265	+/- 50 years (assuming that thinning model is appropriate)

Table 2.1 Error estimates for the derived BC1 timescale. Error estimates are based on uncertainty in the counting of annual dust peaks.

Year of sulfate / fluoride peaks in BC1	Negative Offset from historical record	Positive Offset from historical record	Volcanic Events
1912	0	0	Katmai
1882	0	1	Augustine Krakatoa
1830	-1	0	Kiluchevskoi
1822	0	3	Anianchak Hokkaido Java
1815	0	1	Tambora
1797	-2	3	Pavlof Sister, West Dahl, Chirpoi, Mt. St. Helens
1783	0	0	Laki
1734	0	5	Hokkaido
1691	-1	3	Hokkaido, Amukta
1668	-1	5	Honshu,Halmahera
1648	-6	7	Avachinsky, unknown Greenland
1607	-7	0	Huaynaputina
1596	0	4	Huaynaputina
1578	0	2	unknown 1580
1554	-1	3	unknown 1553 and 1557
1517	-6	1	Hekla,Iceland/Unknown Pr Col
1487	-7	0	Greenland/ Iceland/ St. Helens
1369	-7	0	ORAEFAJOKULL
1362	0	0	ORAEFAJOKULL
1352	0	10	ORAEFAJOKULL
1266	-7	1	unknown 1259 and 1267
1176	0	3	Icelandic: Katla
1092	0	12	Icelandic: Hekla
940	-8	0	Large in Greenland

Table 2.2 List of volcanic events and relationship to BC1.

2.3.2 The 1963 peak in β- and ^{3}H

Radioactive fallout was incorporated into precipitation as a result of open-air nuclear testing during the 1950s and 1960s. The year 1951 marks the earliest detection of ß- activity in the atmosphere at Kodiak (*Crozaz et al.,* 1966). Concentrations of total beta radioactivity in the atmosphere increased from 1951 onward and peaked in the early part of 1963 before gradually decreasing (*Crozaz et al.,* 1966). The 1963 peak is identifiable in both BC1 and BC2 (Fig. 2.4) and has been identified in numerous other ice cores, including the ice core obtained from the Eclipse ice field (60° 30' N and 139° 28' W; 3017 m), (*Wake et al.,* 2002).

Historical records from Adak, Palmer, and Bethel in Alaska and Ottawa, Canada show a prominent peak in the concentration of ^3H in precipitation during the summer of 1963 and smaller subsequent peaks that decrease in magnitude with time. The 1963 peak in ^3H confirms the timeline results using ß- and it too can be used as a time equivalent horizon (Fig. 2.4). The Alaskan records of ^3H in precipitation cover the period of interest in the early 1960s, and the record from Ottawa begins in 1953 and extends to the present.

2.3.3 Volcanic events as time horizons

The record from BC1 contains SO_4^{2-} and F^- peaks produced by volcanic eruptions that can be matched with the historical record of volcanic eruptions (Table 2.2). This is complicated by the fact that the drilling site is downwind from the Aleutian Arc, an active volcanic region with a poorly documented historical record due to its remote location (*Waythomas et al.,* 1998). As a result, many of the SO_4^{2-} and F^- peaks in the BC1 record may not match those of known eruptions and may rather be associated with undocumented eruptions from volcanoes of the Aleutian Arc.

The eruption of Katmai (59° 16’N, 154° 59’W--Fig. 2.1), which occurred in June 1912, was one of the largest to occur on a global basis during the past 100 years. It stands out clearly in the time series of SO_4^{2-} and F^- in BC1 (Fig. 2.7). The SO_4^{2-} peak serves as a key time horizon, and because it matches the annually derived timescale based on layer counting, it serves as an important cross-verification. The eruption itself lasted 60 hours and resulted in an estimated ejection of 30-35 km^3 of ash and tephra. Light ash fall was reported as far away as Puget Sound, and ash that entered into the stratosphere remained in suspension for months (*Miller et al.,* 1988).

Improvements in the monitoring of volcanic eruptions and satellite tracking of volcanic ash clouds demonstrate that eruptions perhaps even smaller than that of Katmai may be recorded by BC1. One example would be the eruption of Mt. St. Augustine, one of the volcanoes of the Aleutian Arc (59º 36’ N, 153º 43’ N- Fig. 2.1), which occurred on January 23, 1976. The trajectory of the ash cloud, as plotted in the study (*Meinel et al.,* 1976), places the ash cloud near the Bona Churchill drilling site. The sulfate and fluoride peaks associated with the Mt. Augustine eruption are the second largest seen in the ice core record during the past 100 years. The timing of these spikes is consistent with the annual dating derived from both the dust and calcium record.

Several other well-documented historical eruptions of global significance can be matched with the record of SO_4^{2-} from BC1. A clear and fairly obvious match can be made between the A.D. 1783 eruption of Laki and a prominent sulfate peak in BC1. Additionally, the eruption of Tambora may correspond to a minor peak in SO_4^{2-} that occurred in A.D. 1815 (Fig. 2.8). The 1815 peak in SO_4^{2-} was preceded by elevated levels of SO_4^{2-} in 1810, which may also correspond to an unknown volcanic event that shows up in many other ice core records (*Dai et al.,* 1991; *Simkin and Siebert*, 1994).

An unknown volcanic event occurring in either A.D. 1516 or 1517 may serve as an important stratigraphic horizon in BC1. The most elevated levels of SO_4^{2-} in the Eclipse and PRCol ice cores in the last 500 years correspond with the year A.D. 1516 (*Fisher et al.,* 2004). The event is also seen in the BC1 core, which is marked by peaks in both SO_4^{2-} and F^-. No known historical eruption matches this exact timing, but peaks in SO_4^{2-} and F^- occur in ice cores from Greenland (Dye 3 and GRIP) in A.D. 1509 and 1513. The A.D. 1509 event in the Greenland cores matches the timing of the Icelandic eruption of Hekla in 1510 (*Simkin and Siebert*, 1994).

In order to find other possible matches with other known historical eruptions, the timing of peaks in SO_4^{2-} and F^- from BC1 were compared with data collected and complied by *Simkin and Sieber* (1994) in <u>Volcanoes of the World</u> and with the records of peaks in SO_4^{2-} from the Greenland ice cores Dye 3 and GRIP. The results of this analysis are presented in Tables A.2 through A.5 in Appendix A. Table A.2 shows the difference in timing between known volcanic events and SO_4^{2-} and F^- peaks in BC1, and one can observe that the values associated with negative offsets are more consistent then the values associated with positive offsets. This could result from excluding approximately 7 years from the BC1 record between A.D. 1648 and 1783. However, the strong signal from Katmai and more recently Mt. Augustine suggests that other undocumented eruptions associated with the Aleutian Arc are present in the ice core record, and this complicates comparisons with other historical records.

2.3.4 The White River Ash

2.3.4.1 Background

White River Ash deposits are widespread across much of the Yukon and southeastern Alaska and are an important regional chronostratigraphic marker (*Lerbekmo and Campbell*, 1969). Two primary ash lobes are recognized and have been attributed to separate eruptions (*Lerbekmo and Campbell*, 1969). The northerly lobe is older, and ash deposits associated with it have been dated to between A.D. 1900 and 1500 ^{14}C YBP (*Lerbekmo and Campbell*, 1969). The more recent and easterly directed lobe has been dated to A.D. 803 based on the weighted mean of four calibrated ^{14}C dates (*Clague et al.,* 1995). Radiocarbon samples were taken from trees buried in the ash and preserved in growth positions. Making use of the two most precise ^{14}C dates, the 2σ age range is given as A.D. 694-936 (*Clague et al.,* 1995).

Recent research has pointed toward Mt. Churchill as being the source of the White River Ash (*McGimsey et al.,* 1992; *Richter et al.,* 1995). However, the source of the White River Ash is an issue that has undergone considerable debate over the last 100 years. Mt. Natazhat, located approximately 40 kilometers northwest of Mt. Churchill, was originally suggested as the source of the White River Ash by Charles Hayes in 1892 and was the accepted source until Hanson in 1965 suggested Mt. Churchill as a probable source (*Richter et al.,* 1995). To add further to the confusion, a study by *Lerbkemo and Cambell* (1969) concluded that a pumice mound adjacent to the Klutlan Glacier was the remains of a tephra cone and the actual vent of the White River Ash.

2.3.4.2 White River Ash and the BC1 Record

When the Bona Churchill drilling project began, a high probability was given to encountering the White River Ash, and a special drill bit was designed to penetrate this layer if it was encountered during drilling. Given the proximity of the crater to the drill site, as proposed by *Richter et al.* (1995), one would expect the presence of a large layer of ash regardless of wind conditions. The absence of any visible ash in the ice core is strong evidence that Mount Churchill is not the source of the White River Ash. However, before proceeding with this discussion, it should be noted that the dates given for BC1 that are older than A.D. 1000 are not based on layer counting, and they are approximations based entirely upon a simple time depth model.

Several lines of evidence suggest the presence of a White River Ash signature in BC1 despite the fact that a large layer of ash was not encountered. It should be noted that a strong relationship between δ^{18}O and dust is seen in BC1 throughout the entire time series, but a number of outliers in this regression appear during approximately A.D. 760 to 777 (Fig. 2.10 and 2.11). Figure 2.14 is the time series of dust and δ^{18}O from BC1, and an examination of the figure highlights the period A.D. 760 to 777 because the dust concentrations here are higher than anywhere else in the ice core. Second, two SO_4^{2-} peaks that are similar in magnitude to those associated with the Katami eruption occur at A.D. 747 and 750 (according to the BC1 timeline), and it is possible that these correspond to the eruption of the White River Ash.

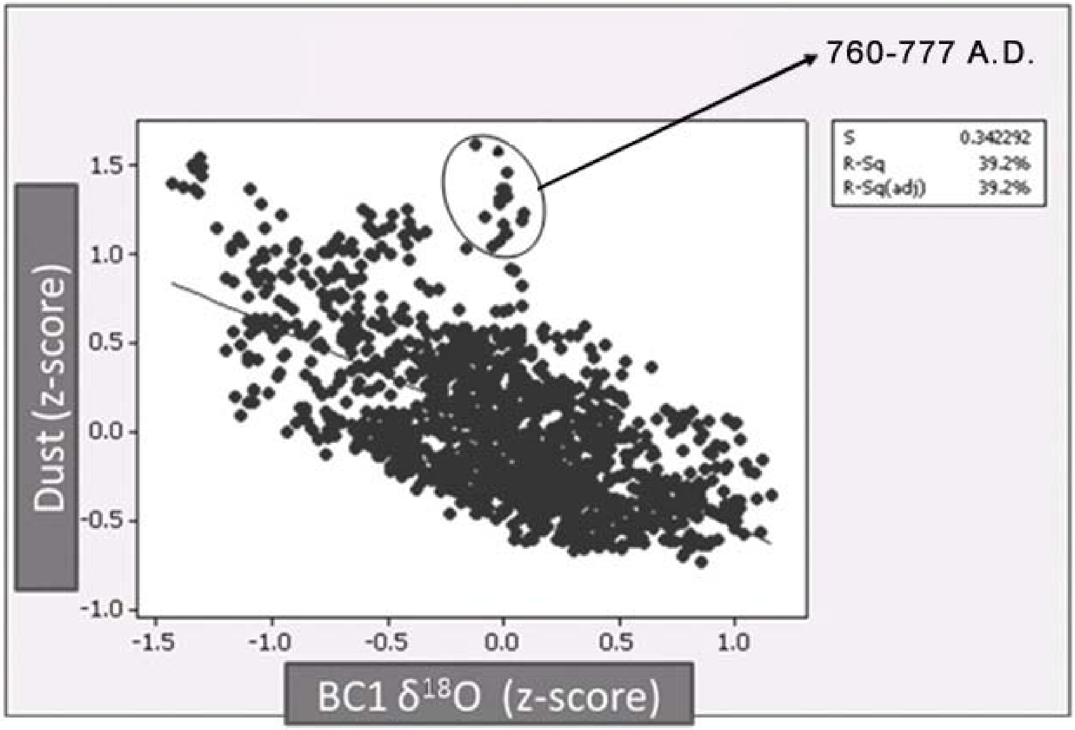

Figure 2.10 Regression plot of BC1 δ^{18}O and BC1 dust. In general, a strong correlation is observed between δ^{18}O and dust, but a group of years between A.D. 760 and 777 are seen as outliers to this general relationship. This could occur as background dust levels increased during this period in association with the eruption of the White River Ash.

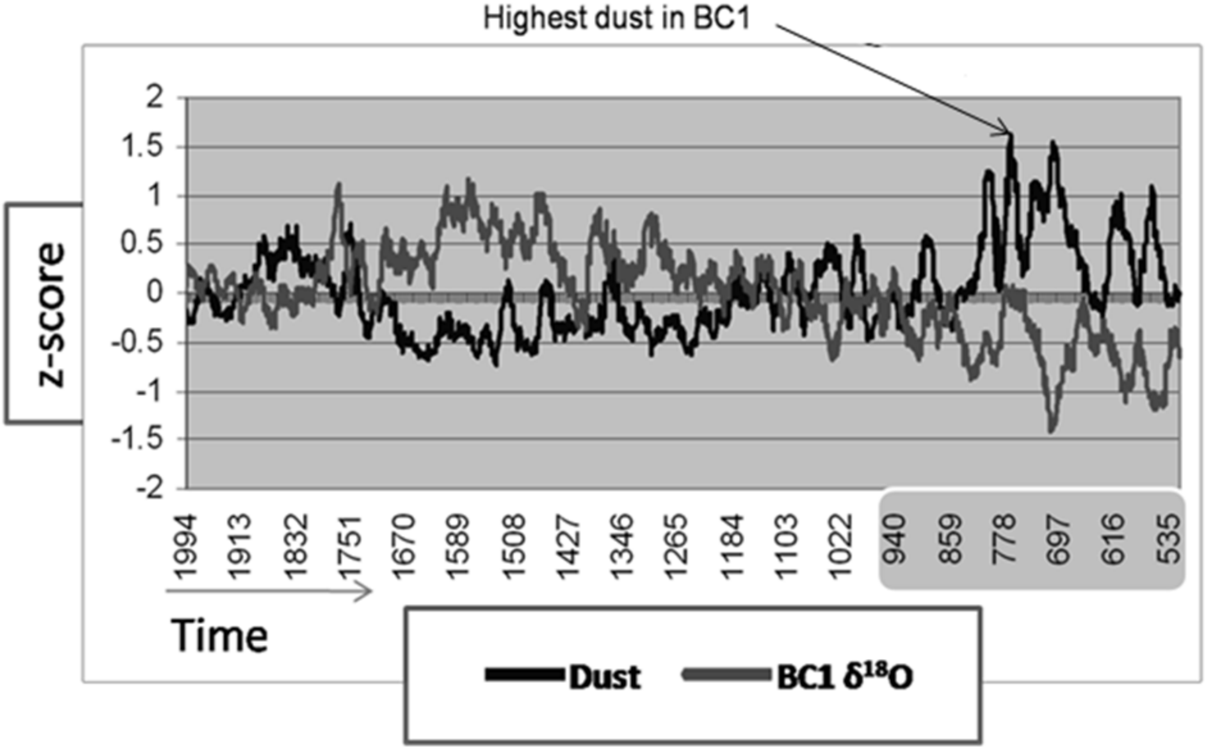

Figure 2.11 Time series of $\delta^{18}O$ and dust from BC1 from A.D. 500 to 2001. The high dust concentrations (denoted with arrow) occurring between A.D. 760 and 777 could be associated with White River Ash. Note that the dating prior to A.D. 1000 is based on the model described in the text and is uncertain (this period of the x-axis is shaded).

A scanning electron microscope was used by myself and Natalie Kehrwald to examine the dust particles at 416 m depth in BC1 (corresponding to A.D. 760 to 777) to determine the physical composition. Typical particles in the samples viewed were between 10 and 20 µm in size and appear to have visual and chemical characteristics similar to volcanic glass shards (Fig. 2.12). The chemistry of one of these shards is given in Figure 2.12 as well by weight %. Unfortunately, a comparison of the chemistry with that of actual White River Ash yields inconclusive results, and it is difficult to say with certainty whether the particles in Figure 2.12 are reworked White River Ash.

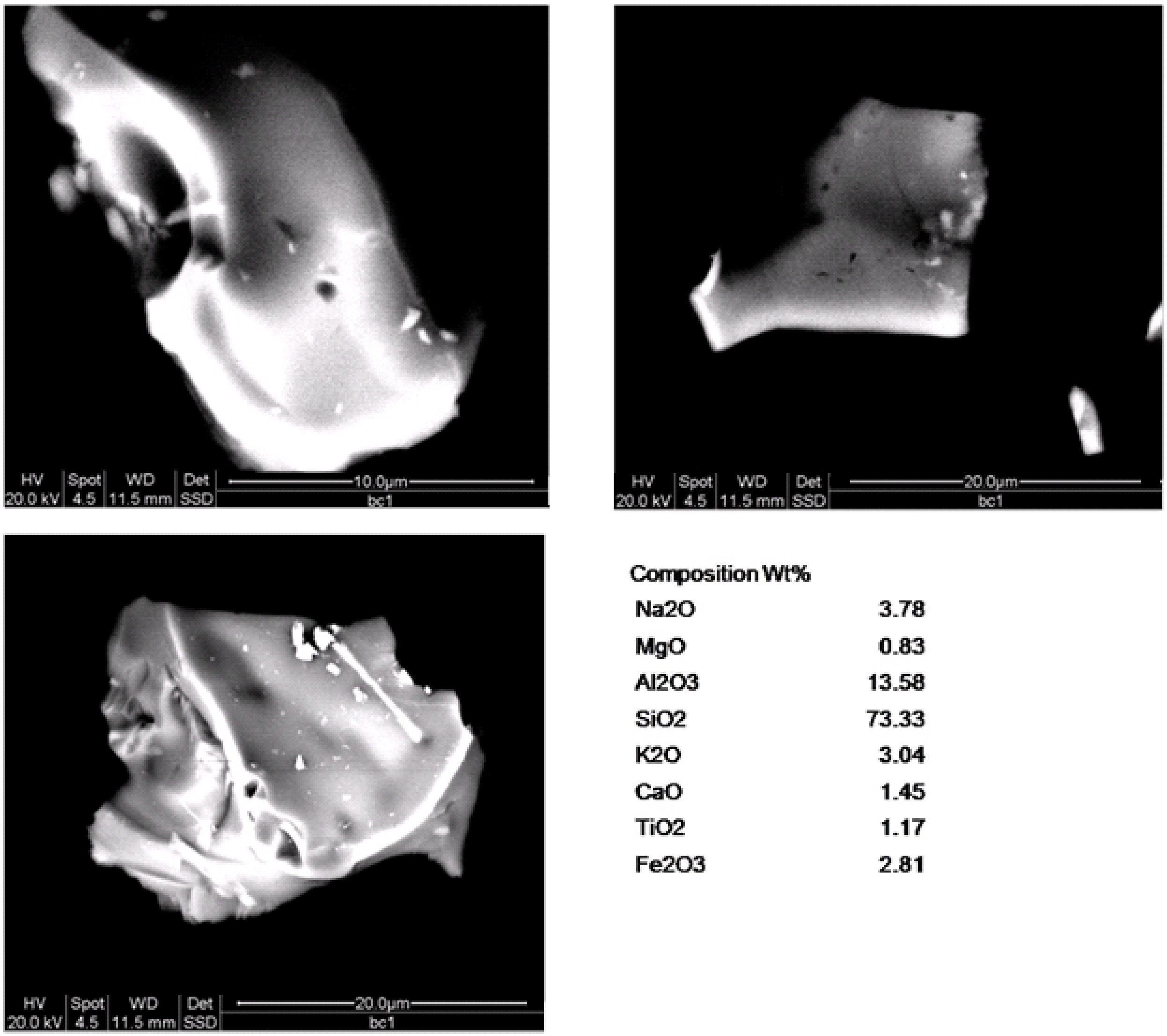

Composition Wt%	
Na_2O	3.78
MgO	0.83
Al_2O_3	13.58
SiO_2	73.33
K_2O	3.04
CaO	1.45
TiO_2	1.17
Fe_2O_3	2.81

Figure 2.12 Photos of ash at 416 m in BC1 that could be reworked White River Ash. The depth approximately corresponds to the period A.D. 760 to 770, assuming that the modeled timescale is correct. The portion of the core between 416 and 417 m where this material is found has the highest dust concentration other than the bottom of the core. The volcanic shards are quite small, and the ice core itself is not as transparent and has almost grayish milky coloring here, as compared to the rest of the core.

During the period A.D. 750 to 850, the background concentration of dust in BC1 rose to an unusually high level. This was measured by examining the ratio of Q3 (third quartile) to Q1 (first quartile) of dust samples within each annual layer. In general, the peak in dust is well constrained and limited in duration, and the remainder of the year is marked by relatively low values. This results in the well-defined relationship between Q1 and Q3 that is seen in Figure 2.13. However, Figure 2.13 also shows that the period A.D. 750 to 800 is marked by an anomalous increase in background dust levels that is unprecedented in the entire ice core record.

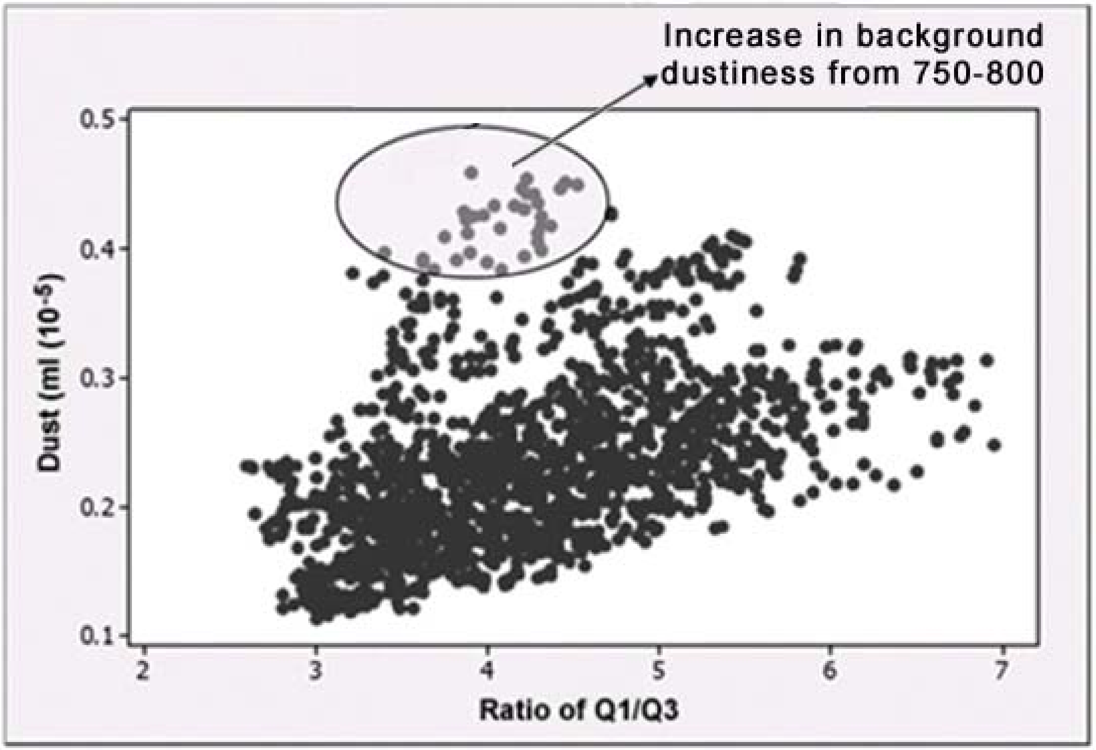

Figure 2.13 Correlation plot of 20-year averages of BC1 mean dust (pink) and ratio of 1st quartile (Q1)/3rd quartile (Q3) dust. In general, the ratio Q1/Q3 has a strong relationship to the average annual dust, but a group of years between A.D. 760 and 777 are seen as outliers to this general relationship. This occurs because the actual dust peak (Q3) is not changed but the background dust level is higher (Q1). The general relationship is that higher average dust is associated with larger dust peaks or higher Q3 values (where Q1 is relatively constant). The increase in background levels of dust is unusual and could be the result of reworking of the White River Ash in the environment.

A likely scenario is that the peak in dust at A.D. 760 to 777 seen in BC1 occurred just after the eruption of the White River Ash and that it is associated with reworking of the ash in the local environment. This would explain the increased levels of background dust, as the recently deposited White River Ash was probably mobile in the environment for some time. Although a visual inspection of the ice core reveals no signs of a volcanic ash layer at this depth. It might also be considered that no ash layers of any type are detected throughout the length of the ice core. This might suggest that the drilling location is in a position that doesn't favor the accumulation of ash, whether from the White River Eruption or from any other eruption. In summary, multiple lines of evidence do in fact suggest a White River Ash signature in the ice core:

1. The largest dust peak in the last 1,500 years in BC1 occurs at A.D. 760 to 777 (Fig. 2.11).
2. The large dust peak is not matched by a response in $\delta^{18}O$. This is unique in the entire ice core, and as such it appears as an outlier in the normal relationship between dust and $\delta^{18}O$, indicating the absence of the normal weather-related relationship between these two variables (Fig. 2.10).
3. The timing of A.D. 760 to 777 matches the A.D. 803 timing of the White River Ash.
4. A general increase in background dust is evident from the ratio of Q1/Q3. This is unique in the ice core because the typical pattern is for the dust peak to be fairly well defined and localized stratigraphically, but the dust within this interval of the core is more disseminated (Fig. 2.13).
5. The material in the core is volcanic in nature (Fig. 2.12).

2.4 Defining annual and seasonal cycles in BC1

2.4.1 Development of a seasonal composite

To define the intra-annual cycles in BC1, composites of each measured ice core parameter were developed based on the 39 annual layers deposited between 1963 and 2002. The seasonal composites represent an average of the individual seasonal cycles observed during the 39 individual years and were developed in order to clearly identify seasonal cycles in the ice core chemistry that are not as easily discernible in the unprocessed record. The seasonal composites were developed using the following procedure:

1. The 39 years representing the accumulation between the 1963 beta horizon, located at 78.5 m, and 2002, the top of the ice core, were selected for analysis.
2. The measured depths of each individual sample within each year were linearly transformed and assigned new standardized values of thickness between 0 and 1, which will be referenced as standardized thickness (ST). The sample thickness of transformed samples was calculated by dividing sample thickness by annual layer thickness. This process is illustrated in step B of Figure 2.14.
3. The values of all the ice core parameters were obtained at 0.05 ST increments. This process is illustrated in step C of Figure 2.14, where it is noted that each 0.05 ST increment can easily be matched to a specific sample, such as "A" in Figure 2.14 panel C, in order to arrive at a specific value.
4. All the values calculated at each increment in the previous step were standardized separately between 0 and 1 for each individual year so that outlying years would not skew the results.
5. The last step was to average the values at each 0.05 increment for all 39 years in order to obtain one composite representing the average year (Fig. 2.15).

The seasonal composites showing annual cycles in $\delta^{18}O$, d-excess, dust, SO_4^{2-}, Ca^{2+}, NO_3^-, NH_4^+, Na^+, Cl^-, Mg^{2+}, K^+, and F^- are presented in Figures 2.16c to 2.26c, and the findings and results can be summarized as follows:

1. Peaks in dust, calcium, magnesium, ammonium, sodium, chlorine, and nitrate occur at the same time as the lowest isotope values.
2. O18 and d-excess are strongly correlated. The primary difference is that d-excess exhibits a broader peak than O18.
3. Despite significant year-to-year variability in the profiles of $\delta^{18}O$ and d-excess, there is "on average" a well-defined seasonal pattern.
4. Contrasting patterns are observed in concentrations of sodium and nitrate. Both have primary peaks that correspond with the peak in dust levels. However, the yearly

cycles differ in that nitrate concentrations fall rapidly after the peak in dust and then gradually rise throughout the rest of the year. In contrast, sodium falls slowly following the peak in dust, reaching a minimum only just before the next dust peak.

5. Potassium unlike the other ions exhibits a summer peak.

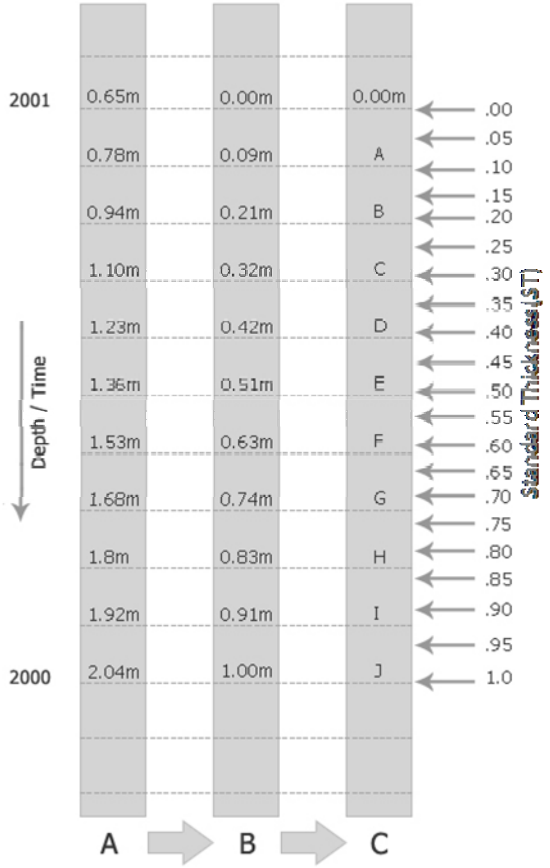

Figure 2.14 Illustrates the process of the construction of seasonal composites. (A) The original unprocessed ice core data is shown in detail for the year 2001. Depths correspond with top of each sample. (B) The transformed depths are shown with values between 0 and 1. (C) The .05 Standard Thickness (ST) increments are shown, and which sample corresponds with each arrow can be seen.

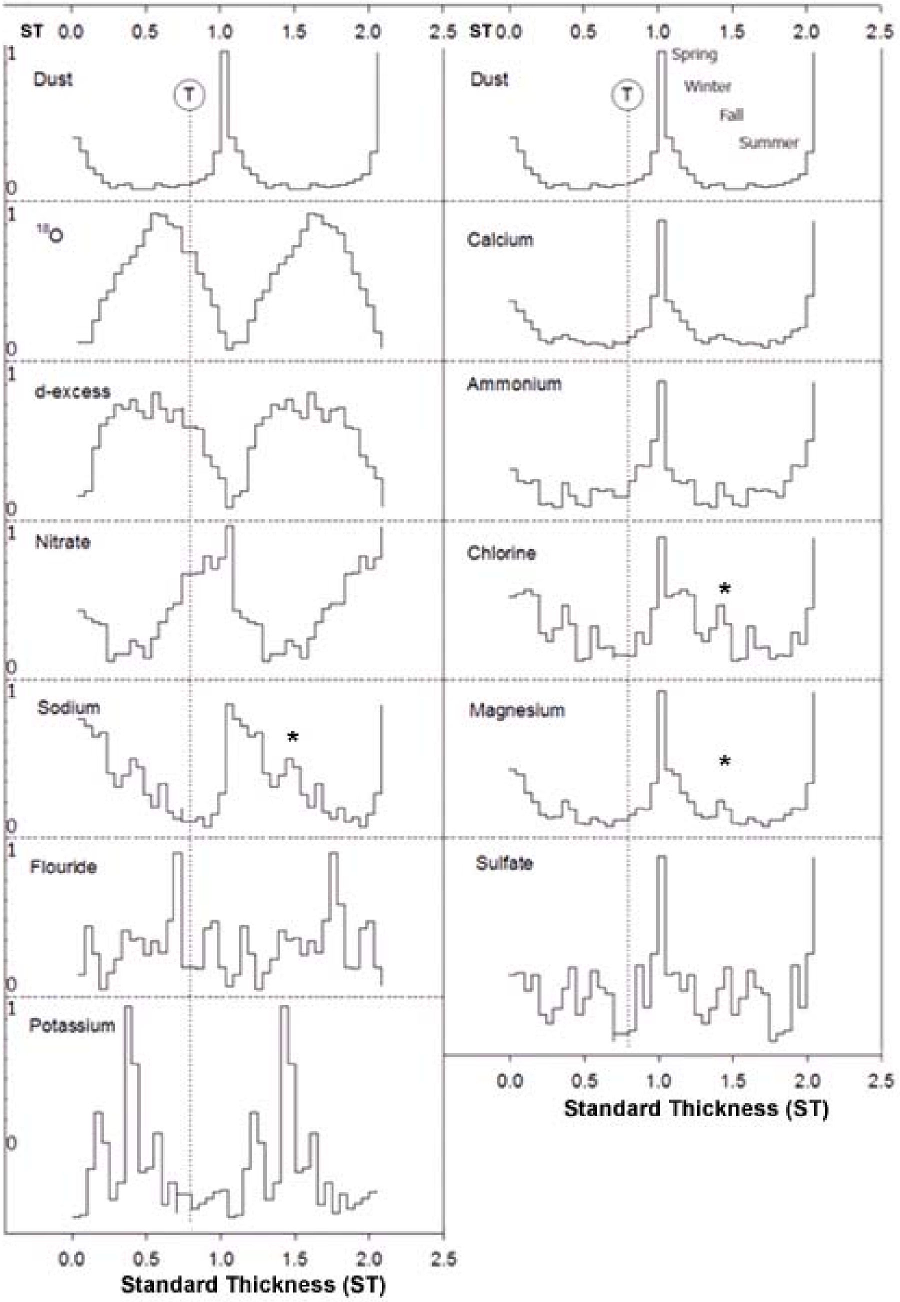

Figure 2.15 Seasonal composites of each ice core variable. Each is shown for a 2- year interval. Age increases with depth to the right in units of Standard Thickness (ST) as defined in the text. The "T" in the circle with the attached dashed line marks the location of the ^{3}H peak, based on 3 years of data discussed in Section 2.3.2, and * marks the location of a possible winter peak in Na^+, Cl^-, and Mg^{2+}.

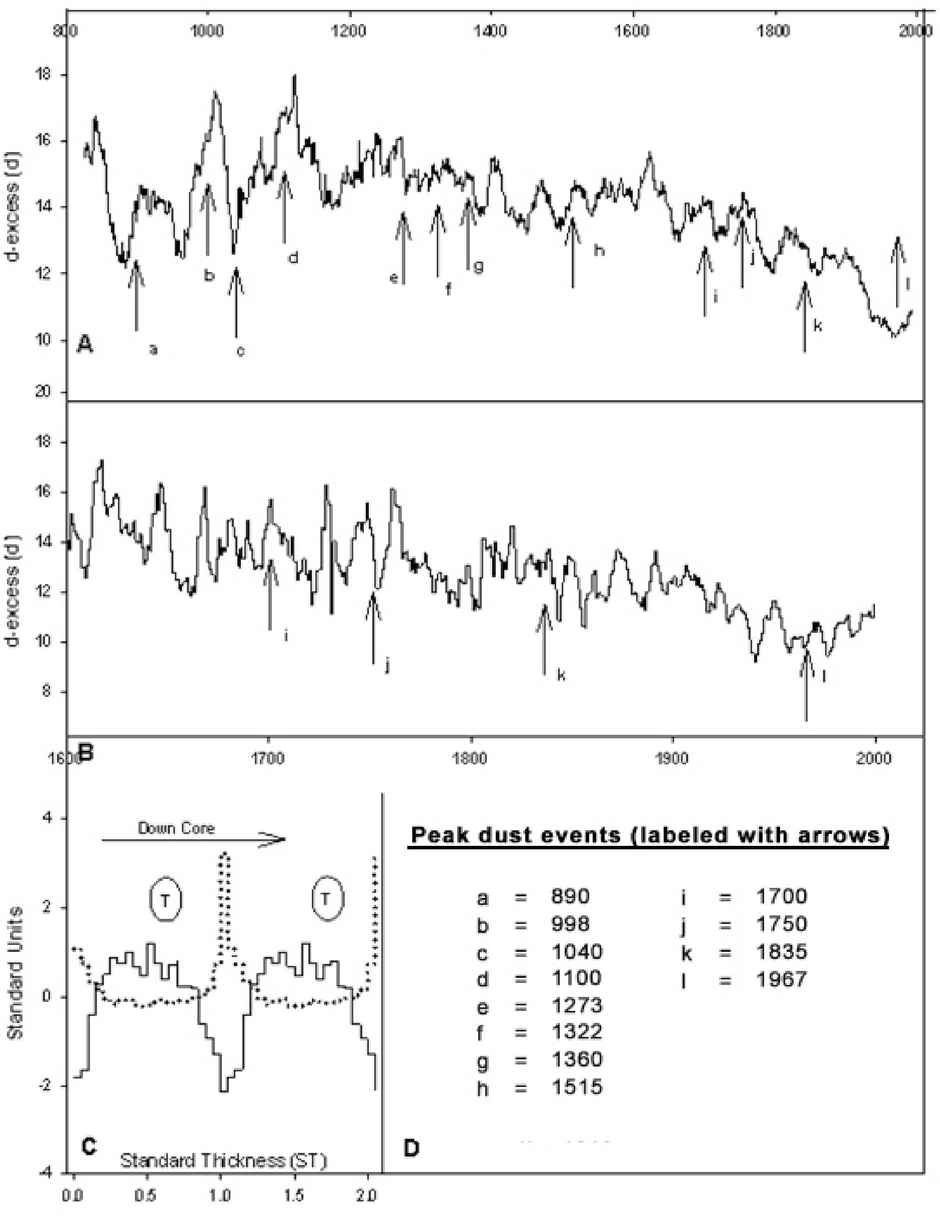

Figure 2.16 Profiles of time series of d-excess and correspondence with major events as derived from the time series of dust in Figure 2.17. (A) A 30-year centered average of d-excess since A.D. 820. (B) A 5-year centered average of d-excess since A.D. 1600. (C) Black line depicts the annual cycle of d-excess. Circled T depicts the observed Tritium peak. Dust cycle is shown as a gray dashed line. Two complete annual cycles are shown. (D) This box gives the timing of large dust events that are labeled in (A) and (B) with arrows.

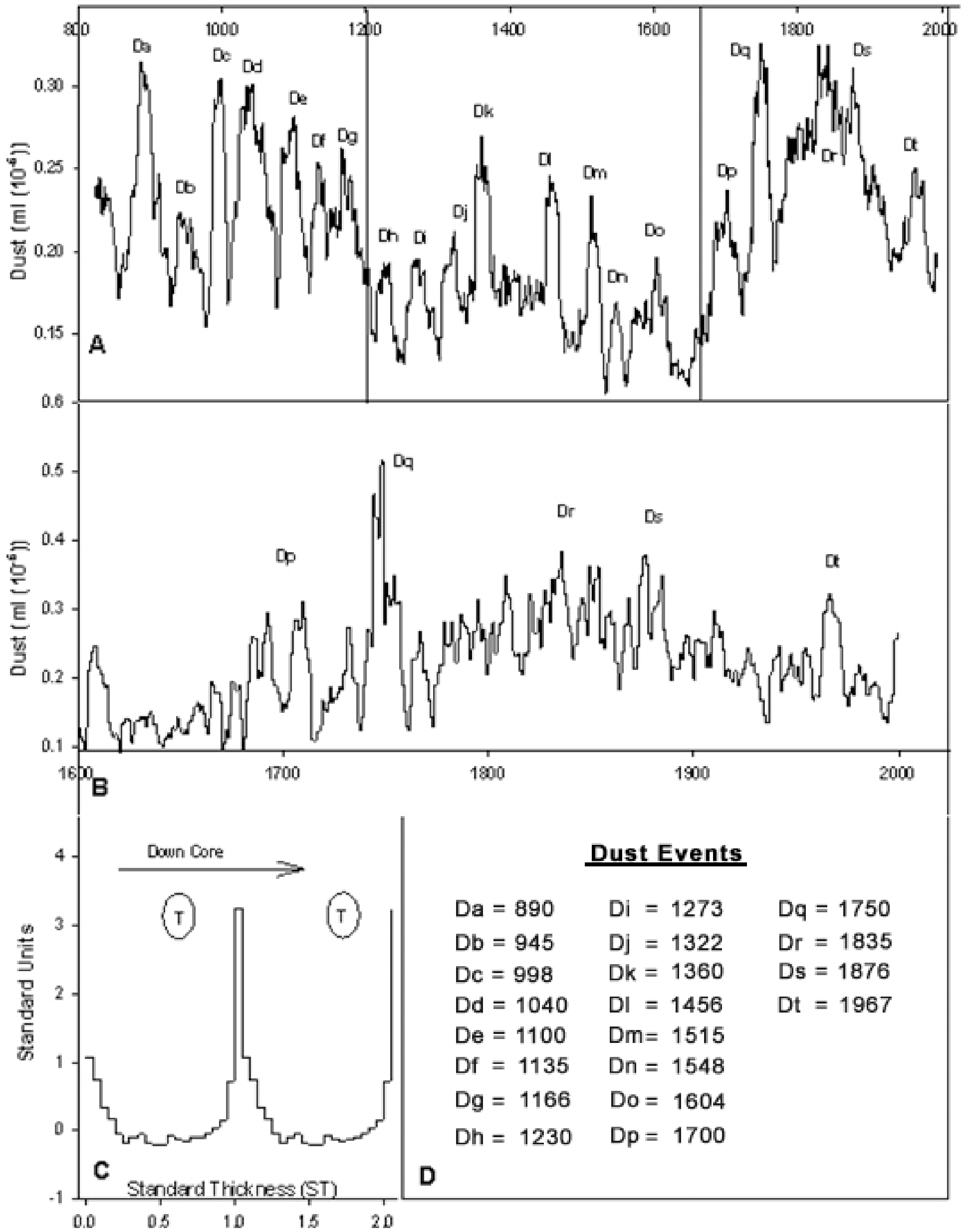

Figure 2.17 Profiles of time series of dust and demarcation of major events. (A) Depicts a 30-year centered average of dust since A.D. 820. (B) Depicts a 5-year centered average of dust since A.D. 1600. (C) The black line depicts the annual cycle of dust. The circled T depicts the observed Tritium peak. Two complete annual cycles are shown. (D) This box gives the timing of large dust events that are labeled in (A) and (B) with arrows.

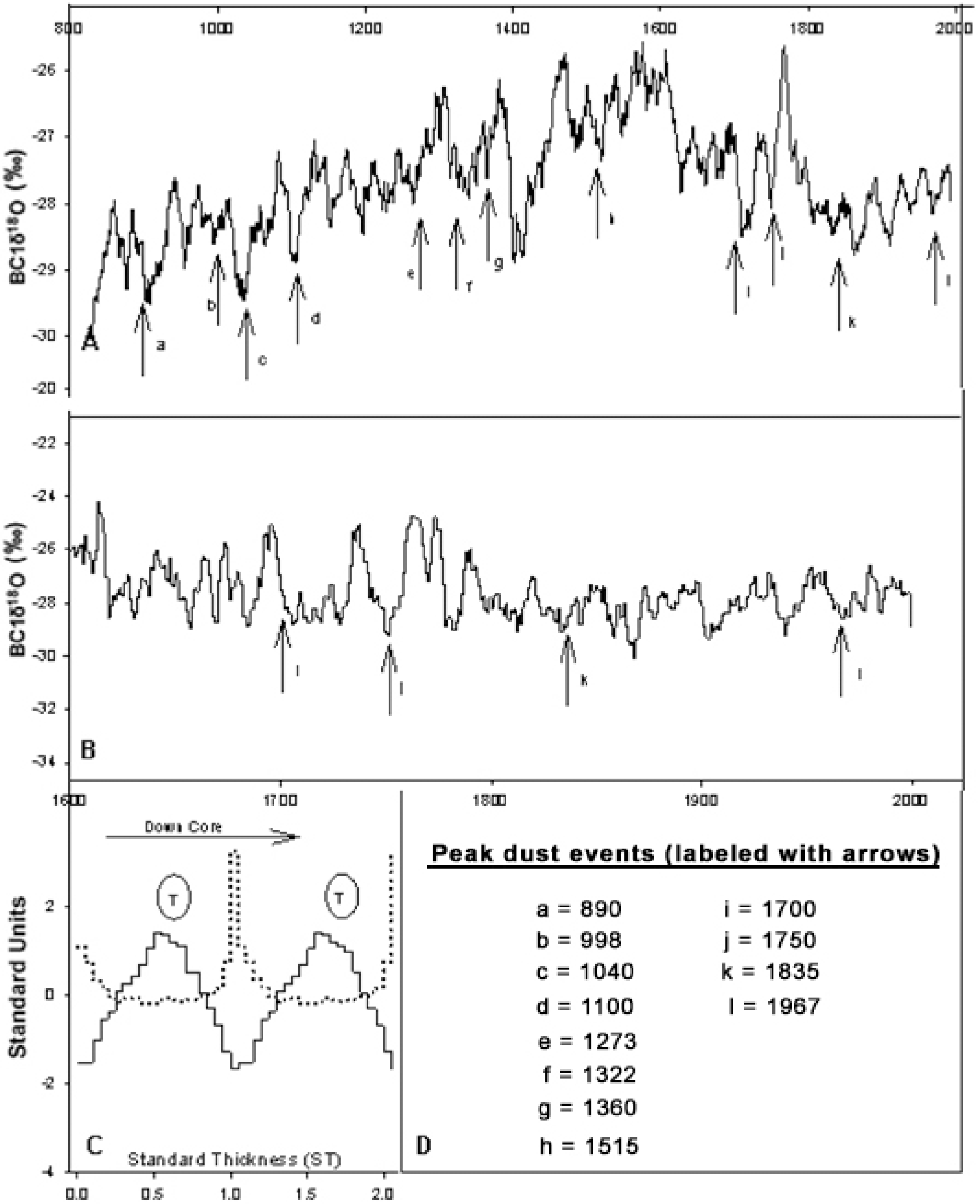

Figure 2.18 Profiles of time series of δ^{18}O and correspondence with major events, as derived from the time series of dust in Figure 2.17. (A) Depicts a 30-year centered average of δ^{18}O since A.D. 820. (B) Depicts a 5-year centered average of d-excess since A.D. 1600. (C) The black line depicts the annual cycle of δ^{18}O. The circled T depicts the observed Tritium peak. The dust cycle is shown as a gray dashed line. Two complete annual cycles are shown. (D) This box gives the timing of large dust events that are labeled in (A) and (B) with arrows.

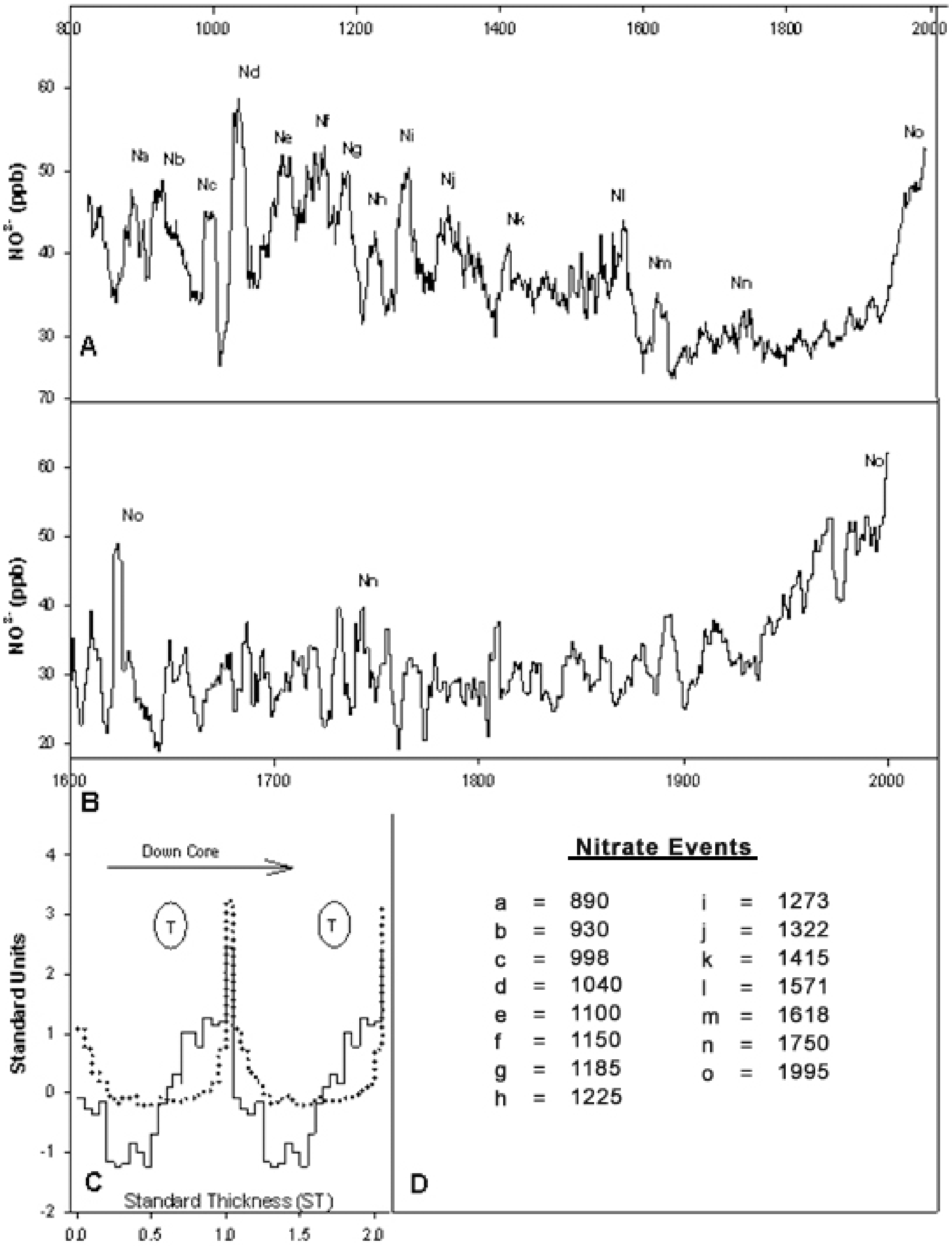

Figure 2.19 Profiles of time series of nitrate and demarcation of major events. (A) A 30-year centered average of nitrate since A.D. 820. (B) 5-year centered average of nitrate since A.D. 1600. (C) The black line depicts annual cycle of nitrate. Circled T depicts observed Tritium peak. Two complete annual cycles are shown. (D) Gives timing of labeled nitrate events from (A) and (B).

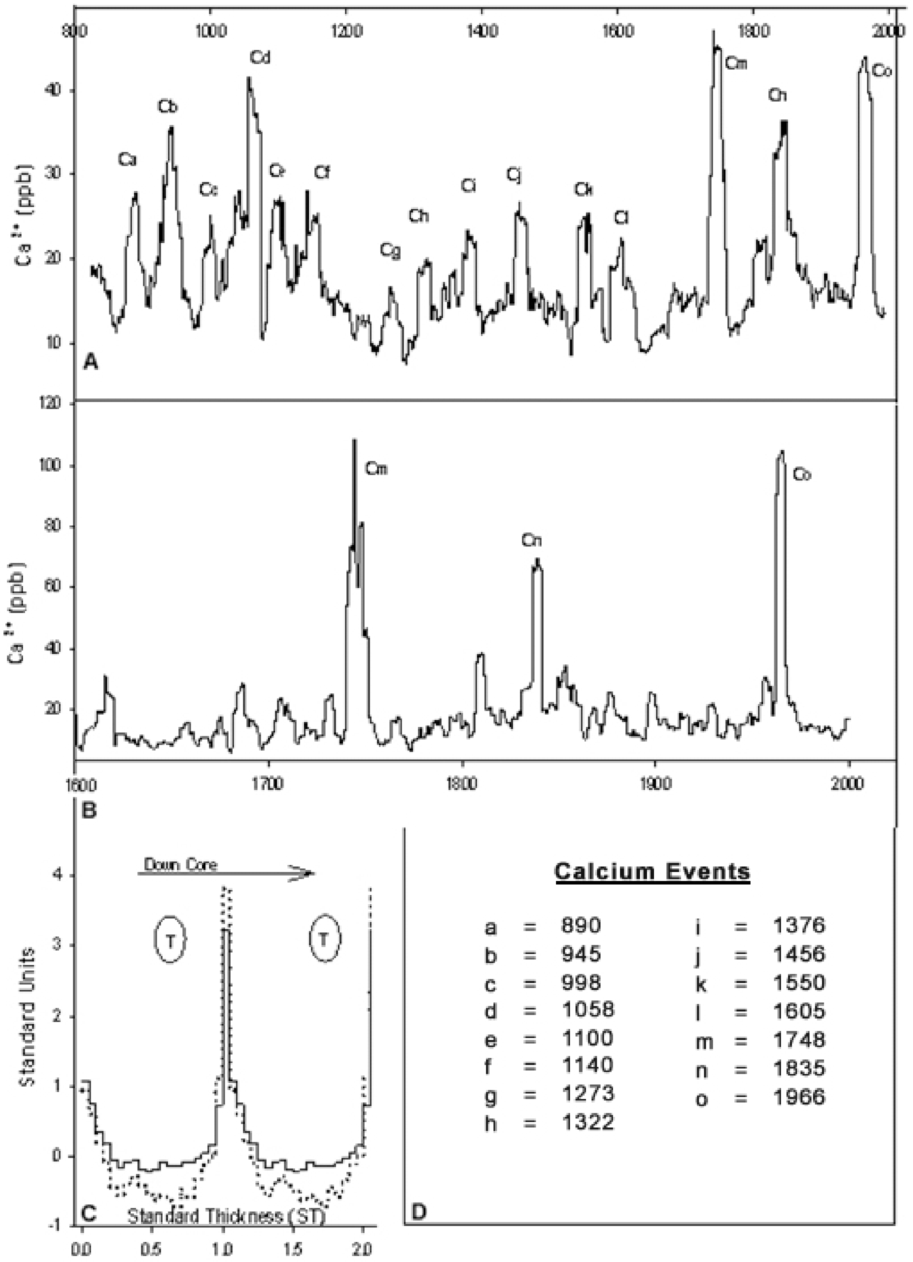

Figure 2.20 Profiles of time series of calcium and demarcation of major events. (A) Depicts a 30-year centered average of calcium since A.D. 820. (B) Depicts a 5-year centered average of calcium since A.D. 1600. (C) The black line depicts the annual cycle of calcium. The circled T depicts the observed Tritium peak. Two complete annual cycles are shown. (D) This box gives the timing of large calcium events that are labeled in (A) and (B) with arrows.

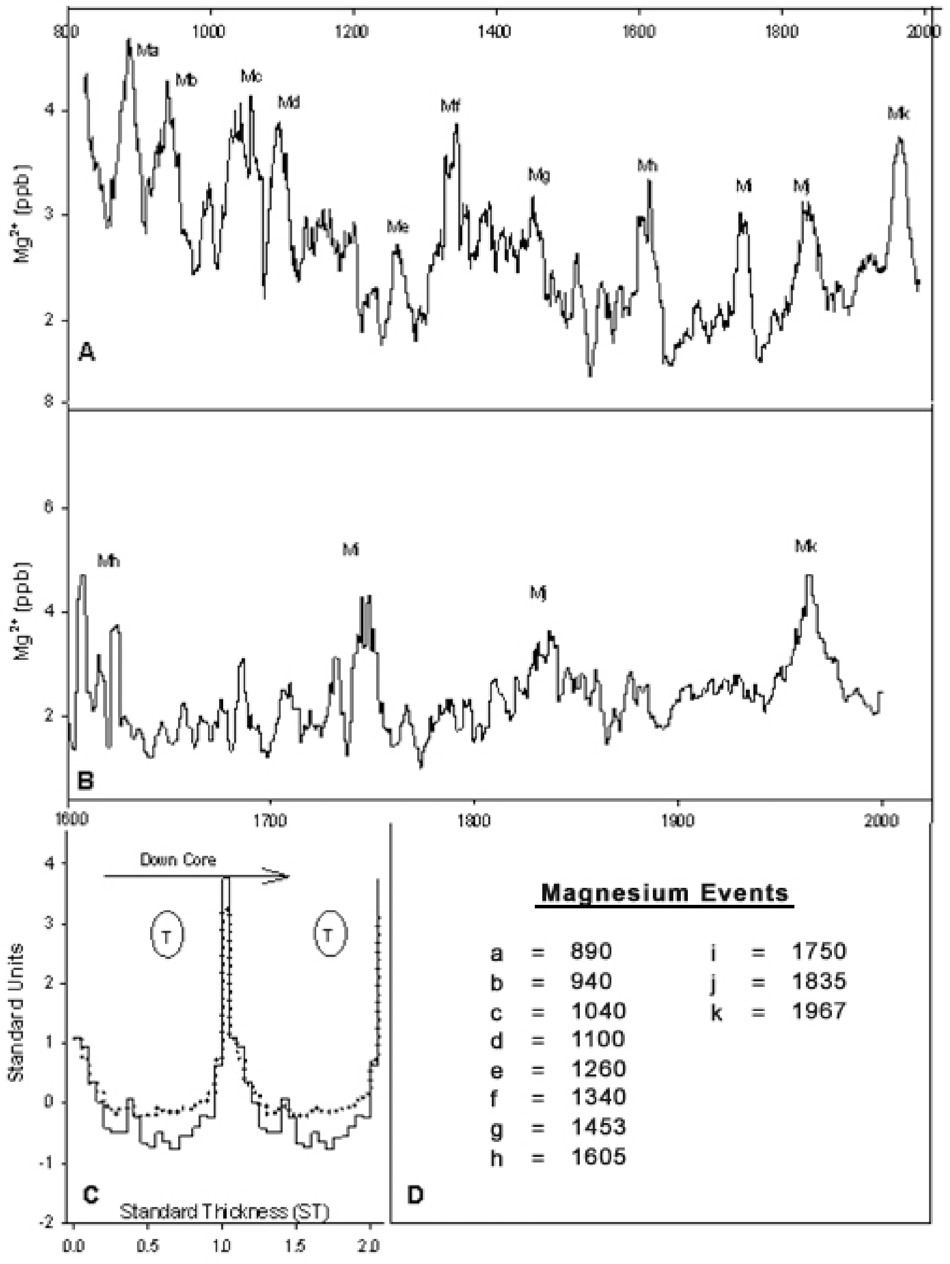

Magnesium Events

a =	890	i =	1750
b =	940	j =	1835
c =	1040	k =	1967
d =	1100		
e =	1260		
f =	1340		
g =	1453		
h =	1605		

Figure 2.21 Profiles of time series of magnesium and demarcation of major events. (A) Depicts a 30-year centered average of magnesium since A.D. 820. (B) Depicts a 5-year centered average of magnesium since A.D. 1600. (C) The black line depicts the annual cycle of magnesium. The circled T depicts the observed Tritium peak. Two complete annual cycles are shown. (D) This box gives the timing of large magnesium events that are labeled in (A) and (B) with arrows.

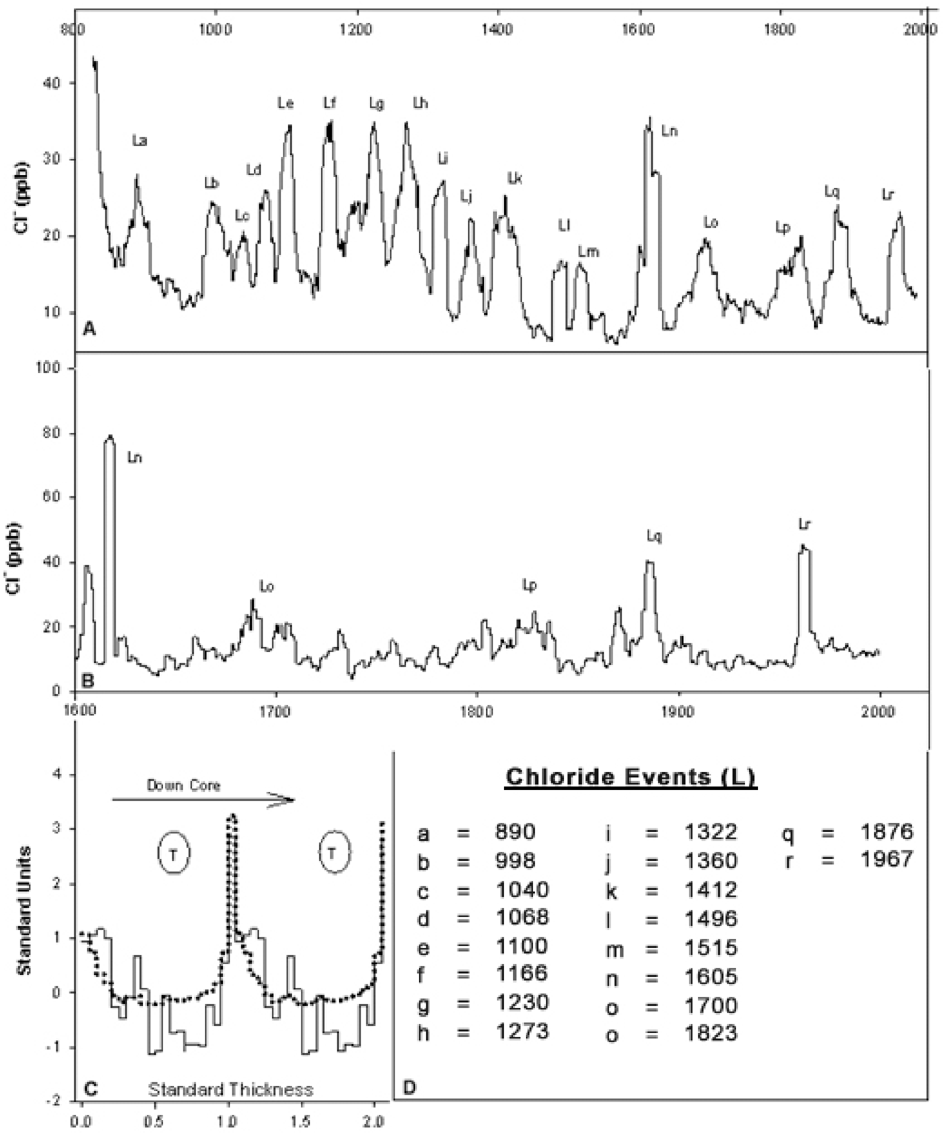

Chloride Events (L)

a = 890
b = 998
c = 1040
d = 1068
e = 1100
f = 1166
g = 1230
h = 1273
i = 1322
j = 1360
k = 1412
l = 1496
m = 1515
n = 1605
o = 1700
o = 1823
q = 1876
r = 1967

Figure 2.22 Profiles of time series of chloride and demarcation of major events. (A) Depicts a 30-year centered average of chloride since A.D. 820. (B) Depicts a 5-year centered average of chloride since A.D. 1600. (C) The black line depicts the annual cycle of chloride. The circled T depicts the observed Tritium peak. Two complete annual cycles are shown. (D) This box gives the timing of large chloride events that are labeled in (A) and (B) with arrows.

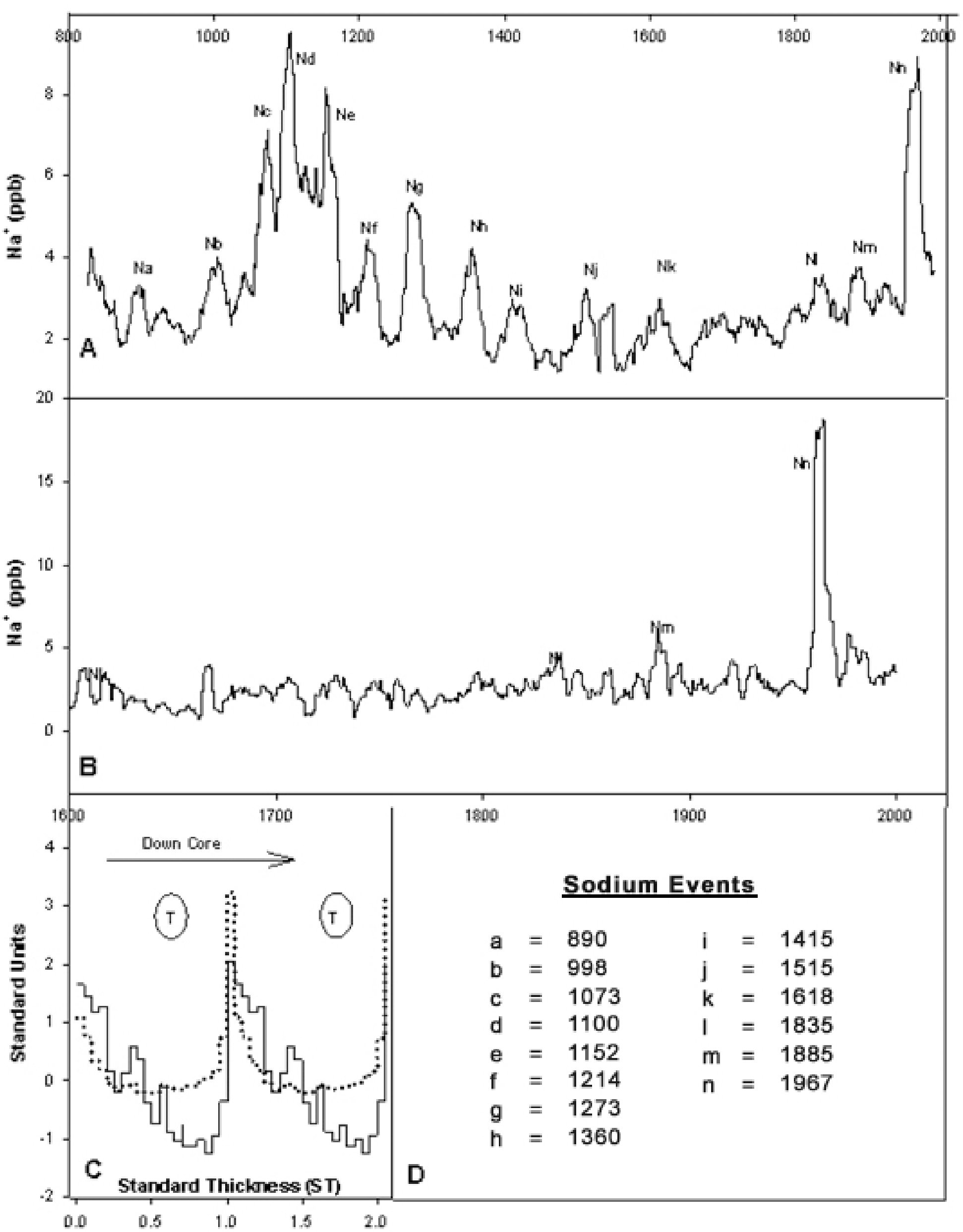

Sodium Events

a = 890
b = 998
c = 1073
d = 1100
e = 1152
f = 1214
g = 1273
h = 1360
i = 1415
j = 1515
k = 1618
l = 1835
m = 1885
n = 1967

Figure 2.23 Profiles of time series of sodium and demarcation of major events. (A) Depicts a 30-year centered average of sodium since A.D. 820. (B) Depicts a 5-year centered average of sodium since A.D. 1600. (C) The black line depicts the annual cycle of sodium. The circled T depicts the observed Tritium peak. Two complete annual cycles are shown. (D) This box gives the timing of large sodium events that are labeled in (A) and (B) with arrows.

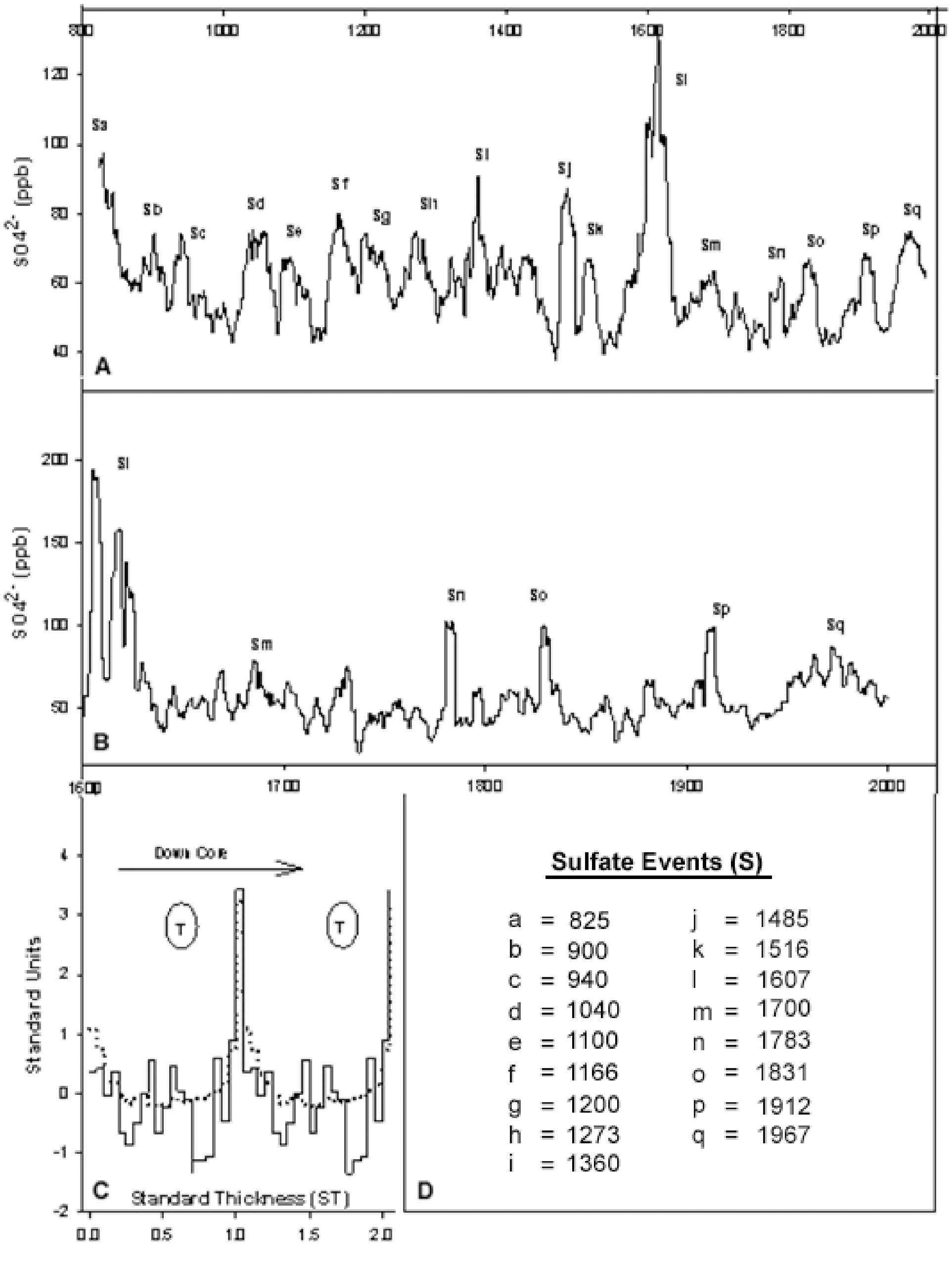

Figure 2.24 Profiles of time series of sulfate and demarcation of major events. (A) A 30-year centered average of sulfide since A.D. 820. (B) Depicts a 5-year centered average of sulfide since A.D. 1600. (C) The black line depicts the annual cycle of sulfide. The circled T depicts the observed Tritium peak. Two complete annual cycles are shown. (D) This box gives the timing of large sulfide events that are labeled in (A) and (B) with arrows.

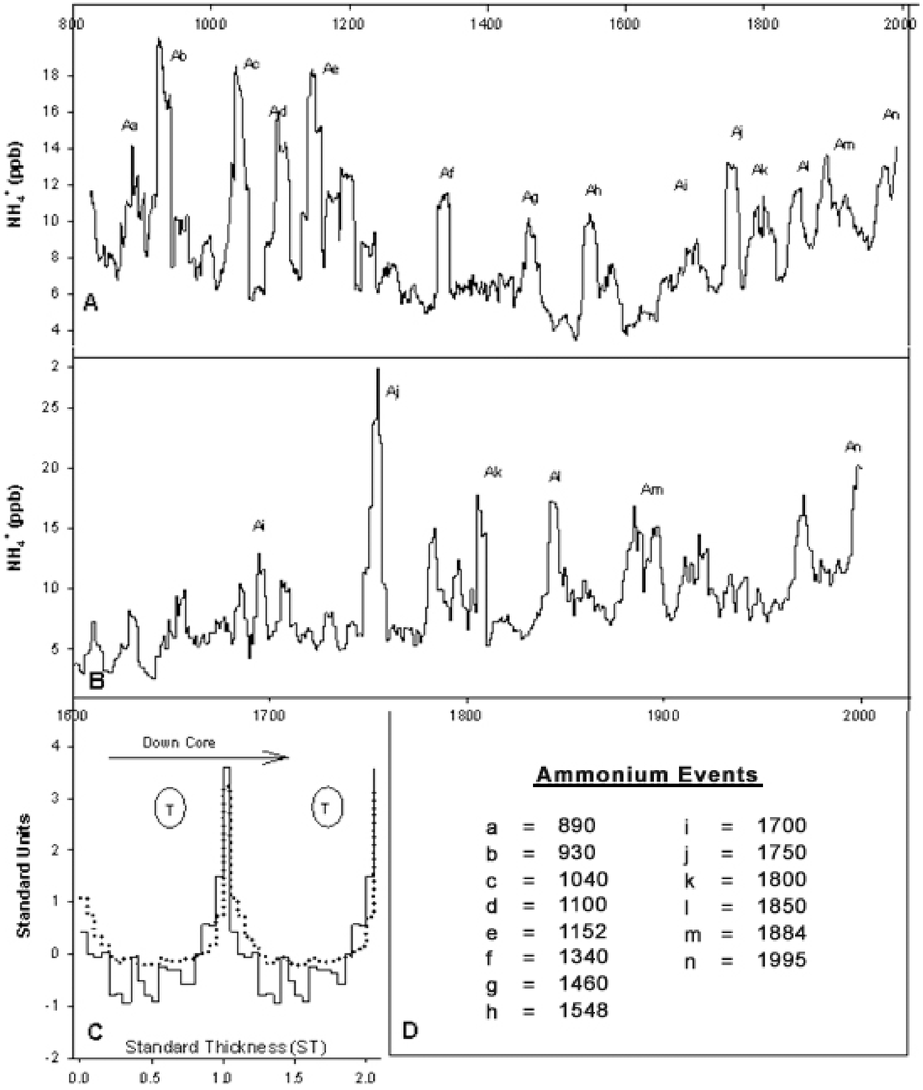

Figure 2.25 Profiles of time series of ammonium and demarcation of major events. (A) Depicts a 30-year centered average of ammonium since A.D. 820. (B) Depicts a 5-year centered average of ammonium since A.D. 1600. (C) The black line depicts the annual cycle of ammonium. The circled T depicts the observed Tritium peak. Two complete annual cycles are shown. (D) This box gives the timing of large ammonium events that are labeled in (A) and (B) with arrows.

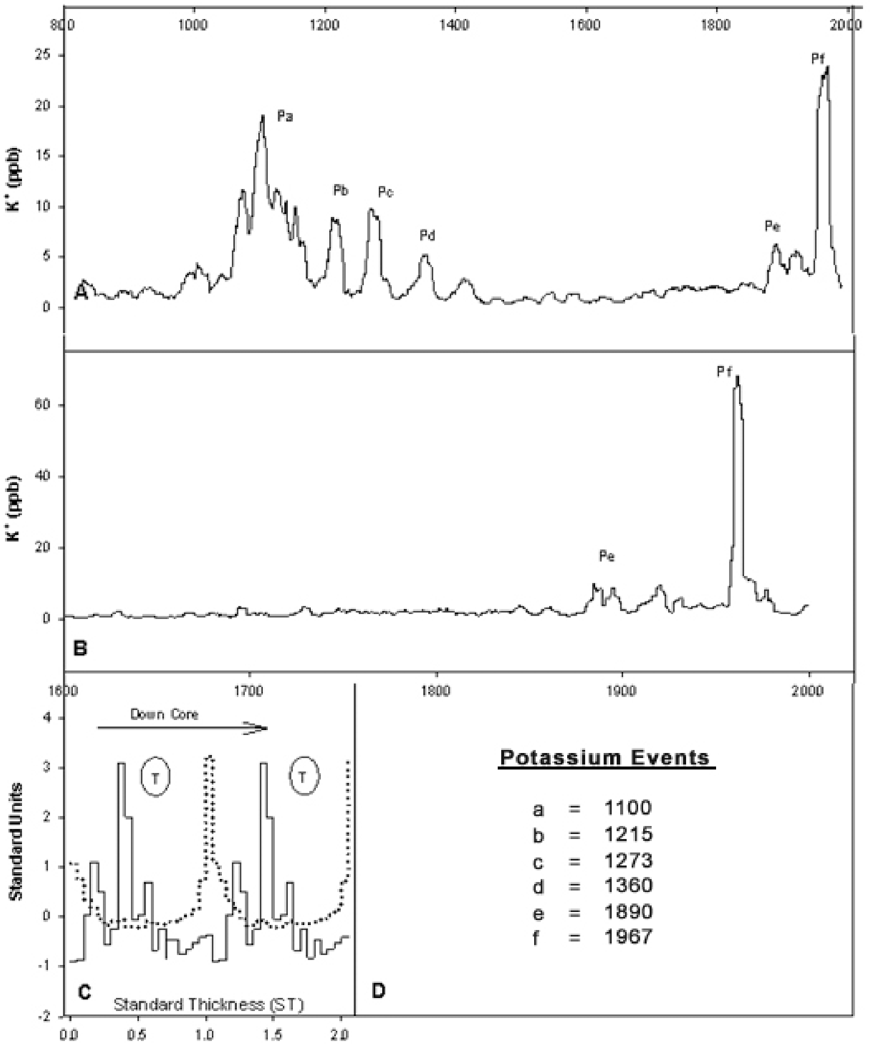

Figure 2.26 Profiles of time series of potassium and demarcation of major events. (A) Depicts a 30-year centered average of potassium since A.D. 820. (B) Depicts a 5-year centered average of potassium since A.D. 1600. (C) The black line depicts the annual cycle of potassium. The circled T depicts the observed Tritium peak. Two complete annual cycles are shown. (D) This box gives the timing of large potassium events that are labeled in (A) and (B) with arrows.

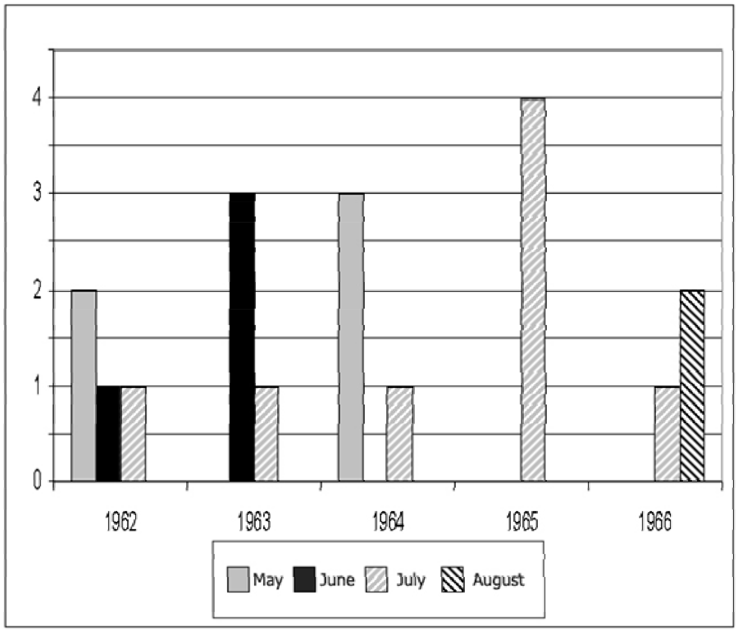

Figure 2.27 Number of weather stations reporting peaks in ^{3}H in each month between 1962 and 1966.Based on weather station data from four different locations and collected from GNIP (Global Network of Isotopes in Precipitation). Stations shown are Adak, Bethel, and Palmer in Alaska and Ottawa, Canada.

2.4.2 Timing of the seasonal peak in dust

There are several lines of evidence that constrain the timing of the annual peak in BC1 dust to sometime between February and May. Constraining the timing of the peak in dust is of particular importance, as the seasonal composites (Fig. 2.15) show that enrichment of δ^{18}O, minimum values in d-excess, and maximum values in all other ice core parameters, which include SO_4^{2-}, Ca^{2+}, NO_3^-, NH_4^+, Na^+, Cl^-, and Mg^{2+} (but exclude K^+ and F^-), all occur at the same time. Several lines of evidence are employed to constrain the timing of the dust peak. First off, the timing of dust peaks in BC1 between A.D. 1963 and A.D. 1966 are compared with the known timing of the peaks in ^{3}H (Fig. 2.4). Second, possible causative agents of the dust peaks are investigated, such as transport of dust into the region via dust storms from Asia and changes in the rate of accumulation related to seasonal patterns of precipitation.

Historical measurements of ^{3}H in precipitation from Bethel, Adak, and Palmer, Alaska and Ottawa, Canada were examined to identify the seasonal cycle of ^{3}H in regional precipitation. These datasets were derived from the GNIP (Global Network of Isotopes in Precipitation) database at: http://isohis.iaea.org. The Alaska records cover the period of interest in the early 1960s, and the record from Ottawa begins in A.D. 1953 and extends to the present. An examination of these four time series during the period A.D. 1962-1966 shows that in most cases the ^{3}H peak occurs in June or July, but in some cases it is seen as early as May or as late as August (Figure 2.27). Out of a total of 20 observations from the various stations, 12 of the ^{3}H peaks occurred in either June or July, and for the purposes of this study it is assumed that the peaks in ^{3}H in the ice core coincide with this time period.

The results of the high-resolution ^{3}H sampling of BC1 from 1963 to 1966 are presented in Figure 2.4, which shows the relationship between the timing of the ^{3}H peak with δ^{18}O, dust, and K^{+}. In each of the three years shown in Figure 2.4, it can be seen that the peak in dust lies stratigraphically below the peak in ^{3}H, but stratigraphically above the minimum concentrations of ^{3}H that occur during the winter. This places the dust peak within a period in which ^{3}H concentrations have begun to increase from a winter trough but have not yet reached maximum summer values. The time series of ^{3}H in precipitation from Bethel, Adak, and Palmer, Alaska and from Ottawa, Canada suggest that the timing of the dust event must occur sometime between February and May. The timing of the ^{3}H peak in relationship to the composites, labeled as a "t" in a circle and shown in Figure 2.15, was inferred from the relationships identified in Figure 2.4.

Several other independent lines of reasoning also suggest that the dust peaks in BC1 occur sometime between February and May. For example, this timing matches that of Asian dust storms. These storms are large enough that they can clearly be seen in satellite pictures, and individual dust events can be tracked as they leave Asia and cross the Pacific. An analysis of dust samples from Denali, Alaska taken between 1989 and 1999 shows that Asian dust concentrations peak in the atmosphere between March and May and that Asian dust accounts for between 30% to 50% of the total concentration of fine aerosols (*VanCuren and Cahill*, 2002). Another line of evidence for timing of the deposition of insoluble aerosols in BC1 comes from data from meteorological stations in the surrounding valleys, which show that minimum precipitation occurs during April (*Urmann*, 2003). If one assumes that the rate of dust fallout is constant throughout the year and that seasonal precipitation patterns at the drilling site matched those in the valleys, then the lack of accumulation may also contribute to the spring dust peaks.

Studies of other ice cores drilled from sites in the Northern Hemisphere also show the occurrence of a spring dust peak. For instance, a study of two ice cores from central Greenland indicates that dust concentration peaks in spring/summer (*Whitlow*, 1992). Additionally, in the ice core from Mt. Wrangell (62° N, 144° W, 4100 m), which is near the Bona Churchill site, *Yasunari* (2007) found evidence for springtime peaks in both fine and coarse particles. *Yasunari* (2007) constrained the seasonal progression by making use of ^{3}H in a similar manner to this study and by making use of the known timing of the A.D. 1992 eruption of Mt. Spur, which left a visible ash layer in the ice core.

2.4.3 Seasonal divisions

Each annual layer in BC1 corresponds to a year running from the spring of one year to the spring of the next. This is not ideal, as spring-based years split by definition the highest dust concentrations and lowest values of δ^{18}O into separate years and as a result contain a signal from the winter/spring periods of two different years. Fall-based years are better for looking at winter variability, as they capture the entire seasonal dust peak and that of the other major ions that peak in the spring along with the complete trough in δ^{18}O values. The fall-winter break was defined by the peak in K^+ when it was identifiable, as it is the only measured ion that does not exhibit a peak coincident with the dust peak (Fig. 2.15). As a secondary indicator, I looked for the lowest concentrations of NO_3^- and when K^+ and NO_3^- didn't give a clear signal, either Na^+ and/or values of δ^{18}O were used. Figure 2.28 presents the seasonal composites used to identify an average fall-based year and shows the location where the yearly break was made in relationship to each individual composite.

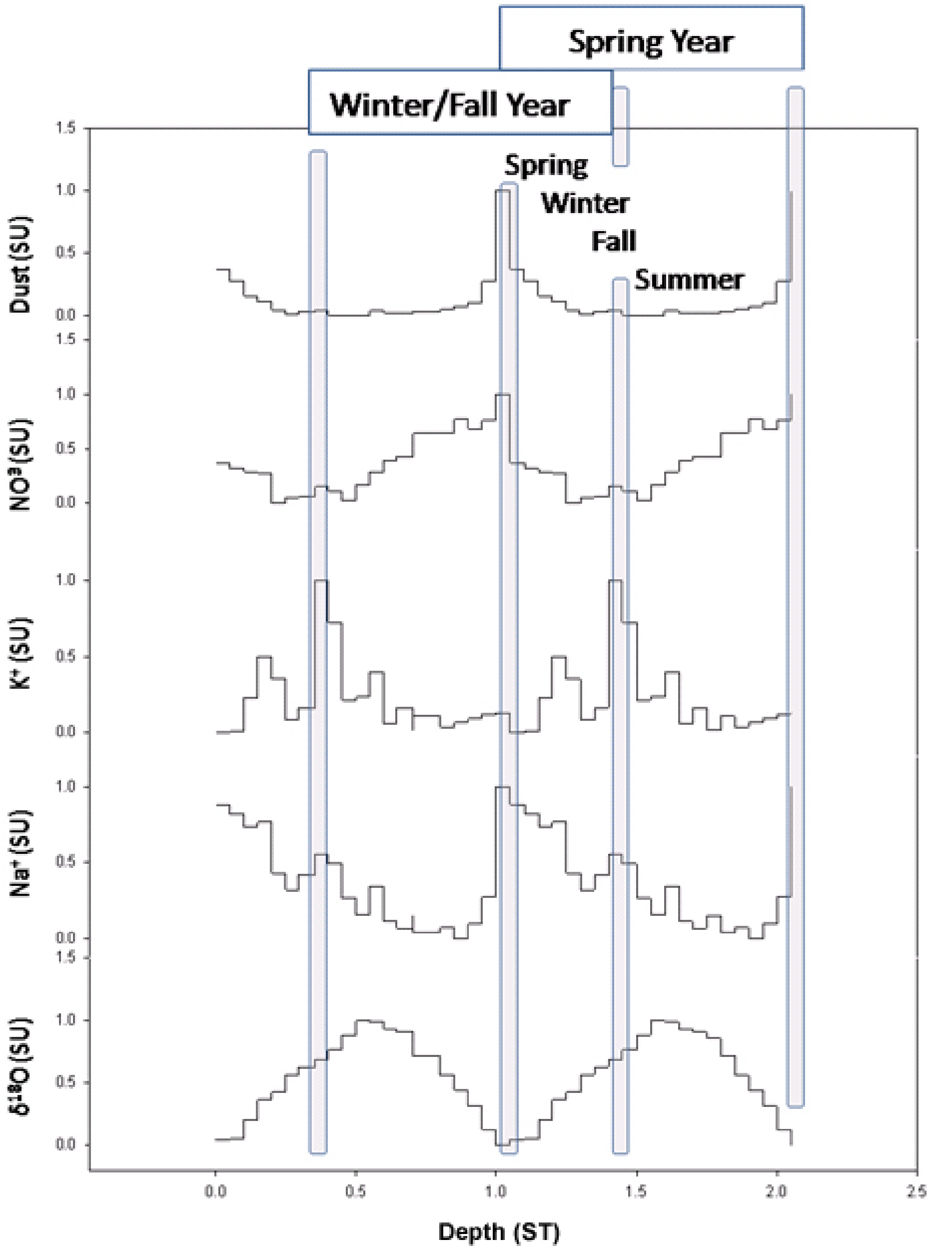

Figure 2.28 Location of seasonal breaks used in order to define spring and winter/fall-based years in BC1. The seasonal breaks are shown with gray bars. The profiles displayed are average yearly cycles, as shown in Figure 2.15, and values of the y- and x-axis for all parameters are shown as standardized units (SU) calculated between 0 and 1 for ease of comparison.

A time series of fall-based years was reconstructed for the period A.D. 1902-2000, and Figures 2.29 and 2.30 show how the individually derived partitions of the ice core year or fraction of a year are defined. The exact timing of the breaks defining these segments is difficult to determine, as the complete yearly cycle is only constrained by the timing of the summer H^3 peaks. Also, it is important to note that the different time series are quite similar at longer time scales. The partitions defined in Figures 2.29 and 2.30 are abbreviated as follows in the remainder of this work:

Fall-Based (FB) Years (BC_{XFB}): For years based on late summer or early fall divisions in the ice core. (The variable X references a particular ice core, such as BC1 or 2.)

Spring-Based (SB) Years (BC_{XSB}): For years based on late winter or early spring divisions in the ice core.

Summer Spring Segment (BC_{XSSS}): A spring-based year minus the fall winter segment (FWS), which represents the portion of the ice core between the fall division and the next spring division in a down-core direction.

Fall Winter Segment (BC_{XFWS}): A fall-based year minus the Spring Summer Segment (SSS).

BC_{XFBQ1}: Refers to the lowest quartile of values for a FB year. Best used to capture the winter low in $\delta^{18}O$ and d-excess.

BC_{XFBQ3}: Refers to the highest quartile of values for a FB year. This time series is used to capture peak values in SO_4^{2-}, Ca^{2+}, NO_3^-, NH_4^+, Na^+, Cl^-, Mg^{2+}, and F^-.

BC_{XSBQ3}: Refers to the highest quartile of values for a SB year. This time series is used to capture peak values in K^+.

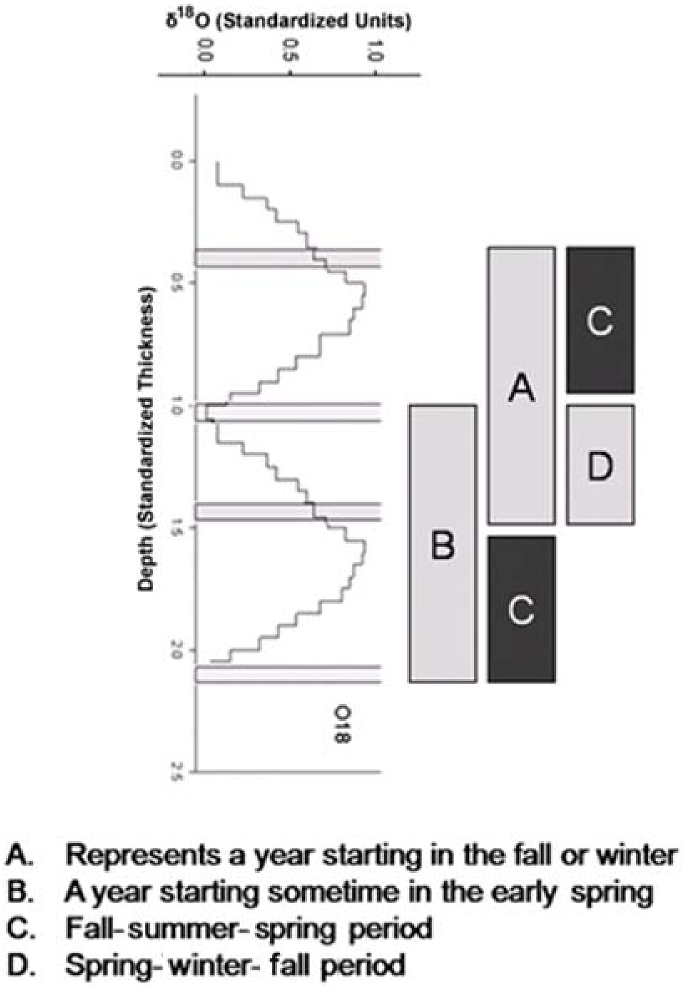

A. Represents a year starting in the fall or winter
B. A year starting sometime in the early spring
C. Fall-summer-spring period
D. Spring-winter-fall period

Figure 2.29 Ice Core δ^{18}O and possible subdivision of the ice core year, based on the seasonal divisions presented in Figure 2.28. The δ^{18}O profile is the average yearly cycles as defined in Figure 2.15 and as described in the text.

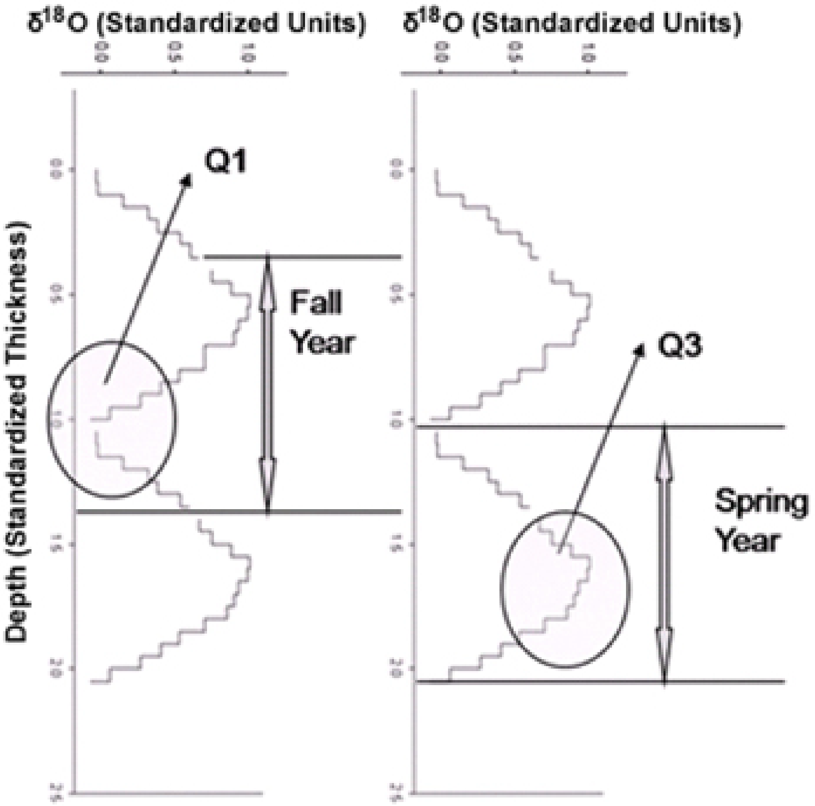

Figure 2.30 Ice Core δ^{18}O and subdivision of the ice core year illustrating the values used to calculate the third quartile (Q3) and the first quartile (Q1). The δ^{18}O profile is the average yearly cycles as defined in Figure 2.15 and as described in the text.

2.5 Comparisons and reproducibility of results

2.5.1 Short and long cores: the first 10 meters

Comparisons of the Bona Churchill ice cores (BCS 1-4 and BC1 and BC2) shows that these records have similar isotopic and chemical profiles and that time equivalent horizons can be traced between the cores. These findings suggest that the derived ice core signal is primarily a function of large-scale processes that act over the entire drilling area. Additionally, these results demonstrate that the ice core record obtained from BC1 is reproducible and wouldn't substantially differ if the ice core had been drilled at an alternate site on the saddle separating Mt. Bona and Mt. Churchill.

The similarity between all the ice cores is illustrated in Figure 2.35, which displays the dust and $\delta^{18}O$ profiles for the first 10 m of all six cores. The similarity between the $\delta^{18}O$ profiles is best exhibited by examining how two different time-equivalent points (labeled 2 and 3 on Fig. 2.31) can be identified in all of the different ice cores. Figure 2.32 illustrates the similarities between the dust and $\delta^{18}O$ using a standardized depth scale based on the $\delta^{18}O$ profiles of BC1. This figure was constructed by standardizing the depths of BC2 and BCS1-4 to BC1 at points 2, 3, and 4 to 4 in BC1 (Fig. 2.32) and replotting the profiles. The resultant alignment of the dust peaks seen between the cores, using the standardized depths scales derived independently from the $\delta^{18}O$ profile of BC1, supports the selection and designation of points A-D as time equivalent throughout all the ice cores. A significant portion of the variation occurring between the different ice cores can be accounted for by difference in depth between the surface and point 1 (Fig. 2.31).

2.5.2 The two long cores: A 114 m comparison

The comparison of the $\delta^{18}O$ profiles between BC1 and BC2 demonstrates that reproducibility exists at depth as well. Space constraints limit the publication of a detailed comparison of all 114 m of overlap between BC1 and BC2. Figure 2.33 shows the absolute differences in depths between the two cores at 13 different time-equivalent horizons and indicates that with increasing depth, there is a decrease in the rate of change between the depths of time-equivalent layers. The 13 points used to identify stratigraphic equivalence were clearly identifiable in both cores, and to support this conclusion five of the 13 points are presented, four of them in Figure 2.31 (labeled as Points 1-4). The fifth is presented in Figure 2.3 (labeled as Point A). The time equivalence of point A in Figure 2.3 is not in question, because it coincides with the beta horizon in both cores. In summary, both ice cores have similar isotopic profiles, and it is shown that differences in depth between time-equivalent layers and between the two cores are most significant in the upper portions of the ice cores (Fig. 2.33).

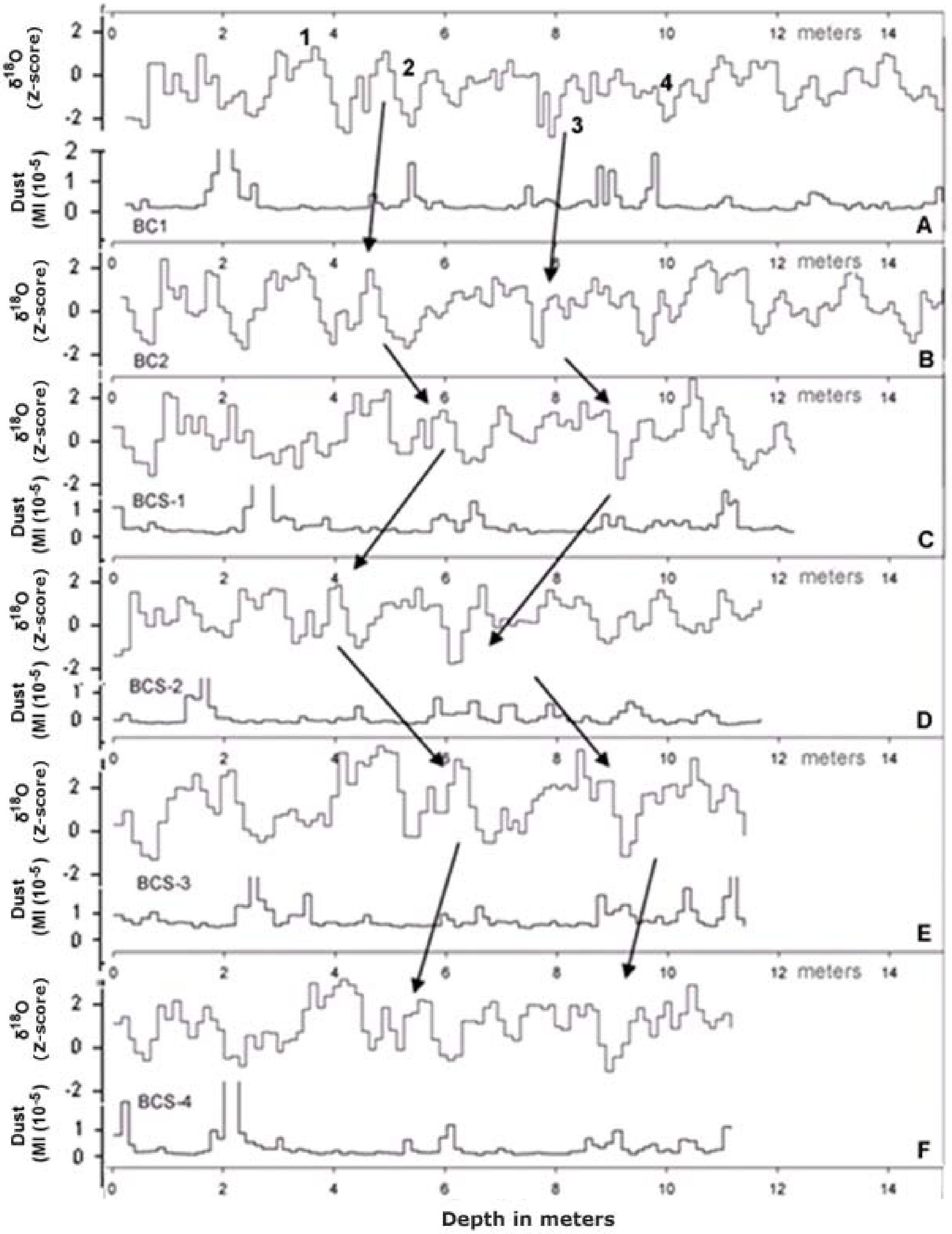

Figure 2.31 Comparison of dust and $\delta^{18}O$ profiles from short and long cores drilled at Bona Churchill. Points B and C are labeled for BC1, and arrows point to time-equivalent horizons on the other shorter cores.

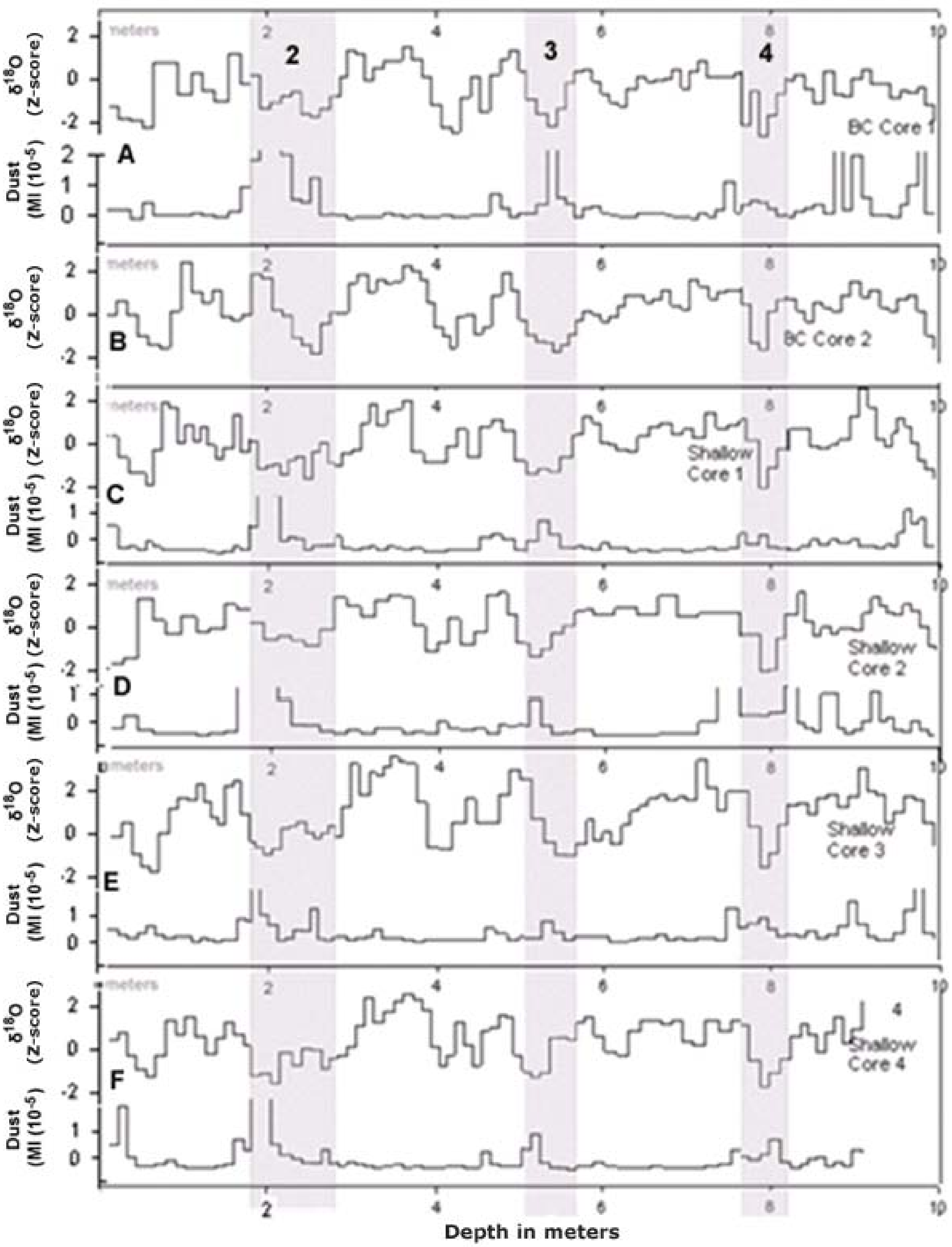

Figure 2.32 Depth-adjusted **c**omparison of dust and $\delta^{18}O$ profiles from short and long cores drilled at Bona Churchill. Points 2, 3, and 4, which were shown in Figure 2.31, are shown in this figure, and vertically shaded bars were placed so that these horizons could be easily seen in the other cores. The depth of each core was adjusted so that it would match BC1.

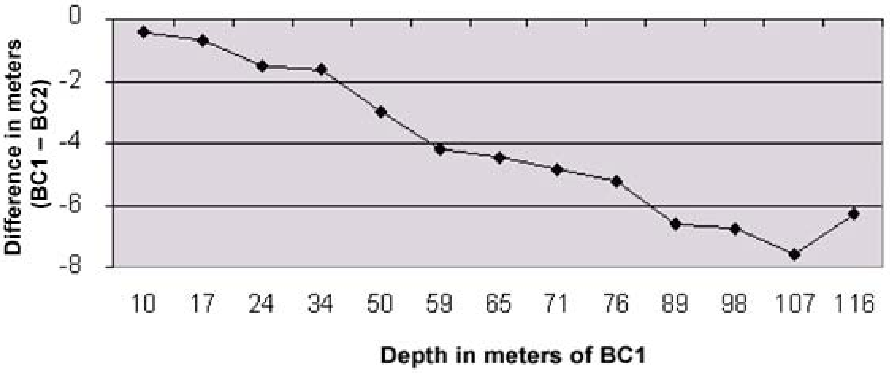

Figure 2.33 Difference at time-equivalent horizons recognizable in both BC1 and BC2 in meters between BC1 and BC2. The depth of BC1 is plotted as the x-axis, and the difference between BC1 and BC2 at time-equivalent points is plotted on the y-axis.

2.5.3 The development of the accumulation record

Annual values of accumulation were obtained by measuring accumulation between individual dust layers. These measurements were then adjusted to account for changes in density and thinning. Measurements of density were made on 80 individual ice segments, each approximately one meter in length, within the top 150 meters of the core. Density increases with depth before gradually leveling off between 0.90-0.91 g/cm3 at approximately 110 m. The following procedure was used to convert measured ice thickness into water or ice-equivalent thickness.

1. The length of each sample was measured.

2. The density of each sample was derived from the measured density of the roughly meter-long section. If density was not measured on a particular tube, then the preceding and succeeding measurements were averaged for use.

3. Water-equivalent depth of each sample was calculated as follows:
(Sample length x density of sample) / (Maximum density of ice 0.92)

4. Annual layer thickness was calculated by summing the ice-equivalent thickness of all the samples grouped within a particular year.

The value of 0.92 is the maximum density that ice reaches in polar ice cores and can be viewed as a good estimate of the maximum density of glacial ice (*Henderson*, 1996).

At depth, ice often undergoes a thinning process that results in the stretching of layers due to ice flow. The amount of thinning is due to a number of factors, such as the slope of the bed, the amount of overlying ice, and the temperature of the ice. Some of these factors, such as the amount of the overlying ice, may vary through time as accumulation rates change. In order to remove the effects of thinning from the time series, all long-term trends were removed (Fig. 2.34). Although these trends are of primary interest when it comes to determining long-term climate changes, they are not as important if the primary concern is interannual ENSO variability, as is the case for this thesis.

2.6 Calibration, time series, and seasonal composites

2.6.1 Introduction

The process of calibration is undertaken to define the modern ice core-climate relationship between the datasets of BC1 $\delta^{18}O$, d-excess, dust, and accumulation. Additionally, this section reviews and summarizes the major trends, significant events, and seasonal cycles in the time series of dust, accumulation, $\delta^{18}O$, d-excess, SO_4^{2-}, Ca^{2+}, NO_3^-, NH_4^+, Na^+, Cl^-, Mg^{2+}, K^+, and F^- from A.D. 750 to the present. The time period from A.D. 1000 to 750 is based primarily on an age-depth model that takes into consideration the rates of thinning observed in the upper part of the ice core. The calibration process presented in this section is consciously biased toward climate variability during the months of December January February (DJF), as this corresponds to the period of year when the effects of changes in ENSO, the AL, and AO are most pronounced in the Northern Hemisphere. The word "event" is used in this chapter as an occurrence when a variable in time series exhibits values that far exceed typical background values.

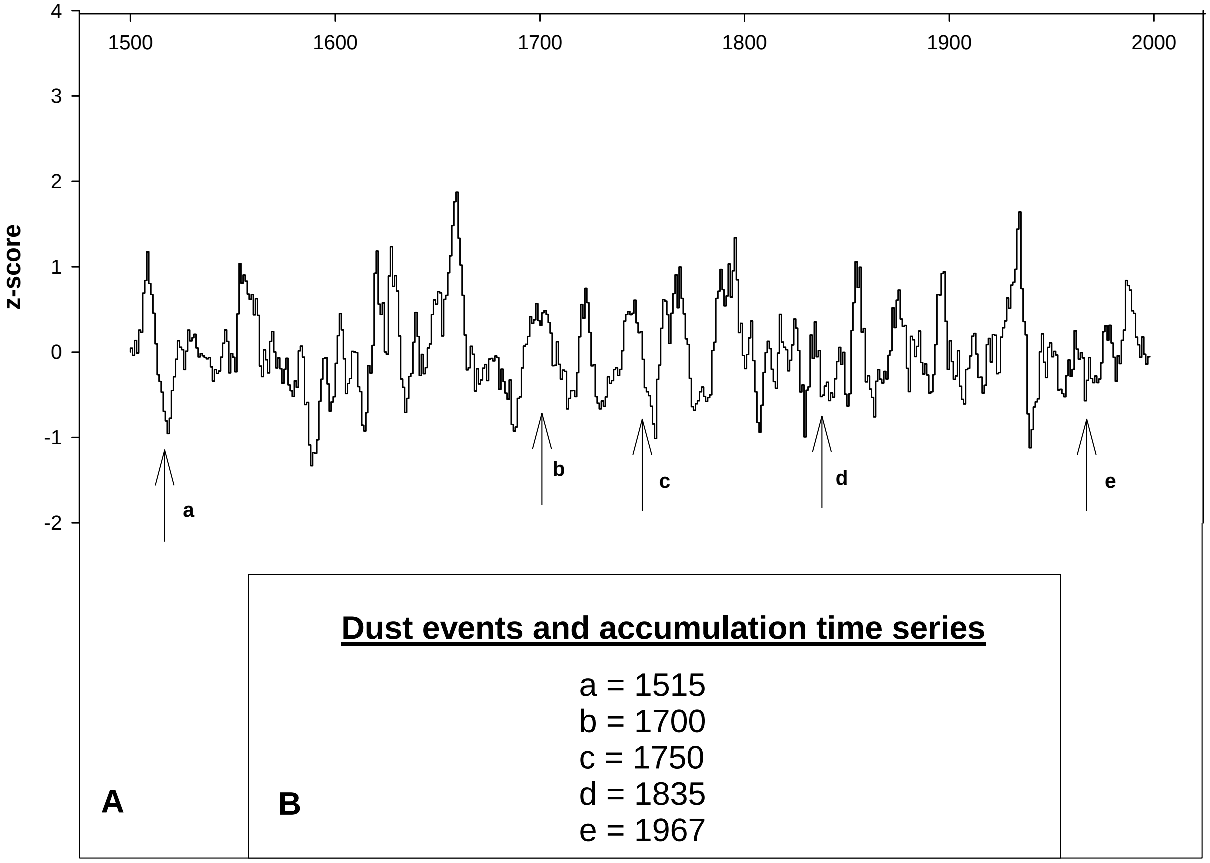

Figure 2.34 The 500-year record of BC accumulation (5-year average) and the timing of large BC dust events. The large dust events are shown with arrows and labeled A-E. The timing of these dust events is given in Box B. Note: The accumulation time series was processed so that long-term variability was removed from the data set (see Section 2.5.3).

2.6.2 Regional precipitation and temperature data sets

Historical records from individual weather stations in southeastern Alaska are of a shorter duration than might be desired for the purpose of calibration, and in many cases the record of observations is incomplete. To overcome these limitations, two different composite records of summer and winter temperature and precipitation were constructed that are referred to separately as the Alaskan Short Composites (ASC) and the Alaska Long Composites (ALC). These were constructed by combining multiple station records during the winter months of December through February. (Appendix A fully details the construction of these composites.) It is noted that strong correlations exist between both the ALC and ASC, with indices of the AL, ENSO, and the PDO (Table 2.3).

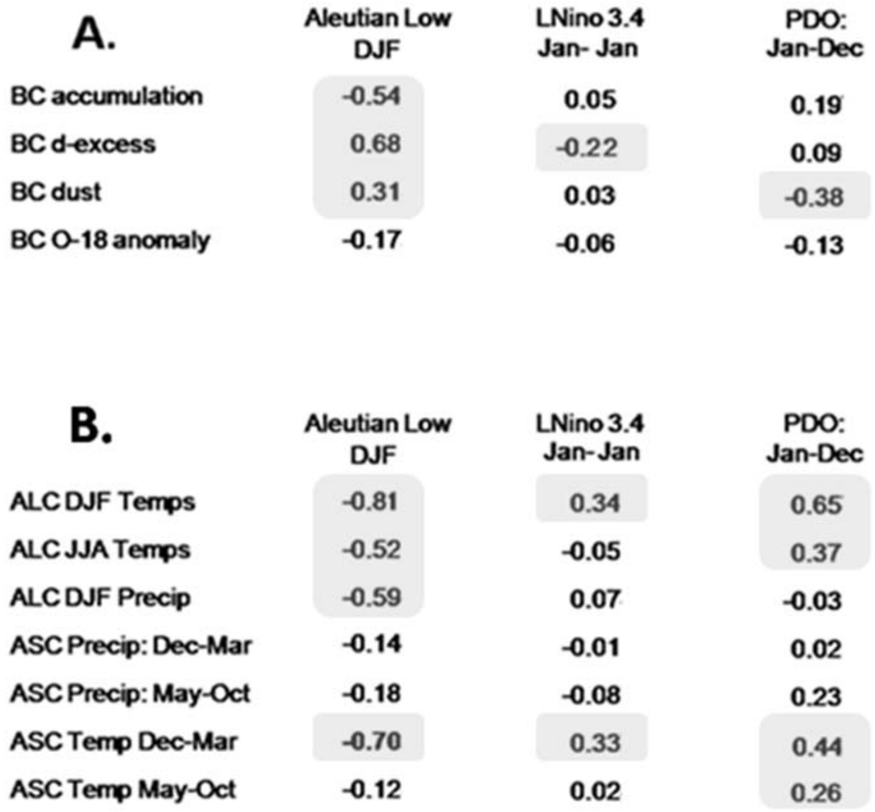

A.

	Aleutian Low DJF	LNino 3.4 Jan- Jan	PDO: Jan-Dec
BC accumulation	-0.54	0.05	0.19
BC d-excess	0.68	-0.22	0.09
BC dust	0.31	0.03	-0.38
BC O-18 anomaly	-0.17	-0.06	-0.13

B.

	Aleutian Low DJF	LNino 3.4 Jan- Jan	PDO: Jan-Dec
ALC DJF Temps	-0.81	0.34	0.65
ALC JJA Temps	-0.52	-0.05	0.37
ALC DJF Precip	-0.59	0.07	-0.03
ASC Precip: Dec-Mar	-0.14	-0.01	0.02
ASC Precip: May-Oct	-0.18	-0.08	0.23
ASC Temp Dec-Mar	-0.70	0.33	0.44
ASC Temp May-Oct	-0.12	0.02	0.26

Table 2.3 Relationship between BC1 (Table 2.3A) and Alaska weather station data (Table 2.3B) with indices of Pacific Climate Variability. Pierson correlation coefficients that are shaded are significant at a 95% CI or better.

The ASC composite is based upon precipitation and temperature records obtained from the National Climate Data Center (NCDC) for McCarthy (two separate records), Kennecott, Chitina, Gulkana, and Paxson (station summaries are given in Appendix A). These stations are all within the immediate vicinity of the drilling site (Fig. 2.1B) and together are used to reconstruct regional time series of precipitation and temperature from 1923-2002. The ALC are based upon a subset of records from the Alaska Historical Climate Network. (A summary of this dataset is given in Appendix A.) This data set includes records from the Sitka Magnetic Station, where records have been kept on a discontinuous basis since A.D. 1828 (the longest record of climate for the entire west coast of the Americas). In fact, in almost every year between A.D. 1828 and 1990, there is some type of meteorological measurement from at least one of the stations in the network. (Some exceptions are A.D. 1830-1831, 1879-1880, and 1892-1893.)

One advantage of using the reconstructed composite records is that they are longer and more continuous than the individual time series. Additionally, errors that exist within individual an data set are likely minimized when they are averaged with other data sets. A potential drawback is that certain weather stations may disproportionately weight the record during those time intervals when the composite record is based on a small number of total records. For instance, the Kennecott record is the only record available between A.D. 1922 and 1942. A second drawback is that long-term trends are de-emphasized in the composite time series as a result of combining separate short segments of standardized data.

2.6.3 Calibration of accumulation

Variability in the amount of annual $BC1_{sp}$ accumulation is strongly correlated with the strength of the Aleutian Low ($r=-0.57$ and $p<0.0001$, 1902-1992) and 700 mb heights at Yakutat ($r=0.70$ and $p<0.0001$, 1960-1999). Table 3 shows that $BC1_{sp}$ accumulation is positively correlated with ASC and ALC winter temperatures and with ASC and ALC winter precipitation. The strongest and most persistent of these correlations is observed with ALC winter precipitation ($r=0.57$ and $p<0.0001$, 1900-1990), and weaker correlations are observed with both ASC/ALC winter temperature time series and the ASC precipitation time series (Table 2.3). The ALC precipitation and temperature time series are more heavily weighted by data from coastal stations, and as a result they exhibit stronger correlations with regional climate indices (PDO, Aleutian Low, NINO 3.4) than do ACS time series. The strong correlation between the ALC time series and the record of $BC1_{sp}$ accumulation suggest that the accumulation record is more representative of regional climate patterns.

A visual comparison of the time series of BC1 accumulation and ALC winter precipitation reveals several prominent features that both time series share in common (Figure 2.35). For instance, periods of above-average precipitation are centered on A.D.

1879 and 1894, and an extended period of low precipitation is centered on A.D. 1908. Also evident in this extended comparison is a step change in precipitation beginning at approximately A.D. 1920. It can be seen in both the historical time series and the time series of $BC1_{sp}$ accumulation that before A.D. 1920 generally lower values of accumulation and precipitation occur than after 1920. (For more on this 1920 step change, see Section 2.7.3.) The relationship between $BC1_{sp}$ accumulation and regional precipitation variability is consistent through time, as evidenced by the strong correlation between accumulation and the ALC winter precipitation time series ($r=0.57$ and $p<0.0001$, 1900-1990).

The relationship between radiosonde data from Yakutat with $BC1_{sp}$ accumulation supports the conclusion that the accumulation record is representative of broad-scale weather patterns (Fig. 2.36). Geopotential height data from the 200 mb and 700 mb levels was obtained for the winter months from 1958 to 2006 from the NOAA Integrated Global Radiosonde Archive. Yakutat is the closest station to the Bona Churchill drilling site for which radiosonde data is available. The time series of geopotential height at 700 mb is strongly correlated with the strength of the Aleutian Low ($r=-0.70$ and $p<0.0001$, 1960-1992) and $BC1_{sp}$ accumulation ($r=0.70$ and $p<0.0001$, 1960-1999). Table 2.4 indicates that $BC1_{sp}$ accumulation is negatively correlated with 200 mb DJF temperatures ($r=-0.50$ and $p<0.001$, 1953-1999) while at the same time positively correlated with the time series of ALC winter temperatures ($r=0.28$ and $p<.01$, 1900-1990) and with 925 mb DJF temperatures ($r=0.60$ and $p<.001$). The 200 and 925 mb DJF time series were obtained for the point closest to Bona Churchill (142’30° N, 62’ 305° W) from the NCEP/NCAR reanalysis data set (Appendix A). The difference in the sign of the correlation between the 925 mb and 200 mb levels suggests that higher lapse rates are associated with increased accumulation.

	Alaska Long DJF Precip	Alaska Long DJF Temps	Alaska Long JJA Temps	Alaska Precip Dec-Mar	Alaska Precip May-Oct	Alaska Temp Dec-Mar	Alaska Temp May-Oct
925 mb	0.70	0.89	0.50	0.50	0.49	0.81	0.24
200 mb	-0.69	-0.72	-0.27	-0.51	-0.43	-0.58	-0.34
Slope	0.72	0.89	0.50	0.47	0.48	0.78	0.30
Pwat	0.71	0.93	0.33	0.41	0.48	0.85	0.20

	Aleutian Low	LNino 3.4 Jan-Jan	PDO (Jan-Dec Long version)
925 mb	-0.61	0.33	0.62
200 mb	0.42	-0.24	-0.33
Slope	-0.60	0.32	0.61
Pwat	-0.50	0.45	0.65

	BC accumulation	BC d-excess	BC O-18 anomaly
925 mb	0.60	0.13	0.28
200 mb	-0.53	0.06	-0.18
Slope	0.59	0.11	0.29
Pwat	0.62	0.20	0.04

Table 2.4 Correlations between radiosonde data from Yakutat (1958 to 2006) with weather station data, teleconnection indices, and ice core time series. Pierson correlation coefficients higher than r = 0.32 are significant at a 95% CI or better. All datasets were smoothed with a centered 5-year average.

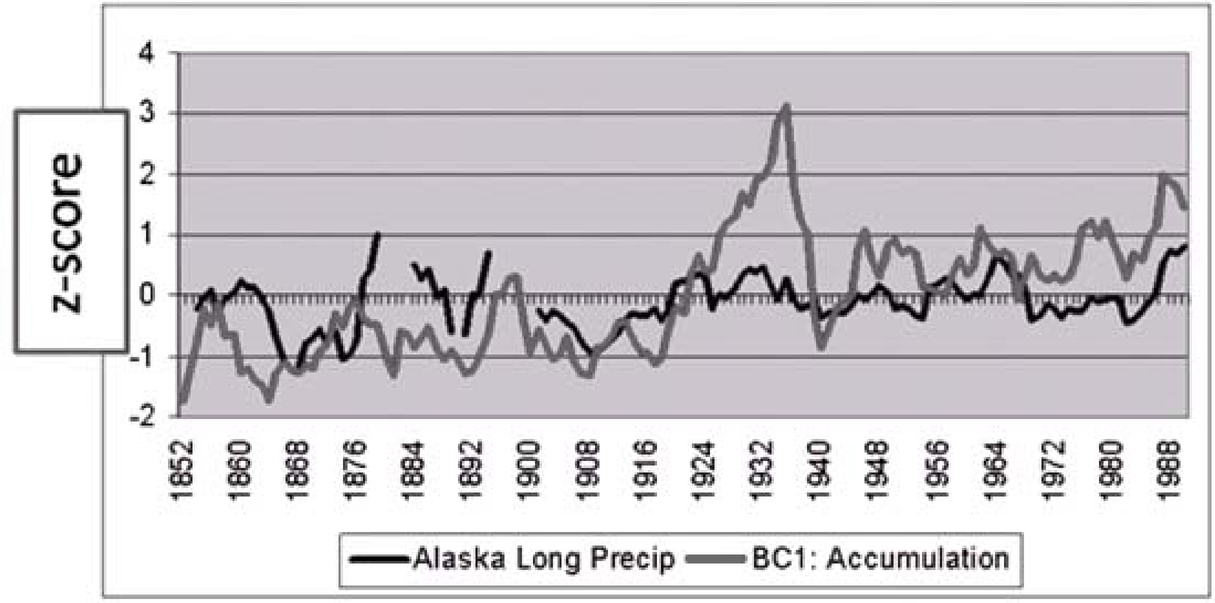

Figure 2.35 Time series of Alaska Long Precipitation Record (see text) and BC1 Accumulation. The 5-year moving average of both time series are plotted as z-scores from A.D. 1852 to 1988. Note step increase in precipitation and accumulation in both records after 1920.

An index of the environmental lapse rate was constructed to further investigate a potential relationship with accumulation by calculating the difference between standardized values of the winter ACS temperature time series and 200 mb DJF temperatures. Large values in this index represent large temperature differences (high lapse rates) between the surface and temperatures at the 200 mb level. Regression analysis indicates that this index is highly correlated with BC1 accumulation ($r=0.69$ and $p<0.001$, 1953-1999, Fig. 2.36A), the strength of the Aleutian Low ($r=0.52$ and $p<0.001$, 1953-1999), and the ALC winter precipitation time series ($r=0.72$, 1953-1990). The reproducibility of this index was tested by calculating a lapse rate index using only the NCEP-NCAR reanalysis time series winter temperature data from the 925 mb and 200 mb levels. The correlation between these two indices is quite high ($r=0.87$ and $p<0.0001$, 1953-1999), suggesting that the derived conclusions are not data set-dependent.

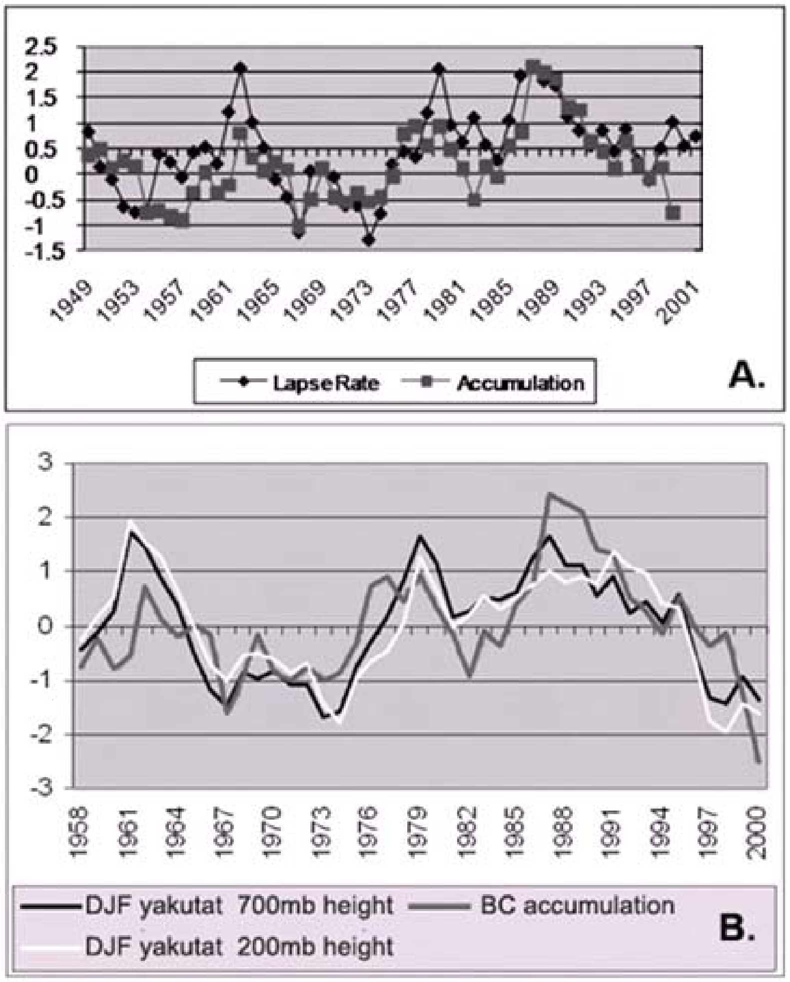

Figure 2.36 BC1 accumulation time series, (A) NCEP/NCAR Lapse Rate calculated as described in text, and (B) Yakutat 200 mb and 700 mb Radiosonde data. All times series in A and B were standardized (z-scores) and smoothed with a 5-year moving average.

Note: Accumulation records were compared with time series of precipitation from local meteorological stations. Separate annual time series were constructed for precipitation records based on different definitions of what was defined as a year. The record of accumulation correlated most strongly with the precipitation time series that corresponded with years ending in April through June. It displayed weaker correlations with the precipitation time series that were based on the years ending in August, October, and December. This is another line of evidence supporting the spring timing of the dust peaks.

2.6.3.1 Accumulation time series summary

The development of the 500-year record of accumulation is discussed in Section 2.5.3, and the reconstructed time series is presented in Figure 2.34. Two primary features stand out in this record during the last 500 years. The first is a step increase in precipitation during the 1920s that is discussed in Section 2.7.3. The second is a change from more decadal toward more interannual variability at approximately A.D. 1800. This is probably not an artifact of the standardization process, because time series of $\delta^{18}O$ from both BC1 and PrCOl (*Fisher*, 2004) exhibits markedly higher amplitude decadal scale fluctuations before A.D. 1800. The time series of accumulation has been detrended, and variability has been standardized so that it equals that of the last century.

2.6.4 Calibration of the d-excess record

The time series of $BC1_{q1}$ d-excess is correlated with changes in the strength of the AL ($r=0.60$ and $p<0.0001$, 1902-1992) and the AO ($r=0.51$ and $p<0.0001$, 1902-2000). Figure 2.37 compares the time series of $BC1_{sp}$ d-excess with that of the Aleutian Low from A.D. 1902 to 1992. In general, values of d-excess are generally high near the beginning of the 20th century and lower toward the end. For the purpose of calibration, the focus will be limited primarily to the detrended time series so that an emphasis can be placed on the shorter decadal and interannual variations, which are the primary focus of this thesis. Reported correlations will be in reference to the detrended time series in this section unless otherwise specified.

The time series of the AL and $BC1_{q1}$ d-excess are very closely correlated during the majority of the period of record, but they go out of phase from the mid-1970s to 1980s, with the year 1976 corresponding approximately with this shift. The year 1976 marks a major reorganization in the climate of the North Pacific (Section 1.4.3), and this may be attributed to the breakdown in the relationship between d-excess and the AL. Another possibility for the recent lack of correlation between d-excess and the AL could be a result of a nonlinear response to the strength of the AL that occurs only when the Aleutian Low is much stronger than normal (Fig. 2.38). An actual example that may be representative of this nonlinear response can be seen in the precipitation amounts during the winter of 1982-1983, which was characterized by an exceptionally deep Aleutian

Low (that likely developed in response to an ongoing El Niño event). Precipitation patterns during the winter of 1982-1983 were just the opposite of what normally occurs when the AL is strong. In this case, dry conditions prevailed in Alaska, and there were wet conditions across the Pacific Northwest opposite to what might be expected on average.

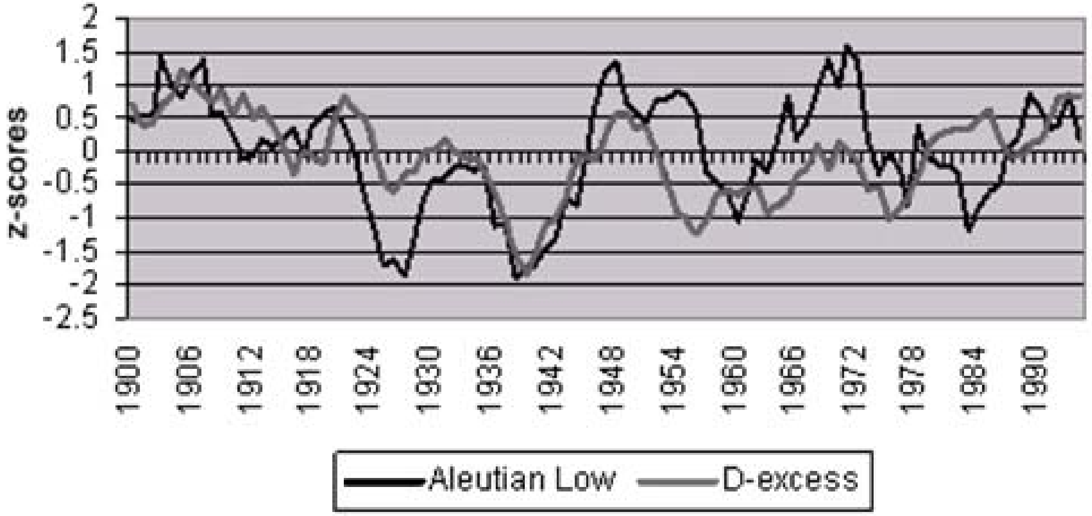

Figure 2.37 Comparison of the time series of BC1 d-excess and the Aleutian Low time from A.D. 1902 to 1992. Both times series were standardized (z-scores) and smoothed with a 5-year moving average. Note the excellent match between these time series up to about 1975.

In addition to being strongly correlated with the strength of the Aleutian Low, the record of $BC1_{q1,sp}$ d-excess is strongly correlated with the strength of the AO and temperatures in Greenland (Fig. 2.39). The correlations between $BC1_{sp}$ d-excess and Godthab DJF temperatures are significant using both smoothed data ($r = -0.62$ and $p<0.0001$, 1902-2000) and unsmoothed data (-0.33 and $p<0.001$, 1902-2002). A longer examination of the temperature time series shows that this relationship is not consistent prior to the 20th century. A sliding correlation plot (not shown) shows that the strong relationship between $BC1_{sp}$ d-excess and both Godthab DJF and Iceland DJF SLP goes out of phase sometime between A.D. 1890 and 1900. However, an examination of the entire record of Iceland DJF SLP shows a general lack of correlation between the two time series during the 19th century.

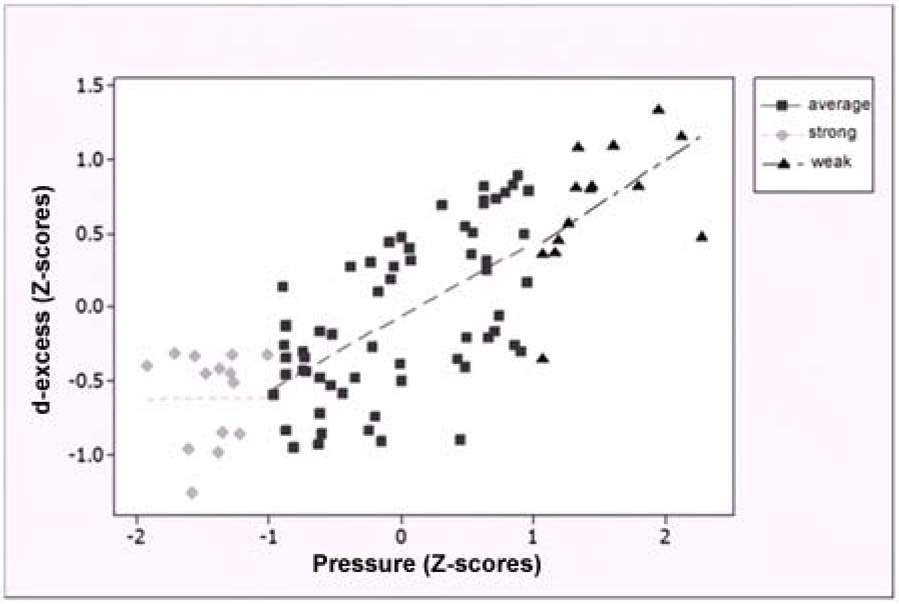

Figure 2.38 Correlation plot of the standardized 5-year averages of the AL index and BC1 d-excess. Higher values of pressure equate with a weaker AL. Regression lines were calculated separately for periods when the AL was strong (diamonds), average (squares), and weak (triangles). Note the lack of correlation between these two variables when the AL is strong.

Identifying the physical mechanism to explain the relationship between either the AO or AL with d-excess is difficult, as both exhibit strong positive correlations with d-excess and with each other. Thus, when the Aleutian Low is weak (strong), the AO is strong (weak). The strong AO and weak AL regime can be thought of as one in which zonal flow predominates around the pole and through the mid latitudes. Meridional flow anomalies in the Pacific tend to be more variable and located further to the west (*Zhu et al.,* 2006). Lower values of d-excess resulting from a reduced kinetic effect could be a response to lower SSTs, increased mixing of surface waters, or higher humidity at the source area (*Bradley*, 1999). When the Aleutian Low is strong, values of d-excess are generally lower, and one might suspect that this is a response to either one or a combination of lower SSTs, increased wind speeds, or higher humidity at the source area. All of the conditions are consistent with a strengthening of the Aleutian Low, so it is difficult to rule out the effects of one from the other. Another entirely different possibility is that changes in d-excess are driven by changes in the moisture source area.

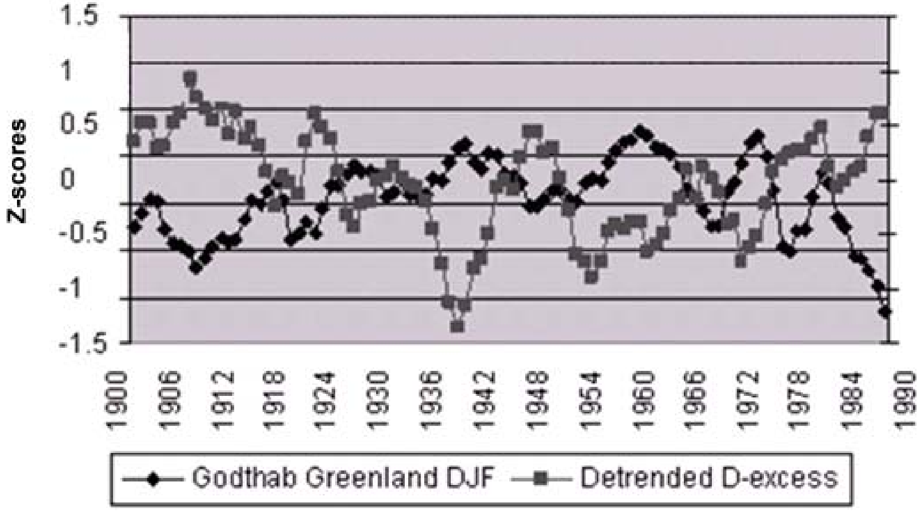

Figure 2.39 Comparison of the time series of BC1 d-excess and DJF temperatures from Godthab Greenland from A.D. 1902 to 1992. Both times series were standardized (z-scores) and smoothed with a 5-year moving average. If this graph was plotted through to the year 2000, we would see that d-excess values fall as predicted along with the end-of-century rise in temperatures at Godthab. (The extremely low temperatures in the early 1990s are not an anomaly.) The graph is presented as is for the sake of uniformity, because most of the temperature data used in this thesis are from Global Historical Climate Network (GHCN), and this data set was only available up to 1994 when this analysis was made.

The 1920s shift in d-excess is marked by a transition to a stronger AL and weaker AO (for more on this 1920s step change, see Section 2.7.3). The most recent regime shift in 1976 exhibits a somewhat different pattern in that while the AL deepened, the AO has been generally positive. However, despite the fact that the AO has remained positive, it is still positively correlated with the AL on an interannual basis, just not on a decadal basis. The difference in circumstances between the regime shifts is of interest, as the relationship between d-excess and the AO is weaker after 1976 and the relationship with the AL goes out of phase. This compares to the 1920s shift in which the correlation between d-excess and both these variables remained consistently positive.

2.6.4.1 Time series summary and seasonal cycles

The MWP between A.D. 800 and 1200 is marked by higher variability than the rest of the time series of d-excess, and the highest values in the entire time series are centered at A.D. 1100 and 1000 (Fig. 2.16). These exceptionally high values are followed by a gradual trend toward lower values that began in A.D. 1200 and accelerated after A.D. 1775. The last 150 years also stand out in that they are the lowest values during the entire time series. $\delta^{18}O$ and d-excess exhibit broadly similar seasonal profiles, except that d-excess exhibits a broader plateau of peak values, and transitions between maxima and minima are more rapid than variations exhibited by $\delta^{18}O$. The interpretation of this time series may be limited due to possible contamination of samples during thermal drilling. The number of samples affected by this is shown in Figure 2.40, and it can be seen that by A.D. 1800, up to 30% of samples in a given year may be contaminated. However, if the contamination occurred randomly, one would not expect it to affect the long-term trends seen in Figure 2.16.

2.6.5 Calibration of $\delta^{18}O$ and dust

The records of $\delta^{18}O$ and dust from BC1 can be related to long-term shifts in the primary modes of Northern Hemisphere circulation, as expressed by the Aleutian Low (AL) and the Arctic Oscillation (AO). A strong correlation is evident between $BC1_{sp}$ $\delta^{18}O$ and dust ($r=-0.62$ and $p<0.0001$, A.D. 500-2000, shown in Fig. 2.10 and 2.11) for the entire length of the time series, which could attend to the stability of the relationship between climatic factors and both of these variables. A strong response is seen in BC dust and to a lesser extent $\delta^{18}O$ when a weak AL occurs at the same time as a negative AO (Fig. 2.41). Higher concentrations of dust occur in years with a weak AL, and negative AO occur in A.D. 1951, 1956, 1965, 1969, and 1979. These were identified by sorting all the years since A.D. 1950 by the strength of the winter AL and the mode of the AO. Although this situation does not account for all dust peaks, it certainly accounts for the largest dust peaks and also provides a physical cause to explain their existence. In the longer record depicted in Figure 2.11, it can be observed that every significant dust peak (trough) is accompanied by more positive (negative) values of $\delta^{18}O$.

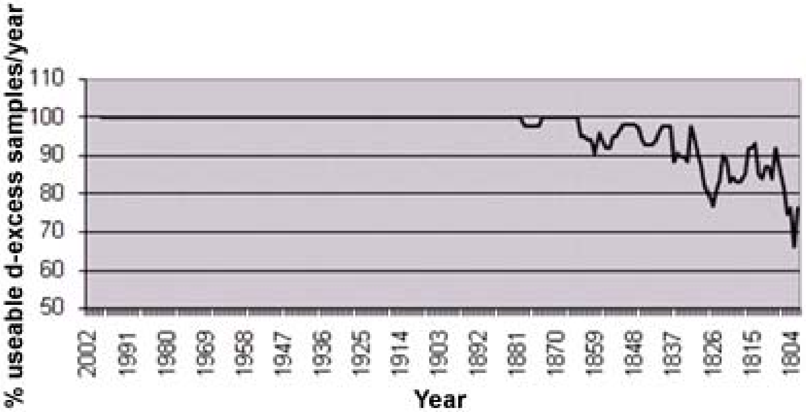

Figure 2.40 This graph shows the percent of useable d-excess samples per year. Some samples were unusable because of possible contamination with drilling fluid. This graph was not extended beyond A.D. 1800, but prior years also have missing samples, although most years have more than 50% useable samples. The contamination of the samples was sporadic and random in nature and does not change the long-term trends exhibited in Figure 2.16A, which depicts the 30-year average of the time series from A.D. 800 to 2000.

Composite plots of the 15 years with the enriched and depleted values of $\delta^{18}O$ were generated to examine contributing meteorological differences. These composites (Fig. 2.42 and 2.43) show that when $\delta^{18}O$ is negative, the Aleutian Low is centered far to the west, almost over the Kamchatka Peninsula, and that when $\delta^{18}O$ is more positive, the Aleutian Low is centered further eastward in the Gulf of Alaska. These composites are nearly identical to the composite anomaly plots at the 850 mb level, showing years with the most and least dust.

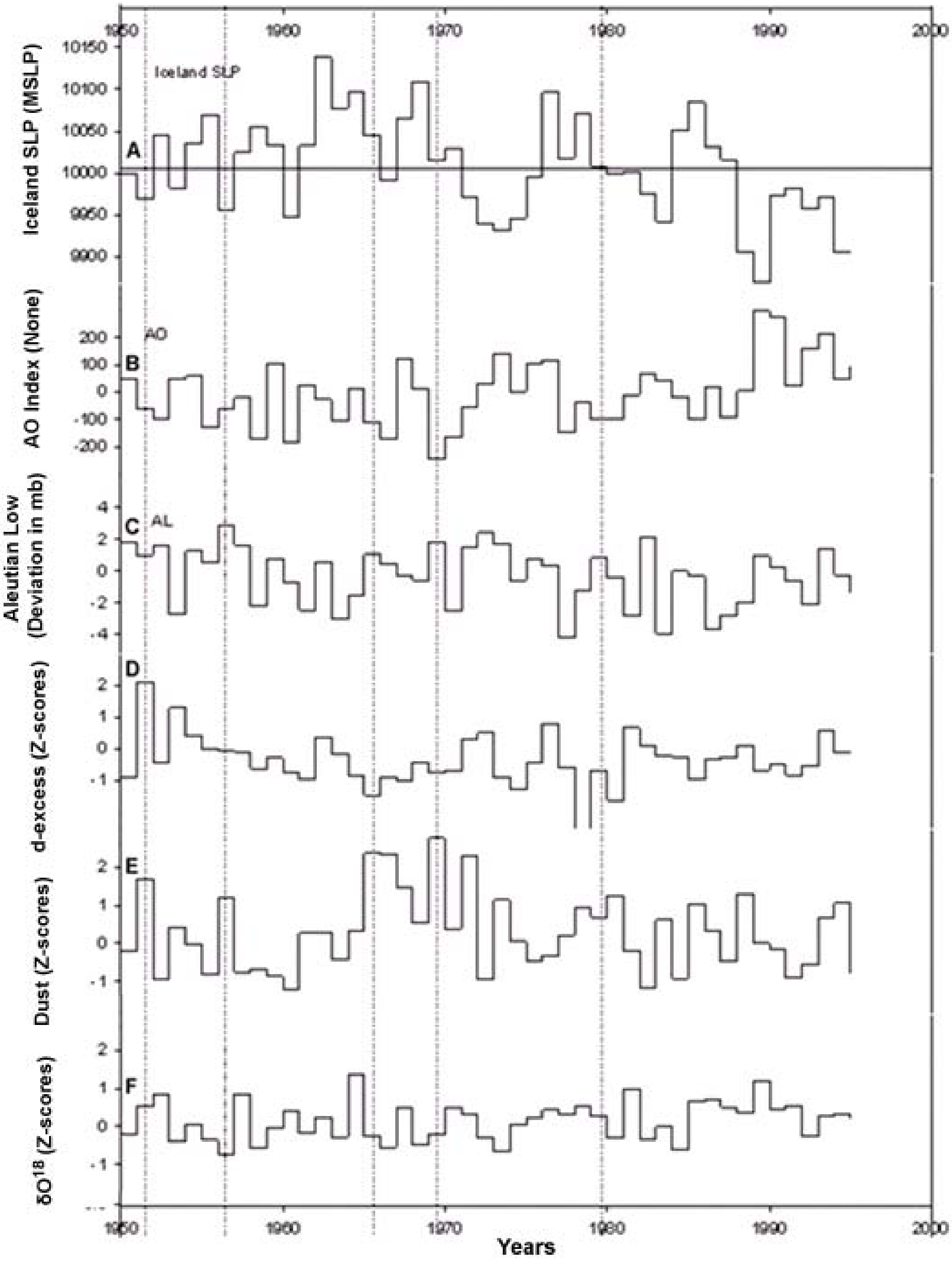

Figure 2.41 Dust peaks associated with a weak AL and negative AO. Dotted lines represent the 5 years with the most negative AO and weakest AL. The largest dust events in the last 50 years are noted to coincide with the dotted lines. BC1 values are annual values of winter-based years. Winter-based years were used so those individual dust peaks were not split.

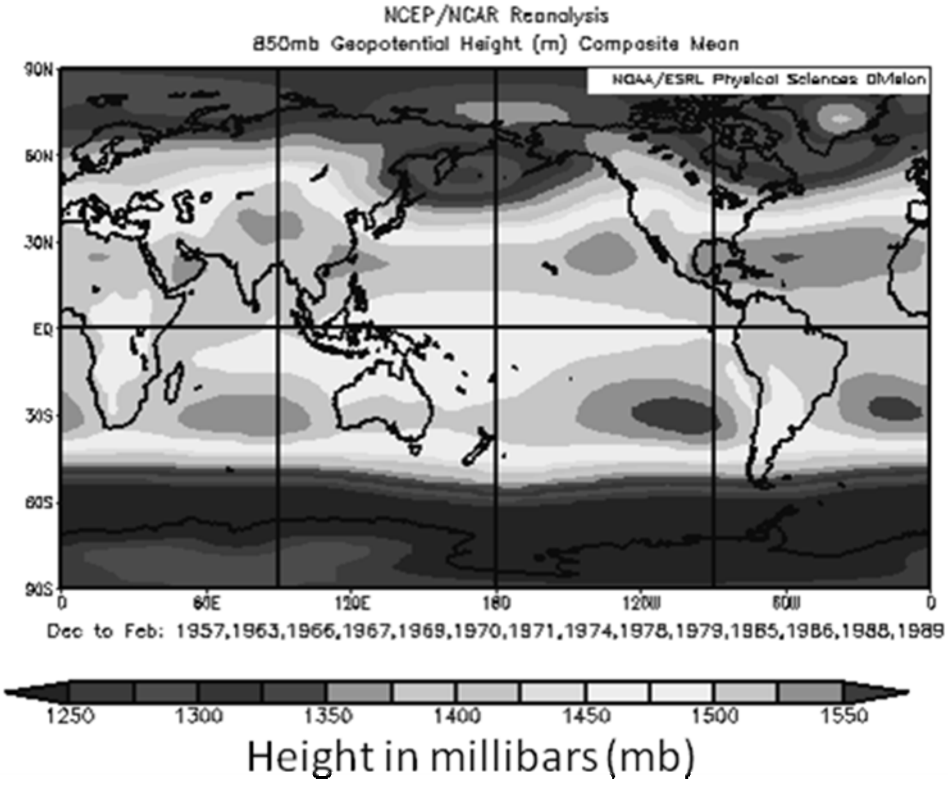

Figure 2.42 Mean 850 mb geopotential height during the 15 years from 1950-2000 with most negative values of BC1$_{q1}$ δ^{18}O. Negative values of δ^{18}O occur when the Aleutian Low is shifted to the west and is weaker than normal. The years used in this analysis are shown under the figure. This graph was plotted using: http://www.cdc.noaa.gov/cgi-bin/Composites/printpage.pl

The spring minimum in δ^{18}O wouldn’t at first appear to support a strong isotope-temperature relationship, because the coldest air temperatures at the drilling site occur in January. However, SSTs (Sea Surface Temperatures) in the Gulf of Alaska (GOA), a primary moisture source area for BC1, are at their coldest in the early spring. This is documented at the GAK1 station (59° 50' N, 149° 28' W), where records of SST have been kept by the University of Alaska Fairbanks since 1970 (*Stabeno et al.,* 2004). Additionally, regional snapshots of averaged monthly SST temperatures (NCEP/NCAR reanalysis--www.cdc.noaa.gov/cgi-bin/Composites/) indicate that SSTs are coldest, on average, during March all the way from the GOA to the Aleutian Arc. One might assume that the SST data correspond better with the $\delta^{18}O$ data, but another possibility is that changing patterns of atmospheric circulation play the primary role. Composites of vector winds at 300 mb (from NCEP/NCAR reanalysis) show that significant changes in circulation occur between January and April, and these may play an important role in explaining the observed cycle in $\delta^{18}O$. For instance, it can be observed that in January when the Aleutian Low (AL) is strong, the cyclonic motion around the low entrains warm, moisture-laden air from the subtropical jet stream and delivers it to the drilling site, but as spring progresses, the AL weakens and the average flow across the North Pacific becomes increasingly more zonal and as a result colder.

Table 2.5 shows that $\delta^{18}O$ values are strongly correlated with the Arctic Oscillation ($r = 0.46$ and $p<0.0001$, A.D. 1950-2000), and with weather station records of DJF temperatures from Boston/Logan, Godthab, Mumansk, and Helsinki. It is noted that these weather station time series are also strongly correlated with the AO. Another line of evidence linking the AO to $\delta^{18}O$ values comes from plots of surface temperature anomalies generated by creating composites based on the difference between the 10 most enriched years minus the 10 most depleted years since A.D. 1950. These plots yield a surface temperature pattern that is similar to that associated with the AO (Fig. 2.44).

A strong relationship is evident between $BC1_{sp}$ $\delta^{18}O$ with the strength of the AL ($r = -0.31$ and $p<.01$, A.D. 1902-1992) and the longitude of the AL ($r=-0.33$ and $p<.001$, A.D. 1902-1992). These correlations provide a physical reference by which to explain the observed relationships between $BC1_{q1}$ $\delta^{18}O$ with accumulation and precipitation. A positive correlation is identified between $BC1_{q1}$ $\delta^{18}O$ and ALC winter precipitation ($r = 0.44$ and $p<.0001$, A.D. 1902-2000). The relationship with regional precipitation patterns is substantiated by the strong correlation observed between $BC1_{q1}$ $\delta^{18}O$ and BC1 accumulation ($r = 0.48$ and $p<.0001$, A.D. 1903-2000). Figure 2.45 shows the correlation field between annual values of $BC1_{q1}$ $\delta^{18}O$ and DJF 200 mb geopotential height (A.D. 1949-2000, NCEP/NCAR reanalysis data). Values of $BC1_{q1}$ $\delta^{18}O$ are negatively correlated geopotential height in the GOA and in the proximity of the drilling site. In general, a positive correlation exists in the mid latitudes, and there are negative correlations around the North Pole and high latitudes; this produces an overall pattern that is very similar to the AO.

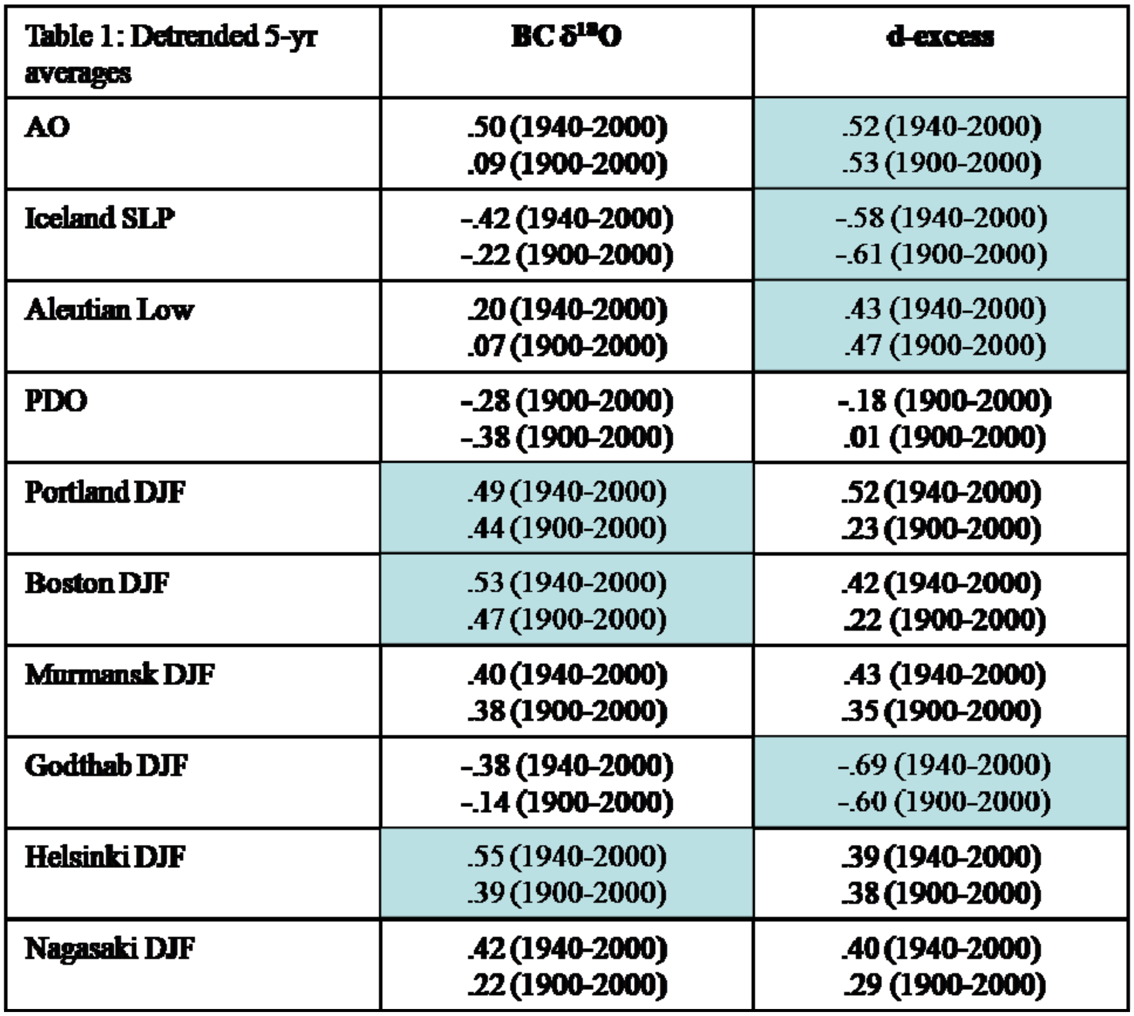

Table 1: Detrended 5-yr averages	BC δ^{18}O	d-excess
AO	.50 (1940-2000) .09 (1900-2000)	.52 (1940-2000) .53 (1900-2000)
Iceland SLP	-.42 (1940-2000) -.22 (1900-2000)	-.58 (1940-2000) -.61 (1900-2000)
Aleutian Low	.20 (1940-2000) .07 (1900-2000)	.43 (1940-2000) .47 (1900-2000)
PDO	-.28 (1900-2000) -.38 (1900-2000)	-.18 (1900-2000) .01 (1900-2000)
Portland DJF	.49 (1940-2000) .44 (1900-2000)	.52 (1940-2000) .23 (1900-2000)
Boston DJF	.53 (1940-2000) .47 (1900-2000)	.42 (1940-2000) .22 (1900-2000)
Murmansk DJF	.40 (1940-2000) .38 (1900-2000)	.43 (1940-2000) .35 (1900-2000)
Godthab DJF	-.38 (1940-2000) -.14 (1900-2000)	-.69 (1940-2000) -.60 (1900-2000)
Helsinki DJF	.55 (1940-2000) .39 (1900-2000)	.39 (1940-2000) .38 (1900-2000)
Nagasaki DJF	.42 (1940-2000) .22 (1900-2000)	.40 (1940-2000) .29 (1900-2000)

Table 2.5 Correlation analysis: Spring-based--BC d-excess and δ^{18}O (5-year averages). Pierson correlation coefficients greater than an absolute value of 0.26 are significant at a 95% level for correlations using data from 1940 to 2000, and those using the larger data set from 1900 to 2000 are significant at the same level when greater than an absolute value of 0.20.

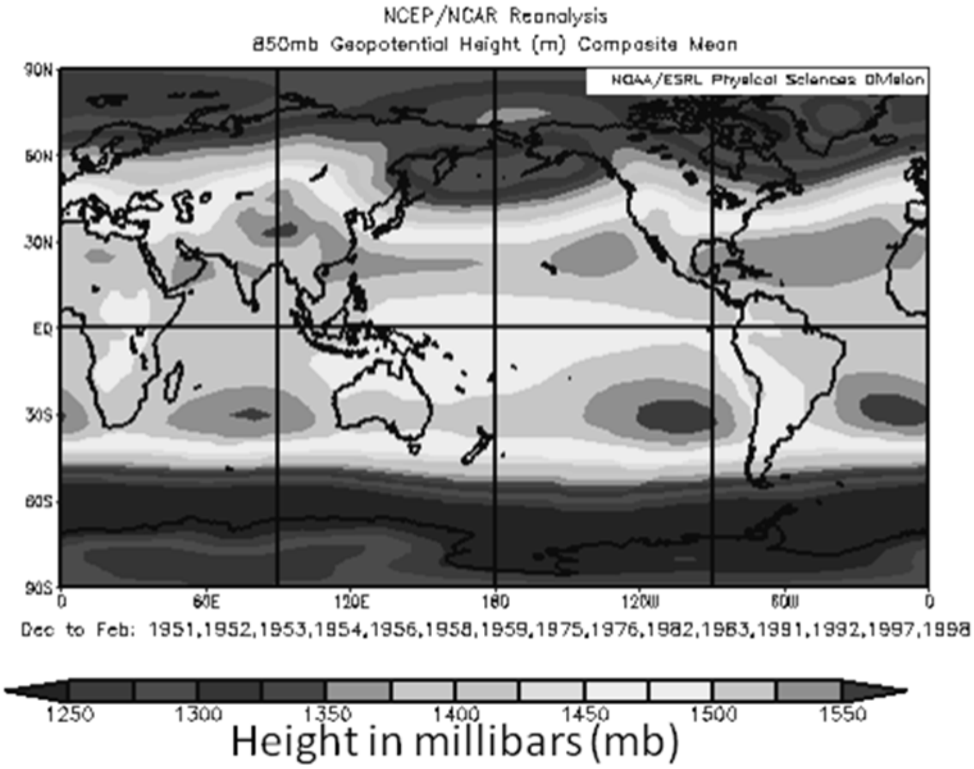

Figure 2.43 Mean 850 mb geopotential height during the 15 years from 1950-2000 with most positive values of BC1$_{q1}$ δ^{18}O. Positive values of δ^{18}O occur when the Aleutian Low is shifted to the east, and during these periods the low is more elongated and stronger. The years used in this analysis are shown under the figure. This graph was plotted using: http://www.cdc.noaa.gov/cgi-bin/Composites/printpage.pl

Strong relationships are noted between BC1$_{sp}$ δ^{18}O with the Siberian Index ($r = 0.47$ and $p<0.0001$, A.D. 1947-2000) and between BC1$_{fq1}$ δ^{18}O and the West Pacific Index (WPI) ($r=-0.60$ and $p<0.0001$, A.D. 1952-2000). The WPI is an important mode of Pacific climate variability with centers of action over Kamchatka and Southeastern Asia. The index is primarily related to the mean location of the Pacific Jet as it leaves Asia and enters the Pacific. This relationship helps to explain connections between both BC1$_{q1}$ δ^{18}O and BC1$_{q1}$ d-excess with the AO. As previous studies have shown, the AO variability may modulate the strength of the Siberian High and the strength of the 200 mb wind off the coast of Japan (*Panagiotopoulos et al.*, 2005). Studies of the Siberian High by *Jhun and Lee* (2004) show that it is more closely correlated with the AO than other teleconnection indices and that the strength of this correlation increases at decadal timescales. The location and strength of 200 mb wind anomalies off the coast of Japan, which define the East Asian Winter Monsoon (EAWM), have been related to the strength of the Aleutian Low and to the amount of convection in the western Pacific. This is supported by the work of *Chang* (2005), who suggests that patterns of upper-level airflow across Asia can set the stage for the path that cyclones take as they cross the Pacific. The strong correlation observed between $\delta^{18}O$ and the WP index suggests that $BC1_{q1}$ $\delta^{18}O$ reflects not only local Aleutian Low variability, but also the history of the air masses as it traverses Asia and enters the Pacific.

2.6.5.1 Time series summary and seasonal cycle of $\delta^{18}O$

The most striking feature of the BC1 $\delta^{18}O$ record is a sustained and gradual shift from -30‰ to -26‰ between A.D. 500 and 1400 (Fig. 2.11). This long trend of steadily increasing values of $\delta^{18}O$ ends abruptly at A.D. 1400, as values quickly drop but then rebound and remain relatively high until A.D. 1800. The 19th and 20th century values of $\delta^{18}O$ have been on average more negative than during the preceding period from A.D. 1400 to 1800. Values are for the most part high during the period A.D. 1400 to 1800, but a significant shift from high to low is seen at A.D. 1618. The seasonal cycle of $\delta^{18}O$ is depicted in Figure 2.18c, and lower values are associated with the spring peak in dust. As noted previously, it should be considered that the dates given for BC1 that are older than A.D. 1000 are not based on layer counting; they are only approximations that are based entirely upon a simple time depth model and the assumptions that are inherent to the model.

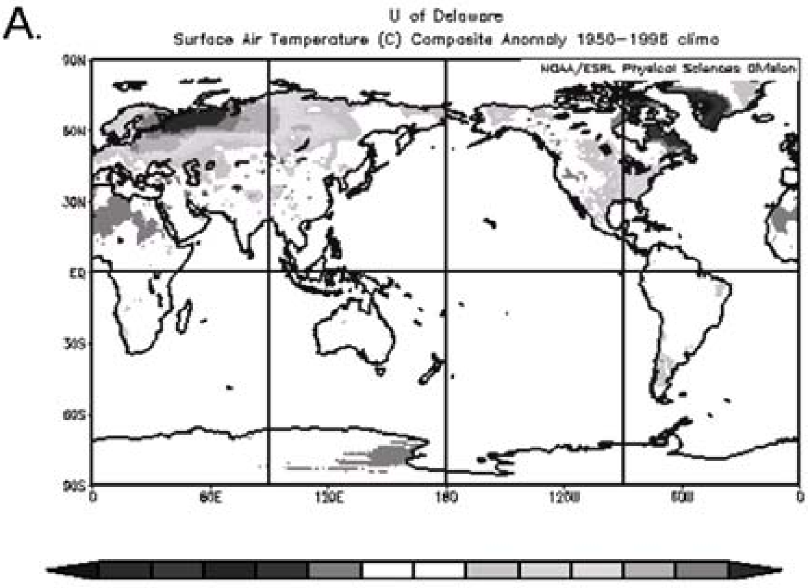

Depleted years BC δ¹⁸O

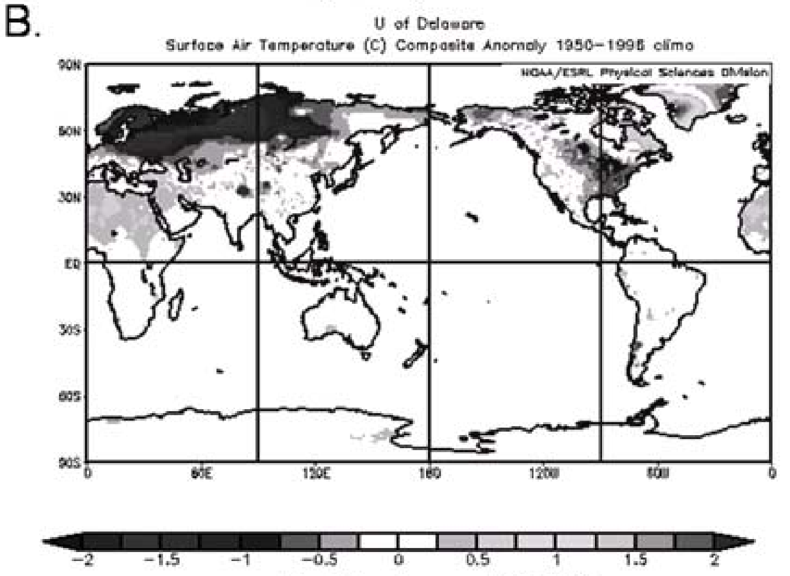

Enriched years BC δ¹⁸O

Figure 2.44 Surface temperature anomalies associated with the 20 most depleted BC1$_{q1}$ δ^{18}O (A) and the 20 most enriched BC1$_{q1}$ δ^{18}O (B) years since 1950. The temperature anomalies are very similar to those generated by AO. Although this figure is in grayscale, it should be noted that in (A) negative temperature anomalies occur in Greenland and positive in northern Russia, and that in (B) this situation is reversed. This graph was plotted using: http://www.cdc.noaa.gov/cgi-bin/Composites/printpage.pl

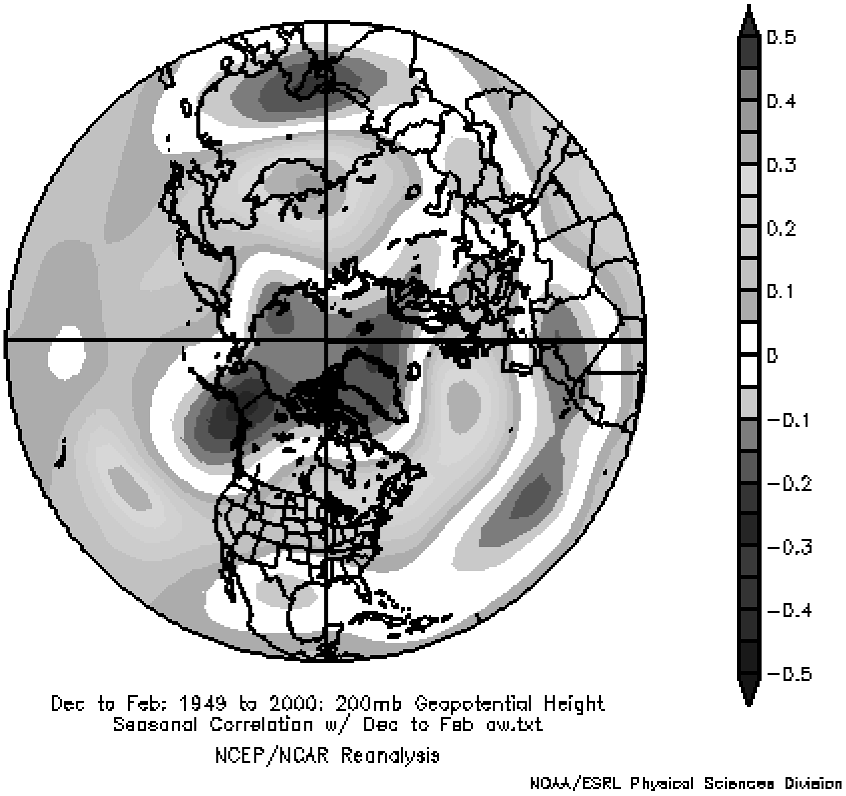

Figure 2.45 Correlation field between annual values of $BC1_{q1}$ $\delta^{18}O$ and DJF 200 mb geopotential height. Positive correlations are found in the middle latitudes, and negative correlations are found over Greenland, the Gulf of Alaska, and northern Siberia. This zonal reversal in the sign of the correlation is very similar to the correlation pattern produced by the AO. This graph was plotted with: http://www.cdc.noaa.gov/Correlation/

2.6.5.2 Time series summary of dust

A gradual trend toward decreased dust concentration characterizes the entire record of BC1 (Fig. 2.17). Annual dust spikes are larger toward the start of the record, and background concentrations of dust (Q1) are higher. During the last 1,200 years, dustier conditions prevailed from A.D. 825 to A.D. 1200 and from A.D. 1685 to the present, while the intervening interval was characterized by a general decrease in dust (Fig. 2.17). The 50 years just before A.D. 825 are unique in the record in that background dust concentrations increase relative to the annually observed spikes and may be associated with local reworking of the White River Ash (Section 2.3.4). Over the last 400 years, relatively low values of dust occur before A.D. 1685, followed by higher values persisting from A.D. 1685-1760, and subsequently by another period of even higher values between A.D. 1775 and 1885 (Fig. 2.17). Modern values have been relatively constant since A.D. 1885 and are roughly equal to the mean of the period A.D. 1685-1775. Values from A.D. 1685 onward are similar to the values seen before A.D. 1200 that occurred during the LIA. Large dust events often overlap with events in the other measured parameters, and a summary of the most significant events that occur simultaneously in multiple parameters is given in Table 2.6.

2.6.6 Nitrate overview

2.6.6.1 Time series

Values of nitrate in the last 10 years are the highest recorded during at least the last 400 years. An examination of the time series of mean nitrate concentrations shows that relatively high values occurred during the early part of the record between A.D. 825 and 1180 (Fig. 2.19). The largest fluctuations in the entire record occur between A.D. 995 and A.D. 1050, and a greater range of variability is present during this small time period than in the rest of the record. The period from A.D. 1180 to 1760 was marked by generally decreasing concentrations, and the lowest values of nitrate in the entire time series are centered at A.D. 1650 and 1750. Values of nitrate begin to increase after 1760, and this trend is seen accelerating after A.D. 1875, with a large proportion of the modern increase occurring between A.D. 1935 and 1975. It is interesting to note that the dramatic 20th-century rise began in the 1930s, lagging the period of dramatic Arctic warming that began in the 1920s. Compared to the other time series of major ions in BC1, that of nitrate most strongly matches those of reconstructed Northern Hemisphere temperatures with a distinct MWP, LIA, and modern warming. Most Arctic ice cores show increasing trends in nitrate levels, starting primarily after A.D. 1950 (*Kekonen et al.,* 2002).

2.6.6.2 Seasonal cycle

Nitrate, and to a lesser degree ammonium, exhibit peaks that are skewed toward the summer (Fig. 2.19c). Nitrate and ammonium concentrations both reach a maximum at the same time as dust, but values decrease only gradually into the summer and fall before decreasing to winter minima. The persistence of higher ammonium levels into summer would be consistent with Greenland ice core records, which show strong summer NO_3- maxima due to increased biospheric emissions over the continents in the Northern Hemisphere (*Legrand and Mayewski*, 1997). A study of NO in the Arctic troposphere conducted at Barrow, Alaska speculates that a spring peak in NO is a result of PAN (Peroxyacytyl nitrate) decomposition due to increasing insolation (*Honrath and Jaffe*, 1992). Measurements taken during this study indicate that nitrate levels exhibit a March/April peak in the Arctic troposphere and are lower during the summer (*Honrath and Jaffe*, 1992). An alternate explanation for the timing of the NO_3^- signal is that concentrations may be inversely proportional to accumulation rates, as studies have shown that nitrate has a reactive gaseous precursor that is formed at a constant rate over the ice (*Herron*, 1982). This factor could also play a role at the Bona Churchill site, where the maximum precipitation also likely occurs in the summer or early fall and is at a minimum in the spring.

A spring nitrate peak is absent in the seasonal profiles from the Mt. Logan core, and *Yang et al.* (1995) suggest that the elevation of the site is high enough to be in the relatively pollution-free troposphere. The elevation of Bona Churchill is approximately 1300 m lower than Mt. Logan. Nitrate concentrations begin to increase in the Eclipse Ice core (60° 30' N and 139° 29' W; 3017 m) at approximately A.D. 1940, and composites of mean sea level pressure for high and low nitrate and sulfate years from the Eclipse Ice core indicate that these variables might be linked with changes in the strength of the Siberian High, Icelandic Low, and AL (*Wake et al.,* 2002).

2.6.7 Calcium overview: time series and seasonal cycle

Seasonal calcium peaks occur at the same time of the year as dust peaks, are short-lived, and exhibit relatively low background concentrations during the remainder of the year (Fig. 2.20c). The time series of calcium is dominated primarily by large events that occur semi-periodically and that are superimposed on relatively low-amplitude centennial scale variability. The phasing of the low-amplitude century scale trends is very similar to that exhibited by the time series of dust. Significant spikes in calcium are observed in the mid-1960s, the late 1830s, the late 1740s, and the mid-1060s (the complete list is presented in Fig. 2.20).

2.6.8 Magnesium overview: time series and seasonal cycle

The time series of magnesium is primarily characterized and dominated by events that are observed in the mid-1960s, the late 1830s, the late 1740s, and the mid 1060s (for a complete list, see Fig. 2.21). The seasonal profile (Fig. 2.21c) and centennial-to-decadal scale variability in the time series (Fig. 2.21) of magnesium is similar to that of dust. In general, higher concentrations of magnesium occur before A.D. 1200, and lower values are observed after A.D. 1200. A period of relatively low concentrations persists until about A.D. 1600 and is followed by a gradual increase in concentrations until the present.

2.6.9 Chloride overview

2.6.9.1 Time series

The most significant feature in the chloride record is a large step increase that occurs at a depth of 441 m, or approximately A.D. 600, according to the age depth model. A similar step increase is observed in the time series of sulfate but is not seen in any of the other variables. Given the limited occurrence of this event to these two ions, it can be assumed that this even is not associated with any type of unconformity in the ice core. Following the shift at A.D. 600, values gradually decrease until A.D. 975 but never again approach the low values seen before A.D. 600. Values gradually rise after A.D. 975 and increase until A.D. 1250, where they peak and begin a gradual decline that lasts until A.D. 1560. Following 1560, values begin a very gradual increase toward the present. Significant events are observed at A.D. 703, 1315, 1620, 1885, and during the mid-1960s. (A complete list is given in Fig. 2.22.)

2.6.9.2 Seasonal cycle

The seasonal profiles of chloride and sodium show that maximum concentrations occur at the same time as dust, but sodium and to a lesser degree chloride exhibit peaks that are skewed toward the winter. Figure 2.22c shows that concentrations gradually increase during the fall and winter, peak in the spring, and then abruptly decrease before reaching summer minimums. The sodium profile from BC1 is different from the results obtained from both Mt. Logan and from the Eclipse Ice Field, where sodium concentrations have been shown to reach peak concentrations in winter (*Wake et al.,* 2002; *Yalcin et al.,* 2006). The winter timing of the peak in the Mt. Logan and Eclipse

Cores is attributed to the fact that chloride and sodium are primarily marine aerosols and that higher winter concentrations are due to the more frequent intrusions of marine air masses. It should be noted that a small secondary winter peak in BC1 sodium and chloride is exhibited in the chemistry composites (labeled as "*" in Fig. 2.15). It is possible that this secondary peak could be attributed to the occurrence of more frequent winter storms from the Pacific, and the cause of the primary peak may be linked with the influx of particulates that occurs with the spring dust event.

2.6.10 Sodium overview: time series and seasonal cycle

The record of sodium is dominated by several long multi-century trends that culminate in high sodium events. Values are generally low at A.D. 950, increase until A.D. 1100, decrease until A.D. 1530, and then increase very gradually until 1966. Significant events in the record of sodium stand out at A.D. 703, 1100, and 1966. (The complete list is given in Fig. 2.23.) The record of sodium most resembles that of potassium, given the large peaks at A.D. 1100 and 1966, and the relatively low intervening background values otherwise prevalent. The seasonal composite shows that peak sodium concentrations correspond with dust, but that the annual cycle most resembles that of chloride (see Section 2.6.9 for a more detailed discussion).

2.6.11 Sulfate overview: time series and seasonal cycle

The time series of sulfate (Fig. 2.24), like that of chloride, shows that a dramatic step increase occurs at A.D. 600. This event is followed by a gradual decrease until A.D. 975 and relatively range-bound values during the last 1,000 years, with little in the way of a significant trend. One exception to this is the period from A.D. 1610 to 1630, when unusually high values persisted for several decades. A number of sulfate events are found within the record and can be correlated with episodes of volcanism (these are discussed in detail in Section 2.3.3). During the 20th century, values generally increased from 1930 to 1970 but have decreased from 1970 onward. A similar trend is observed in the record from the Eclipse ice core, where concentration of sulfates start to increase in the 1940s (*Wake et al.,* 2002). The seasonal cycle of sulfate is similar to that of dust, but with increased background variability (Fig. 2.24c).

2.6.12 Ammonium overview: time series and seasonal cycle

The time series of NH_4 exhibits higher values before A.D. 1180 and lower values after A.D. 1680. During the 20th century, values begin increasing in the 1960s, and by the end of the century they reach values not seen since the 1750s. A number of large events occur where peak values far exceed mean background concentrations, and a complete list is given in Figure 2.25. The seasonal composite of NH_4 is very similar to that of dust, although background variability is slightly higher (Fig. 2.25c).

2.6.13 Potassium overview

2.6.13.1 Time series

Higher concentrations of potassium are associated with the present century and the period A.D. 1060 to 1160. The highest values in the entire record are centered on A.D. 1100 and 1963. A continuous period of low values is witnessed between A.D. 1425 and 1650. What is striking about the events in the potassium time series is their size, as compared to the average background fluctuations (Fig. 2.26). As mentioned in Section 5.4.1.1, the 1100 event coincides with a period of drought that is well recognized in the Sierra Nevada and in the southwestern United States.

2.6.13.2 Seasonal cycle

Peak concentrations of potassium occur between fall and winter (Fig. 2.26c). The seasonal cycle of this ion is strikingly different than that of dust and other ions. The other marine aerosols, such as sodium and chloride, exhibit a smaller secondary winter peak that occurs at the same time as potassium, but these ions have a primary dominant peak that occurs in the spring and is coincident with the peak in dust. The secondary peaks observed in the other ions may be overshadowed by the influx of dust in the spring, which is also high in sodium and chloride. A possible interpretation for the timing of the potassium peak is that the spring influx of dust may not contain any significant potassium, so that the winter peak stands out in this record but is overshadowed in the others.

2.7 Discussion and results

The strongest climate signal recorded by dust and $\delta^{18}O$ is the response in these time series to changes in circulation over the drill site between a pattern dominated by northerly flow and one dominated by flow from the Pacific. Northerly flow is uncommon and only occurs when the AO is negative and the AL is weak. Pacific flow is common and occurs whenever the AO is positive and during periods when the AO is negative and the AL is strong. This section introduces and examines the evidence for linking $\delta^{18}O$ and dust with circulation patterns related to the AO and AL. Additionally, this section examines the relationship between the record from BC1 with that of other regional ice cores and tree ring records.

2.7.1 Introduction: interactions between the AO/AL

The different possible phases of the AO and AL can be associated with four different climatic end members (Fig. 2.46). The pattern of flow over the drilling site generated by the occurrence of a weak AL at the same time as a negative AO is unique from the other three situations in that it brings a westerly airflow over the drilling site. This difference is depicted in Figure 2.47, which shows the 300 mb vector wind anomalies that occur when the AO is negative and the AL weak. The occurrence of a weak AL and a negative AO is unusual because these two indices usually correspond so that a positive (negative) AO is associated with a weak (strong) AL. Table 2.7 examines the effects of different phases of the AL and AO on the BC drilling site. In general, when the AO is negative the effects of the AL are accentuated, and when the AO is positive they are diminished.

2.7.2 The 1960s dust event: evidence of the AL/AO connection

A significant dust event is recorded in BC1 in the late 1960s, and the modern conditions associated with one of these events can be examined in more detail so that past conditions can be extrapolated for similar events. The timing of the 1960s event coincides with a period during which the AL was much weaker than normal, the AO was negative, and one in which prevailing winds at the 500 mb are offshore rather than onshore, which is typical in the region. The relatively rare pattern of offshore winds during this period resulted in record cold temperatures at Yakutat during January of A.D. 1966 and 1969.

Negative AO/Strong AL

Negative AO/Weak AL*

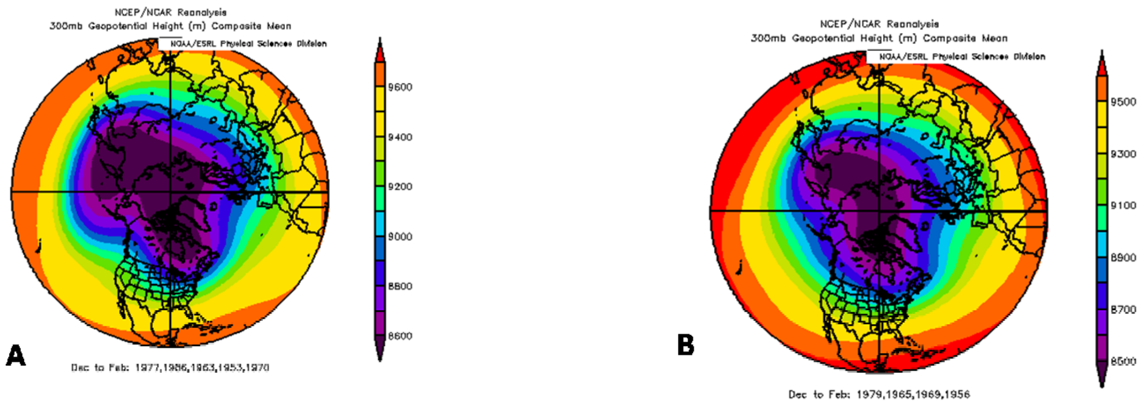

Positive AO/Strong AL*

Positive AO/Weak AL

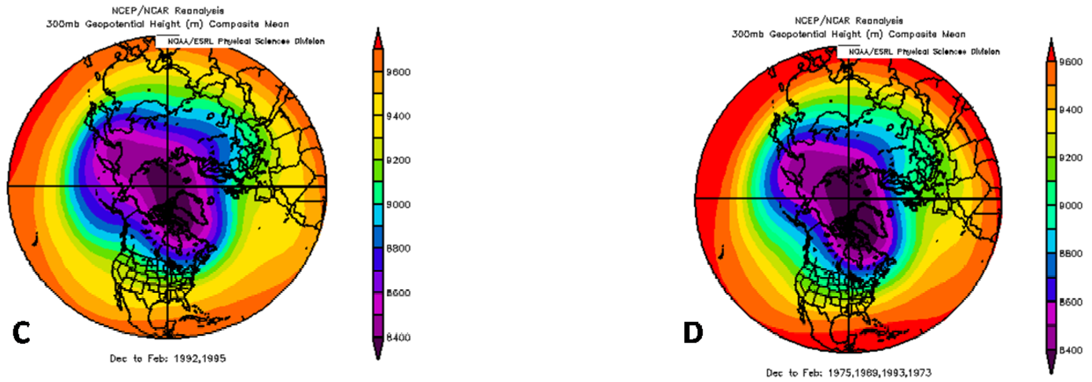

*** Not the typical relationship**

Figure 2.46 This figure shows four different end members of circulation based on the different extremes of the Aleutian Low (AL) and Arctic Oscillation (AO). The circulation associated with each is explored in more detail in Table 2.7. In general it is noted that all the patterns except (B) result in southwest flow over the site. This graph was plotted using: http://www.cdc.noaa.gov/cgi-bin/Composites/printpage.pl

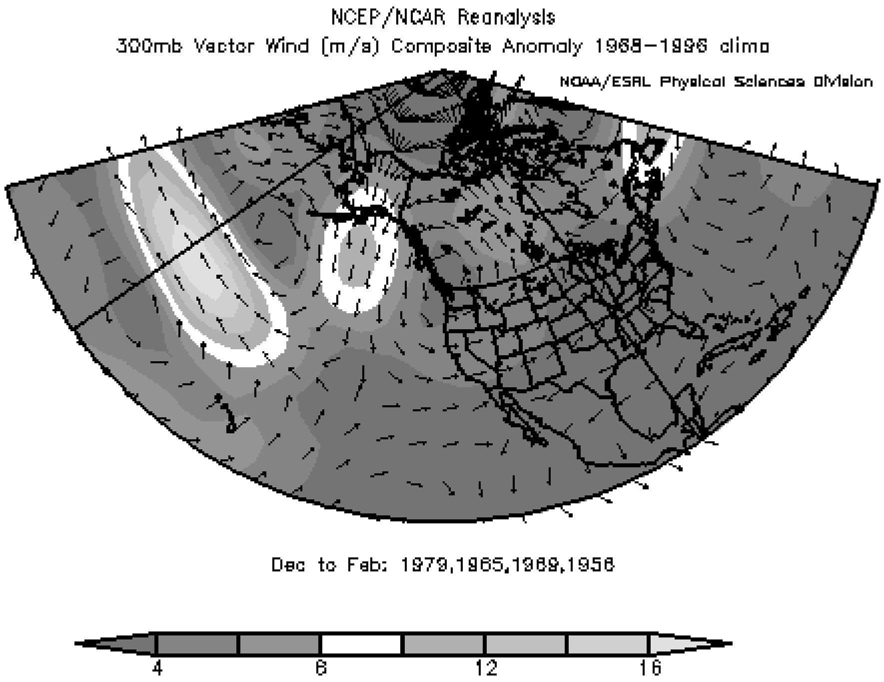

Figure 2.47 Anomalous northerly flow at 300 mb associated with weak AL and negative AO. This figure depicts anomalies from the mean flow that occur during the four years with the most negative AO and weakest AL. High dust in the BC1 core and record cold temperatures were recorded in Alaska in both 1965 and 1969. This graph was plotted using: http://www.cdc.noaa.gov/cgi-bin/Composites/printpage.pl

The relationship between the mode of the AL and the AO can be extended to other smaller dust events that occurred during the period for which we have a historical record. For instance, a strong response is seen in BC dust and to a lesser extent δ^{18}O during the years A.D. 1951, 1956, 1965, 1969, and 1979 (Fig. 2.41). (All these years had a weak AL and negative AO.) Atmospheric flow is offshore during the years with the five largest amounts of dust since A.D. 1950, as can be seen in Figure 2.48, which depicts the mean winds at 300 mb and the mean flow.

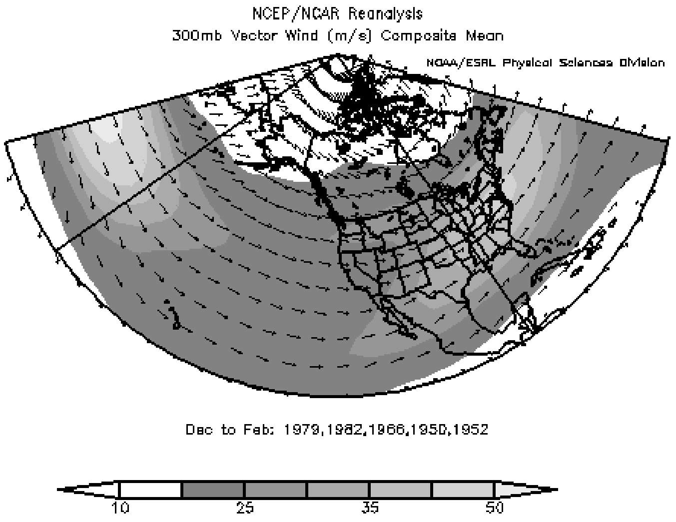

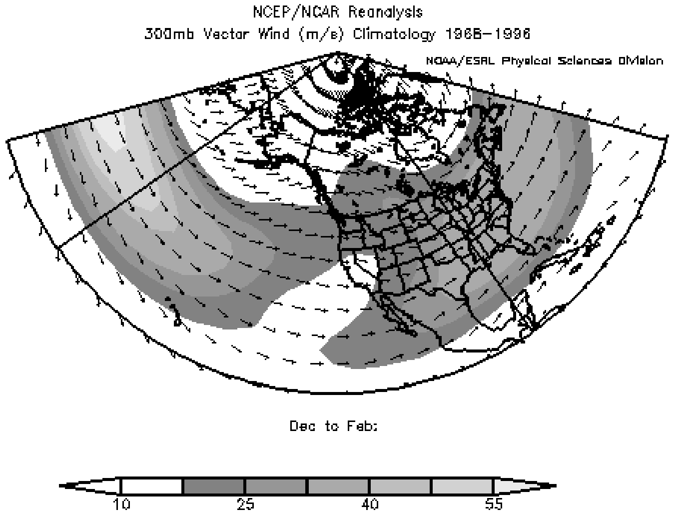

Figure 2.48 Mean DJF winds at 300 mb compared to winds during the five years with highest dust concentrations at BC1. Notice the large difference in flow between mean conditions (top) and flow that results in high dust concentrations at BC1 (bottom). These two different flow patterns are the strongest signal in the record of dust and isotopes from BC1. BC1 values are annual values of Winter-Based (WB) years. WB years were used so those individual dust peaks were not split. This graph was plotted using: http://www.cdc.noaa.gov/cgi-bin/Composites/printpage.pl

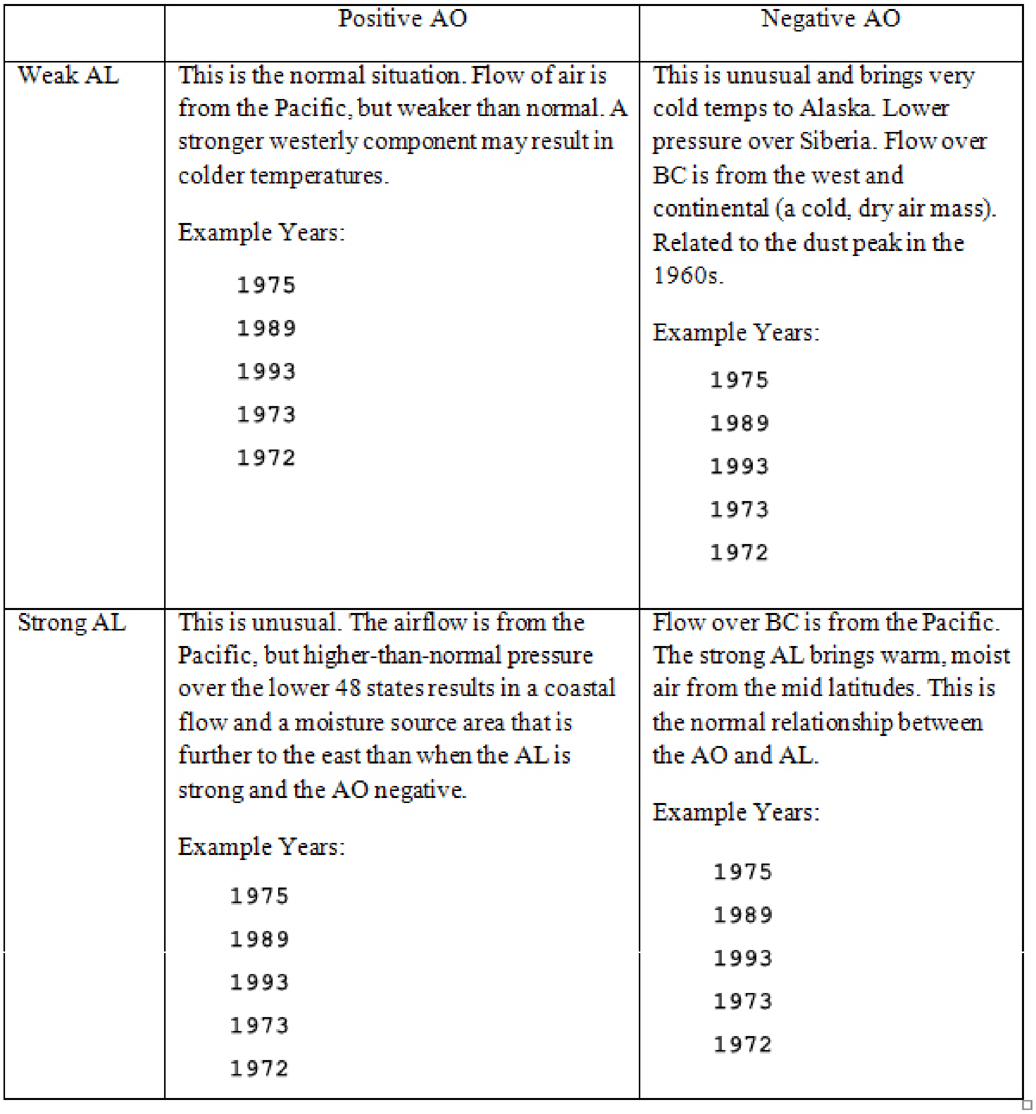

	Positive AO	Negative AO
Weak AL	This is the normal situation. Flow of air is from the Pacific, but weaker than normal. A stronger westerly component may result in colder temperatures. Example Years: 1975 1989 1993 1973 1972	This is unusual and brings very cold temps to Alaska. Lower pressure over Siberia. Flow over BC is from the west and continental (a cold, dry air mass). Related to the dust peak in the 1960s. Example Years: 1975 1989 1993 1973 1972
Strong AL	This is unusual. The airflow is from the Pacific, but higher-than-normal pressure over the lower 48 states results in a coastal flow and a moisture source area that is further to the east than when the AL is strong and the AO negative. Example Years: 1975 1989 1993 1973 1972	Flow over BC is from the Pacific. The strong AL brings warm, moist air from the mid latitudes. This is the normal relationship between the AO and AL. Example Years: 1975 1989 1993 1973 1972

Table 2.7 Different modes of the AL and AO and example years in which they occurred.

The relationship dust and a weak AL/negative AO can be extended to the other measured ions in BC1. Dust concentrations in the ice core are unusually high during the mid- to late-1960s relative to the past 100 years, and the 1960s dust event is coincident with peaks in the other measured ions. Specifically, peaks of fluoride occur in A.D. 1966 and 1967, calcium in 1965 and 1966, dust in 1966 and 1969, sodium in 1963 and 1967, magnesium in 1966, and chloride in 1963. The significance of this event is evident in the longer-term time series of Ca^{2+}, which shows that the only other event of greater magnitude occurred at A.D. 1750. In the case of Na+ the only event of larger magnitude is centered at A.D. 1100, and in the case of K+ the 1960s event is the largest in the entire time series.

A significant peak in magnesium is observed in the mid 1960s (Fig. 2.21). This event begins with gradually increasing values in the late 1940s before peaking in the middle 1960s and then gradually decreasing values until the early 1980s. This broader peak seems to better correspond with the low values witnessed in the time series of coastal temperatures during that period, and it may suggest that the record of magnesium is a more sensitive indicator of the climate conditions that are associated with the 1960s dust peak. Looking at pre-1960 events such as those labeled Mj and Mi in Figure 2.21 and comparing them to the width and duration of the time equivalent peaks Cm and Cn in calcium (Fig. 2.20), it is noted that this pattern is more than a one-time occurrence.

2.7.3 A regime shift in the 1920s: evidence of an AO-modulated signal

Historical records of Northern Hemisphere temperatures and records of temperature from Greenland show that the majority of 20th-century warming took place in the 1920s and after 1976 (*Hansen et al.,* 2006; *Chylek et al.,* 2006). The rapid warming of the 1920s is coincident with shifts in the strength of the AL and AO, with changes in the ice-climate relationship, and in patterns of accumulation and values of d-excess at BC1. These changes are illustrated in Figure 2.49 and are briefly summarized as follows:

1. The rapid warming of the 1920s was accompanied by a transition to a negative AO and strengthening of the AL. A negative AO accentuates the circulation anomalies related to the AL and may explain why the signal from the AL in BC1 is strongest when the AO is in a negative phase (Fig. 2.49).

2. A step change in both d-excess and accumulation occurred in the early 1920s (Fig. 2.50).

3. A stronger relationship is observed between $\delta^{18}O$ and Godthab DJF temperatures, the AO, and Icelandic SLP after the mid-1920s (Fig. 2.49).

4. A stronger relationship is observed between BC1$_{sp}$ d-excess and Iceland SLP/Godthab DJF after A.D. 1890. Note: This occurs earlier than the change in relationship between δ^{18}O and Godthab DJF/Icelandic SLP (Fig. 2.49).

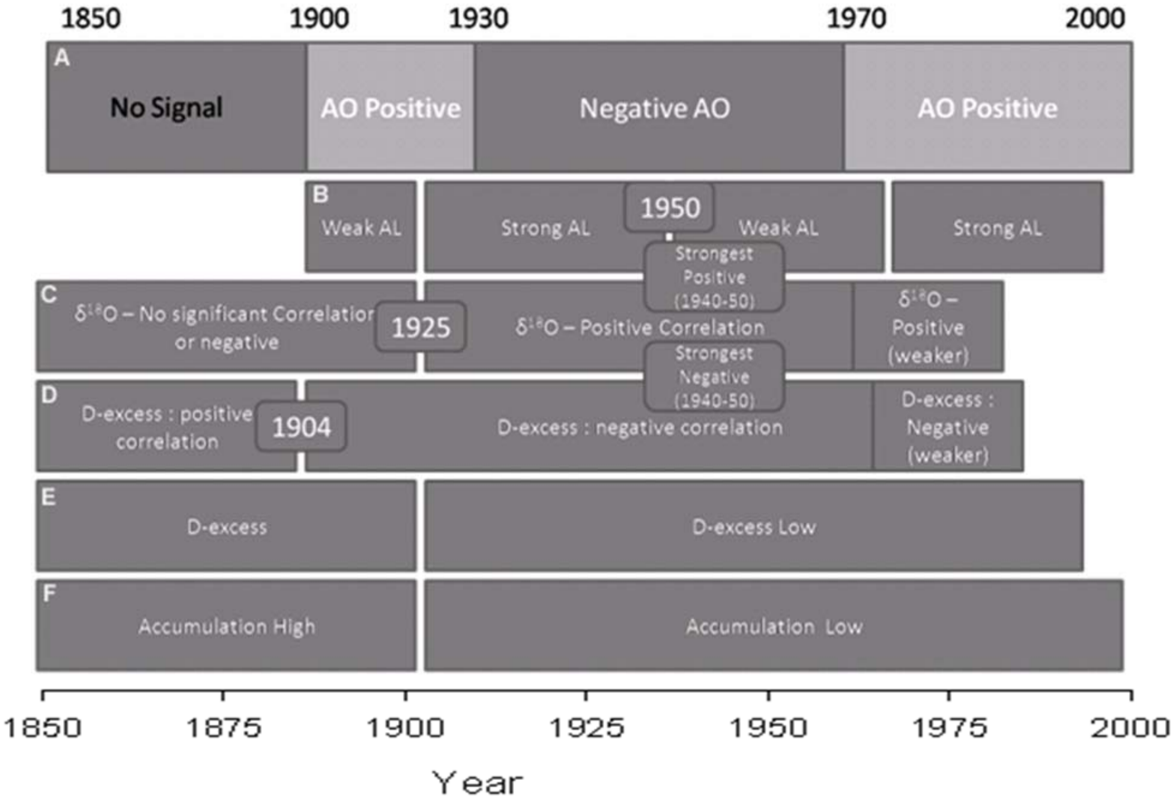

Figure 2.49 Changing relationships through time between BC1 and the mode of the Arctic Oscillation. (A) Shifts in the strength of the AL do not correspond with changes in the AO. (B) and (C) show changes in the strength of the correlation between d-excess, δ^{18}O with Iceland SLP (a proxy of the AO) through time. (Note the stronger correlations when the AO is negative.) (D) and (E) shows step changes in values of d-excess and accumulation that match shift in strength of the Aleutian Low.

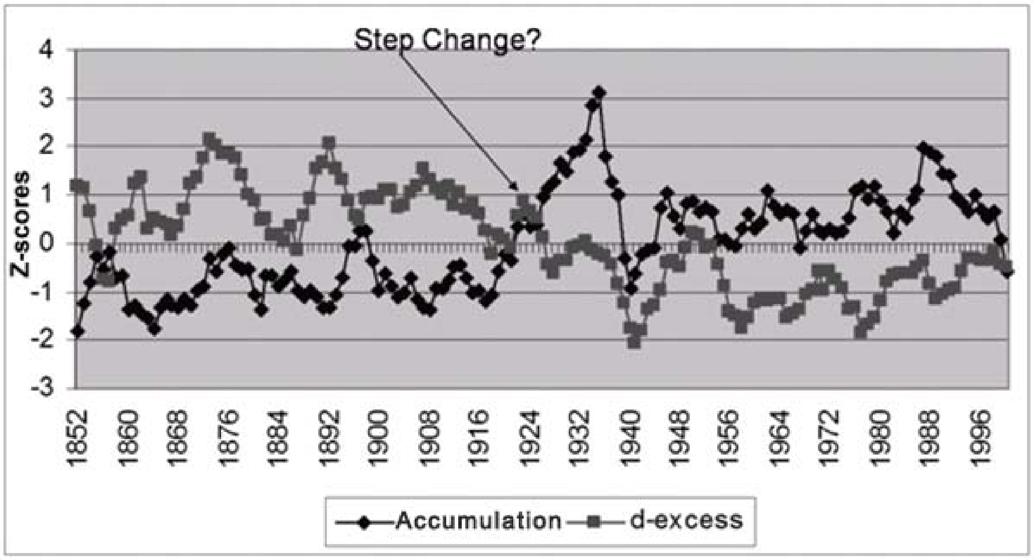

Figure 2.50 Prominent step change in the 1920s that occurs at the same time in BC1 d-excess and accumulation (5-year averages) time series. This occurs at the same time as a strengthening of the Aleutian Low and a period of rapid global warming.

A general correlation is observed between the AO and the AL during the 20th century so that when the AL is weak (strong), the AO is strong (weak). As expected, the 1920s shift in d-excess is marked by a transition to a stronger AL and weaker AO, but the most recent regime shift in A.D. 1976 exhibits a somewhat different pattern, in that while the AL deepened, the AO has been generally positive. The difference in circumstances between the regime shifts is of interest, as the relationship between d-excess and the AO is weaker after 1976 and the relationship with the AL goes out of phase. This compares to the 1920s shift in which the correlation between d-excess and both these variables remained consistently positive. It is possible that this shift in the relationship between the AO and AL can explain the change in relationship between d-excess and the AL that occurs after 1976.

2.7.4 Dust and δ^{18}O: paleothermometers or records of AO/AL variability?

The most striking features of the time series of both δ^{18}O and dust are the large-scale events that are shared in both records (Fig. 2.11). However, an examination of the time series of δ^{18}O (Fig. 2.18) shows that most of the peaks and troughs are not associated with dust events even though almost all of the significant dust events correspond with troughs in $\delta^{18}O$. This makes sense, as the record of dust only records times when the AO is negative and the AL weak and hence only encapsulates a small percentage of modern variability. The record of $\delta^{18}O$ likely represents a more complex signal that is not fully explained by climatic conditions associated with dust events.

Strong relationships are observed between dust with both the strength of the AL ($r=0.54$ and $p<0.0001$, A.D. 1903-1993) and the record of ALC DJF temperatures ($r=-0.45$ and $p<0.001$, A.D. 1940-1989). However, the longer-term time series of both $\delta^{18}O$ and dust over the last 1,000 years don't match well with Northern Hemisphere temperature reconstructions, as seen in *Mann and Jones* (2004), perhaps suggesting a more complex forcing mechanism. For instance, high concentrations of dust characterize both the MWP and LIA. Additionally, the lowest dust concentrations occur between A.D. 1200 and 1600, and if dust were used as a thermometer it would suggest that this period was warmer than the MWP and that temperatures were similar during both the MWP and LIA.

Despite this fact, several of the key shifts in the amount of dust occurred at the same time as well-recognized shifts in temperature. For instance, lower values of dust occur after A.D. 1200, a date that marks the end of the Alaskan MWP. Additionally, an abrupt shift in values and an increase in variability of BC1 $\delta^{18}O$ stands out at A.D. 1400 and matches records from Greenland and Antarctica ice cores. *Kreutz* (1997) found that levels of sodium increased in ice cores from Greenland and Antarctica and attributed this shift to increased global storminess due to a stronger temperature gradient between the poles and the tropics. The timing of this shift coincides with the end of the MWP in Europe, but not in Alaska.

Because the record from BC1 contains a signal from both the AO and the AL, it would suggest that if one could use an alternate reconstruction of either the AO or the AL, it would be possible to back out this signal from the record of BC1 and derive information about the unknown variable. This may be true, but several complexities exist and are summarized as follows:

1. First, very few records of either AO or AL variability exist for the last 1,000 years, and the ones that do exist often correlate poorly.

2. Second, studies of the AO show a general lack of any persistent or low-frequency trends from A.D. 1400 to the present (*Cook and D'Arrigo,* 2001). The exception to this is a study by *Meeker and Mayewski* (2002) of Greenland ice cores, which shows that before A.D. 1400, the Icelandic Low was significantly weaker than today.

3. Pacific AO variability may exhibit independent variability from Atlantic variability, and reconstructions of Atlantic AO variability may not be representative of conditions in the Pacific.

4. A recent study by *Huth* (2006) shows that the Pacific component of AO variability may be independent of NAO variability and instead dependent on local variability. This would suggest that Atlantic-based reconstructions of the NAO/AO may not fully capture the AO signal in BC1.

The lack of any low-frequency AO signal, with the exception of the event at A.D. 1400, may suggest that the longer-term shifts in the record $\delta^{18}O$ are indeed reflective of AL variability. This would be supported by comparisons of the record of BC1 $\delta^{18}O$ and reconstructions of salmon productivity constructed by *Finney* (2002), which show that productivity began a gradual increase around A.D. 100 and continued gradually increasing until A.D. 1200. Overall higher levels of productivity persisted between A.D. 1200 and 1900. This general trend corresponds well with BC1 $\delta^{18}O$, where it is observed that values of $\delta^{18}O$ increase gradually in the early part of the record and are less negative in general after A.D. 1200. *Finney* (2000) speculates that the gradual increase in productivity seen in the earlier part of the record might have occurred due to intensification and eastward migration of the AL during this period (*Anderson*, 2005).

2.7.5 Conditions associated with pre-1960 dust events in BC1

Several lines of evidence suggest that past dust events were also associated with both the occurrence of a weak AL and negative AO. Significant dust events that coincide with peaks in at least four of the other measured ions that took place during the last 1,000 years occur in BC1 at A.D. 1040, 1100, 1273, 1322, 1360, 1515, 1700, 1750, 1835, and 1966 (Table 2.6). A comparison of the timing of these events with the time series of $\delta^{18}O$ shows that almost all of these events coincide with periods when values of $\delta^{18}O$ are more negative than normal (Fig. 2.18). This suggests that they are large-scale climatic events, perhaps similar to the one in the 1960s. Little relationship is observed between these events and the time series of either accumulation or d-excess (Fig. 2.34 and 2.16).

La Niña events are associated with a weaker-than-normal AL, so it might not be surprising to find that some of these events coincide with La Niña-like conditions in other regions. For instance, the largest event in BC1 recorded by nine of the measured variables as well as $\delta^{18}O$ is centered at A.D. 1100 (Table 2.6). Additionally, higher values of d-excess that are currently associated with a weaker AL are evident at A.D. 1100. This event coincides with a possibly La Niña-induced megadrought event that was identified in the Sierras of California at A.D. 1100 (*Stine*, 1994). The event at 1273 that was recorded in BC1 coincides with another megadrought in the Southwest, which has been associated with the disappearance of the Anasazi (*Cook et al.,* 1999; *deMenocal*, 2001).

Not all of the dust events in BC1 line up with droughts in the Southwest, and one would not expect them to, as a weak AL is not exclusive to La Niña events. For instance, a drought identified by *Stahle* (2000) as occurring between A.D. 1540 and 1590 does not seem to stand out as any specific event in the record of BC1, and a period of wetter-than-average conditions in the Southwest is centered at A.D. 1322 (*Cook*, 2004). Some evidence would suggest that large dust events may be related to regional volcanic events and are unassociated with climatic patterns. This would certainly explain why some dust events correlate with droughts and some seem unrelated. For instance, the most elevated levels of sulfate in the Eclipse and PR Col ice cores in the last 500 years correspond with A.D. 1516 (*Fisher et al.,* 2004). The event is seen as a significant dust event that is marked by peaks in both sulfate and fluoride in BC1. It is likely that other events at A.D. 1835, 1605, 1456, and 1322 may also match not-yet undocumented volcanic eruptions in the region.

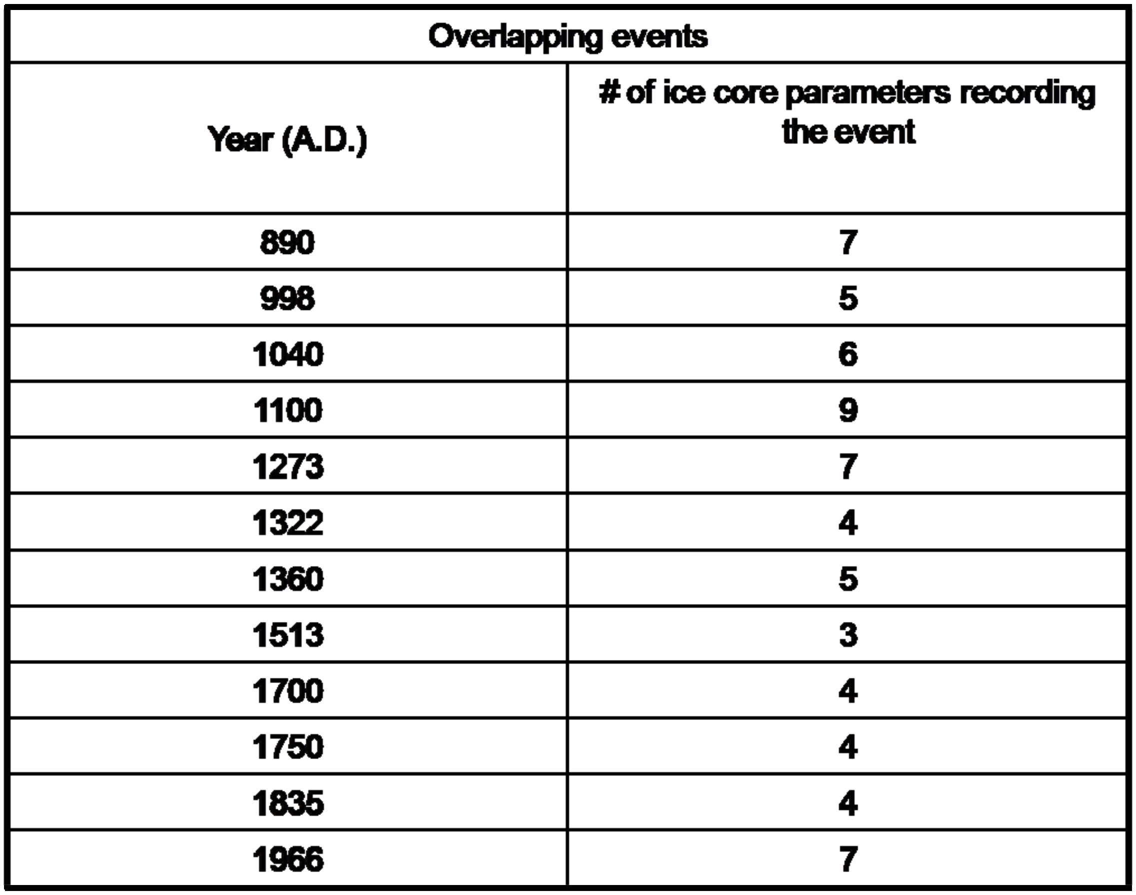

Overlapping events	
Year (A.D.)	# of ice core parameters recording the event
890	7
998	5
1040	6
1100	9
1273	7
1322	4
1360	5
1513	3
1700	4
1750	4
1835	4
1966	7

Table 2.6 Number of BC1 ice core variables recording specific events.

2.7.5.1 Comparisons of BC1 with other regional climate records

2.7.5.2 Dust and Yukon tree ring records: a shared AO signal

A study by *Szeicz and MacDonald* (1995) reconstructed summer temperatures from White Spruce in the Mackenzie and Franklin Mountains of northwestern Canada. This site is further north than most tree ring reconstructions and is near the northern tree line, and as such it may record more of influence of the AO rather than a Pacific climate signal. A comparison of this record with the time series of dust from BC1 is given in Figure 2.51, and it can be seen that a strong correlation exists between the two time series since 1750. One might expect that when temperatures are cold in the Franklin Mountains, a more northerly flow is in place and that this colder, more continental flow is also responsible for deposition of dust at BC.

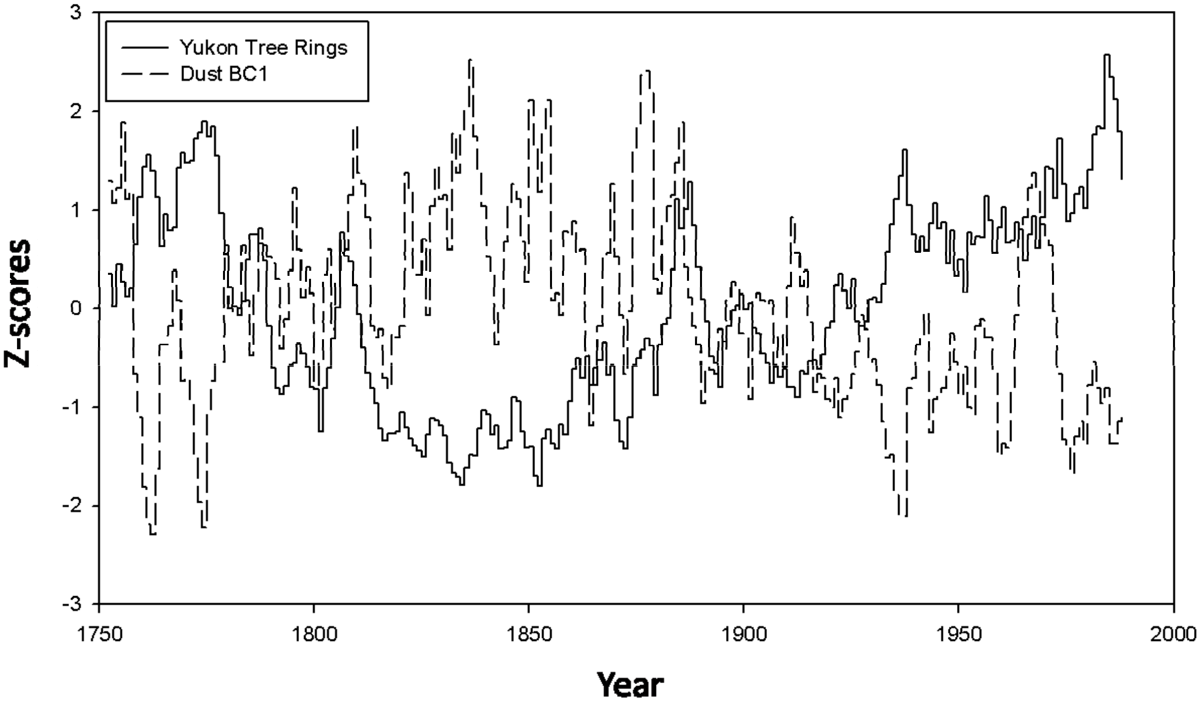

Figure 2.51 Strong correlation between 5-year average z-scores of dust and summer temperatures reconstructed from trees rings in the Yukon in a study by *Szeicz and MacDonald* (1995). Colder conditions in the Yukon are associated with increased dust at BC1, probably in response to changes in the AO. Note the crossover in the 1920s; as temperatures increase, dust concentrations decrease.

2.7.5.3 The Mount Logan Ice Core

Mt. Logan (60° 33' N, 140° 14' W, 5340 m) is located along the Canadian-U.S. border in the St. Elias Range and is less than 200 miles from the Bona Churchill drill site. A 103 m-ice core was obtained from the mountain in 1980, and shallow cores taken more recently have been used to extend the record from 1980 to the present. The record from this core dates back to A.D. 1693, and annual data are available online from the national climate data center (ncdc.noaa.gov/paleo) from 1736 to the present (*Moore et al.,* 2002). A second long core referred to as the PR Col ice core was drilled to bedrock by the Geological Survey of Canada during the summers of 2001 and 2002 (*Fisher et al.,* 2004). This core provides an 8,000-year record of climate change in the region with annual resolution during the period A.D. 1700 to 1998. It should be noted that the entire 8,000-

year record has not yet been published, and as a result it is not available for comparisons with the record from BC1.

The Mt. Logan ice core exhibits a trend toward increased snow accumulation during the last century and particularly during the period A.D. 1976-2000. Measurements of accumulation made over the course of a 1-year period near the ice core site show that peaks in accumulation occur in August and September as well as in January and February (*Rupper et al.,* 2004). Increased accumulation at the site is associated with higher geopotential (500 mb) heights over western North America and lower heights over the North Pacific. This dipole-like pattern resembles at least two of the nodes of the PNA pattern and supports the view that the Mt. Logan accumulation record might act as a long-term proxy for the PNA index (*Moore et al.,* 2002). This is similar to the results found for BC1 accumulation, which is strongly related to the strength of the AL.

The record of $\delta^{18}O$ from the PR Col ice core has been related to large-scale shifts between mixed (strong AL) and pure zonal (weak AL) flow regimes (*Fisher et al.,* 2004). *Fisher* (2004) identifies two important regime shifts, one at A.D. 800 and another at 1840, which may mark abrupt transitions between zonal and mixed flow regimes. *Fisher* (2004) suggests that the period before each shift was dominated by zonal flow and colder conditions, while the period after the shift was dominated by mixed flow and warmer conditions. Although the transitions from zonal to mixed regimes occurred abruptly in the time series of Mt. Logan $\delta^{18}O$, the transitions from mixed back to zonal occurred gradually following each regime shift. The results of *Fisher* (2004) would suggest an abrupt end to the LIA and abrupt start to the MWP. The results of *Fisher* (2004) also suggest that the AL was weaker during the LIA and stronger during the MWP.

A record of ^{18}O deposited in sedimentary calcite from Jelly Bean Lake provides a high-resolution record (5 to 30 years) of North Pacific circulation for the last 7,500 years (*Anderson et al.,* 2005). *Anderson* (2005) suggests that fractionation of ^{18}O is driven by changes in the position and strength of the Aleutian Low. This argument is supported by the fact that during the last 100 years, the record of $\delta^{18}O$ corresponds well to changes in the North Pacific Index. Evidence from both Jelly Bean Lake and the Mt. Logan core suggests that a rapid intensification of the AL at A.D. 800 marks the start of the MWP (*Anderson*, 2005; *Fisher*, 2004). The rapid intensification of the AL at A.D. 800 is followed in the Mt. Logan core by a gradual increase toward more positive values of $\delta^{18}O$ from A.D. 800 to 1840 that represent a weakening of the AL. A similar trend is seen in the Jelly Bean Lake record, but the reversal occurs around A.D. 1700 (rather than 1840) and according to *Anderson* (2005) coincides with the start of the LIA. Both of these records indicate a gradual transition out of the MWP and into the LIA.

The results of *Andrews* (2005) and *Fisher* (2004) are inconsistent both in timing and consistency of mechanism. However, both studies agree that an abrupt shift in isotopes at A.D. 800 was associated with intensification of the AL low and warming associated with the MWP. Furthermore, both studies agree in that after A.D. 800 a gradual weakening of the low took place that terminated with an abrupt shift to a stronger AL. However, the timing of the termination is quite different between the records occurring in 1840, in the case of the Mt. Logan record, and A.D. 1700, in the case of the Jelly Bean Lake Record. The mechanism of the second shift is poorly explained by the records since then. *Fisher* (2004) suggests that the abrupt shift at A.D. 1840 is associated with warming and strengthening of the AL that is associated with the end of the LIA. *Anderson* (2005), on the other hand, suggests that an intensification of the AL at A.D. 1700 resulted from LIA cooling. In other words, the Mt. Logan record would suggest the occurrence of a weaker low during the LIA before A.D. 1840, and in the Jelly Bean Lake record, just the opposite occurred.

Although the long records from Mt. Logan would seem to poorly fit the record from BC, as it is dominated by step changes at A.D. 800 and at A.D. 1840, a look at the last 500 years shows some important similarities between these records (Fig. 2.52). Both the Mt. Logan and BC1 $\delta^{18}O$ records show a transition to more negative $\delta^{18}O$ values. In the case of Mt. Logan, this transition occurred in A.D. 1840, and in the case of BC1 the transition occurred earlier, at approximately A.D. 1780. Before this transition to more negative $\delta^{18}O$ values, both records exhibit higher amplitude shifts in $\delta^{18}O$.

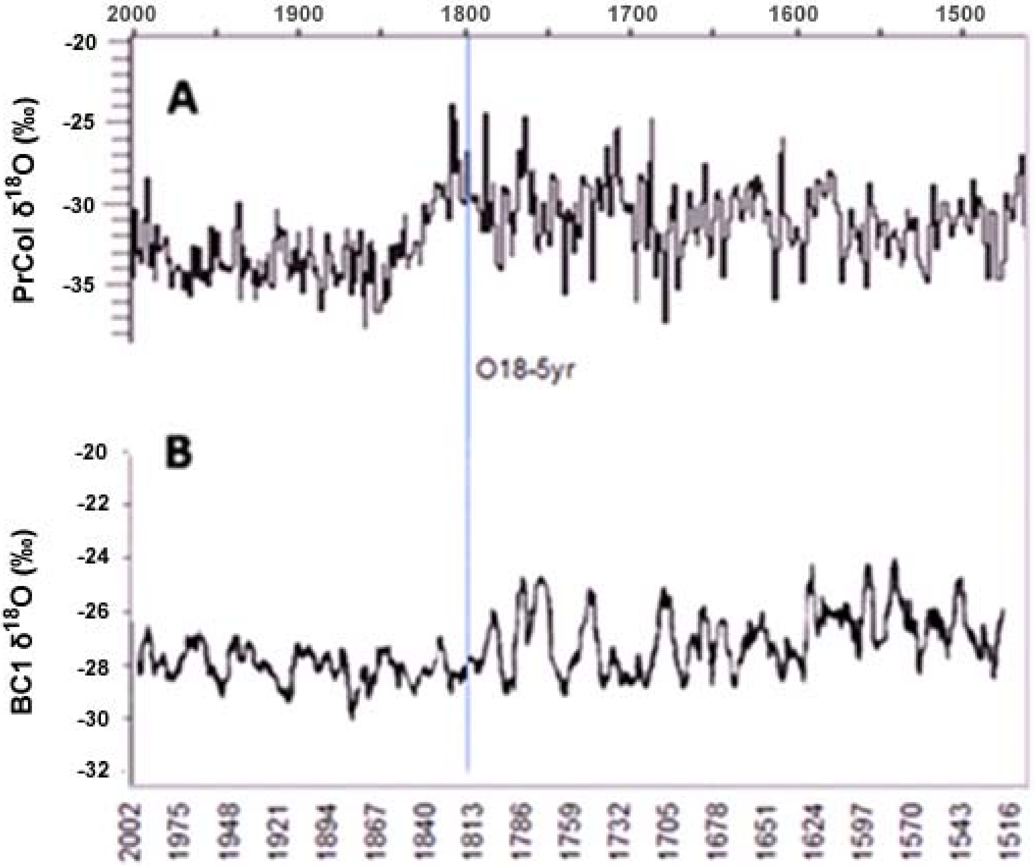

Figure 2.52 Comparison of record of 5-year average of BC1 δ^{18}O with last 500 years from PrCol Mt. Logan (modified from *Fisher*, 2004). Note that the timescales in (A) and (B) do not line up. The record from PrCol Mt. Logan shows a transition to more negative values of δ^{18}O at A. D. 1840, and a transition from more decadal variability to more interannual variability also occurs at the same time. Similar trends are noted in the record from BC1, but the transition occurs just before A.D. 1800.

2.7.5.4 The Mount Wrangell Ice Core

In the summer of 2003, a 50 m-long ice core was retrieved from the summit of Mt. Wrangell (60º N, 144º W, 4317 m) in southeastern Alaska (*Shiraiwa*, 2004). A study of ions, microparticles, and δ^{18}O by *Yasunari* (2007) examined the seasonal cycles observed in the Mt. Wrangell Core. Although this study and the work of *Yasunari* (2007) agree on the spring timing of the dust peak, they differ in that this study concludes that the δ^{18}O minima occurred at the same time as the peak in dust, while the study by

Yasunari (2007) suggests a winter minimum. It should be stressed that the composites from BC1 represent the average response and that in fact the seasonal cycles of BC $\delta^{18}O$ exhibit a great deal of variability. For instance, in the response of BC $\delta^{18}O$, minimum values occur both stratigraphically above and below the peak in dust, depending on the year. This variability is not specific to BC1, as the isotope profile presented by the Mt. Wrangell core also shows similar variability (*Yasunari*, 2007). The conclusions regarding the timing of the $\delta^{18}O$ trough in BC1 are based on average conditions during 39 years, and the conclusions drawn from the Mt. Wrangell core are only based on the period from A.D. 1981 to 2003. Furthermore, no average composite was constructed for Mt. Wrangell, and the observation that $\delta^{18}O$ troughs in the winter is based only upon a visual inspection of the time series, which is made difficult by the variability observed in the record.

2.7.5.5 Eclipse Ice Core

A 160 m-long ice core was collected from the Eclipse Ice Field (60.51° N and 139.47° W; 3017 m) during the summer of A.D. 1996 (*Wake et al.,* 2002). The drilling location is near both the Bona Churchill and Mt. Logan ice cores but is 1400 m below the Bona Churchill drilling site and 2000 m below the Mt. Logan drilling site. Eclipse $\delta^{18}O$ is most significantly correlated with regional summer temperatures, but it is only able to explain 10%-15% of the total variance. The accumulation record even explains less of the variance in seasonal precipitation, only accounting for between 4% and 10% of the variability in precipitation records (*Wake et al.,* 2002).

A comparison of the time series of major ions, accumulation and $\delta^{18}O$ from the Eclipse Ice core, as presented in *Wake* (2002), with the same time series from Bona Churchill, reveals several important similarities and differences. First, the beta Peak observed in both cores occurs at approximately 65 m, indicating a similar pattern of accumulation between the two sites. Second, both time series of accumulation show that a period of high accumulation in the late 1930s was followed by years with accumulation deficits in the early 1940s. Finally, both cores show increasing trends in nitrate during the last 100 years, and the long-term fluctuations in sulfate records from both records share similar values in that they are high between A.D. 1900 and 1920, low between the mid-1920s to mid 1950s, and relatively high since the mid-1950s to the present.

Several differences are also apparent between BC1 and the Eclipse record. A major sodium/dust event occurs in the late 1960s in the BC1 record, which is not coincident with any peak in the Eclipse ice core record. However, in the Eclipse record a major peak, relative to the last 100 years, in these ions occurs in the mid-1970s. The difference in timing of these events may reflect some type of more local source for these events or an error in the dating of one of the ice cores. In the nitrate record, a reversal from high to low levels is seen in the BC record between A.D. 1971 and 1976. A similar reversal is noted in the Eclipse record, but the timing is offset by approximately 5 years so that it occurs in the late 1970s. This is a prominent feature in both records despite the discrepancy in timing.

2.8 Conclusions

Alternating patterns of on and offshore flow over the drill site (Fig. 2.48) are responsible for the large-scale δ^{18}O and dust events that are shared in both records (Fig. 2.11). The mean flow pattern at the drill site is onshore (Fig. 2.48 bottom) and occurs whenever the AO is positive or when the AO is negative and the AL is strong. An unusual pattern of offshore flow (Fig. 2.48 top) occurs when the AO is negative and the AL weak. This pattern results in colder-than-normal conditions and the emplacement of a drier and more continental air mass that results in both dustier conditions and more negative values of δ^{18}O. Despite this strong signal, an examination of the time series of δ^{18}O (Fig. 2.18) shows that most of the peaks and troughs are not associated with dust events, even though almost all of the significant dust events correspond with troughs in δ^{18}O. This makes sense, as the record of dust events only records times when the AO is negative and the AL weak and hence only encapsulates a small percentage of modern variability.

The record from BC1 provides an important record of past AO variability at a time when more investigators are just beginning to take an in-depth look at the effects of this feature on the climate in Alaska. For instance, a recent study by *Bond and Harrison* (2006) found that the effects of ENSO are weaker when the AO is positive and enhanced when the AO is negative. Additionally, it appears that much of the signal from the SOI occurred during years when the AO was negative (*Bond and Harrison*, 2006). These findings are very similar to what is observed in the record of BC1, in that the AO modulates the signal of the AL in the ice core record.

The lowest dust concentrations occur between A.D. 1200 and 1600, and high concentrations occur during the MWP and LIA, suggesting that δ^{18}O and dust are not simple records of temperature. While the long-term changes in these records may not be a simple record of temperature, they may reflect long-term changes in the strength of the AL. This would be supported by comparisons of the record of BC1 δ^{18}O and dust with reconstructions of salmon productivity constructed by *Finney* (2002), which show that productivity began a gradual increase around A.D. 100 and continued gradually increasing until A.D. 1200. Overall higher levels of productivity persisted between A.D. 1200 and 1900. This general trend corresponds well with BC1 δ^{18}O, where it is observed that values of δ^{18}O increase gradually in the early part of the record and are less negative in general after A.D. 1200.

The Mt. Logan record and the record from Jelly Bean Lake both indicate that an abrupt transition in circulation took place at A.D. 800. Although a large swing in isotopes is noted in the BC1 record, labeled "A" in Figure 2.53, no large-scale change in trend is noted in the record from BC1. In fact, the record from BC1 is very similar to the records of fishery productivities from Alaska and California (*Finney*, 2002; *Baumgartner*, 1992; *Tunicliffe et al.,* 2001). These records, like the BC1 record, suggest that the transition from a weak to strong AL was a gradual process that began at approximately A.D. 100 and culminated by A.D. 1200. This is in agreement with the records of fishery productivities, which also show that A.D. 1200 coincides with the termination of the MWP.

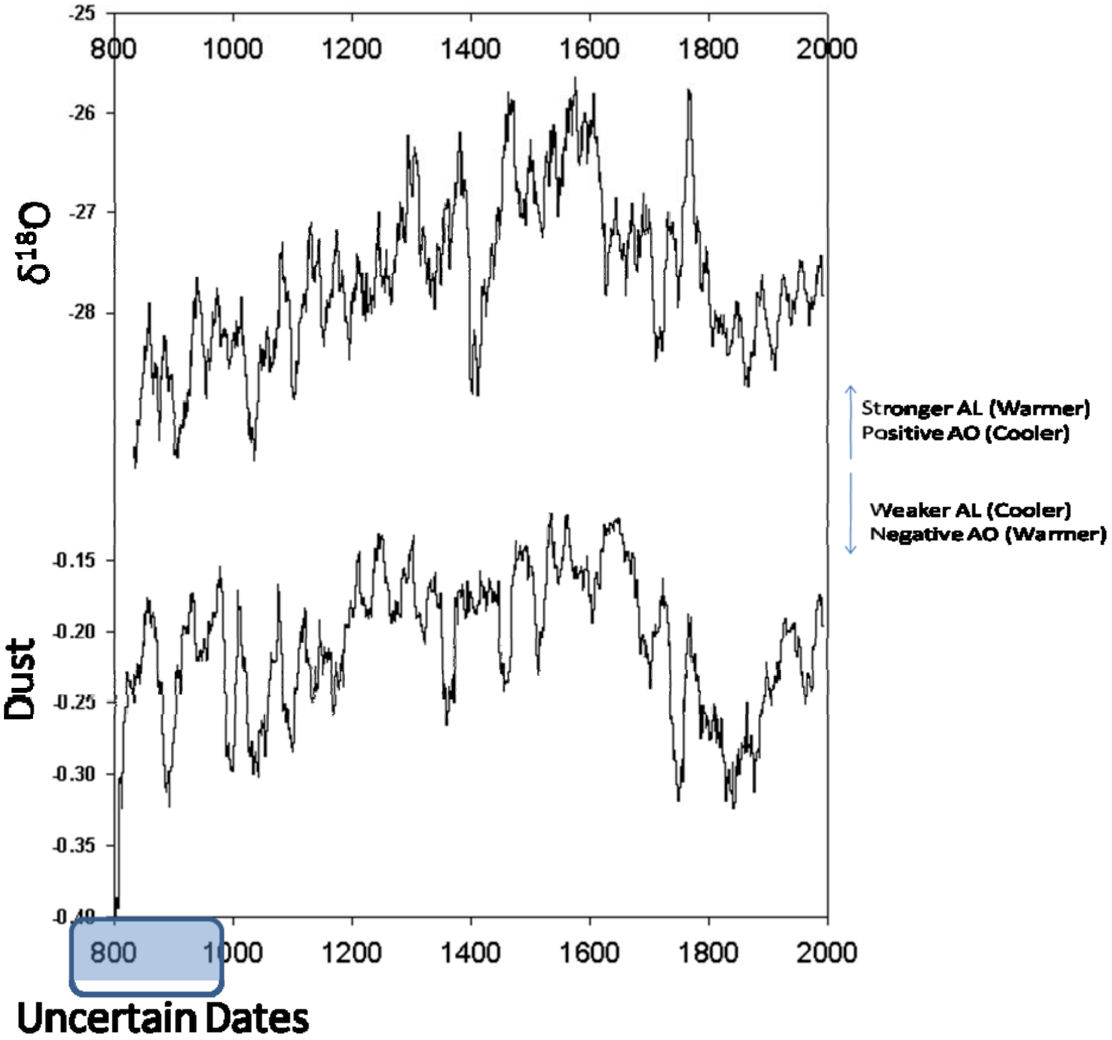

Figure 2.53 Record of the 21-year averages of δ^{18}O and dust from BC1. The record of dust is multiplied by 1 so that the response is the same as δ^{18}O and comparison is easier. The interpretation of the isotopes and dust, seen in profiles A and B, is given to the right of the figures.

The record from BC1 records both AO and AL variability and may help to unravel the long-term relationship between these two modes of climate variability. *Rossby* (1939) first identified a correlation between the strength of the AL with the mean pressure difference between 35° N and 55° N (essentially the modern AO). The degree to which the AO and AL exhibit independent variability and the amount that is shared is the subject of debate, as is the question as to whether these relationships have changed through time. A study by *Fu* (2001) of changes in Northern Hemisphere circulation related to warming during the 1920s found that both the Pacific and Atlantic Highs weakened and moved northward in conjunction with a deepening of the Icelandic Low. However, *Fu* (2001) states that the AL exhibited characteristics that were independent of these other centers of action during the time period and furthermore speculates that the independent variability of the AL is perhaps due to a strong tropical connection. These findings are similar to a recent study by *Huth* (2006), which shows that the Pacific component of AO variability is independent of NAO variability and instead depends on local variability.

The relationships identified between $\delta^{18}O$ and dust with both the AO and AL suggests that the temperature response recorded by BC1 cannot be defined, because more negative values of $\delta^{18}O$ are associated with a weaker AL and/or a negative AO, and more positive values of $\delta^{18}O$ are associated with a stronger AL and/or a positive AO (Fig. 2.53). Historical records show that a weaker (stronger) AL is associated with cooler (warmer) conditions, and a negative (positive) AO is associated with warmer (cooler) conditions. This ambiguous relationship also may explain why the record of BC1 $\delta^{18}O$ shows no definite temperature response to global warming.

During the last 25 years the AL has gotten stronger and the AO has been more positive, suggesting at least cooler temperatures in the upper atmosphere due to the influence of the AO and warmer temperatures at the surface due to the influence of a stronger AL. These results are consistent with the accumulation record from BC1, as well as historical records of precipitation and temperature, which show increased accumulation during this period. This might be expected given an overall increase in the regional lapse rate and increased moisture flux into the region, which is associated with a strong AL.

CHAPTER 3

RESULTS FROM THE 2003 QUELCCAYA SUMMIT CORE

3.1 Abstract

The year 2003 marked the completion of the second major drilling project in which an ice core was drilled to bedrock and retrieved from Quelccaya, a large volcanic plateau in the eastern cordillera of the central Peruvian Andes. Three ice cores, two of which were drilled to bedrock, were retrieved. The Summit Core (168.8m) can be dated back to A.D. 315 by making use of both a time depth model and annual layer counting. Counting of annual layers was possible from A.D. 615 to 2003. This chapter outlines the development of the Summit Core record in full detail.

This analysis of the 2003 Quelccaya core identifies a strong correlation between Quelccaya $\delta^{18}O$ and NIÑO 4 Sea Surface Temperatures (SST) ($r=0.646$, $p<0.001$, 1856-2003). These findings are similar to those of a study by *Bradley* (2003), which identified a strong linkage between Quelccaya $\delta^{18}O$ and the tropical Pacific. However, they differ in that they indicate that Quelccaya $\delta^{18}O$ is most strongly related to the decadal variability observed in the tropical Pacific rather than the interannual variability that is associated with El Niño Southern Oscillation (ENSO). This finding is supported by previous studies of the 1983 Quelccaya $\delta^{18}O$ record by *Henderson* (1996) and of NIÑO 4 SSTs by *Lohmann and Latif* (2005), which show that the dominant mode of climate variability in these records is decadal.

The signal in Quelccaya $\delta^{18}O$ is most likely driven by changes in the Walker Circulation, which result from changes in the size, temperature, and distribution of the Pacific Warm Pool (PWP). Quelccaya $\delta^{18}O$ is most strongly related to SST in the easternmost margin of the PWP. The marginal regions of the PWP are likely better recorders of warm pool contraction and expansion, because they exhibit a larger degree of SST variability than the interior, where SSTs are most consistent.

Previous studies indicate that increased convection in the eastern portion of the warm pool results in weaker trade winds in the Atlantic and warmer SST in the northern tropical Atlantic (*Cobb*, 2001). *Cobb* (2001) suggests that decadal variability associated with the NIÑO 4 is related to patterns of decadal variability in the Atlantic, Indian, and North Pacific. Establishing a connection between decadal variability in the Pacific and Atlantic is key, because the Atlantic is the primary moisture source area for Quelccaya.

This analysis of the 2003 core suggests that the effects of individual ENSO events are superimposed upon the decadal variations observed in the Quelccaya $\delta^{18}O$ record. Previous studies of the 1983 Quelccaya ice core by Dr. Thompson show that El Niño events result in reduced accumulation, increased concentrations of dust, and more positive values of $\delta^{18}O$ (*Thompson*, 1984, 1985, and 1992). ENSO events modify the strength of the mean easterly flow that is responsible for transporting moisture from the Atlantic and Amazon Basin to both locations. Variability in the Quelccaya ice core record is preserved across a range of timescales. The interplay of these various cycles creates a complex pattern, as the interannual variability is superimposed on the decadal variability, which is itself superimposed on the longer centennial variability.

3.2 Introduction and background

3.2.1 Quelccaya drilling projects from 1976 to 2003

Dr. Lonnie Thompson has led glacial research studies in the Quelccaya (13º 56’S, 70º 50’W, 5670m) region since 1976 (Fig. 3.1). These studies included major drilling projects in 1983 and 2003, as well as more frequently occurring studies, such as:

- Mapping the retreat of the Quelccaya Ice Cap using surface and aerial photos
- Documentary photography of the retreat of the Kori Qalis glacier
- Setting up and recording data from automated weather stations

Of these past studies, the most significant to this research is the 1983 expedition, in which the first two ice cores from Quelccaya were drilled to bedrock (*Thompson et al.,* 1984 and 1985).

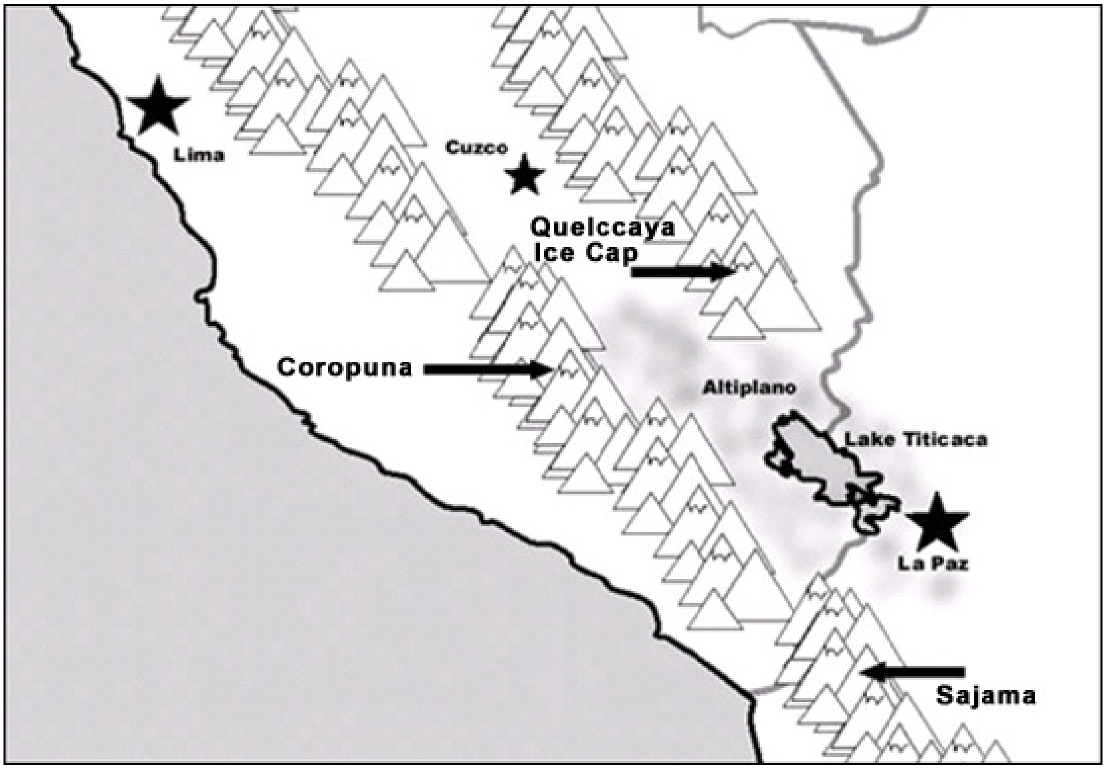

Figure 3.1 Location of the Quelccaya drill site and the Andes of central Peru, which consist of western and eastern mountain ranges that are separated by a large, high elevation plateau known as the Altiplano. The Coropuna drill site is in the western cordillera and is labeled on the map. Ice core drill sites are labeled with a larger font.

I participated in the most recent drilling project, in which Dr. Thompson led an international team of scientists, occurred during the summer of 2003 and resulted in the retrieval of three ice cores, two of which were drilled to bedrock, from the Quelccaya Ice Cap. The Summit Core (168.8m), the longest of the three ice cores, was drilled to bedrock at the Summit Dome (5670m) and is the primary focus of this chapter. The two other cores were drilled at the summit of the Quelccaya North Dome and provide a means to confirm the spatial continuity of the chemical profiles among the ice cores. Upon completion of drilling, the ice cores were transported in a frozen state to the facilities at the Byrd Polar Research Center (BPRC) for further analysis.

3.2.2 Analysis and sampling of the 2003 ice core

Mary Davis, Tracy Mashiotta, Ping-Nan Lin, and myself completed analysis, preparation, and sampling of the concentrations of isotopes, as well as particulates and major ions for the Quelccaya 2003 ice cores, at BPRC. The concentrations of different particulate size fractions, d-excess, $\delta^{18}O$, SO_4^{2-}, $Ca^{2+,}$ NO_3^-, NH_4^+, Na^+, Cl^-, Mg^{2+}, K^+, and F^- were measured for each sample in a fashion similar to that outlined in Chapter 2 on the Bona-Churchill Ice Core (Section 2.2.2). The ion, isotope, and dust profiles of the Summit Core are based on measurements from 6,802 individual samples. The number of samples taken per meter increases with depth so that annual cycles remain discernible despite the effects of thinning and compaction.

The study of ice cores and the procedures by which they are analyzed has advanced significantly since the first major drilling project at Quelccaya in 1983. The 1983 cores were cut and sampled in the field, and 6,000 bottled water samples were returned to the BPRC, where they were sampled for $\delta^{18}O$, dust, and liquid conductivity. In comparison, the 2003 ice cores were returned to the BPRC for analysis in a frozen state, and concentrations of specific major ions were measured for each sample rather than just the liquid conductivity. Despite the differences in sampling, comparisons of the isotopic profiles of the 2003 and 1983 ice core over the last 500 years show that both records are nearly identical (*Thompson et al.,* 2006). This attests to the stability of the derived $\delta^{18}O$ profiles through time and serves as a verification of the original timeline developed in 1983.

3.2.3 Quelccaya geography

The Andes of central Peru consist of both western and eastern ranges of mountains, which are separated by a large high-elevation plateau known as the Altiplano (Fig. 3.1). The Quelccaya Ice Cap (13º 56'S, 70º 50'W, 5,670 m) is located just south of the eastern end of the Cordillera Vilcanota and stretches across a relatively broad, flat volcanic plateau. The flat profile of the ice cap makes it an ideal location for drilling, because the simple pattern of radial ice flow away from the central domes allows for selection of a drill site where complicated flow reconstructions can be avoided. Furthermore, the ice cap itself is very sensitive to climate change, because the flat profile means that small changes in the elevation of the equilibrium line have a large impact on the overall size and structure of the ice cap. The summit of the ice cap reaches an elevation of 5,670 m, and outlet glaciers extend to elevations as low as 4,950 m (*Mark et al.,* 2002). Runoff from the western and southern slopes of the Quelccaya Ice Cap drains into Lake Titicaca.

3.2.4 General climatology of the Altiplano and Quelccaya

The Andes disrupt zonal wind flow and precipitation to such a degree that they essentially divide the South American continent into two separate climatic zones. To the west of the Andes lie the dry deserts of the coastal lowlands and to the east the tropical rainforests of the Amazon. The coastal deserts are the result of a dry, subsiding air mass that is associated with the South Pacific High. The persistent stability of the coastal air mass is further amplified by inland advection of cool air from the ocean. The Humboldt Current, which extends as far north as Punta Pariñas, transports unusually cold waters (given the latitude) northward along the coast of Peru. El Niño events cause the South Pacific High to weaken and waters off the coast to warm up. This results in heavy rains in northern Peru and drought conditions in southern Peru, where Quelccaya is located.

Despite Quelccaya's proximity to the Pacific, the Atlantic is the primary moisture source, and moisture delivery largely depends on the strength of easterly flow out of the Amazon during the austral summer of December, January, and February (DJF). The strength of the easterly flow is impacted by the Bolivian High, a feature whose strength is modulated by ENSO events. The Bolivian high is an upper tropospheric high that develops over western Bolivia and southern Peru during the austral summer. When the Bolivian High is strong (weak), precipitation over the Altiplano is higher (lower) than normal (*Vuille*, 1999). Additionally, when the Bolivian High is strong (weak), it is generally displaced to the north (south), and easterly flow is stronger (weaker) than normal. This easterly flow is moist and, coupled with intense surface heating over the Altiplano, results in intense convective thunderstorms during the summer.

Seasonal rainfall patterns are primarily controlled by the migration of the Inter-tropical Convergence Zone (ITCZ). During the austral summer, the ITCZ moves as far south as the central Amazon Basin (wet season), and during the austral winter it is generally located over the northern part of the continent (dry season). The Quelccaya ice core is primarily a record of summer (DJFM) precipitation, because 80% of the annual precipitation falls in the region during the wet season (*Vuille*, 1999).

3.2.5 Recent warming in the Andes

Strong evidence suggests that both the tropical Andes and the tropics in general have undergone a period of rapid warming during the 20th century. Retreat of the outlet glaciers fed by the Quelccaya ice cap has dramatically accelerated during the past 30 years (*Thompson et al.,* 2006). The retreat of the Qori Kalis glacier, one of the outlet glaciers from the Quelccaya ice cap, is particularly well documented. The rate of retreat between 1963 and 1978 was estimated to be 4.9 meters per year based on aerial photographs and observations. The most recent rate of retreat during the period 1991 to 2005 has been on average 60 m/yr, or more than 10 times faster than the average rate of retreat during the period 1963 to 1978 (*Thompson et al.* 2006).

Aside from the retreat of the glaciers, the ice cores themselves provide several lines of evidence suggesting that recent warming is historically significant. For instance, values of δ^{18}O from the Huascarán (Cordillera Blanca, Peru) and the Quelccaya ice cores for the past 100 years are the most enriched values seen during the past 6,000 and 600 years, respectively. An additional line of evidence for warming at Quelccaya comes from differences observed in shallow ice cores taken between 1979 and 1995. Based on differences in the year they were retrieved, as well as their elevation, location, and the degree of smoothing of the δ^{18}O record resulting from percolating melt-water, these cores suggest that the 0°C isotherm has risen more than 100 m in elevation since 1979 (*Thompson et al.,* 2000).

3.3 Timeline verification and development

The timescale for the 2003 Quelccaya Summit Core is based upon multiple lines of evidence, including annual layer counting based on peaks in dust; a well-defined annual cycle in $\delta^{18}O$; the identification of ash layers in the ice core corresponding to historic volcanic eruptions; and comparisons of the Quelccaya core with other regional ice cores.

3.3.1 Seasonal cycles

Previous studies by Dr. Thompson clearly identified the seasonal cycles that are preserved in the Quelccaya ice core (*Thompson et al.,* 1984). Yearly divisions are based upon the greatest particle concentration in the ice, which occurs during the dry season between May and August (*Thompson et al.,* 1984). Thus yearly accumulation totals and $\delta^{18}O$ values are based on a water year running from June to July. In addition to the seasonal cycle of dust, a strong seasonal cycle occurs in $\delta^{18}O$, with the most negative values occurring during the wet season.

3.3.2 Layer counting

The 2003 summit core can be dated back to A.D. 315 by using both a time-depth model and annual layer counting. Dr. Thompson and Dr. Davis assisted in the counting of annual layers that was possible from A.D. 615 to 2003. The estimated error at A.D. 615 is approximately 10 years due to uncertainties in the counting process (Table 3.1). The dating of the ice core between A.D. 615 and 315 is based on the development of a time-depth model, and the estimated error at A.D. 315 is approximately 40 years. Counting of individual layers is straightforward, given the presence of a well-defined seasonal cycle coupled with a high rate of accumulation. For instance, annual layers within the top 100 years average 0.75 m in thickness, while annual layers at a depth of 161 m, a depth that corresponds with the limit of annually detectable layers, are on average 2.5 cm thick (calculated as an average from A.D. 615 to 715).

Estimated range of error associated with the derived timescale for the Quelccaya 2003 Core	
Derived Age	Estimated Error
2000-1600	+/- 1 year
1600-1400	+/- 2 years
1400-1000	+/- 5 years
1000-615	+/- 10 years
615-315	+/- 50 years (assuming that thinning model is appropriate)

Table 3.1 Errors associated with the timescale of the 2003 Quelccaya Core

3.3.3 Volcanic events as time horizons

The eruption of Huaynaputina in A.D. 1600 is a well-documented historical event identifiable in both the 1983 and 2003 Quelccaya ice cores (*Thompson*, 1986; *de Silva et al.,* 2000). A simple count of the annual dust peaks back to 1600 verifies layer counting as an accurate method of dating. The eruption itself can be seen in the dust profile as a broad peak lasting a number of years, as the ash was likely deposited across the ice cap and surrounding environment and then further reworked by local physical processes influencing the ice cap. The amplitude of the seasonal shifts in the record of $\delta^{18}O$ is subdued in the period following the eruption. One possibility is that the albedo of the ice cap was temporarily altered by the ash, and more of the sun's energy was absorbed, resulting in melting of surface ice (personal communication, Dr. Thompson).

3.3.4 Comparison with the Coropuna Ice Core

The summit of Coropuna (15° 31'S 72° 39'W, 6,377 m) is 1,000 m higher than that of Quelccaya and is located in the western Cordillera of the Peruvian Andes (Fig. 3.1). Three ice cores were obtained from the summit of Coropuna in 2003 during the same drilling season in which the 2003 Quelccaya core was obtained. The Coropuna cores were dated by Dr. Thompson, Dr. Davis, and myself, using the same methods outlined for the Quelccaya ice core. The Coropuna core was sampled for ^3H, and the 1963 bomb horizon was identified as a stratigraphic control point. Although a similar ^3H horizon hasn't been identified in the Quelccaya core,* matching up the two isotope profiles from Quelccaya and Coropuna allows one to see where the 1963 ^3H would be located. The isotope profiles from the two cores are similar enough during the last 200 years that individual years can be identified and matched peak for peak. This comparison with the Coropuna Core serves as a valid cross-check on the derived timeline and shows that the isotope profiles are not unique to either ice core but are rather preserved systematically across this entire region of the Andes.

**As the timeline is well constrained, no effort has been made in this regard.*

3.4 Record development

3.4.1 Accumulation

Annual values of accumulation were obtained by measuring ice accumulation between dust layers. These measurements were then adjusted to account for changes in density and thinning using the same procedures outlined in Section 2.5.3. Measurements of ice density were performed on the top 38 meters at approximately one-meter intervals. Density increases with depth before gradually leveling off between 0.92 and 0.93 g/cm^3 at approximately 38 m.

At depth, ice often undergoes a thinning process that results in the stretching of layers due to ice flow in the horizontal direction. Some of the factors contributing to this process may vary through time; as a result, it is difficult to access long-term changes in accumulation rates without making some estimates of these processes. Some examples of the processes that cause thinning are the slope of the bed, the amount of overlying ice, and the temperature of the ice. Rather than attempt to estimate these factors, I have selected a process to reconstruct accumulation that simply removes all long-term variability from the data set. Although these trends are of primary interest when it comes to determining long-term climatic changes, they are not as important if the primary concern is interannual to decadal scale climate variability, as is the case for this thesis.

To remove the long-term variability from the accumulation time series, the following steps were taken. First off, a best-fit curve [1.0489*(2.718)^(-0.0112)*(year)] was found, which accounted for more than 90% of the variance in the time series from A.D. 800 to the present and was then removed from the data. Second, z-scores were calculated for each year based upon mean values and standard deviations, which were recalculated at yearly intervals by making use of a 19-year centered window. This process by which the effects of thinning were removed resulted in the loss of all the long-term variability from the data set.

One final consideration is that as the average number of samples that constitute a year decreases, the quality of the accumulation record also deteriorates. Thinning and increasing density results in a decrease in the number of samples that constitute a year as depth increases. For instance, during the 20th century, most years are the sum of 10 to 20 samples, but during the 11th century, each year is made up of only 2 to 4 samples. The loss of resolution with depth makes the results in the earlier part of the record much more subject to where the yearly division is drawn so that if 4 samples make up one year and 2 samples the next, it appears to be a huge change in accumulation. This obviously isn't the case, but it must be considered when examining the accumulation data.

3.5 Calibration and time series summaries

3.5.1 Calibration of δ^{18}O

3.5.1.1 Summary of previous studies: δ^{18}O and the 1983 Quelccaya Ice Core

The mechanisms producing seasonal δ^{18}O variations in ice cores from the tropics are not the same as in those producing variations in polar ice cores. The values of δ^{18}O seen in polar ice cores are typically related to the temperature of condensation. By comparison, the seasonal differences in δ^{18}O values from tropical cores depend on a number of factors, including the relative depletion the air mass undergoes before reaching the accumulation site; the temperature at condensation; and changes in the moisture source area. However, over periods of decades to centuries, the δ^{18}O records of tropical ice cores preserve the same global temperature trends observed in the records obtained from polar ice cores (*Thompson et al.,* 2000). One difficulty in interpreting records from tropical ice cores is the lack of data from on-site weather monitoring stations. Without knowledge of the specific weather at the ice core drilling site, the calibration of δ^{18}O with meteorological variables must be based on one of the following: whatever limited data is available, modeled simulations of past conditions, or data from more distant weather stations.

A ubiquitous trait of tropical climates is the absence of a cold season. With little mean change in temperatures between seasons, it is difficult to explain the large swings in δ^{18}O, up to 20 parts per mil, on the basis of temperature differences alone (*Thompson et al.,* 2000). Additionally, the seasonal swings in isotope values from Quelccaya are opposite to those found in polar regions, so that the most depleted values are found during the summer (DJF) (*Thompson et al.,* 2000). Although little seasonal change in temperature is observed at Quelccaya, a distinct wet and dry season is observed.

Differences in the precipitation pathway between the wet and dry season have been studied to account for the seasonal fluctuations seen in the δ^{18}O record from Quelccaya.

Grootes et al. (1989) developed a model to explain seasonal differences in δ^{18}O values at Quelccaya. The model examines how the isotopic composition of precipitation changes as it is transported over the Amazon basin. The model assumes that the Atlantic is the source of both dry and wet season precipitation, and that the isotopic composition of moisture at the source area in the Atlantic is basically the same throughout the year. What varies throughout the year is the amount of precipitation that falls out over the Amazon Basin. Changes in the amount of depletion that occurs as moisture crosses the Amazon Basin account for most of the seasonal cycle observed in Quelccaya δ^{18}O.

3.5.1.2 δ^{18}O and the 2003 Quelccaya Ice Core

Values of δ^{18}O derived from the 2003 Quelccaya Ice Core are strongly correlated ($r=0.646$, $p<0.001$, 1856-2003) with NIÑO 4 SSTs (Fig. 3.2). The correlation field produced by regressing Quelccaya δ^{18}O with Pacific SSTs (Fig. 3.3) is similar to that produced by ENSO, but it bears some important differences. For instance, ENSO is most strongly correlated with SST anomalies along the equator and adjacent to the South American coast, while anomalies produced by Quelccaya δ^{18}O are strongest in the northern equatorial Pacific from 150°W to 160°E. The pattern of SST correlations associated with Quelccaya δ^{18}O is very similar to that produced by decadal ENSO variability, as presented in the study by *Lohmann and Latif* (2005). A comparison, shown in Fig. 3.4, of the δ^{18}O time series with NIÑO 4 and NIÑO 1+2 SST illustrates the predominantly decadal nature of the δ^{18}O signal. Although ENSO events appear to be superimposed on the δ^{18}O time series, they are certainly not the dominant feature that they are in the time series of SST in the NIÑO 1+2 region.

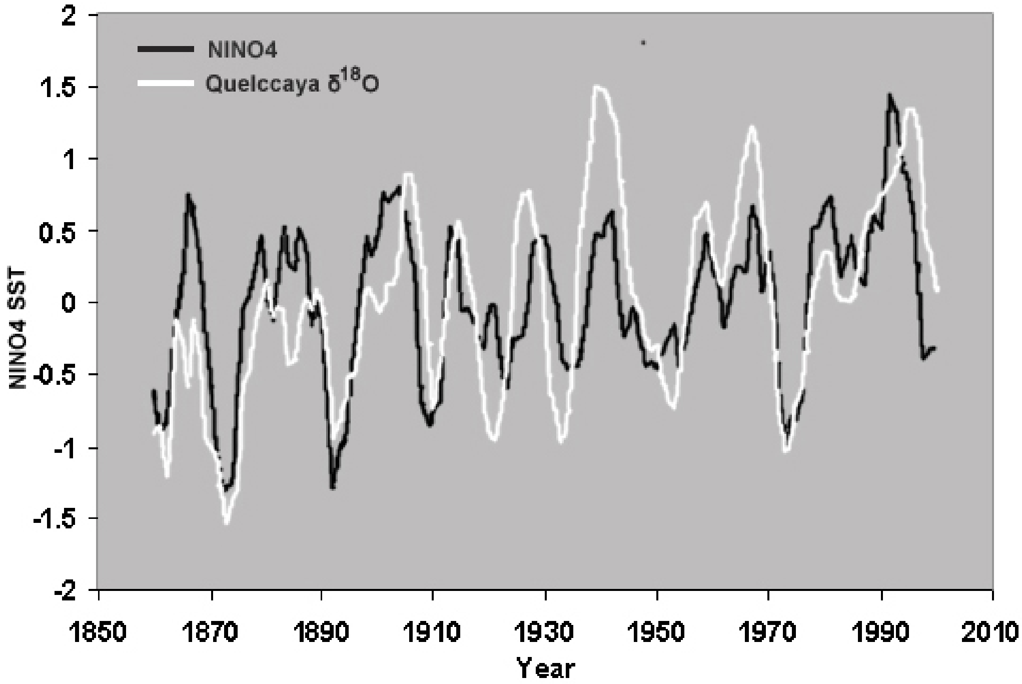

Figure 3.2 Quelccaya δ^{18}O and NINO 4: SSTs time series in the NINO 4 4 region in the tropical Pacific Basin and the Quelccaya δ^{18}O record show a strong relationship for the entire 142-year record ($r=0.646$, $p<0.001$). (Y-axis represents normalized values.)

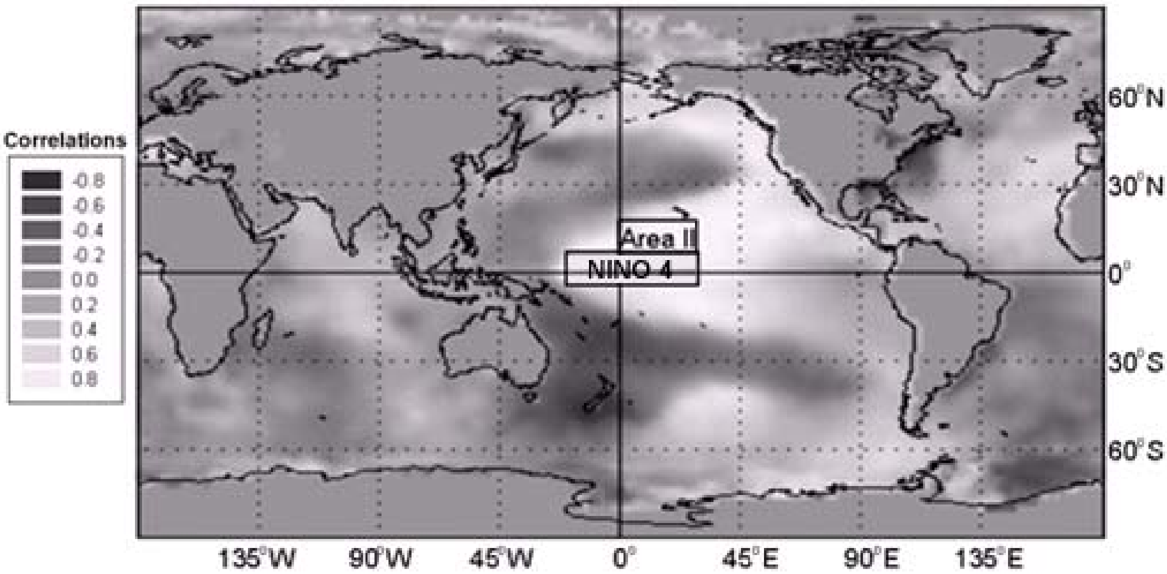

Figure 3.3 Quelccaya δ^{18}O and Pacific SSTs. Correlation field map of Quelccaya δ^{18}O and SST for the period 1945-2003. Correlations are derived from SST and δ^{18}O values that were smoothed with a 5-year centered average.

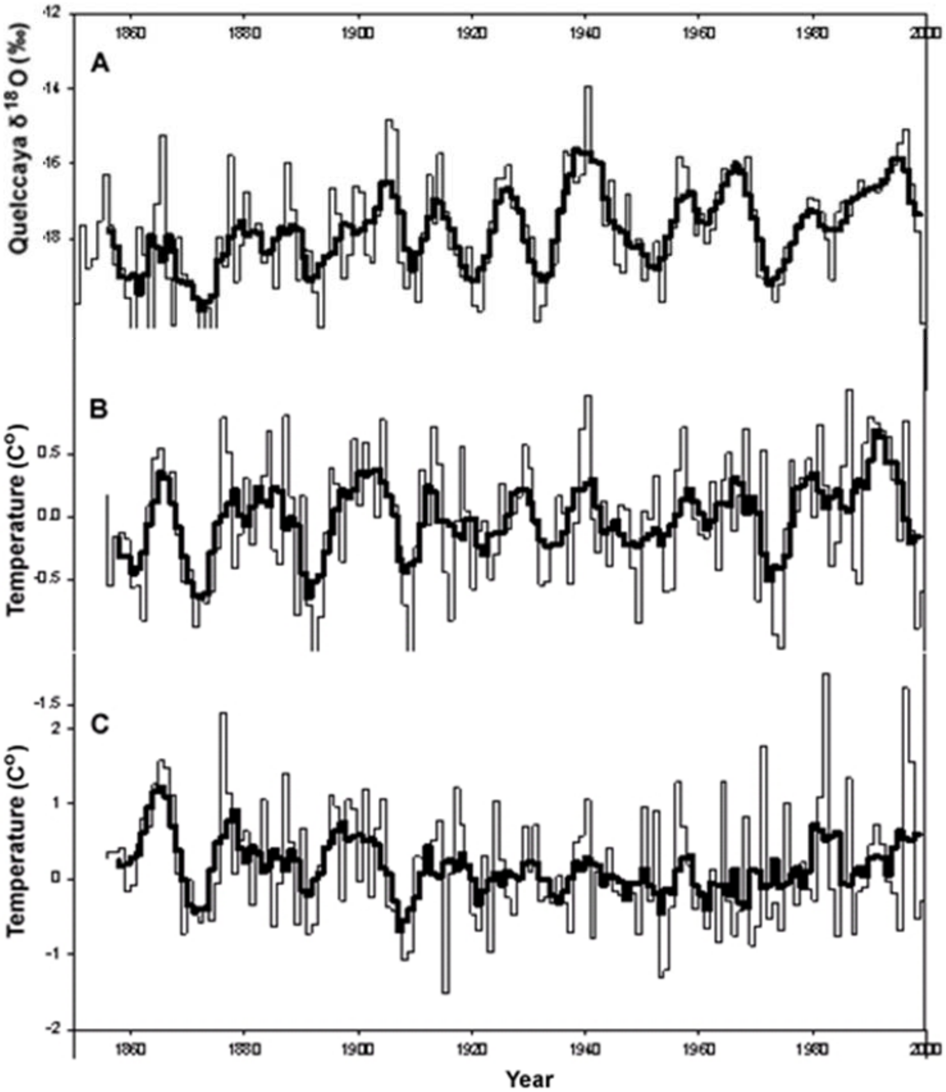

Figure 3.4 Time series of (A) Quelccaya δ^{18}O, (B) NINO 4 SST, and (C) NINO 1+2 SST. The annual values of each time series are plotted using a thin line, and the dark line represents the 5-year average of each. Note that for NINO 4 and Quelccaya δ^{18}O, the 5-year average captures the majority of the variability in the time series, whereas this is not the case for NINO 1+2. It can be seen with NINO 1+2 that annual values are often fluctuating above and below the 5-year average. This is because interannual variability is prominent in the NINO 1+2 region, and decadal variability is prominent in the NINO 4 region.

A primary difficulty in assessing whether $\delta^{18}O$ is more reflective of temperature or accumulation is that warm (cold) and dry (wet) anomalies often occur together, making it difficult to separate out the effects of temperature from those of precipitation. A study at Sajama by *Bradley et al.* (2003) showed that amount of precipitation is negatively correlated with $\delta^{18}O$ (r=-0.61), and my examination (*Urmann*, 2003) of the 1983 Quelccaya core shows that this same relationship exists (r=-0.66 p <0.005, 1900-1961).

A strong and persistent relationship (r= -0.74 and p <0.005, 1916-2000) is observed between Quelccaya $\delta^{18}O$ and the elevation of Lake Titicaca. In fact, the relationship between $\delta^{18}O$ and the elevation of Lake Titicaca is stronger and more consistent than the relationship between accumulation and the elevation of the lake, which prompts one to ask if $\delta^{18}O$ makes a better proxy of accumulation than the record of accumulation itself. This certainly could be the case, as the record of accumulation could be complicated by a number of factors, including but not limited to surface snow transport, surface melting, and surface sublimation. Furthermore, strong relationships are observed between the level of Lake Titicaca and NINO 4 SST (r=-0.71 and p <0.005, 1916-2000). These correlations support the conclusion that SST in the central equatorial Pacific have a large influence on both the general circulation patterns of the Peruvian Andes and on the amount of precipitation that falls in the Lake Titicaca basin.

The strongest connection between the record of $\delta^{18}O$ and climate in the North Pacific is the relationship between $\delta^{18}O$ and the East Pacific Oscillation (EPO). The pattern of SST anomalies associated with the Quelccaya $\delta^{18}O$ is very similar to that produced by the winter EPO, and not surprisingly Quelccaya $\delta^{18}O$ is strongly correlated with an index of the EPO (r=-0.63 and p <0.01, 1950-2000). Typically a positive phase of the EPO persists during La Niña years and is described as follows by the Climate Diagnostic Center: “During strong positive phases of the EPO pattern, a deeper than normal trough is located in the vicinity of the Gulf of Alaska/western North America, and positive height anomalies are observed farther south. This phase of the pattern is associated with a pronounced northeastward extension of the Pacific jet stream toward western North America, and with enhanced westerlies over the Pacific Northwest states, northern California, and sometimes, southwestern British Columbia."

3.5.1.3 Stability of the Quelccaya δ^{18}O calibration during the Little Ice Age (LIA)

The end of the LIA occurs in 1882 in the Quelccaya core and is marked by an abrupt decrease in the concentration of dust and a shift from more depleted to more enriched values of δ^{18}O. As global climate conditions were substantially different during the LIA than they are today, it is worth considering whether the same relationships observed between historical data and δ^{18}O were similar to those that occurred during the LIA. This is possible because the record of historical SST for the Pacific extends to 1856 and therefore overlaps with a period of the LIA that is recorded by the Quelccaya Ice Core. The Pierson correlation coefficient between Jan-Dec Niño 4 SST and Quelccaya δ^{18}O during the period 1856 to 1882 is 0.75 (as opposed to 0.65 for the modern period of record from 1882 to 2000). This indicates that a strong relationship between δ^{18}O and SST persisted even during the LIA despite a substantially different background climate.

3.5.1.4 δ^{18}O time series summary

Values of δ^{18}O generally fluctuate between -17.5‰ and -16.5 ‰ on average between A.D. 1000 and 1400 (Fig. 3.5). Following A.D. 1400, values of δ^{18}O become progressively more negative. This trend toward more negative values lasts until approximately 1810, when it reverses and values begin to increase until the modern day. Modern values of δ^{18}O are similar to those exhibited before A.D. 1400. The most negative values, averaging -18.5‰ to -19.0 ‰, correspond with the cold temperatures that occurred globally during the LIA between A.D. 1625 and 1825. A 30-year average was used to find periods with higher- and lower-than-background values of δ^{18}O. Higher-than-background values of δ^{18}O are centered at A.D. 886, 933, 1019, 1110, 1145, 1234, 1326, 1380, 1441, 1516, 1727, 1792, 1835, and 1953, while lower-than-average values occurred in A.D. 920, 988, 1080, 1190, 1284, 1350, 1413, 1470, 1563, 1675, 1765, 1811, and 1863.

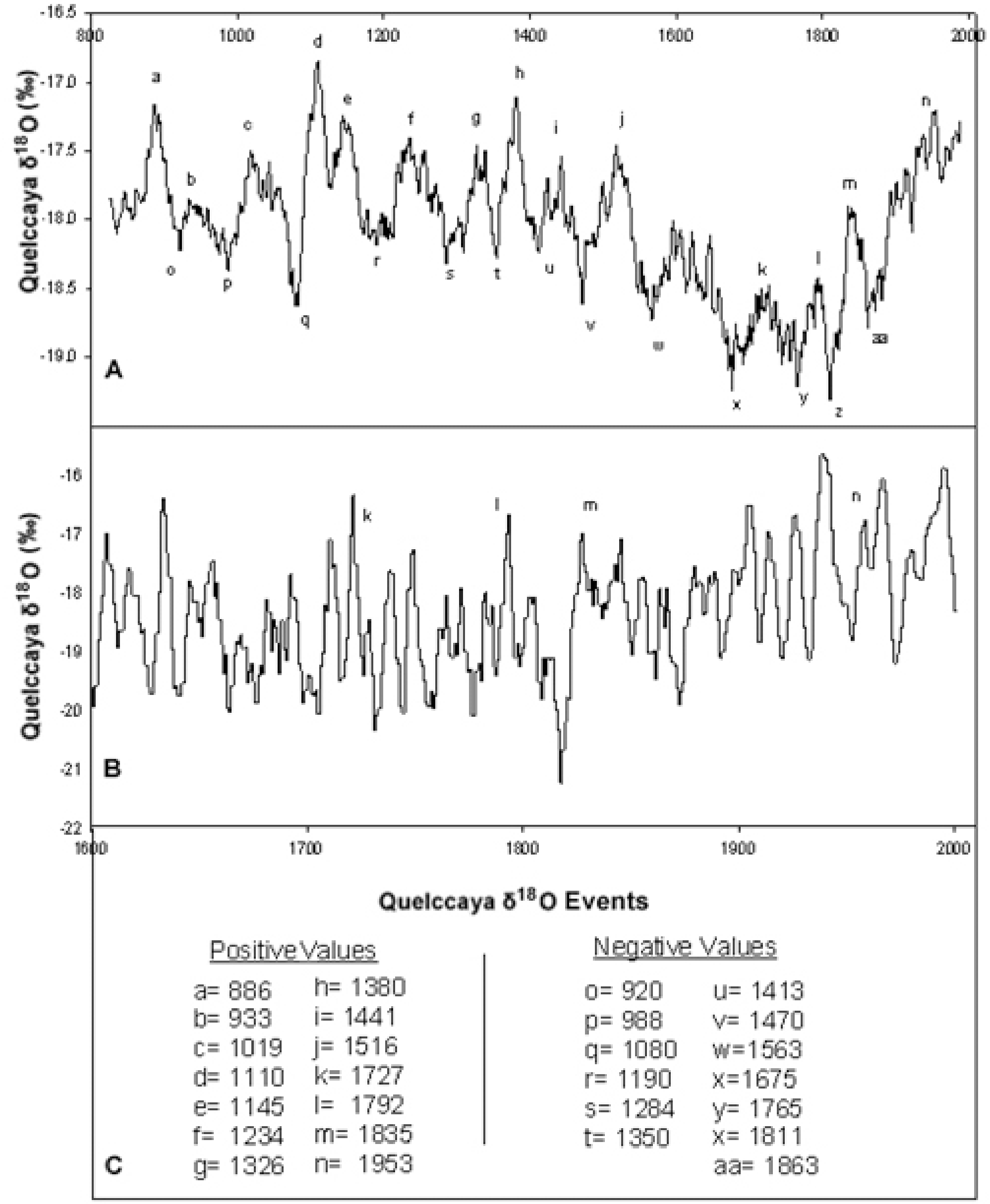

Figure 3.5 Time series of δ^{18}O and demarcation of major events. (A) Depicts a 30-year centered average of δ^{18}O since A.D. 820. (B) Depicts a 5-year centered average of δ^{18}O since A.D. 1600. (C) This box gives the timing of large δ^{18}O events that are labeled in (A) and (B).

An abrupt end to the LIA is seen in the 1983 Quelccaya core at 1880 and is marked by decreased variability in $\delta^{18}O$ and increased levels of accumulation (*Thompson,* 1985). Following the end of the LIA, values of $\delta^{18}O$ progressively increased from 1880 until 1940. This was followed by a gradual decrease in the values of $\delta^{18}O$ starting about 1940 and continuing until the mid-1970s before a reversal in trend occurred once again. In general, these trends are seen in the time series of $\delta^{18}O$ and correspond well with averaged decadal Northern Hemisphere temperatures (*Thompson et al.,* 1992; *Thompson et al.,* 2006).

3.5.2 Accumulation and dust: calibration and time series overview

The relationships identified in the earlier studies of the 1983 accumulation data sets are also observed in the 2003 ice core. For instance, a strong positive correlation ($r=0.54$ and $p <0.01$, 1917-1995) is noted between the accumulation time series and that of Lake Titicaca. On the other hand, negative correlations are observed between accumulation and $\delta^{18}O$ ($r=-0.54$ and $p <0.01$, 1900-1995) and with NIÑO 4 ($r=-0.53$ and $p <0.01$, 1900-1995). It is interesting to note that the strength of the correlation between $\delta^{18}O$ and accumulation is weaker before 1900, and in some years it is even a reverse sign. Accumulation anomalies are less persistent and show more year-to-year variability than $\delta^{18}O$ anomalies (*Urmann,* 2003). Singular Spectrum Analysis of the 1983 Quelccaya accumulation record shows that 42% of the variance in the detrended accumulation record has a periodicity of between 2.5 and 4 years (*Henderson,* 1996). Periodicities associated with accumulation time series are closer to those associated with ENSO (Section 1.1.1) and contrast with the decadal periodicities dominant in the record of $\delta^{18}O$.

The reconstructed record of accumulation from the 1983 Quelccaya Ice Core shows that the period from 1160 to 1500 was drier than usual and that the period 1250 to 1310 was especially dry (*Thompson,* 1985). Previous studies of the 1983 Quelccaya core also indicate that the LIA consisted of a wet and cool period lasting from 1500 to 1720 and a dry and cool period from 1720 to 1860 (*Thompson,* 1985). The timing of changes in precipitation as recorded by Quelccaya is nearly synchronous with observed changes in pollen assemblages from the Sajama ice core (*Liu, K., et al.,* 2005). These conclusions are also supported by evidence from Huascarán in northern Peru, which similarly indicates that the period 1730 to 1870 was drier than normal (*Thompson,* 1995).

Previous studies of the 1983 Quelccaya Ice Core noted that increased dust concentrations occurred at the same time as decreased accumulation and more positive $\delta^{18}O$ values (*Thompson et al,* 1992), and this analysis of the 2003 time series reveals these same features. For instance, a negative correlation is observed with the accumulation time series (-0.37 and $p < 0.01$, 1900-1995). Dust concentrations during the period 1980 to 2000 are higher than at any other time during the entire record, with the exception of the increased period of dustiness associated with the eruption of Huaynaputina in A.D. 1600.

Several features stand out in the dust record preserved in the Quelccaya Ice Core during the last 1,000 years (Fig. 3.6). First off, generally high dust concentrations occurred between 1550 and 1950. The highest dust concentrations, with the exception of the Huaynaputina, occurred in the last 25 years of the 20th century. The exception to this is a brief period of lower-than-average dust values between 1880 and 1950. It is noted that 1880 coincides with the termination of the LIA (*Thompson et al.,* 1985). Lower-than-average values are exhibited during the period 800 to 1550, but several large dust events occurred during this period as well. For instance, periods of high dust concentration are centered at 909, 1032, 1164, 1245, 1375, 1425, and 1487. It may be just as informative to examine the occurrence of low concentrations of dust or low-dust events.

3.6 Discussion

3.6.1 Quelccaya $\delta^{18}O$: A record of decadal or interannual variability?

Interannual to decadal shifts in the location and size of the PWP alter precipitation patterns throughout the tropics and are the dominant signal in the record of Quelccaya $\delta^{18}O$. Decadal variability is prominent in the record of Quelccaya $\delta^{18}O$ (*Thompson et al.,* 1992). Time series analysis of the 1983 Quelccaya core by *Henderson* (1996) identified a dominant periodicity of 10-13 years. These decadal fluctuations are easily visible in the time series of the 5-year moving average of $\delta^{18}O$ from the 2003 Quelccaya Ice Core (Fig. 3.2). Quelccaya $\delta^{18}O$ is most strongly correlated with the NIÑO 4 region of the Pacific. Singular Spectrum Analysis of NIÑO 4 SSTs by *Lohmann* and *Latif* (2005) found that the primary mode of variability in this region of the Pacific is decadal and that interannual

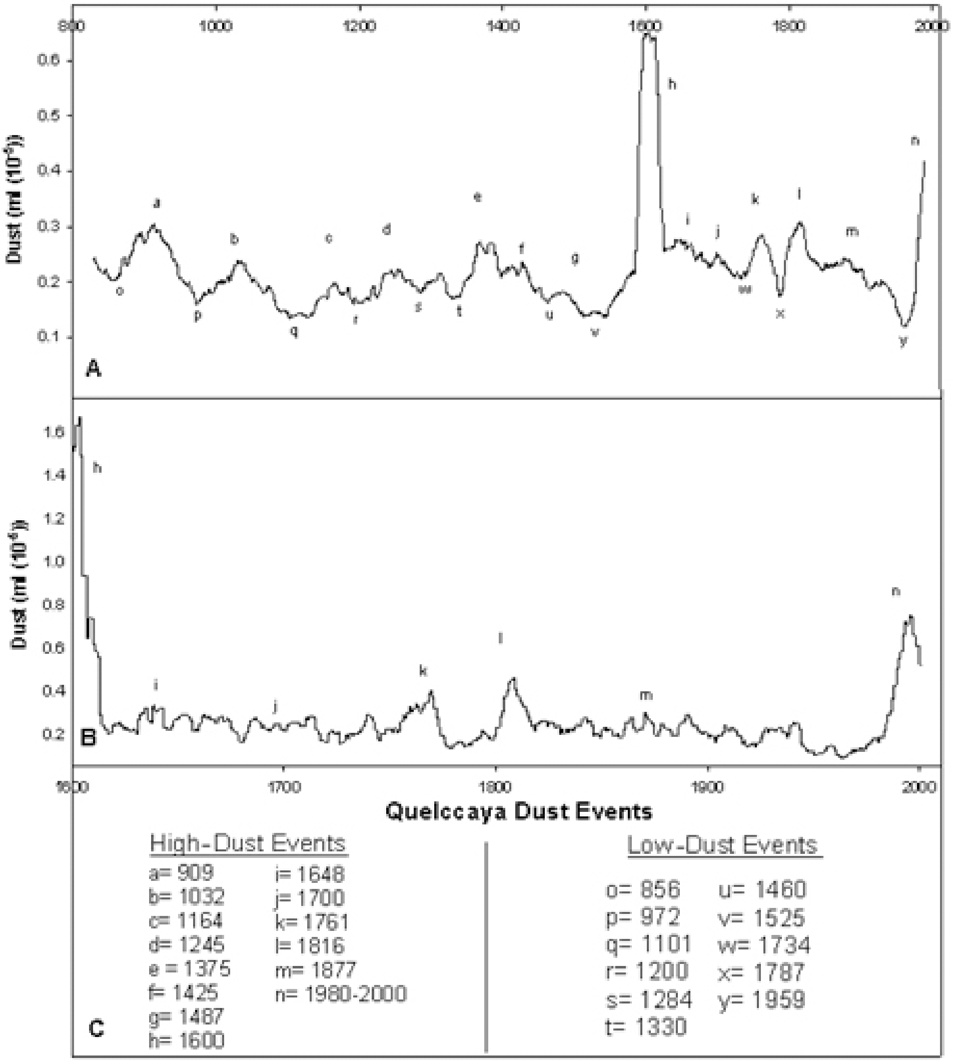

Figure 3.6 Time series of dust and demarcation of major events. (A) Depicts a 30-year centered average of dust since A.D. 820. (B) Depicts a 5-year centered average of dust since A.D. 1600. (C) This box gives the timing of large dust events that are labeled in (A) and (B).

variability associated with ENSO is a secondary mode of variability. In general, SST anomalies in the western Pacific are more persistent and evolve on slower timescales than those in the eastern Pacific (*Klotzbach and Gray,* 2004). It is speculated that background changes in SST associated with decadal ENSO variability affect the frequency of ENSO events so that El Niño (La Niña) events occur with greater (decreased) intensity when the decadal ENSO is in positive (negative) mode (*Lohmann and Latif*, 2005).

Previous studies of the Quelccaya Ice Core and studies of climate records from the Atlantic and the Pacific have identified strong decadal signals. A study of timescale variability of the 1983 Quelccaya core by *Melice and Roucou* (1998) found a strong 12-year oscillation in the time series of δ^{18}O that persisted throughout the period of analysis from 1485 to 1984. This study links the 12-year oscillation observed in the Quelccaya core to SST variability in the northern tropical Atlantic that occurs at the same frequency. In addition, *Melice* and *Roucou* (1998) also found evidence of oscillatory behavior at ENSO type periodicities in the Quelccaya record; however, these oscillations were not as strong in amplitude or as consistent through time as the decadal frequencies.

Decadal scale variability has been identified in several Atlantic climate records. Studies of meteorological records by *Xie* and *Tanimoto* (1998) show a dominant mode of 10—to 14-year variability in records of Atlantic SST spanning the entire ocean from 30ºS to 70ºN. A reconstruction of trade winds based on foram productivity in the Cariaco Basin by *Black* (1999) shows that trade winds intensities vary on both decadal and centennial timescales. The study by *Black* (1999) suggests that trade winds were in general stronger during the period 1640 to 1880. This particular period is notable, as it overlaps with the lowest δ^{18}O values from Quelccaya.

A study of a 112-year-long coral record from Palmyra by *Cobb* (2001b) suggests that decadal variability in the Central Tropical Pacific (CTP) has a global footprint and is associated with patterns of decadal variability in the Atlantic, Indian, and North Pacific. Palmyra Island (6° N, 162° W) is located in the region of the Pacific that is most strongly correlated with Quelccaya δ^{18}O (Fig. 3.3). A more detailed comparison of these records is given in Section 5.3. A separate study by *Cobb* (2001b) examined records of δ^{18}O from Seychelles Corals and found that although both data sets are strongly influenced by ENSO, they also exhibit coherent decadal climate variability with each other and with the

Palmyra Coral record at a 12- to 13-year periodicity. *Cobb* (2001b) attributes the relationship between the three regions to large scale changes in the Walker circulation, and the study states specifically that "…CTP warming destabilizes both the descending and ascending branches of the cell which influences the tropical Atlantic and Indian basins, respectively. Observations and climate models show that enhanced convection in the Eastern Pacific affects trade winds in the tropical Atlantic, serving to warm the north tropical Atlantic and shift the Atlantic ITCZ northward, causing Nordeste drought."

It appears that large-scale decadal shifts in the location of the PWP force a global redistribution of the Walker circulation that may account for changes in atmospheric flow patterns that drive the observed changes in the $\delta^{18}O$ record. The strongest correlations between Quelccaya $\delta^{18}O$ and SST occur not within the central portion warm pool but along its easternmost margin, specifically 150° W to 160° E. This region of the PWP may best reflect overall variability, as expansion and contraction of this region result in larger temperature changes than in the central portion of the PWP, where little overall variation occurs.

3.7 Conclusions

Variability in the Quelccaya Ice Core record is preserved across a range of timescales. At interannual timescales, ENSO events have been shown to be preserved in the record as less negative $\delta^{18}O$, reduced accumulation, and increased dustiness (*Thompson et al.,* 1984, 1985, and 1992). At decadal timescales, the broad swings in isotopes closely match the decadal variability observed in NIÑO 4 SSTs. However, at centennial timescales, the record of $\delta^{18}O$ closely matches global temperature reconstructions over the last 100 years (*Thompson et al.,* 1992). The interplay of variability is complex, as the interannual variability is superimposed on the decadal variability, which is superimposed on the longer centennial variability. Uncovering the relationships between the variability at different timescales is difficult because of the lack of high-resolution records of climate of substantial duration in South America or the Tropical Pacific.

CHAPTER 4
ICE CORE-BASED ENSO RECONSTRUCTIONS

4.1 Introduction

This chapter evaluates several methods for reconstructing a record of ENSO events based on the ice core data from Quelccaya and Bona Churchill (BC). At interannual timescales, El Niño (La Niña) events have been shown to be preserved in the Quelccaya record as less negative (positive) $\delta^{18}O$, reduced (increased) accumulation, and increased (reduced) dustiness (*Thompson et al.,* 1984, 1985, and 1992). Given the strong signature that ENSO events leave in the ice core, it is possible to reconstruct records of past ENSO-like signatures in the ice core record. The primary focus is given to reconstructing a record of ENSO from the Quelccaya ice core, because ENSO events have a weak signature in BC. Nonetheless, a multicore ENSO reconstruction and the construction of a tree ring- ice core-based ENSO index are briefly described.

4.2 ENSO and $\delta^{18}O$: results from the 1983 Quelccaya Ice Core

Previous studies of the 1983 Quelccaya ice core show a connection between ENSO events and annual values of both $\delta^{18}O$ and ice layer thickness (*Thompson et al.,* 1984). For instance, strong El Niño events result in an average 30% reduction in accumulation at Quelccaya (*Thompson et al.,* 1984). Studies of snow pits encompassing the period from 1975 to 1984 indicate that reduced accumulation occurred during both the 1982 to 1983 El Niño and the 1976 to 1977 El Niño (*Thompson*, 1992). The relationship between ENSO and Quelccaya has been linked to ENSO-driven circulation anomalies that are associated with changes in moisture flow from the tropical Atlantic to the ice core site in the Andes (*Bradley et al.,* 2003). In general, El Niño (La Niña) events result in decreased (increased) precipitation and increased (decreased) temperature in the region (*Garreaud et al.,* 2003). ENSO events are proposed to have an influence on annual values of $\delta^{18}O$ because of changes in the freezing height associated with warming and cooling during El Niño and La Niña events, respectively (*Thompson et al.,* 2005).

However, sorting out the specific role of either temperature or precipitation on the fractionation process is challenging, as low (high) precipitation occurs alongside higher (lower) temperatures.

ENSO-induced precipitation anomalies result from shifts in the mean zonal flow that are driven by warming (cooling) of the tropical troposphere during El Niño (La Niña) events. One complexity is that an enhanced westerly flow is a common feature during all dry years and not just ENSO dry years (*Vuille,* 1999). Another complexity is that ENSO-induced tropospheric temperature anomalies are also variable; thus, the precipitation response over the Altiplano is not always predictable (*Garreaud and Aceituno,* 2001). Regression analysis shows that a one-degree Celsius rise of SSTs in the Niño 3.4 region corresponds with a 76-meter increase in the freezing heights over the central Andes (*Thompson et al.,* 1992; *Bradley et al.,* 2003). Higher freezing heights result in lower levels of regional accumulation. Thus, higher than average temperatures in the tropical Pacific correlate with drier regional conditions in the central Andes over prolonged periods of time.

4.3 A Quelccaya-based ENSO reconstruction

The strong impact of ENSO events at the Quelccaya drill site make this record ideal for reconstructing ENSO, but it is complicated by the fact that the effects of individual ENSO events are often variable and that not all ENSO-like climate anomalies are attributable to ENSO events. For that reason it should be noted that the following reconstruction is not an actual ENSO reconstruction, but a reconstruction of ENSO-like signatures that may or may not correspond with actual ENSO events. To reconstruct a more reliable record of actual ENSO events, it would be necessary to compare the record from Quelccaya with records from other regions and with ENSO teleconnections so that events could be cross verified.

ENSO events in the ice core can be identified either visually or by using an automated method, relying on a set of fixed criteria, and both approaches are investigated in order to compare and contrast the results. The key idea behind both methods is to highlight significant deviations from average yearly values that might correspond with ENSO events. One problem that was considered is that changes in the standard deviation may be driven at longer timescales by processes other than ENSO. One solution to avoiding this problem is the use of a sliding window to calculate the standard deviation. Another important issue that was considered was selecting a threshold value for defining an ENSO event. This was difficult because little is known about the past frequency of ENSO events, and to compensate results using several possible thresholds were examined.

4.3.1 An automated method for defining ENSO

In order to define an ENSO event, the standard deviation of δ^{18}O was calculated using both a 20- and a 50-year sliding window (Fig. 4.1). Then three different definitions were selected to mark the occurrences of individual ENSO events. An ENSO event was defined when the absolute value of the difference between the measured annual value of δ^{18}O and the mean value exceeded one of the following: a single standard deviation, 80% of one standard deviation, and 60% of one standard deviation. A similar process was followed for the record of accumulation, as it was planned to compare the ENSO sequences using the time series of accumulation and δ^{18}O in more detail. This step was evaluated, but because very few of the events generated from these time series overlap, the idea was not pursued further. A comparison examining the time series of number of ENSO and the ratio of El Niño to La Niña events generated from the 50-year and 20-year sliding windows shows that the general features of variability are captured by both intervals. Figure 4.2 compares the results using the 20-year window and the three different criteria for examining the absolute value of the difference between the annual value of δ^{18}O and the mean (i.e., in excess of one standard deviation, 80% and 60%).

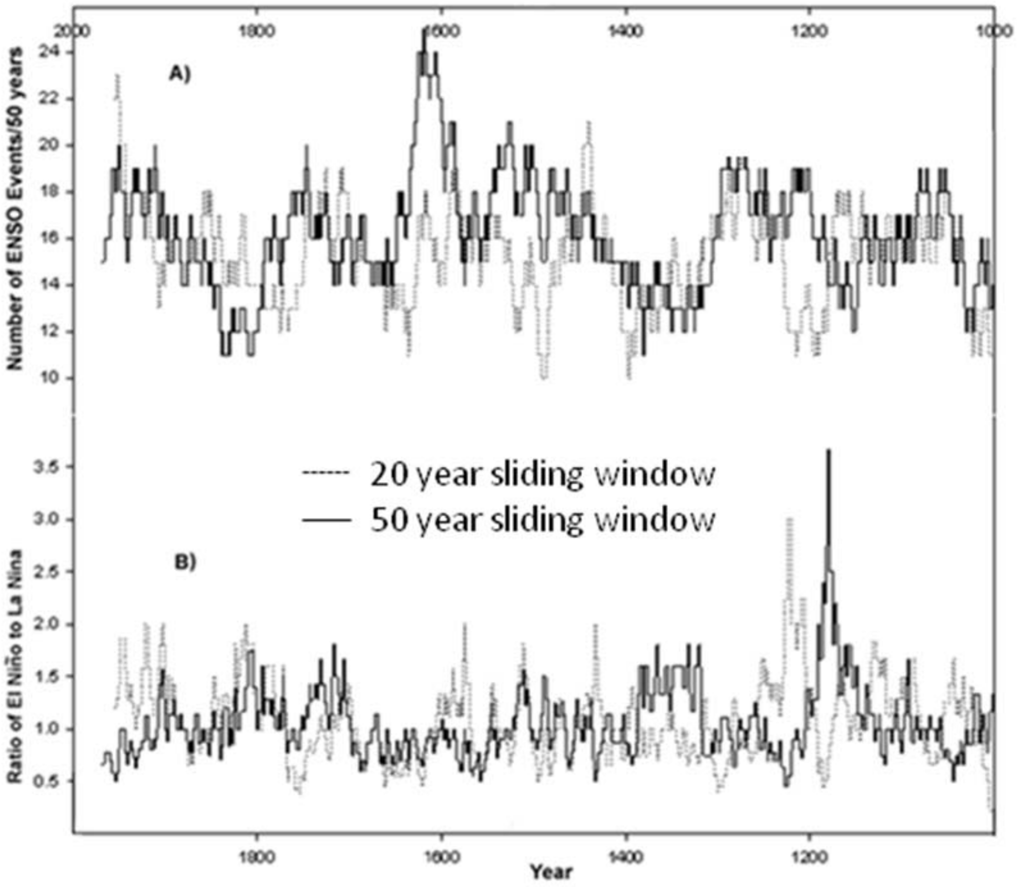

Figure 4.1 Comparison of the use of different sliding windows in the determination of ENSO events using the automated method described in the text. (A) Shows the number of ENSO events in a 50-year centered interval (recalculated annually), using a 50-year sliding window (dashed line), and a 20-year sliding window (bold line). (B) Shows the ratio of El Niño to La Niña events in a 50-year centered interval (recalculated annually), using a 50-year sliding window (dashed line), and a 20-year sliding window (bold line).

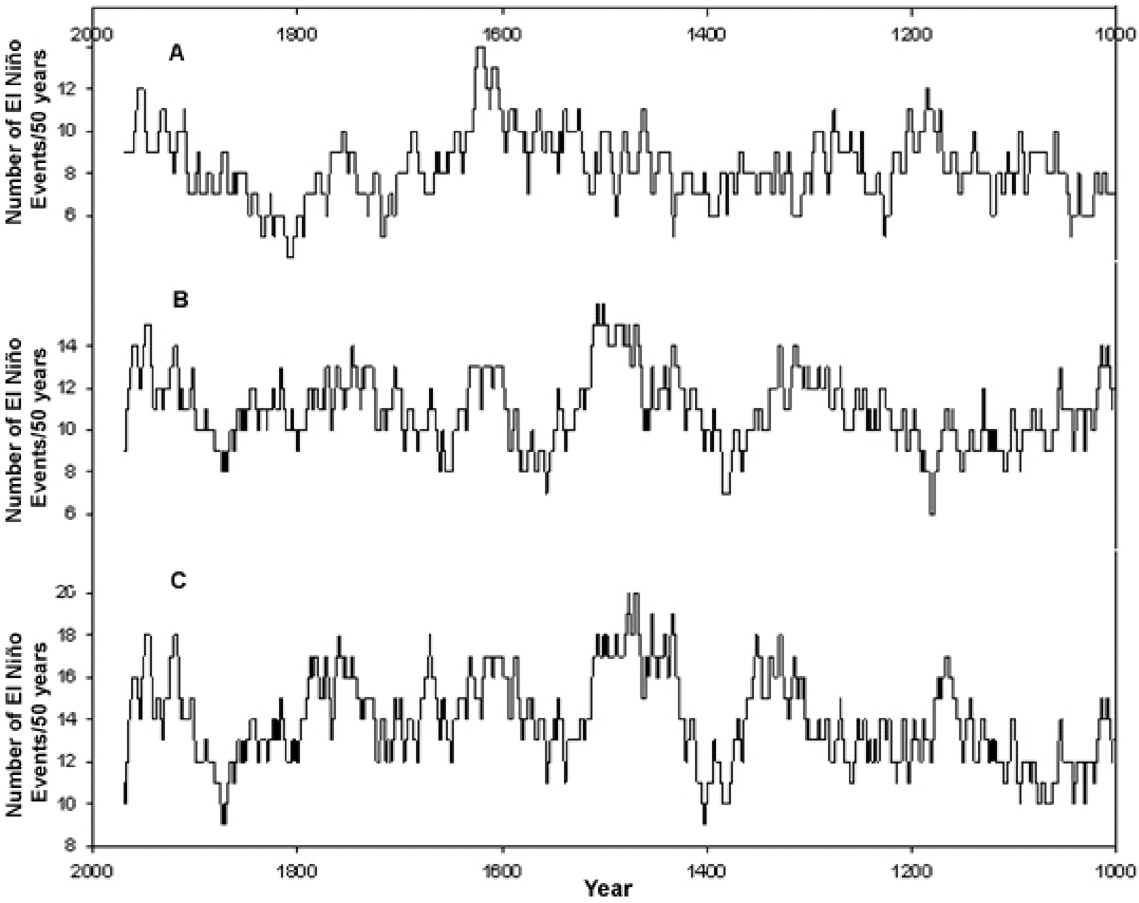

Figure 4.2 Graphs A, B, and C compare the number of El Niño generated with different cutoff criteria, as described in the text. All three graphs show events during a 50-year period using a 20-year window to calculate the standard deviation and the mean. (A) Shows the number of events generated in a 50-year period when an El Niño event is defined during a year in which the standard deviation exceeds 1. (B) Shows the number of events generated in 50-year period when an El Niño event is defined during a year in which the standard deviation exceeds 0.8. (C) Shows the number of events generated in a 50-year period when an El Niño event is defined during a year in which the standard deviation exceeds 0.6.

4.3.2 Hand selection as a means for defining ENSO events

Dr. Thompson demonstrated that El Niño events generally result in reduced accumulation, more positive values of $\delta^{18}O$, and increased dustiness in the 1983 Quelccaya core, and that many of the historically documented El Niño events can be matched with events in the ice core (*Thompson et al.,* 1992). I have picked out the El Niño events recorded in the new 2003 Quelccaya Ice Core for the last 1,000 years by making a visual inspection of the core (Tables 1.1 and 1.2). Several criteria are used to define El Niño events:

1. Years with less negative $\delta^{18}O$
2. Years with reduced accumulation
3. Years with increased dustiness

The years that were selected as El Niño years are listed in Tables 4.1 and 4.2, and a select few are shown to better illustrate the process in Figure 4.3. One difficulty in picking out years by hand is that the process is somewhat subjective. Another difficulty is that the signal preserved in the ice core changes with depth, and compensatory adjustments that are also subjective have to be made to the selection process.

The use of annually derived values of dust concentration is somewhat limited by the method used to calculate these values. This results from the fact that the dust peaks are themselves used to define the annually occurring breaks so that the individual dust peaks are divided into two different years. One can easily imagine a scenario, as illustrated in Figure 4.4, where the calculated dust concentration is extremely high because a single year incorporates large dust peaks from two separate dry seasons, or a scenario where dust is average because it incorporates a lag dust peak from one dry season and a small peak from the other dry season. Although these seasonal divisions complicate the interpretation of the dust signal, this is not the case for $\delta^{18}O$, as the signal from each full wet season is fully contained within one ice core year.

1957
1941
1896
1866
1862
1856
1834
1826
1814
1805
1792
1778
1760
1749
1745
1729
1713
1707
1694
1684
1676
1646
1635
1623
1609
1594
1569
1528
1506
1501
1490
1465
1463
1456
1452
1432
1429
1404
1394
1381
1337
1329
1316
1294
1265
1230
1217
1189
1164
1153
1123
1098
1088
1023

Table 4.1 El Niño years that are clearly identified by both the time series of δ^{18}O and by accumulation, using the hand count method.

1989
1981
1968
1958
1953
1948
1944
1941
1937
1927
1920
1915
1913
1906
1901
1897
1892
1888
1883
1881
1877
1874
1869
1866
1862
1856
1852
1847
1844
1841
1839
1836
1834
1829
1826
1822
1819
1814
1808
1805
1805
1801
1799
1796
1793
1788
1784
1781
1778
1773
1771
1766
1763
1760
1755
1749
1745
1741
1738
1735
1729
1723
1719
1713
1710
1707
1703
1700
1694
1691
1688
1683
1680
1676
1673
1670
1668
1661
1656
1651
1647
1639
1634
1628
1626
1623
1618
1609
1604
1597
1594
1586
1583
1579
1574
1569
1565
1556
1551
1546
1543
1539
1531
1528
1525
1521
1518
1512
1506
1501
1493
1490
1482
1477
1473
1470
1465
1463
1456
1452
1446
1437
1432
1429
1425
1422
1416
1412
1404
1396
1394
1390
1386
1381
1376
1370
1359
1351
1346
1339
1337
1332
1329
1325
1320
1315
1310
1305
1302
1297
1293
1290
1285
1280
1276
1270
1265
1260
1255
1250
1243
1239
1230
1222
1217
1212
1206
1202
1197
1191
1188
1184
1177
1174
1170
1164
1154
1150
1146
1143
1139
1135
1131
1128
1123
1119
1113
1109
1105
1102
1098
1095
1088
1084
1081
1078
1072
1068
1064
1058
1052
1049
1045
1038
1031
1023
1018
1014
1007
1004

Table 4.2 All of the reconstructed El Niño years derived from the process of hand selection, as described in Section 4.3.2.

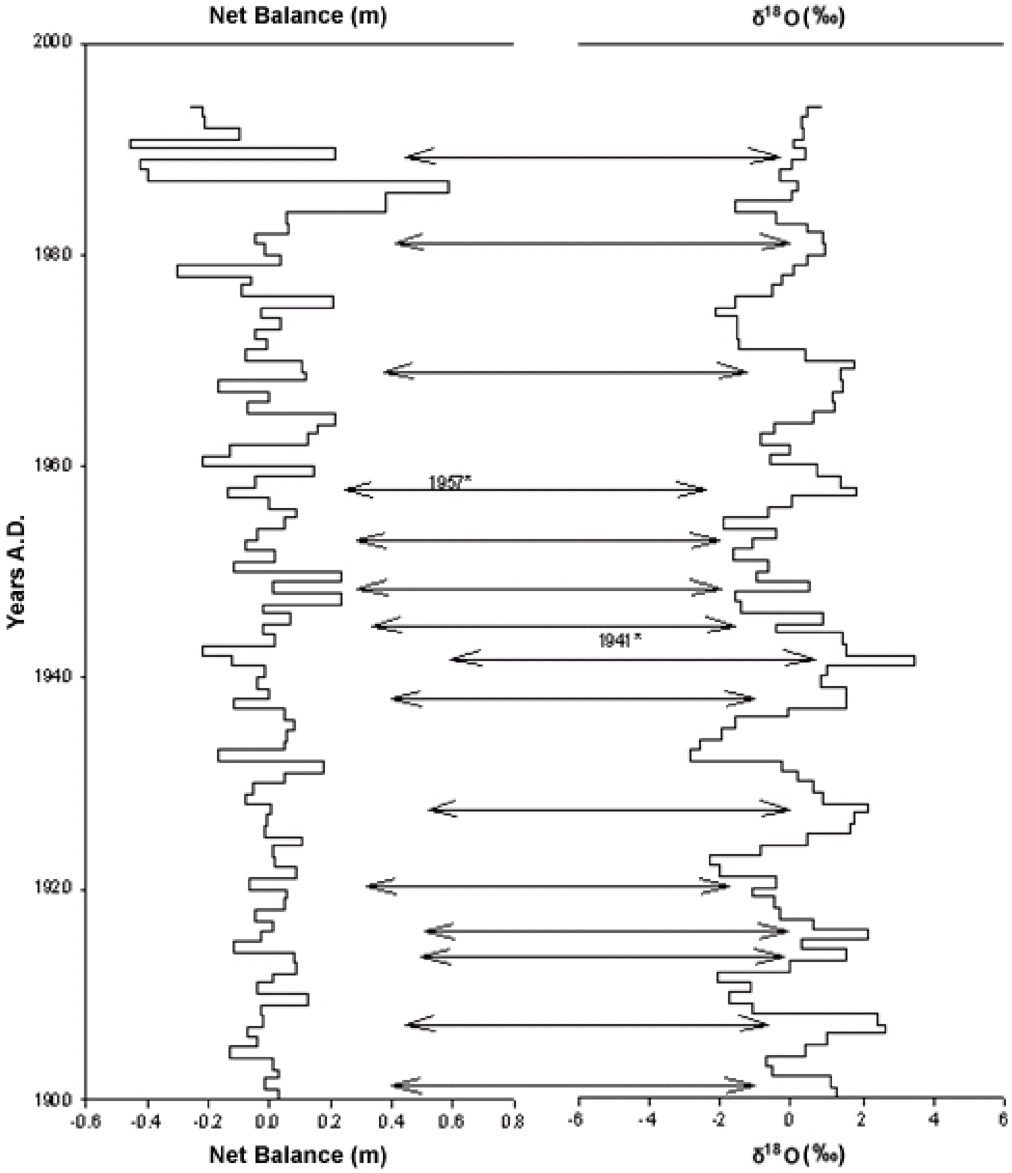

Figure 4.3 Example of hand selection of ENSO events during the last 100 years. Double arrows mark years that were individually selected as El Niño years based on δ^{18}O. Each year in which a strong response is noted in both accumulation and δ^{18}O is labeled and marked with an asterisk.

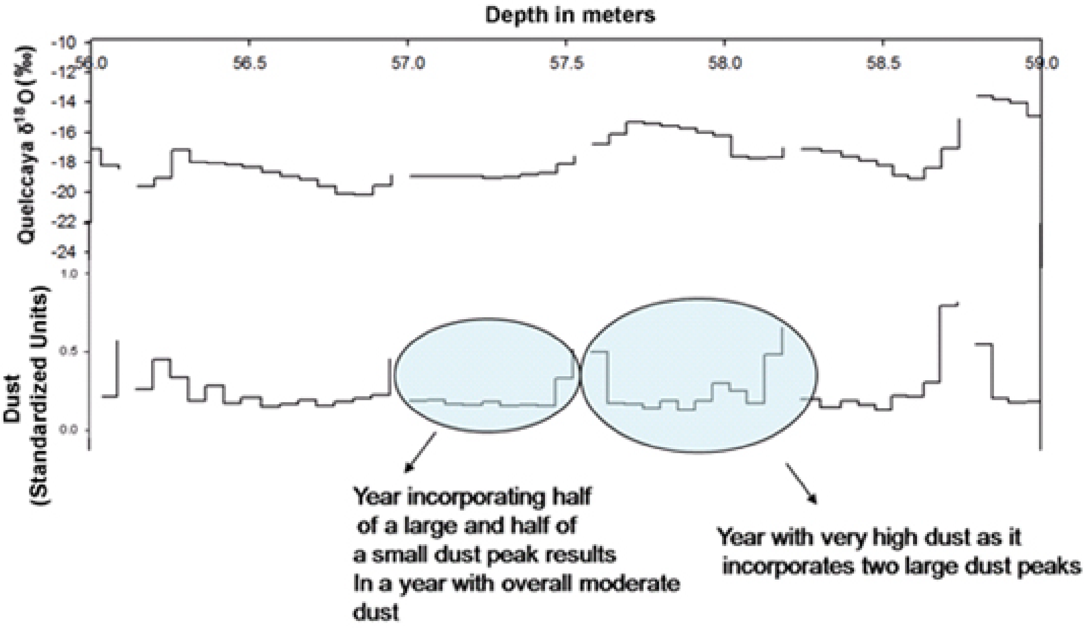

Year incorporating half of a large and half of a small dust peak results In a year with overall moderate dust

Year with very high dust as it incorporates two large dust peaks

Figure 4.4 Shows the effect of splitting annual dust peak on calculated values of dust. Single years may incorporate large dust peaks from two separate dry seasons or large dust peaks from one dry season and a small peak from the other dry season; thus, the results may not relate to climate in any given year, as the signal is from two years.

4.3.3 Discussion: hand counts versus the automated reconstruction

El Niño events were picked out by hand using the methods described in the previous section, and a 50-year centered-sliding window was used to track changes in the frequency of El Niño events through time. A comparison of the 50-year centered-sliding windows generated using the automated method and the hand count method is shown in Figure 4.5. The two time series bear little resemblance, and the Pierson correlation coefficient is 0.05 over the length of the comparison from A.D. 1025 to A.D. 1970. The lack of similarity between the two time series results from the distinctly different counting methods (Fig. 4.6).

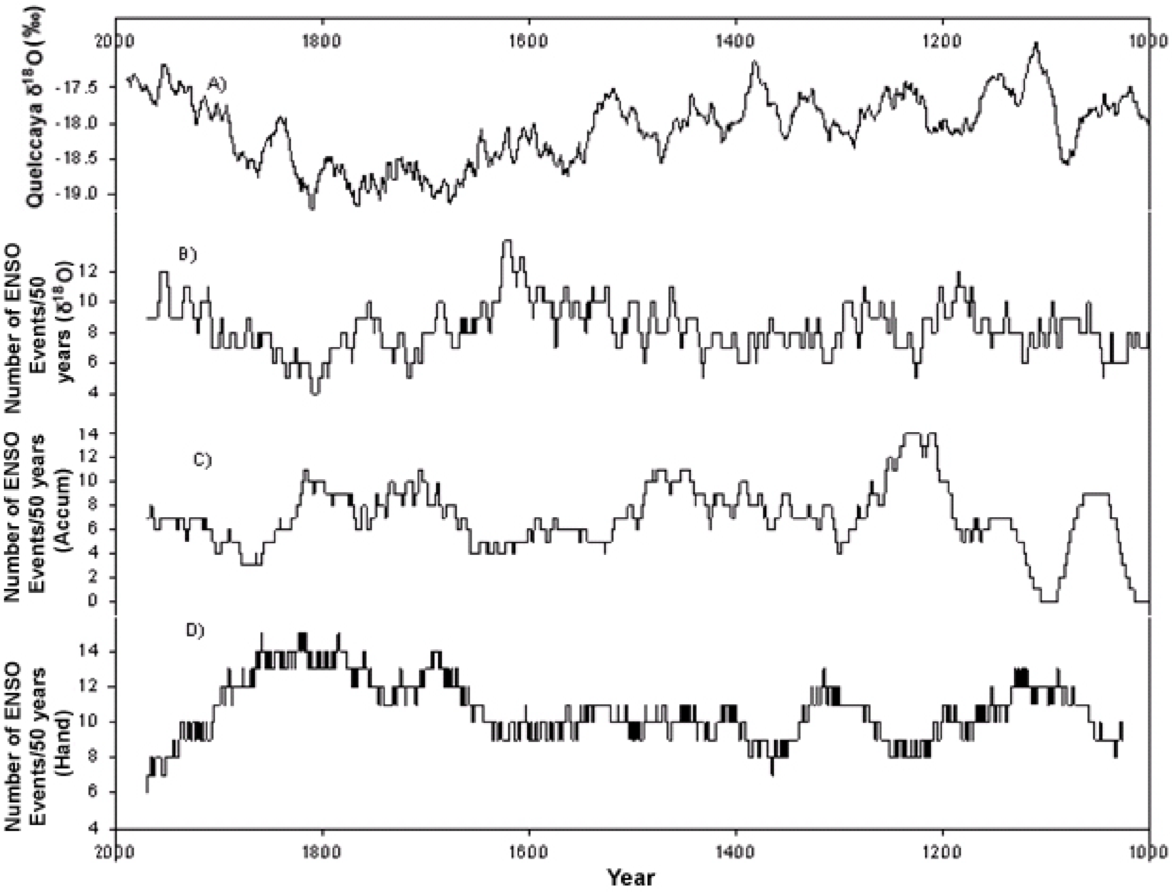

Figure 4.5 Comparison of δ^{18}O time series with the number of events in 50-year interval (recalculated annually) for hand and automated counts. Graph (A) shows the 30-year average δ^{18}O. (B) Shows the 50-year centered sliding window count of El Niño events calculated using the automated process described in section (4.3.1for δ^{18}O. (C) Shows the same as (B) except for accumulation, and (D) shows the number of events generated using the hand count method described in the text.

Figure 4.6 Illustrates differences between automated and hand count systems for selecting El Niño events. Arrows point to events selected with the hand count method, and shaded blocks show groups of years selected using the automated method. The automated method tends to pick groups of years, while the hand count method picks individual years. The hand count method is closer to reality, as El Niño events only last for a year or two at most. The time series of $\delta^{18}O$ is plotted vertically as deviations from mean values during the last 100 years.

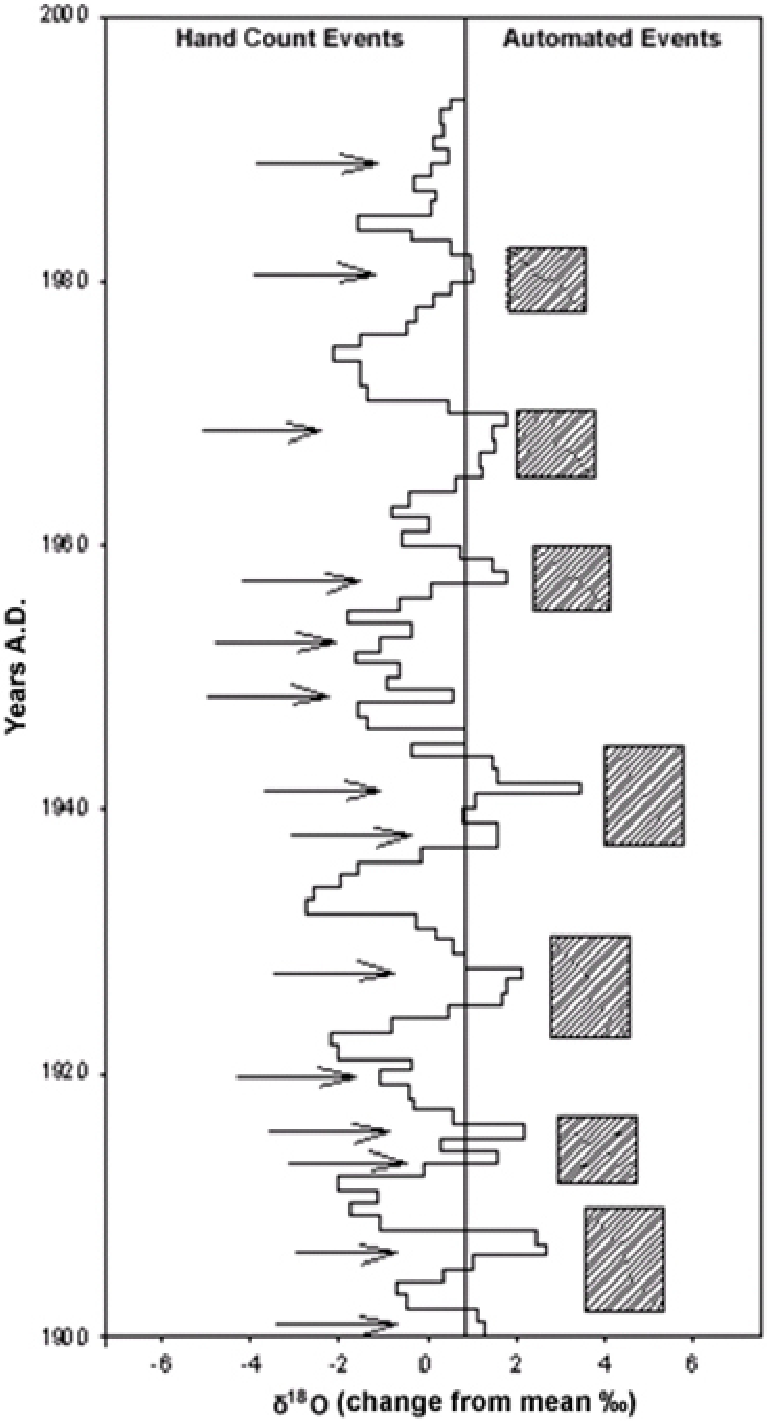
Hand Count Events
Automated Events
2000
1980
1960
1940
1920
1900
Years A.D.
-6
-4
-2
0
2
4
6
δ18O (change from mean ‰)

The primary reason for the discrepancy between the two methods is that during the hand counting process, the focus is on single-year events, where $\delta^{18}O$ values were less negative. In comparison, the automated system identifies events based on a numerical threshold, and as a result it selects groups of years rather than single years (Fig. 4.6). This can be seen during the last 100 years, where the hand-counting system identifies 14 individual El Niño events and the automated counting system identifies only 7. The frequencies of events calculated from both the hand count and automated methods are somewhat different than those of *Quinn* (1987), as seen in Chapter 1, Figure 1.4. The *Quinn* (1987) record shows that a minima in ENSO events occurred in 1600, but in both the hand count and automated methods, a substantial peak in ENSO events is noted just after 1600. This is most likely an artifact of the counting method, as 1600 marks the eruption of Huyanaputina, and the signal in $\delta^{18}O$ is washed out following the eruption.

4.4 A multiple ice core-based ENSO reconstruction

Two approaches are investigated in this section as a means to reconstruct a longer record of ENSO using more than one climate proxy. The first approach, referred to as the ice core-based approach, examines whether a record of ENSO events can be constructed by looking for synchronous shifts in each ice core that reflect the local climatic anomalies produced by ENSO events. The second approach, referred to as the ice core climate approach, only examines the strongest ENSO events, which have been documented by other climatic records. Because these events may be associated with more energetic climatic perturbations, they might be more likely to be recorded in the ice core records. One important difference between the two approaches is that the first approach uses the two ice cores to reconstruct an independent record of ENSO activity, while the second uses the two ice cores to substantiate other climatic records that have identified strong ENSO events during the past 1,000 years.

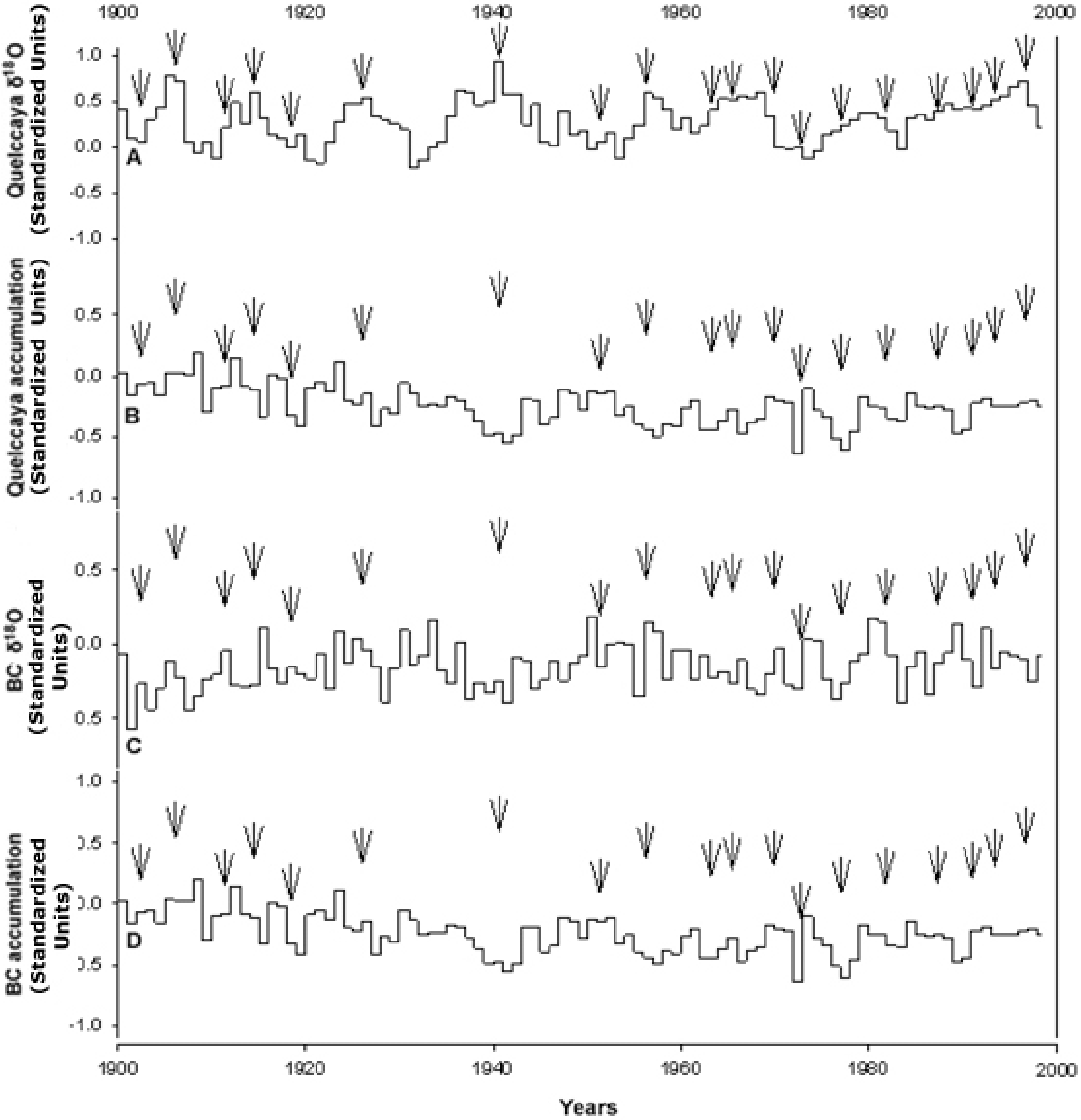

Figure 4.7 El Niño events during the last 100 years and ice core time series from Quelccaya and Bona Churchill. El Niño events are shown at the top of the graph and indicated by arrows. Vertical boxes were placed across all the graphs at the location of each El Niño year. Graph (A) Quelccaya δ^{18}O, (B) Quelccaya accumulation, (C) BC δ^{18}O, and (D) BC accumulation. El Niño events were defined as periods when both NINO 3.4 and the SOI exceeded one standard deviation for more than 6 months in a given year.

4.4.1 An ENSO reconstruction: the ice core-based approach

Assuming that the ice cores from BC and Quelccaya faithfully record ENSO conditions at each site, we would expect to see individual ENSO events recorded in both ice core records. To evaluate this proposal ice core data and historical observations only were examined during the last 100 years rather than the entire 1,000 years for several reasons. First off, the timing of historical ENSO events is well documented so that the effect of individual ENSO events can be accessed in the ice core records. Second, the ice core timelines themselves are well constrained within the last 100 years. It is important to stress that for this type of comparison of ice cores between different regions, a dating error of only one year at any time point within either record could invalidate a substantial part of the entire comparison.

The two ice cores are compared and plotted beside each other along with the historical record of El Niño in Figure 4.7. El Niño events are not associated with any strong response in accumulation, d-excess or $\delta^{18}O$ from BC, but inspection of Figure 4.7 does indicate a strong response between the Quelccaya ice core variables and El Niño events. These visual observations are supported by the low values of the historical correlations between either the annual values of SOI and NINO 3.4 with the ice core variables from BC, as presented in Table 4.3, and the statistically significant correlations between (p less than 0.01) Quelccaya $\delta^{18}O$ and both NIÑO 3.4 and the SOI (Table 4.3). Because El Niño events did not show up well in the records from BC, the analysis was not carried past the last 100 years.

Correlations with ENSO Indices		
	NIÑO 4	SOI
BC d-excess	-.13	.12
BC accumulation	-.1	.06
BC $\delta^{18}O$	-.07	.04
Quelccaya $\delta^{18}O$	-.24	.36

Table 4.3 Correlations between ice core variables and ENSO indices. Correlations between Quelccaya $\delta^{18}O$ and both NINO 4 and SOI are significant at the 95% confidence interval.

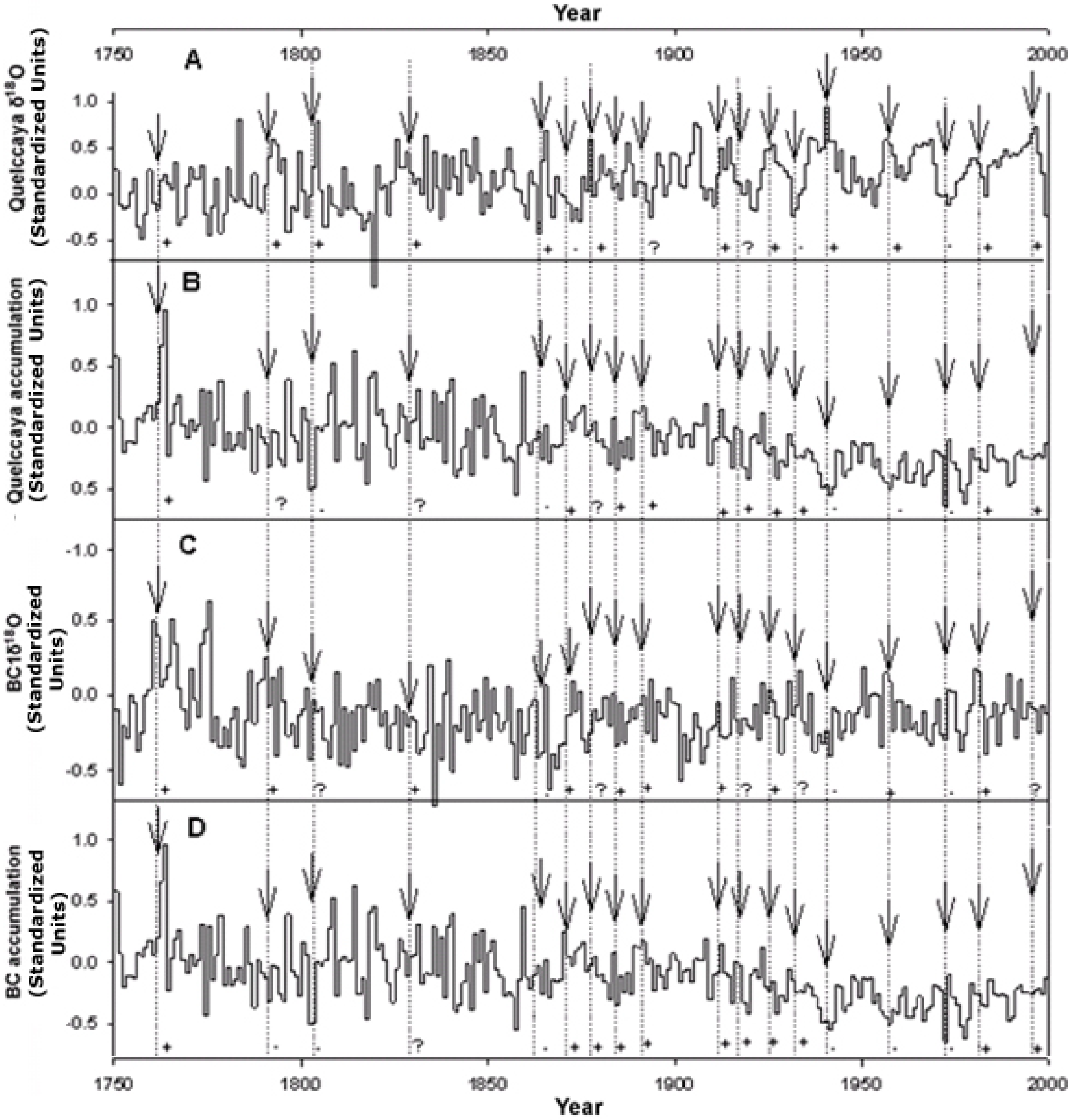

Figure 4.8 Comparison between El Niño events as defined by *Quinn* (1992) and ice core data (A.D. 2000 to 1750). El Niño events are shown at the top of the graph and indicated by arrows. A vertical line was placed across each graph at the location of each El Niño year. Graph (A) Quelccaya $\delta^{18}O$, (B) Quelccaya accumulation, (C) BC $\delta^{18}O$, and (D) BC accumulation. El Niño events were defined as per *Quinn* (1992). All time series are plotted on a scale from -1 to 1 as described in the text.

Year	Strength of Event	Confidence of Event
1607-08	S	5
1614	S	5
1761	S	5
1864	S	5
1911-12	S	5
1917	S	5
1932	S	5
1940-41	S	5
1957-58	S	5
1972-73	S	5
1567-68	S+	5
1624	S+	5
1701	S+	5
1747	S+	5
1803-04	S+	5
1871	S+	5
1884	S+	5
1578	VS	5
1720	VS	5
1728	VS	5
1791	VS	5
1828	VS	5
877-78	VS	5
1891	VS	5
1925-26	VS	5
1982-83	VS	5
1997-98	N/A	N/A

Table 4.4 List of El Niño years as per *Quinn* (1987). This list only includes years defined by *Quinn* (1987) as strong, strong +, or very strong. The strength of the event in 1997-1998 was labeled as N/A, as this was added onto the record of *Quinn* (1987) to bring the record up to date.

4.4.2 An ENSO reconstruction: the ice core-climate approach

Strong ENSO events are associated with more energetic climatic perturbations and are hence more likely to be recorded and clearly documented in the ice core records from both Peru and Alaska. To examine whether this is the case, the strongest known El

Niño events during the last 500 years are compared to the ice core records. Evidence for strong ENSO events that occurred before the time of instrumental records comes from historical records of droughts, storms, shipwrecks, and natural events such as fires, floods, and landslides (Section 1.2). To compile a list of strong events during the last 500 years events from the record of *Quinn* (1987) where the confidence level was defined as a 5 and event strength was defined as either Strong, Strong+, or Very Strong were selected. The 1997 to 1998 event was added to the list from *Quinn* (1987) because it ends with the 1983 El Niño (the entire list is reproduced in Table 4.4).

	Positive Anomaly	Negative Anomaly	Unsure
Quelccaya $\delta^{18}O$	16	6	4
BC d-excess	13	7	6
BC $\delta^{18}O$	13	5	8
BC accumulation	14	7	5

Table 4.5 Ice core response to El Niño years as defined by *Quinn* (1987).

A comparison of the ice core variables from Quelccaya and BC with the strongest ENSO events (Table 4.5) shows that the strongest results occur in the case of Quelccaya $\delta^{18}O$, where out of 26 strong El Niño events, 16 match with positive anomalies in $\delta^{18}O$, 6 match negative anomalies, and in 4 cases the response is unclear (Table 4.5, Fig. 4.8 and 4.9). The sum of undefined and negative matches is approximately equal to the number of positive event matches for BC $\delta^{18}O$ and BC accumulation (Table 4.5). In the case of BC d-excess, 13 positive d-excess anomalies match with El Niño events and 7 negative anomalies match with El Niño events. This is not expected, because the historical relationship between the AL and d-excess suggests that more negative values of d-excess occur alongside El Niño events.

To test whether the combined records of Quelccaya $\delta^{18}O$ and BC $\delta^{18}O$ could be used to reconstruct a long record of strong ENSO events the simultaneous response of both records to strong El Niño events during the last 500 years was examined, and out of the 26 strong El Niño events, only 5 match with positive anomalies in both Quelccaya $\delta^{18}O$ and BC $\delta^{18}O$ (Fig. 4.8 and 4.9).

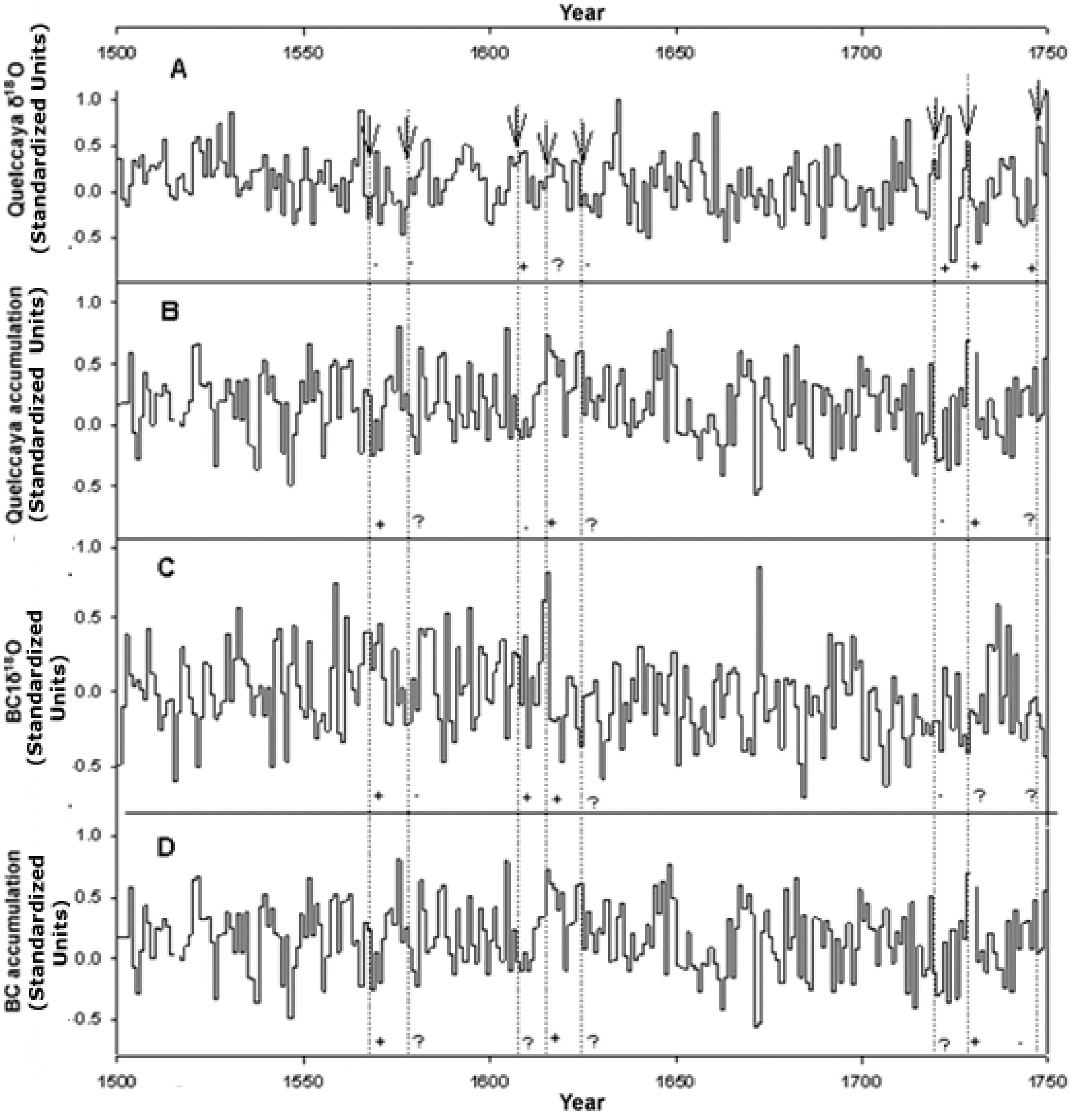

Figure 4.9 Comparison between El Niño events as defined by *Quinn* (1992) and ice core data (A.D. 1500 to 1750). El Niño events are shown at the top of the graph and indicated by arrows. A vertical line was placed across each graph at the location of each El Niño year. Graph (A) Quelccaya $\delta^{18}O$, (B) Quelccaya accumulation, (C) BC $\delta^{18}O$, and (D) BC accumulation. El Niño events were defined as per *Quinn* (1992). All time series are plotted on a scale from -1 to 1 as described in the text.

The results of the comparison between Quelccaya $\delta^{18}O$ and the record of *Quinn* (1987) show that ENSO signal in the Quelccaya $\delta^{18}O$ record is strong enough that the record can serve as a means to cross-verify the events identified in the record of *Quinn* (1987) or other ENSO reconstructions, such as those based on tree rings from the southwestern United States.

Although Quelccaya is a good recorder of ENSO events, no single record should be used to reconstruct a global climate signal, such as ENSO, because that record will incorporate local climate variability that might not be related to the signal.

One limitation of the use of Quelccaya $\delta^{18}O$ for reconstructions of ENSO is the decadal nature of the signal (section 3.6.1) versus that of ENSO, which primarily exhibits interannual variability. This limitation is evident in Figure 4.6, which depicts the occurrence of known ENSO events during the last 100 years alongside the time series of $\delta^{18}O$ from Quelccaya. At first glance it would appear that the record from Quelccaya has a strong response to ENSO, and although this is certainly the case, the prominence of decadal variability rather than interannual variability is also evident. For instance, examine the El Niño events that occurred in 1982 to 1983 and in 1987. Although both correspond with a positive anomaly in the Quelccaya $\delta^{18}O$ record, they both are represented by the same broad positive anomaly. Another earlier example of this is the back-to-back El Niño events occurring in 1911 and 1914 that are both represented by the same multi-year positive anomaly in Quelccaya $\delta^{18}O$. It appears that when El Niño events are closely spaced in time, they are often represented as one broad positive anomaly rather than two distinct positive anomalies in the Quelccaya $\delta^{18}O$ record. In instances where one strong isolated El Niño event is separated by a number of years from another event, the record of Quelccaya does an excellent job of capturing the event.

4.4.3 Creating an ice core-tree ring index composite ENSO index

A simple ENSO Ice Core-Tree Ring (ICTR) Index is calculated and plotted so that one can easily see those occurrences when multiple records all indicate the occurrence of ENSO-like conditions (Fig. 4.10). The index was calculated by summing the standardized values of BC δ^{18}O and d-excess, Quelccaya δ^{18}O and accumulation, and the PDSI reconstruction from the SW and PNW.

To evaluate the potential use of this index, it was compared with the list of El Niño events from Table 4.4. This comparison shows that out of 26 strong El Niño events, 11 match with maxima in the index, 8 match with minima in the index, and for 7 events, no distinct signal is noted in the index. These results are not encouraging, because just assuming a 50% chance of a given year being either negative or positive in the ENSO index, one might expect at least 13 matches between the positive index values and strong El Niño events. The use of this index will not be pursued further, given the poor match with historical events.

4.5 Conclusions

The Quelccaya record offers a great deal of promise for future reconstructions of ENSO variability but needs to be paired with other proxy records that exhibit a strong ENSO signal, such as the record of *Quinn* (1987) or the tree ring records from the SW (Chapter 4, section 4.2.1) as a means for cross verification. One goal of this thesis was initially to construct a longer record of ENSO events using the ice core records from BC and Quelccaya. However, my investigations have shown that the value of the BC record as a proxy of ENSO is limited and especially so in the type of comparison that would be required to construct a long-term history of ENSO events. The records of BC δ^{18}O do not exhibit a strong enough response to either ENSO events; although individual ENSO events may certainly impact the record at BC, not all ENSO events leave a signature, and the variability of the signature limits its usefulness.

Quelccaya exhibits a strong ENSO signal, but the dominance of the decadal signal in the Quelccaya δ^{18}O record complicates reconstructing individual ENSO events, especially when those events are closely spaced in time (Fig. 4.6). The record of Quelccaya δ^{18}O is most strongly correlated with temperatures in the region just north of NIÑO 4 that I have defined as AREA II. The time series of NIÑO 4 temperatures like that of Quelccaya is dominated by a decadal rather than an interannual signal. Although a great deal of discussion has focused on the different modes of decadal climate variability, such as the PDO, PDV, and IPO, the climatic signature associated with decadal variability in the NIÑO 4 is not well documented and should be the subject of

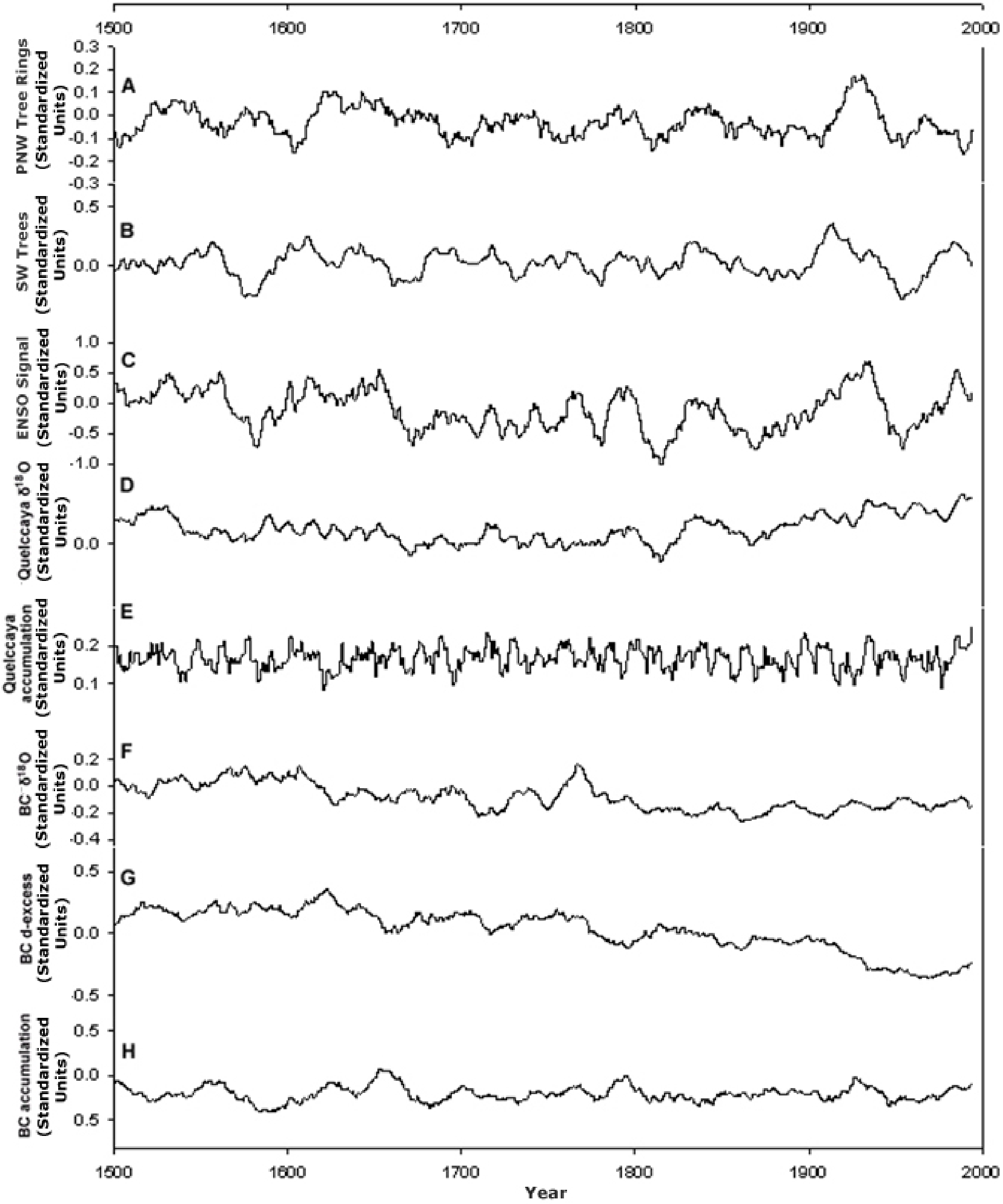

Figure 4.10 Comparison of multirecord ENSO index (see text) and other selected time series. (A) PNW tree rings inverted, (B) SW Tree Rings, (C) ENSO Signal (a,b,d,e,f,g), (D) Quelccaya $\delta^{18}O$, (E) Quelccaya accumulation inverted, (F) BC $\delta^{18}O$, (G) BC d-excess, and (H) BC accumulation. All time series are plotted on a scale from -1 to 1 as described in the text.

further investigation. It is interesting to note that the variability seen in the NIÑO 4 region is similar to that exhibited by the PDO, but it is also distinctly different. In general, both the PDO and IPO seem to contain a signal of longer-scale variability that is disconnected from the Quelccaya δ^{18}O record and that of NINO 4 (Fig. 4.11).

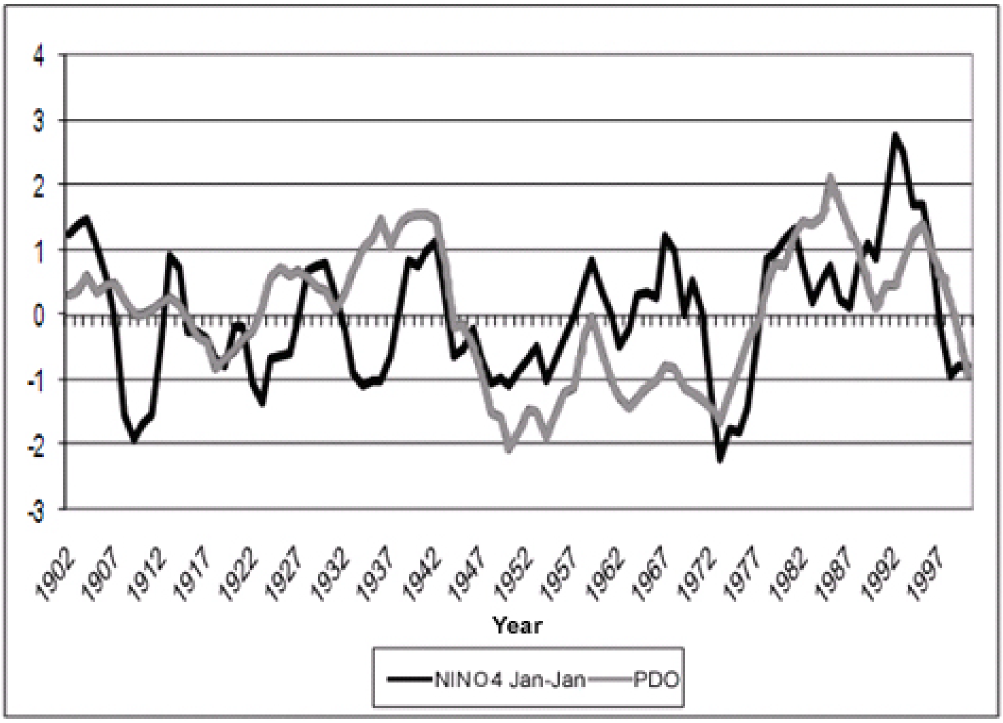

Figure 4.11 Comparison of the time series of the 5-year averages (z-scores) of the PDO and NINO 4 during the last 100 years. Note the dominant decadal variability in NINO 4 SST and the longer-term variability in the PDO. Although both time series share decadal fluctuations, the PDO tends to persist as either negative or positive, and the decadal variability is simply superimposed on this longer-term variability. The longer-term variability exhibited by the PDO is absent from the NINO 4 time series.

CHAPTER 5

ICE CORES, TREE RINGS, AND CORALS

5.1 Introduction

This chapter examines and compares the response in the Quelccaya and Bona Churchill (BC) ice core records to tree ring records in the Southwest (SW) and Pacific Northwest (PNW). Additionally, the record of Quelccaya $\delta^{18}O$ is compared to records of corals from the Pacific to evaluate the past coherency between these signals. The chapter consists of a literary review of climatic conditions as recorded by corals in the Tropical Pacific and tree rings in the PNW and the SW during the last 1,000 years. Summaries of the most important climate events are developed and compared to the ice core data. The PNW and SW were selected due to the availability of high-quality annually dated records and because a strong ENSO teleconnection is present in both regions. Of particular interest are the large-scale "mega-droughts" that occurred primarily during the Medieval Warm Period (MWP) in the southwestern United States. Although the droughts in the MWP were of longer duration than modern droughts, the similar spatial patterns of both, along with evidence from historical and coral-based reconstruction of equatorial Pacific Sea Surface Temperatures (SSTs), have prompted speculation that these paleo-droughts were associated with the persistence of La Niña conditions in the Pacific.

5.2 Comparison of records from BC and Quelccaya

If the primary factors forcing climatic conditions along the west coast of the Americas are the large-scale changes in the size and location of the Pacific Warm Pool (PWP), one might expect to see synchronous changes in climate that are recorded by the Quelccaya and BC ice cores. On the other hand, if local factors or other teleconnections are more important than conditions in the PWP, one might expect that these would dominate the ice core records and that similar features in the ice core records driven by changes in the PWP would only occur whenever local factors or other external teleconnections were not the overriding control.

A first-order comparison of the time series of $\delta^{18}O$ from Quelccaya and BC (Fig. 5.1) shows a lack of correspondence between the large-scale trends in the two records, a poor fit between individual events, and a plot of a 50-year sliding correlation window between $\delta^{18}O$ from Quelccaya and BC calculated using 20-year averages. This demonstrates that the ice core records of $\delta^{18}O$ are never well correlated for any significant length of time (Fig. 5.1C). The most recent 200 years is a good example of this, as the record of $\delta^{18}O$ from BC would indicate that the Aleutian Low (AL) has been weaker since 1800. This is coincident with a period when the Quelccaya $\delta^{18}O$ record would suggest more El Niño-like conditions in the Pacific. In this particular case, the two records seem to be recording different signals, as one would expect more El Niño-like conditions to be related to a stronger rather than weaker AL.

A comparison of BC d-excess with Quelccaya $\delta^{18}O$ (Fig. 5.2) shows that increasing average values of Quelccaya $\delta^{18}O$ since 1800 have been accompanied by decreasing values of d-excess. Both of these indicators suggest that conditions are becoming more El Niño-like. However, a visual examination and comparison of the timing of minima and maxima in both records indicates little similarity in the timing of events between the two records (Fig. 5.2). Before A.D. 1600, both records are broadly similar in that they are without trend, but between A.D. 1600 and 1800, the records are different. This is because Quelccaya $\delta^{18}O$ decreases and reaches a minima before 1800, whereas the d-excess record begins a gradual decrease around A.D. 1600 that only accelerates after A.D. 1800. (In other words, no Little Ice Age [LIA] minima is observed around A.D. 1800 in the record of d-excess.)

To examine whether the largest perturbations in the records of $\delta^{18}O$ and d-excess from BC (Fig. 5.1 and 5.2) share any similarities with the record of $\delta^{18}O$ from Quelccaya, an event analysis based on a 30-year average of each variable was performed and is displayed in Tables 5.1 and 5.2. Table 5.1 shows that in total, 3 of 19 minima (more negative) and 5 of 23 maxima (more positive) could be identified in the BC $\delta^{18}O$ record

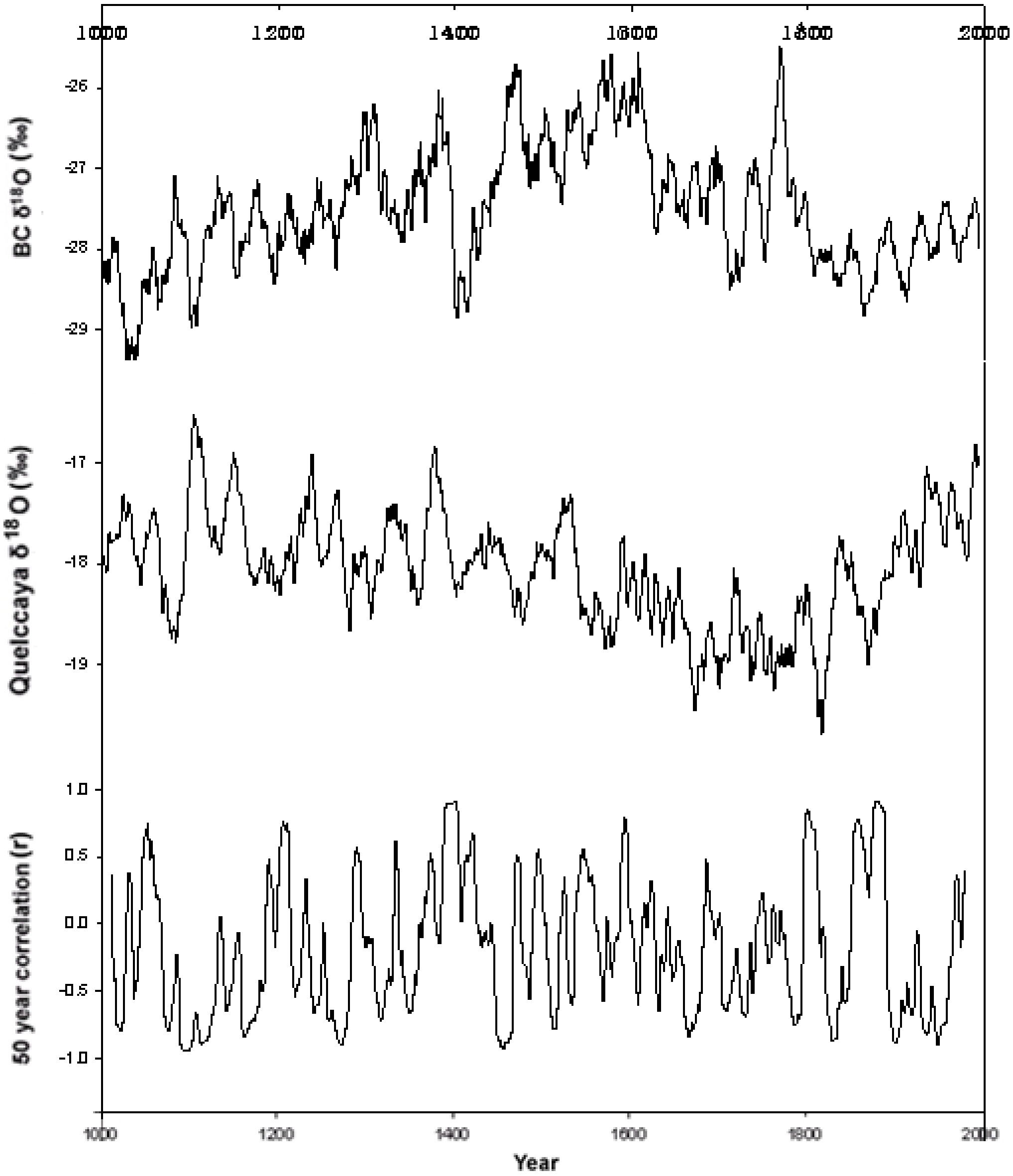

Figure 5.1 Comparison of (A) BC δ^{18} and Quelccaya $\delta^{18}O$ (B) calculated from 20-year averages from A.D. 1000 to 2000. (C) Shows a 50-year sliding correlation window, which was recalculated annually.

and matched with minima/maxima events in the Quelccaya $\delta^{18}O$ record. An event was defined as matching when events in either record occurred within 5 years of each other. Of the five positive excursions from BC $\delta^{18}O$ that were found to coincide with events in Quelccaya $\delta^{18}O$, four events (1081, 1468, 1671, 1769) overlapped with negative excursions in Quelccaya $\delta^{18}O$, and one event (1382) overlapped with positive excursions in the Quelccaya $\delta^{18}O$ record. Given the relationship between ENSO and BC $\delta^{18}O$ (Table 5.1), one might expect more positive (negative) values of BC $\delta^{18}O$ to be associated with more positive (negative) excursions in the Quelccaya $\delta^{18}O$ and not the other way around, as is observed. Of the three negative excursions from the BC $\delta^{18}O$, it is noted that two events (1150 and 1517) coincide with positive events in Quelccaya $\delta^{18}O$ and that the other event (1867) coincides with a negative excursion in Quelccaya $\delta^{18}O$. In total, a statistically insignificant number of events, eight out of 49 (19%), from BC $\delta^{18}O$ overlap with events in the Quelccaya record. In addition, the signature of events that do overlap is inconsistent with the physical processes that would account for the overlap in the first place.

A comparison of the timing of both high and low d-excess events in the BC $\delta^{18}O$ record with high and low Quelccaya $\delta^{18}O$ events is presented in Table 5.2 and was conducted in a similar manner as that just mentioned for BC $\delta^{18}O$. Four of 17 high d-excess events match with events in the Quelccaya $\delta^{18}O$ record, and three of 14 low d-excess events match with events in the Quelccaya $\delta^{18}O$. Because more positive Quelccaya $\delta^{18}O$ and lower values of d-excess are both associated with El Niño conditions, we might expect that low (high) d-excess would correspond with more positive (negative) Quelccaya $\delta^{18}O$, but this is not the case, and in fact the majority of d-excess events, regardless of sign, correspond with negative anomalies in Quelccaya $\delta^{18}O$.

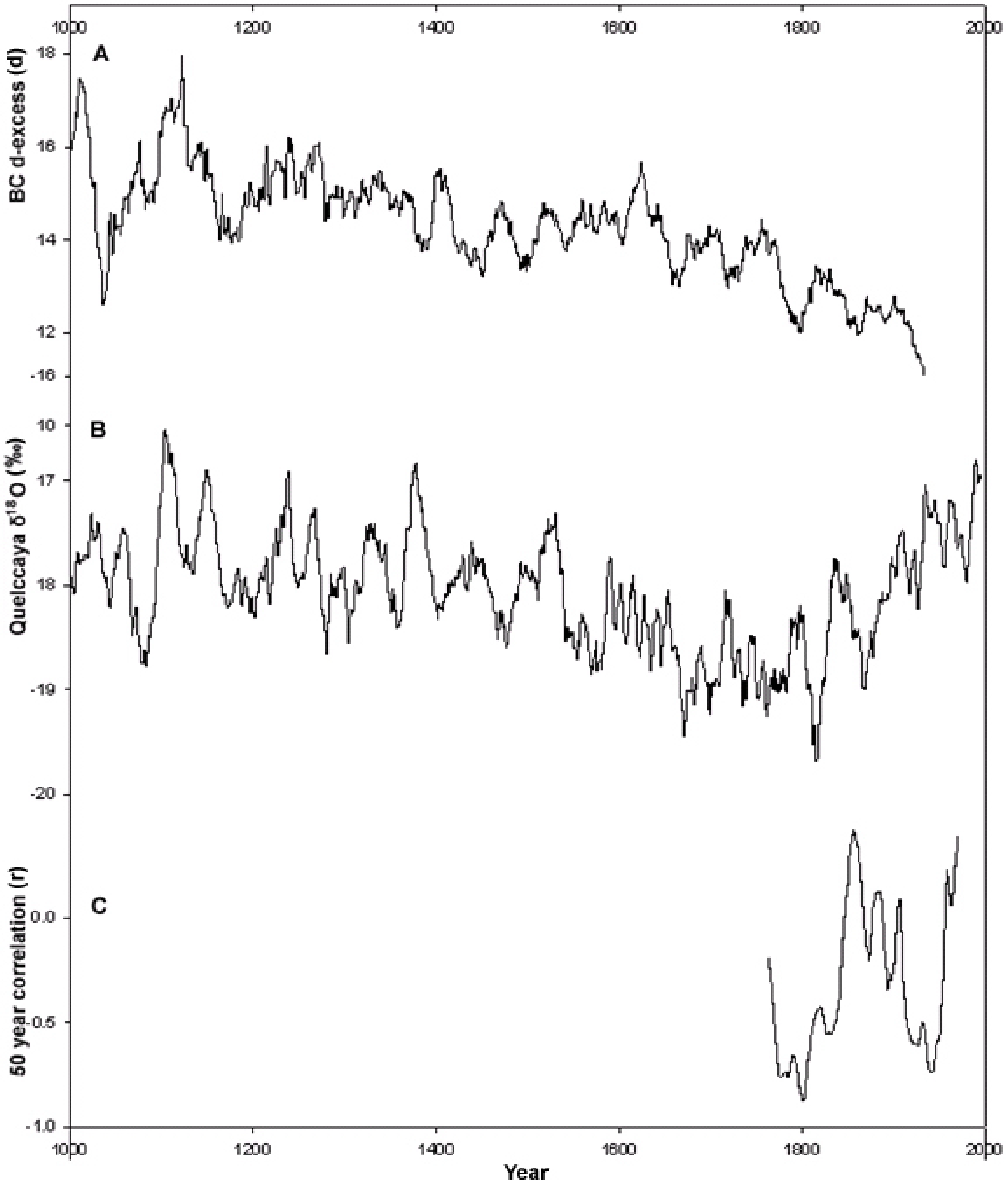

Figure 5.2 Comparison of (A) d-excess and Quelccaya δ^{18}O (B) calculated from 20-year averages from A.D. 1000 to 2000. (C) Shows a 50-year sliding correlation window that was recalculated annually.

BC δ^{18}O (Negative)	BC δ^{18}O (Positive)	Quelccaya δ^{18}O (Positive)	Quelccaya δ^{18}O (Negative)
	1009		
		1019	
1035			
	1081		1080
1104			
		1110	
	1130		
1150-		1145	
	1176		
			1190
1196			
	1209		
1225			
		1234	
	1245		
1265			
			1284
	1304		
		1326	
1340			
			1350
	1382	1380	
1395			
			1413
		1441	
	1468		1470
1484			
	1500		
1517		1516	
	1536		
1550			
	1572		1563
1582			
	1605		
1625			
	1641		
	1671		1675
	1694		
1717			
		1727	
	1733		
1749			
	1769		1765
		1792	
			1811
		1835	
	1847		
1867			1863
	1890		
1912			
	1925		
1939			
	1952	1953	
1972			
	1988		
Matches: 3	Matches: 5	Matches: 3	Matches: 5
Total Events: 19	Total Events: 23	Total Events: 12	Total Events: 11
% Matching: 16%	% Matching: 22%	% Matching: 25%	% Matching: 45%

Table 5.1 Number of δ^{18}O events from BC matching minima and maxima in the record of Quelccaya δ^{18}O.

BC d-excess (low)	BC d-excess (high)	Quelccaya δ^{18}O (H)	Quelccaya δ^{18}O (L)
	1016	1019	
1039			
	1078		1080
1091			
		1110	
	1124		
		1145	
1185			1190
		1234	
	1242		
	1272		
1283			1284
		1326	
	1343		
			1350
		1380	
1389			
	1411		1413
1451			
			1470
	1481		
1502			
		1516	
	1528		
1542			1563
	1593		
1606			
	1626		
1666			
		1675	
	1711		
1719			
		1727	
	1760		1765
		1792	
1798			
			1811
	1825		
		1835	
1865			1863
	1878		
	1910		
		1953	
	1995		
Matches: 3	Matches: 4	Matches: 1	Matches: 6
Total Events: 14	Total Events: 17	Total Events: 12	Total Events: 11
% Matching: 21%	% Matching: 23%	% Matching: 8%	% Matching: 55%

Table 5.2 Number of d-excess events from BC matching minima and maxima in the record of Quelccaya δ^{18}O.

The reasons for the lack of large-scale correspondence and the poor fit between individual events in the records from BC and Quelccaya may be almost as revealing as if a good match between these records existed. Several possible reasons are considered and outlined as follows:

1. The record of BC $\delta^{18}O$ is not just a record of AL variability, as the Arctic Oscillation (AO) appears to modulate the signal of the AL in the record of BC (Section 2.2.3). The strongest signal in BC $\delta^{18}O$ reflects periods of northerly flow that occur when the AO is negative and AL weak, versus periods of southerly flow that are generally prevalent under most other circumstances (Section 2.6.5).
2. The record of BC $\delta^{18}O$ may be more reflective of the position of the AL than of its strength (Section 2.6.5). It has been noted that ENSO events play a larger role in the strength of the AL than its position.
3. The signal from Quelccaya is primarily a signal representing the decadal component of NIÑO 4 variability and only records Pacific Decadal Oscillation/Inter-decadal Pacific Oscillation (PDO/IPO) variability, as these variables are able to capture NIÑO 4 variability. (The PDO is a measure of NP variability that we would expect to relate more to the record from BC.) This is particularly evident from 1962 onward, as Quelccaya $\delta^{18}O$ remains strongly related to NIÑO 4, but the relationship with the PDO goes out of phase.

The record of $\delta^{18}O$ from Quelccaya is most strongly related to SST in the region bounded by 180°-150°W and 5°-20°N and labeled as AREA II in Figure 3.3. In comparison, PDO variability refers to SST variability that originates in the North Pacific and is calculated using SST data from north of 20° latitude. The PDO and NIÑO 4 share similar decadal variability, but the regime shifts in the PDO time series are not as evident in the NIÑO 4 time series or the record of Quelccaya $\delta^{18}O$. Furthermore, the decadal shifts seen in NIÑO 4 and the record of Quelccaya $\delta^{18}O$ are not as prominent in the PDO time series (see Chapter 4, Fig. 4.11). It is important to remember that the Quelccaya ice core best records the decadal variability in the NIÑO 4 region and not the even lower 10- to 30-year variability observed in either the IPO or PDO. The correlation field produced by Quelccaya is also very similar to 4th rotated NON-ENSO EOF produced by *Mestas-Nunex and Enfield* (1999). *Mestas-Nunex and Enfield* (1999) speculate that signature of this field is related to variability of the subtropical front. Subtropical front variability in itself could be related to PDO variability, as described by *Nakamura* (1997), who suggests that PDO variability is the combined variability exhibited by both the subtropical and subpolar fronts (Section 1.4.3).

Changes in the strength of the signal from the Pacific through time (IPO variability) could help to explain the lack of large scale of correspondence between decadal and centennial scale trends in the records of BC and Quelccaya. A number of previous studies have compared tree ring records from North America with coral records from the tropical Pacific and most, but not all, of the studies agree that the 19th century was in general marked by absence of low-amplitude Pacific Decedal Variability (PDV) and that this variability is more coherent during the 20th century. In light of these results, one might expect that the strongest relationship between ENSO-sensitive indices related to both Quelccaya and BC would occur during the 20th century. However, a detailed examination of ice core records and PDO variability during the 20th century (Fig. 5.3) shows that the general lack of relationship between the ice core records also persists during the 20th century, despite the phase of the PDO.

5.3 Relationships between Quelccaya δ^{18}O and Pacific coral records

An examination of the correlation field comparing Quelccaya δ^{18}O and Pacific SSTs (Fig. 3.3) shows that the strongest correlations with SST occur in the northern equatorial Pacific between 150°W to 160°E. Several studies of coral δ^{18}O have been conducted within this same region in order to reconstruct SSTs during the last several hundred years. This section directly compares the δ^{18}O record from Quelccaya to the data sets that were collected by both *Asami* (2005) and *Cobb* (2001).

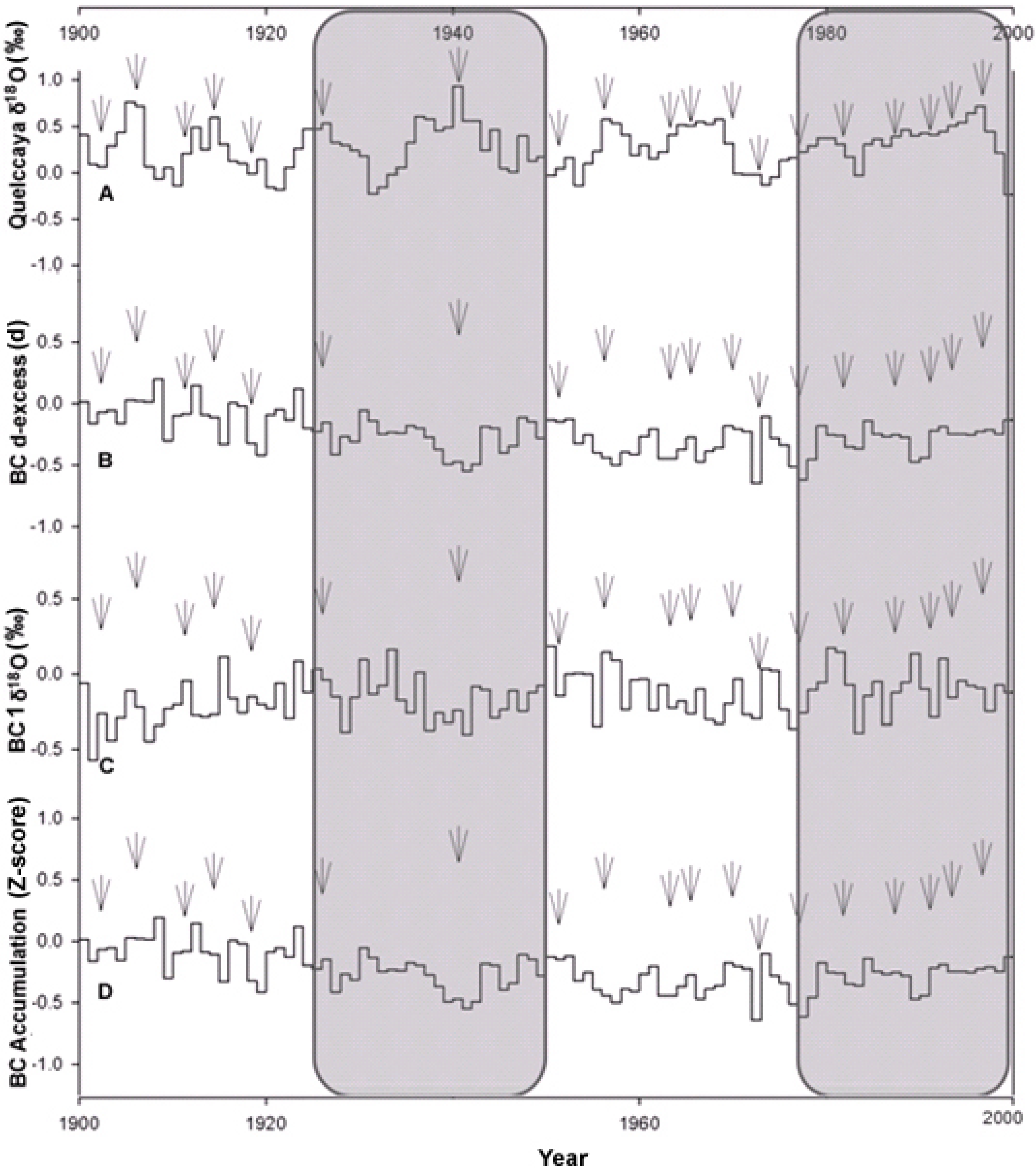

Figure 5.3 Ice core variables, PDO, and ENSO events during the last 100 years. Positive PDO regimes are shaded, and El Niño events are indicated by arrows in each time series. (A) Shows Quelccaya $\delta^{18}O$, (B) BC d-excess, (C) BC $\delta^{18}O$, and (D) BC Accumulation. All of the time series are plotted as standardized values between -1 and 1 as described in the text. ENSO events are defined as periods when both the SOI and NINO 3.4 exceed more than 1 std, for more than 6 months in a year.

A study by *Asami* (2005) of corals from Guam (13º N, 145º E) has been used to reconstruct SST in the equatorial Pacific from 1787 to 2000. *Asami* (2005) was able to identify 46 El Niño phases and 53 La Niña phases during this period. The signal from cool events is somewhat subdued, as changes in the salinity of the ocean water cancel out the signal from temperature. Figure 5.4 examines the occurrence of both cold and warm events as recorded by the Quelccaya core, with the record of warm and cold events before 1870 from the coral record produced by *Asami* (2005). No significant response in values of Quelccaya δ^{18}O is observed when compared with the ENSO events defined by the *Asami* (2005) coral record. The exception to this is the cool event in 1865 and the following warm event in 1866-1867 that is evident in both records. Despite the lack of specific correspondence between these two records, one finds that the general trends exhibited by both are remarkably similar. For instance, the coldest Sea Surface Temperatures (SSTs) recorded by the Guam corals and Quelccaya occur in the 1820s, and a significant step change is observed in both records in the 1880s, marking the end of the Little Ice Age (LIA). Both records indicate a gradual warming in the western and/or central equatorial Pacific over the past two centuries.

Cobb (2001) has retrieved and published the records of several corals from Palmyra Island (162ºW, 6ºN). These coral records are of particular interest, as they come from the region of the Pacific where Quelccaya δ^{18}O is most strongly related to SST, and one might expect a strong correlation with Quelccaya record. In order to compare the coral and Quelccaya δ^{18}O records, several modifications to *Cobb's* (2001) coral data sets were obtained from the NOAA paleoclimatology data center (www.ncdc.noaa.gov/paleo/data.html). First, because the values provided for the modern and fossil coral time series are calculated at monthly intervals, an average annual value was calculated. Second, a 5-year centered average was calculated for each time series. Finally, the coral time series were multiplied by -1 so that the isotopic response to changes in SST would be of similar sign as those generated by Quelccaya δ^{18}O.

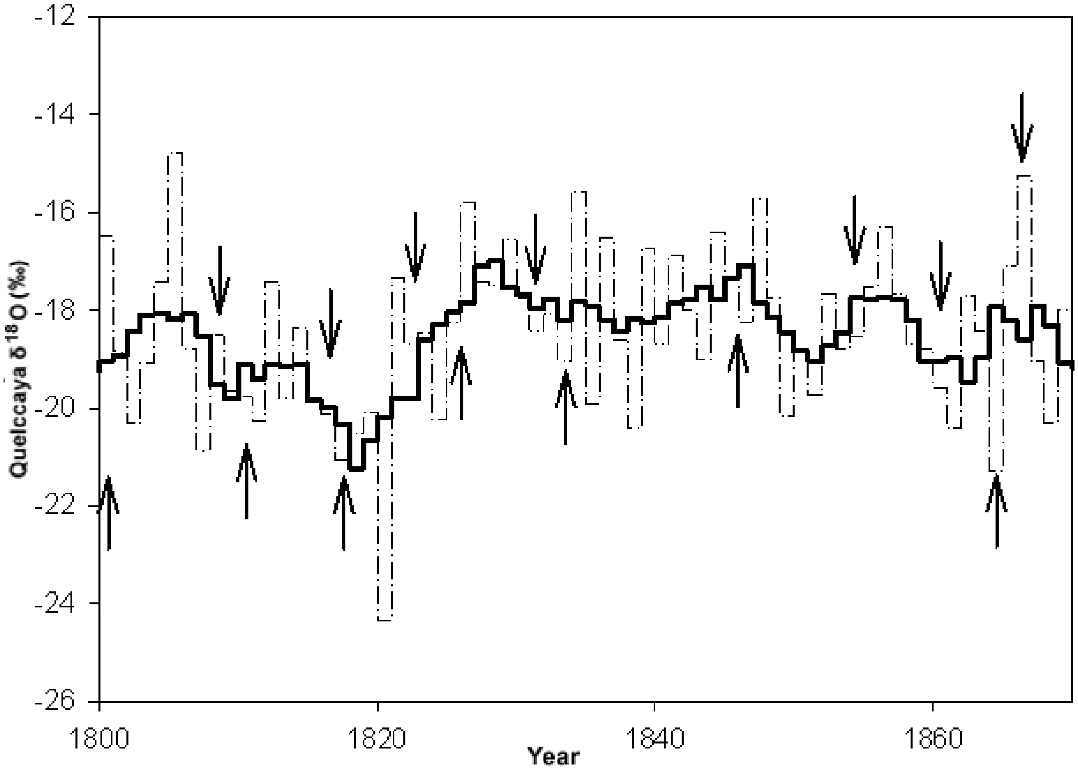

Figure 5.4 Comparison between Quelccaya $\delta^{18}O$ and coral record from Guam by *Asami* (2005). Dashed line represents annual values $\delta^{18}O$, and the dark line is the 5-year average. Up-pointing arrows are cool events as reconstructed by corals from Guam before 1870, and down-pointing arrows are warm events as reconstructed by corals from Guam before 1870 (*Asami*, 2005).

The record of Quelccaya $\delta^{18}O$ was compared to three fossil coral time series that were collected and labeled by *Cobb* (2001) as SB 17 (A.D. 1152-1217), Spl 14 (1320-1462), and Spl 17 (A.D. 1637-1700), along with the record from the living coral (1899-1995). The time series of modern coral $\delta^{18}O$ is strongly correlated with Quelccaya $\delta^{18}O$ ($r=.62$ and $p<0.001$, 1889-1995). Comparisons of the coral time series with the time series of Quelccaya $\delta^{18}O$ are presented in Figures 5.5 to 5.8. Correlations between the fossil coral data sets and Quelccaya $\delta^{18}O$ are not as strong as those observed with the modern coral record. To see if this was a simple dating issue, the data were further compared by generating leads and lags between the data sets and then calculating correlation coefficients, but in general the correlations lacked statistical significance and will not be presented here. It is interesting, however, that visual comparisons of these time series reveal the possibility of offsets and of some type of relationship, but a longer and more continuous coral record will need to be examined before a relationship can be either identified or ruled out.

Coral-based reconstructions of temperature from Palmyra Island (162º W, 6º N) indicate that cooler and dryer conditions prevailed in the central equatorial Pacific between A.D. 1150 and 1220 (*Cobb*, 2001). Reconstructions of ENSO event frequency based on the same fossil coral indicate that ENSO events occurred with a similar frequency to the 20th century but with less frequency than that indicated by a LIA coral (A.D. 1635 to 1700) from the same location. The results from the coral records are inconsistent with predictions of NIÑO 4 SST based on Quelccaya $\delta^{18}O$. As previously shown, $\delta^{18}O$ is positively correlated with NIÑO 4; thus, one would predict from the $\delta^{18}O$ that warmer SST existed in the tropical Pacific during the MWP. One problem with this record is that it is based on only one fossil coral, and the results have yet to be replicated.

A reconstruction by *Urban* (2000) of SSTs from a coral in the Maiana Atoll (1° N, 173° E) from A.D. 1840 to 1955 shows several significant trends that match those observed in the Quelccaya $\delta^{18}O$ record. For instance, both records indicate that during the period of reconstruction, tropical SSTs have become warmer. The trend in the coral record of *Urban* (2000) is the result of two step-like increases, one of which occurred in the mid-1970s and another in the early 20th century. In comparison, the main step-like increase in the Quelccaya record occurs at the end of LIA (A.D. 1882). However, the variability in the record of coral $\delta^{18}O$ records shows that a shift in the frequency of SST variability from primarily decadal to interannual occurred about 1880. *Urban* (2000) suggests that decadal ENSO variability is stronger when background conditions are cooler and drier, and that interannual variability is generally weaker during these conditions.

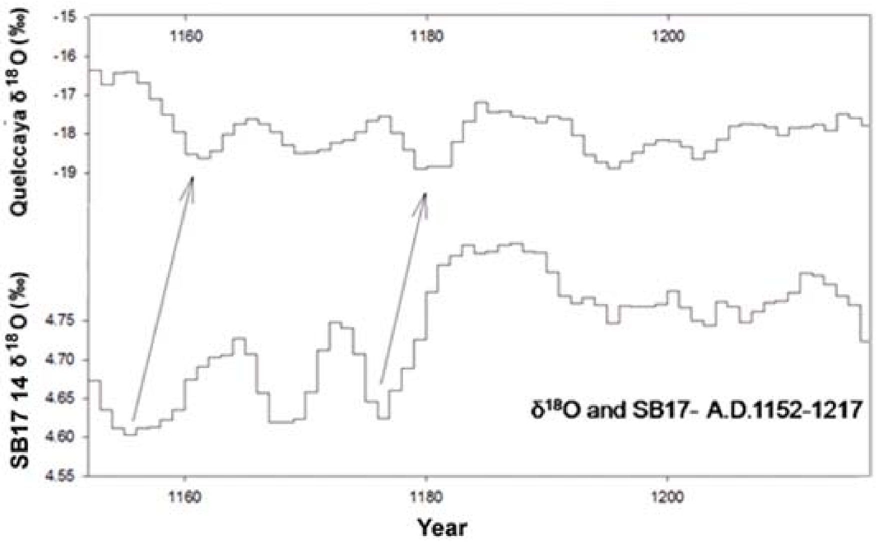

Figure 5.5 Comparison between $\delta^{18}O$ and *Cobb* (2001) SB17 coral record from A.D. 1152 to 1217. Both records are presented as 5-year averages for easy comparison (see text). Arrows are drawn to show a possible lead and lag relationship between the two records.

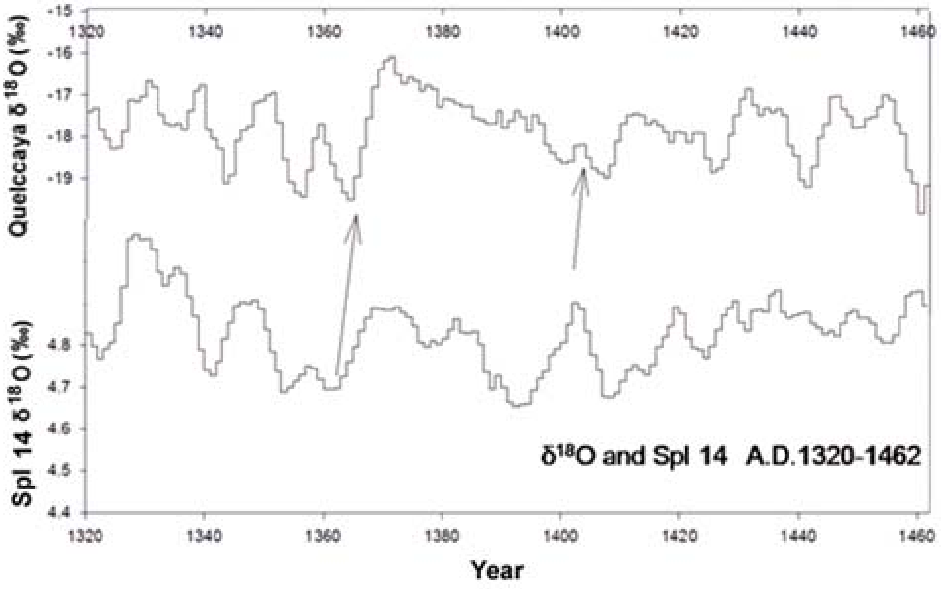

Figure 5.6 Comparison between δ^{18}O and *Cobb* (2001) Spl 14 coral record from A.D. 1320 to 1462. Both records are presented as 5-year averages for easy comparison (see text). Arrows are drawn to show a possible lead and lag relationship between the two records.

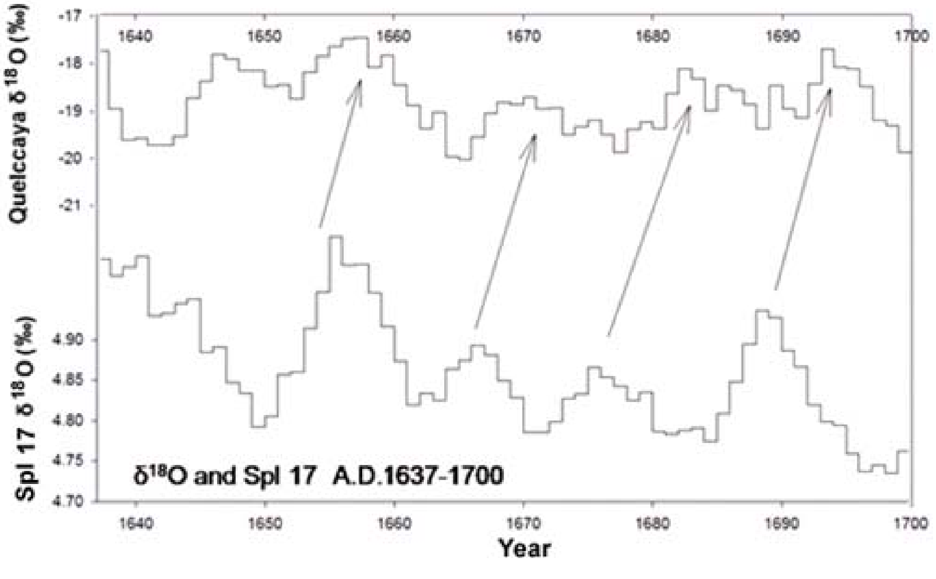

Figure 5.7 Comparison between δ^{18}O and *Cobb* (2001) SB17 coral record from A.D. 1637 to 1700. Both records are presented as 5-year averages for easy comparison (see text). Arrows are drawn to show a possible lead and lag relationship between the two records.

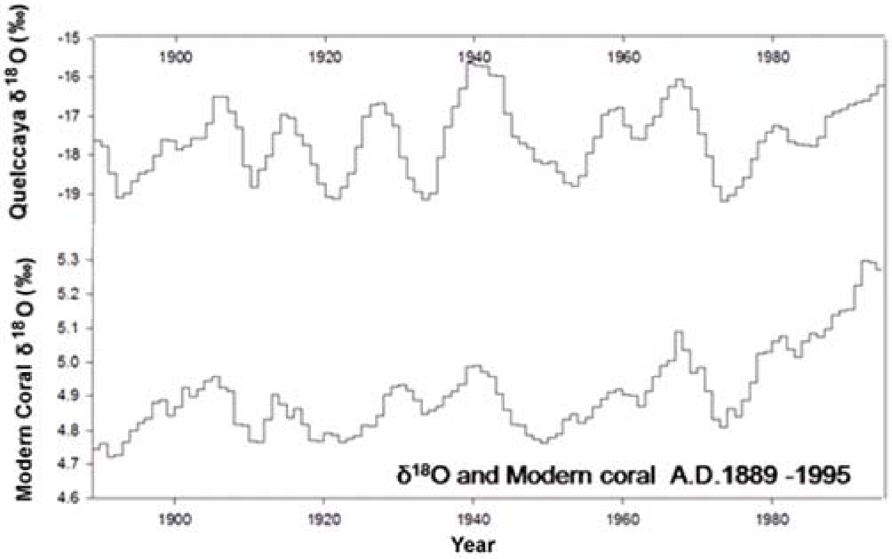

Figure 5.8 A comparison between δ^{18}O and *Cobb* (2001). Modern coral record from A.D. 1889 to 1995 shows that both records are strongly related, as peaks are easily matched in both records. Both records are presented as 5-year averages for easy comparison (see text).

A study of corals at Rarotonga and Fuji in the South Pacific by *Linsley* (2004) suggests, in contrast to the study just mentioned by *Urban* (2000), that weaker Pacific decadal variability occurred before 1880. One line of evidence for this is that the coherency between records of North and South Pacific SST is stronger after 1880 (*Linsley et al.,* 2004). Although the conclusions of *Linsley* (2004) and *Urban* (2000) regarding the strength of decadal variability are not in agreement, both studies agree that a major shift in Pacific climate variability occurred at 1880. The period 1880 to 1950 is marked by both strong inter-hemispheric covariability and large amplitude shifts in coral δ^{18}O. *Linsley* (2004) suggests that other periods marked by large amplitude shifts in coral δ^{18}O might be related to periods of strong inter-hemispheric covariability.

Corals along the Great Barrier Reef of Australia have been used by *Hendy* (2002) to reconstruct SSTs and salinity fluctuations since 1565. *Hendy* (2002) suggests that LIA cooling was confined to the northern latitudes and that mid-latitude glacial advances resulted from increased moisture export from the tropics. In order to reconstruct patterns of temperature, Hendy measured coral δ^{18}O as well as ratios of Sr/Ca and Ur/Ca. Then

Hendy (2002) assumed that the records of Sr/Ca and Ur/Ca functioned as accurate paleo-thermometers so that a record of salinity could be backed out of the δ^{18}O record. Based on this analysis, *Hendy* (2002) found that the end of the LIA at 1880 was marked by a transition to more saline conditions and that SSTs in the early 20th century were generally cooler than during the LIA. This result stands in contrast to a composite of multiple coral records from the tropical Pacific constructed by *Grotolli and Eakin* (2007), which indicates that SST warmed 0.79ºC between 1860 and 1990. The results from this coral composite are supported by analysis of instrumental data from South Pacific Islands from 1911 to 1990 by *Salinger* (1995), which shows that temperatures on average increased by 0.9ºC during the 79 years of record. However, it is noted by *Grotolli and Eakin* (2007) that at least part of this warming, particularly that in the Western Pacific, may be due to decreased salinity. Whatever conclusions one draws from the work of *Hendy* (2002), it is mentioned here as the δ^{18}O record itself exhibits a dramatic shift at the end of LIA coincident with a shift in the Quelccaya record at the termination of the LIA.

5.4 Tree rings and ice cores

5.4.1 Introduction

This section compares the ice core records from Bona Churchill and Quelccaya with annually dated tree ring records from the PNW and the SW United States. Tree ring records from these regions were selected because these regions have a strong historically documented ENSO response. A review of previous research and a summary of significant climate events noted by previous studies is given before comparisons are made with the ice core records. Of particular interest is the tree ring record of La Niña -induced droughts from the SW, as this region provides one of the most reliable ENSO teleconnections (*Cole and Cook,* 1998). Furthermore, the decadal signal identified in Quelccaya δ^{18}O can be better evaluated, as previous research by *Cayan* (2003) indicates that the SW and southern Alaska regions have the largest components of decadal precipitation variability in all of western North America.

5.4.1.1 Literature review: La Niña-induced drought events in the SW

ENSO forcing of the Pacific North American (PNA) pattern (Section 1.4.2) drives changes in the patterns of precipitation along the west coast of North America and in the interior SW so that El Niño events result in wetter conditions in southern California and the SW, drier conditions in the PNW, and wetter conditions in Alaska (*Yarnal and Diaz*, 1986). (La Niña produces the opposite pattern.) Precipitation anomalies generated by ENSO, and more specifically La Niña, are some of the more dependable teleconnections of ENSO (*Cole and Cook*, 1998; *Cayan et al.,* 1999). La Niña events typically last less than 2 years, but longer La Niña events are documented within the historical record. For instance, southwestern droughts that have been associated with prolonged La Niña events occurred from 1856 to 1865, 1870 to 1877, and 1890 to 1896 (*Herweijer,* 2006).

Modern droughts such as the dustbowl drought (1929-1940) and the 1950s drought (1946-1956) appear small in comparison to some of the mega-droughts of the MWP, which are documented by tree ring records and by the disruptions of paleo-societies. Table 5.3 presents a list of both wet and dry precipitation anomalies from the SW based on tree ring studies by *Salzer and Kipfmueller* (2005), *Grissino and Mayer* (1995), *Meko* (2007), *Cook* (2004a), *Herweijer* (2007), and *Stahle* (2000). This list primarily focuses on the largest-scale events mentioned in each study and is biased toward those studies that relate to large-scale drought events during the MWP.

A study of North American drought by *Cook* (2004) based on 255 grid points and 953 chronologies shows that the period A.D. 900 to 1300 was drier than the present and that the LIA between A.D. 1400 and 1800 was wetter. *Cook* (2004) identified two persistent periods of drought during the MWP, one lasting from A.D. 1130 to 1170 and another from A.D. 1220 to 1300. With the exception of the drought identified at the end of the 16th century by *Stahle* (2000), the LIA was not marked by droughts of similar severity (*Herweijer*, 2007). Although modern droughts that have occurred since the end of the LIA, such as the Civil War drought, the Dust Bowl, the 1950s drought, and the 1998 to 2002 drought, have exhibited similar severity to the droughts that occurred during the MWP, they have been of shorter duration (*Herweijer*, 2007).

Grissino-Mayer (2002) used 239 tree rings records from the Rio Grande region of New Mexico to reconstruct the PDSI from A.D. 622 (Table 5.4). *Grissino-Mayer* (2002) identified periods of greater-than-normal precipitation between 1040 and 1125, with the period 1100 to 1125 being particularly wet. This longer-than-average period of above-average precipitation may have resulted in unsustainable patterns of habitation by the Chacoan cultures. It is followed by an unusually dry period between A.D. 1125 and 1150 that may have been associated with cultural collapse in the Southwest. *Meko* (2007) used tree ring records to reconstruct river flow at Lee Ferry on the Colorado from 765 to 2005. The longest period of low flows in the reconstruction occurred during the mid-1100s. According to this reconstruction, river flows between 1130 and 1154 averaged less than 84% of normal (based on 1906 to 2004). The entire period 1118-1179 is characterized by below-average river flow. Resettlement is evident during the period A.D. 1150 to 1200, but it is followed by final abandonment at the end of the 13th century. The 13th century is the driest in the reconstruction, and that is marked by three significant prolonged droughts occurring between A.D. 1213–1221, 1246–1258, and 1272–1297.

A study by *Herweijer* (2007) using the same gridded data set of *Cook* (2004) identified four significant droughts during the MWP that occurred from A.D. 1021-1051, 1130-1170, 1240-1265, and 1360-1382. Modern-day droughts of similar severity but not duration were identified in A.D. 1855-1865, 1889-1896, 1931-1940, and 1950-1957. Spectral analysis by *Herweijer* (2007) suggests that ENSO scale interannual variability is present during the last 1,000 years, but that the period before 1470 is marked by centennial scale variability, whereas the period after 1470 is marked by the dominance of decadal scale variability.

Wet Years	Dry Years
1049–1056a,b	1033–1046a,b, 1021-51e
1060–1066a,b	1090–1101a,b
1109–1119a,b	1144–1154a, 1130-1151b, 1130-1154c, 1130-1170d,e
1159–1167a,b	1182–1191a
1192–1210a,b	1215–1221a,b
1325–1334a,b	1240-1265e, 1220-1300d
1378–1385a,b	1292–1300a,1272-1297b
1427–1434a	1360–1364a,b, 1360-1382e
1482–1486a	1389–1393a
1504–1515a	1435–1450a,b
1549–1560a,b	1455–1464a,b
1564–1570a	1542–1548a
1615–1622a	1571–1593a,b,f,d,g
1640–1647a,b	1623–1628a
1687–1695a,b	1666–1672a,b
1718–1727a	1728–1742a,b
1743–1747a	1751–1757a,b
1760–1771a	1777–1783a,b
1833–1840a,b	1818–1823a
1865–1869a,b	1857–1861a
1905–1922a,b	1870–1883a
1978–1988a,b	1893–1904a,b
	1943–1947a, 1945-63b
	1953–1972a, 1945-63b

- (a) = *Salzer and Kipfmueller* (2005)
- (b) = *Grissino-Mayer* (1995)
- (c) = *Meko* (2007)
- (d) = *Cook* (2004)
- (e) = *Herweijer* (2007)
- (f) = *Stahle* (2000)
- (g) = *Meeko and Woodhouse* (2005)

Table 5.3 Summary of precipitation reconstructions for the southwestern United States.

Prolonged periods of drought and above-average rainfall in the Rio Grande Basin (*Grissino-Mayer*, 2002)	
Positive Flow Anomalies	Negative Flow Anomalies
1553-1557	1571-1593
1627-1653	1272-1297
1978-1992	1943-1963
1377-1396	1131-1151
1112-1130	1818-1826
1193-1203	999-1015
1907-1921	1772-1782
1049-1066	1522-1525
1298-1314	1445-1465
1930-1944	1031-1041
1426-1435	1213-1221

Table 5.4 Reproduction of the results of *Grissino and Mayer* (2002), which depict years with greatest and least flow on the Rio Grande, as reconstructed from tree ring data in the region.

The LIA is marked by continual changing conditions in the Southwest, with unusually wet conditions occurring during the 17th century, dry conditions during the 18th century, and wet conditions during the 19th century (*Grissino-Mayer,* 2002). A "mega-drought" between 1571 and 1593 was identified by *Stahle* (2000) in a study of tree records of the Middle Rio Grande Basin and is noted as the most severe in this region during the LIA. A 538-year tree ring-based reconstruction of stream flows along the Blue River, in western Colorado, and along the Sacramento River in California by *Meeko and Woodhouse* (2005) also identified this drought and demonstrates the geographic scale of the event. Reconstruction of stream flows during the years A.D. 1580, 1581, 1584, 1585, 1590, and 1600 are on average only 25% of the modern average.

Salzer and Kipfmueller (2005) reconstructed a 2,265-year record of temperature and a 1,425-year record of precipitation from two sites within the southern portion of the Colorado Plateau (Table 5.3 – incorporate data from the last 1,000 years of this reconstruction). This reconstruction shows that modern warming is unequalled except for brief periods during the MWP and that precipitation and temperature time series exhibit substantial decadal variability during both the MWP and the LIA. *Salzer and Kipfmueller*

(2005) found that the precipitation reconstruction captured both high- and low-frequency climatic variability, but that the temperature reconstruction based on Bristlecone pines was only able to capture the decadal component of temperature variability.

5.4.1.2 Literature review: –extreme precipitation anomalies in the PNW

This section presents a review of tree ring studies in the PNW and identifies significant events in these studies for comparison with the ice core data sets (Table 5.5). One of the earliest studies of tree rings in the PNW, and to this date one of the most comprehensive, is a reconstruction of precipitation from A.D. 1268 to 1936 by *Keen* (1937), who examined chronologies from more than 1,200 Ponderosa Pine growing in 44 different locations in eastern Oregon. The study by *Keen* (1937) shows that periods of wet and dry climate have alternated at decadal time scales since 1268 with little overall trend, and individual years in the *Keen* (1937) record that show the greatest precipitation anomalies, both positive and negative, are shown in Table 5.5.

A study by *Knapp* (2003) that focused on regions of the interior PNW examined chronologies from 18 precipitation-sensitive Juniper from 1733 to 1980 and identified the occurrence of several long-term droughts in the PNW. Periods of sustained drought were centered at A.D. 1793-1795, 1833-1834, 1917-1919, and 1933-1937. An earlier study by *Knapp* (2002) examined records of tree rings from Western Juniper growing in different climatic subdivisions of the interior PNW in order to identify years with extreme precipitation anomalies from A.D. 1500 to the present. Extreme drought years occurring across multiple study areas, denoted as “super regional CPYs” in the study, were found to occur in A.D. 1502, 1518, 1595, 1600, 1626, 1632, 1657, 1703, 1717, 1924, and 1931. Of note in this study is the lack of extreme drought years during the period 1717 to 1924. This is coincident with a similar period identified by *Woodhouse and Kay* (1990), who suggested that these conditions resulted from a more zonal winter airmass boundary in the PNW (La Niña -like conditions).

Drought Years in the PNW since A.D. 1500
1516c
1600b
1620-1630d, 1626b
1632b
1657b,1650c
1700-1710d, 1703b
1717b
1775e
1793-1795a
1805e
1833-1834a
1840-1855e, 1849c
1890e
1917-1919a
1924b, 1925e
1931b, 1930-1940e,d, 1933-1937a

- (a) = *Knapp* (2003)
- (b) = *Knapp* (2002)
- (c) = *Keen* (1937)
- (d) = *Pohl* (2002)
- (e) = *Gedalof* (2004)

Table 5.5 Summary of drought years in the PNW from multiple tree ring-based studies since A.D. 1500.

Gedalof (2004) used a network of 32 precipitation-sensitive tree-ring chronologies in order to reconstruct yearly mean water year flow on the Columbia River at The Dalles, Oregon since 1750. The lowest flows in the 250-year reconstruction occurred during the 1840s and lasted for 15 years, from 1840 to 1855. Other long-lasting droughts occurred in the 1930s and 1890s, and notable droughts of lesser duration occurred in 1775, 1805, and 1925. Notably, multiyear droughts are absent from the record during the period 1950 to 1987. The drought of the 1840s is also well defined in the reconstructions of *Graumlich* (1987) and *Keen* (1937).

Ware (2000) used tree ring reconstructions of temperature from the National Geophysical Data Center to examine patterns of temperature change along the Pacific Coast of North America for the last 400 years. *Ware* (2000) shows that tree ring reconstructions of temperature from Visalia, Sacramento, Eureka, Aberdeen, and Vancouver all exhibited coherent patterns of variability during the past 400 years. An examination of the Sacramento record (which is in phase with the other records) shows that regime type shifts occurred in A.D. 1630, 1696, 1717, 1746, 1755, 1761, 1782, 1826, 1855, 1879, 1923, 1945, and 1976. Significant and extended periods of warmth occurred from A.D. 1630–1695, 1717–1745, 1755–1760, 1782–1825, 1855–1878, 1923–1944, and since 1976, while significant periods of extended cold occurred before A.D. 1629, from 1696–1716, 1746–1754, 1761–1781, 1826–1854, 1879–1922, and from 1945–1975.

Pohl (2002) used a Ponderosa Pine record from a location near Bend, Oregon to reconstruct a record of precipitation for the past 545 years. The tree ring reconstruction of precipitation shows that decade-long droughts occurred in the 1480s, 1620s, 1700s, and the 1930s. The 1930s drought is significant, as it represents the longest drought during the reconstruction period. Certain years in the record were identified as drought years: A.D. 1465, 1475, 1478, 1486, 1488-1489, 1516, 1529, 1532, 1533, 1546, 1555, 1526, 1652, 1665, 1705-1706, 1708, 1741, 1747, 1840, 1890, 1899, and 1935.

A study by *Pederson* (2004) used tree ring records from Glacier National Park to reconstruct summer precipitation from A.D. 1540. This study identified several low-frequency periods of both prolonged drought and above-average precipitation. Periods with above-average precipitation occurred in A.D. 1672-1680, 1703-1717, 1770-1791, 1800-1810, 1818-1840, 1899-1916, 1942-1950, and 1975-1983. Periods with drier- than-average conditions occurred in A.D. 1566-1571, 1601-1609, 1626-1641, 1681-1702, 1718-1727, 1754-1769, 1861-1883, 1888-1898, 1917-1941, and 1951-1974. *Pederson* (2004) notes that precipitation anomalies in Glacier are similar to those in the PNW and tend to be opposite in phase with those occurring in the southwestern United States.

5.4.2 Comparisons of tree ring and ice core data sets

5.4.2.1 Tree ring data set development

This analysis uses reconstructions of the PDSI from North American Tree Ring to derive indices of drought in the PNW and SW that can be compared to the ice core data sets (*Cook*, 2004b). The tree ring network has excellent spatial coverage, as it is based on 286 grid points at a 2.5º resolution and uses 835 well-dated chronologies (*Cook et al.,* 2004). In addition to calculating indices of the PNW and SW for comparison with the ice core data, the events in Tables 5.3 and 5.5, which summarize extreme events in each region, are examined in more detail.

To compare the tree ring data with the ice core data, it was modified as follows. The data from selected grid points in each region were summed, averaged together, and then smoothed with a 5-year moving average. To reconstruct an index of the PDSI for the SW, the following grid points from the *Cook* (2004b) data set, from the western half of New Mexico and Arizona, were included:

107.5º W by 35.0º N
110.0º W by 35.0º N
110.0º W by 32.5º N
107.5º W by 32.5º N
112.5º W by 32.5º N
112.5º W by 35.0º N

Tree ring data from the PNW are based on the following data points from coastal Washington and Oregon:

125.0º W by 47.5º N
122.5º W by 47.5º N
122.5º W by 45.0º N

A very strong correlation (r=.62 and p<0.001) is found between the 5-year standardized averages of the PDSI from the SW (*Cook*, 2004b), and the reconstruction of the Rio Grande as presented by *Grissino-Mayer* (2002) serves as a cross-check on the validity of the calculated index of the SW PDSI.

To easily compare all of the time series, the data were standardized using the following procedures. First, a centered moving average was calculated at a 5-year and then 20-year interval. Second, the smoothed 5-year and 20-year averages were normalized so that all values would fall between -1 and 1. Finally, the individual values of Quelccaya accumulation and reconstruction PNW PDSI were multiplied by -1 so that the ENSO response of all the time series would be of similar sign.

5.4.2.2 Ice core records and SW tree rings

This analysis evaluates the ice core response to the reconstructed SW PDSI and to specific climatic events (Table 5.3) that were identified in Section 5.4.1.1. Relationships between the 5-year averages of Quelccaya δ^{18}O, BC δ^{18}O, BC d-excess, and BC accumulation, along with the SW PDSI reconstruction, are plotted in Figure 5.9. The dashed lines in Figure 5.9 represent drought events from Table 5.3. However, because Table 5.3 reports drought events as ranges of years, the SW PDSI was used to help pick a specific year on which to center the dashed line. A strong relationship is observed between drought in the SW and negative isotopic values at Quelccaya. For instance, out of 24 drought events defined in Table 5.3, one finds that 13 of the events match negative isotopic anomalies, three match positive anomalies, and eight are difficult to define. It would be difficult to use either the record of SW PDSI or the record Quelccaya δ^{18}O to predict the occurrence of La Niña-like conditions in the Pacific, but perhaps these two records could be combined to identify potential La Niña years based on overlap in the two records.

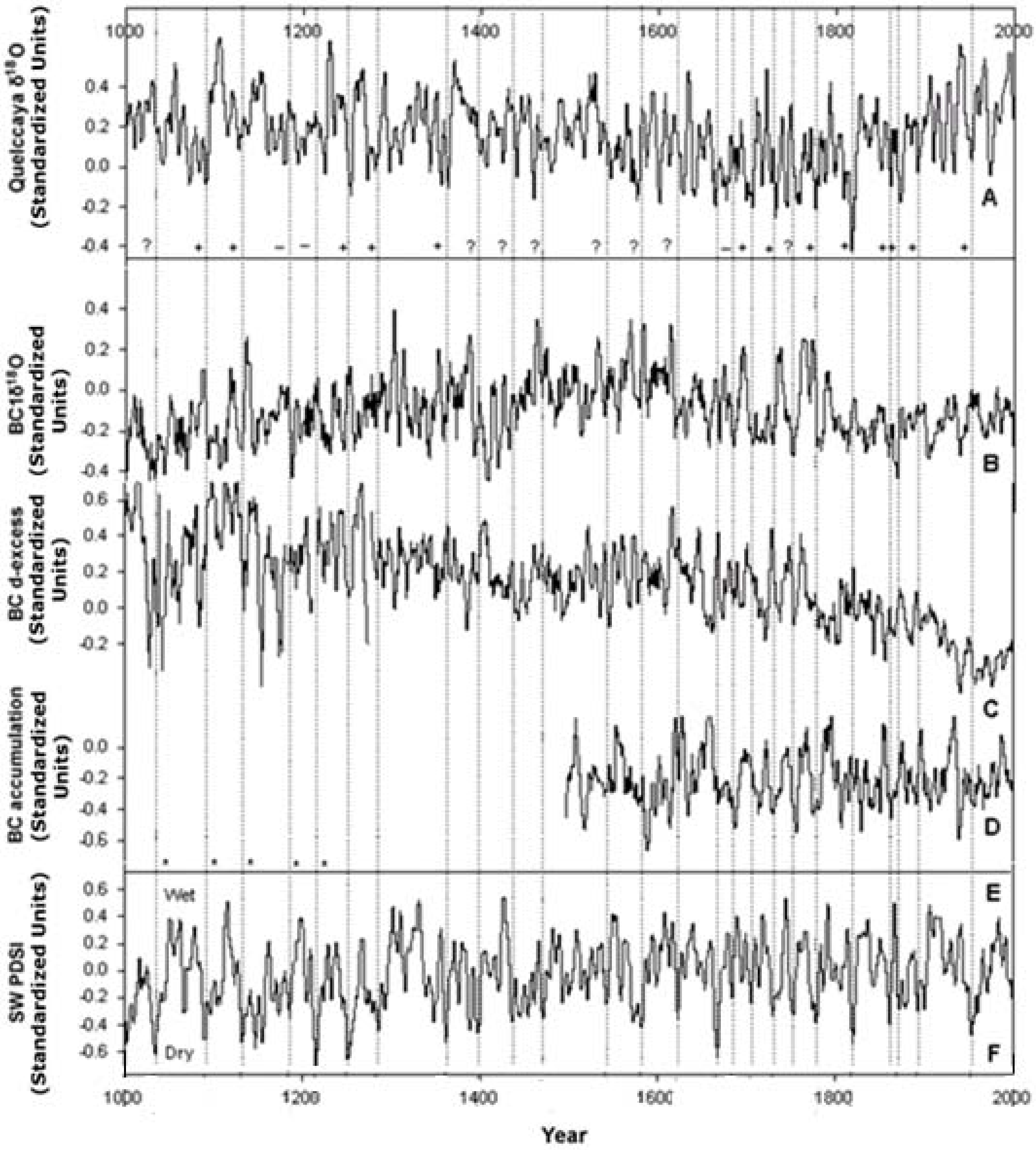

Figure 5.9 Compares the reconstructed SW PDSI and drought events to the response in the ice core records from Quelccaya and Bona Churchill from A.D. 1000 to 2000. Dashed lines represent the largest drought events in the record of SW PDSI. (A) Quelccaya $\delta^{18}O$, (B) BC1 $\delta^{18}O$, (C) BC d-excess, (D) BC accumulation, (E) SW droughts during the MWP from Table 5.8 are shown as "*", (F) SW PDSI Reconstruction. Drought events from the SW PDSI reconstruction that match with Quelccaya $\delta^{18}O$ are indicated underneath (A) as either "+" matching, "-" not matching or "?" difficult to define. All time series are shown as 5-year averages and are scaled between -1 and 1 for easy comparison.

The relationship between Quelccaya $\delta^{18}O$ and SW drought events is further investigated by examining two periods in more detail, specifically the modern period from 1850 to the present and the period A.D. 1200 to 1300. During the period A.D. 1200 to 1300 *Grissino-Mayer* (2002) identified three drought events occurring between A.D. 1213–1221, 1246–1258, and 1272–1297, and during the period A.D. 1850 to 2000. *Herweijer* (2007) identified drought events occurring in A.D. 1855-1865, 1889-1896, 1931-1940, and 1950-1957. Figure 5.10 shows that during the last 150 years, the significant drought events line up with more negative values of Quelccaya $\delta^{18}O$. However, during the period A.D. 1200 to 1300, the results are more ambiguous, as only the drought event occurring in A.D. 1246-1258 matches well with the Quelccaya $\delta^{18}O$ record. However, a partial match exists during the period A.D. 1272–1297, with the only difficulty being the response of the SW PDSI lagging the event in the Quelccaya $\delta^{18}O$ record. *Cook* (2004) identified two persistent periods of drought during the MWP from A.D. 1130 to 1170 and another period that lasted from A.D. 1220–1300. Outside of these two periods, it is noted that a minima in Quelccaya $\delta^{18}O$ occurs from A.D. 1550 to 1580 that coincides with the A.D. 1571 to 1593 drought event identified by *Stahle* (2000).

5.4.2.3 Ice core records and PNW tree rings

This analysis compares the ice core data from Peru and Alaska with the reconstruction of the PNW PDSI and specific climate events outlined in Table 5.5. Figure 5.11 compares the ice core data from Peru and Alaska since A.D. 1600 with reconstructions of climate in the PNW, as summarized in Table 5.5 and developed by *Pohl* (2002), *Gedalof* (2004), *Knapp* (2002 and 2003), and *Keen* (1937). The records of *Verdon and Franks* (2006) and *Ware* (2000) don’t look specifically at climate in the PNW but are added into this section to give a broader picture of past North Pacific climate variability and its relationships to the ice cores.

The record of *Verdon and Franks* (2006) is a composite record of PDO regime shifts (Table 5.6) based on a number of earlier studies, and the record of *Ware* (2000) is a

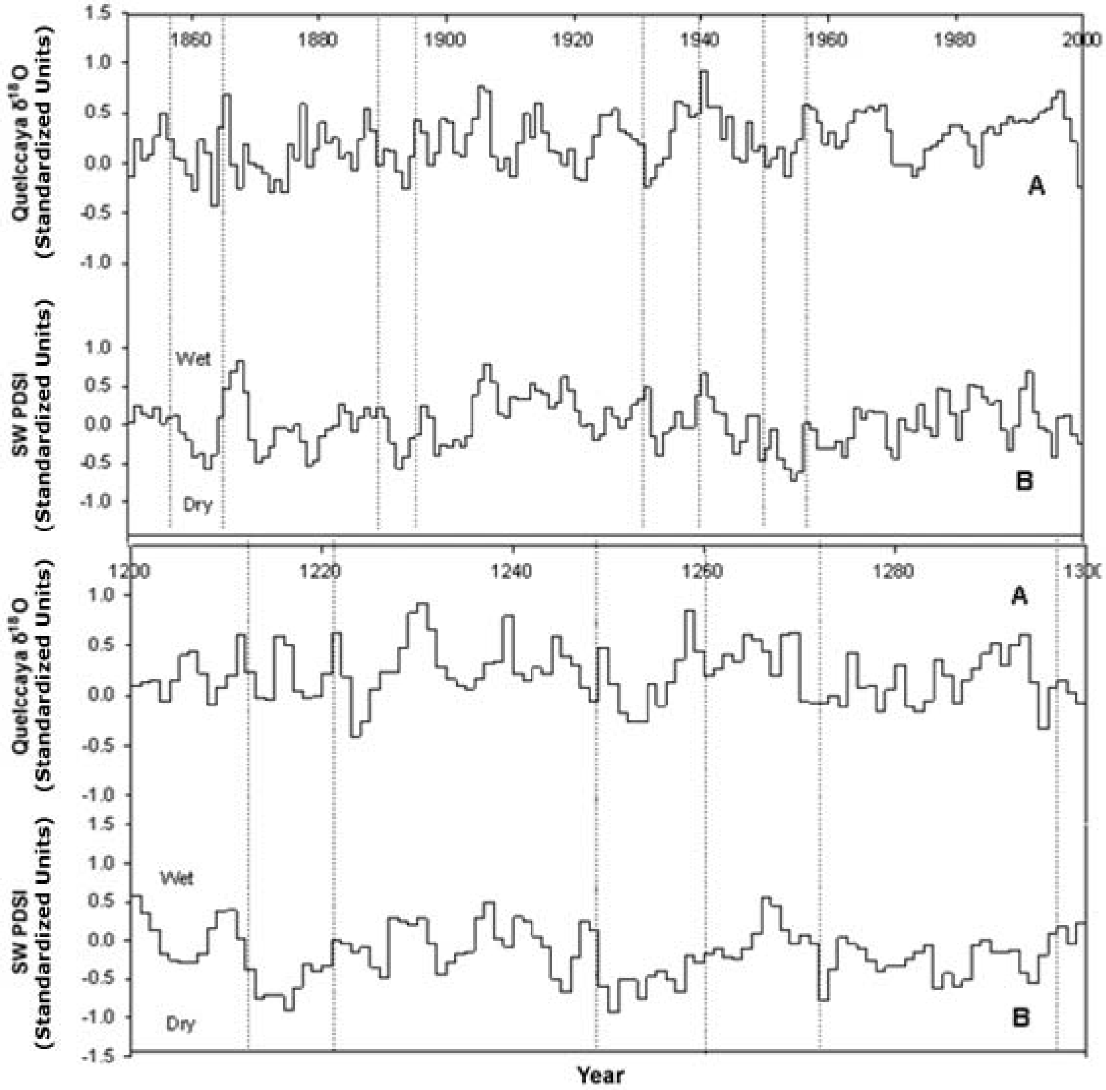

Figure 5.10 Drought events during the MWP (A.D. 1200 to 1300) and during the last 150 years depicted as dashed lines and shown overlaid on the time series of the year averages of SW PDSI and Quelccaya δ^{18}O. Drought events shown as dashed lines occur at 1213–1221, 1246–1258, and 1272–1297, as identified by *Grissino-Mayer* (2002) and in 1855-1865, 1889-1896, 1931-1940, and 1950, as identified by *Herweijer* (2007).

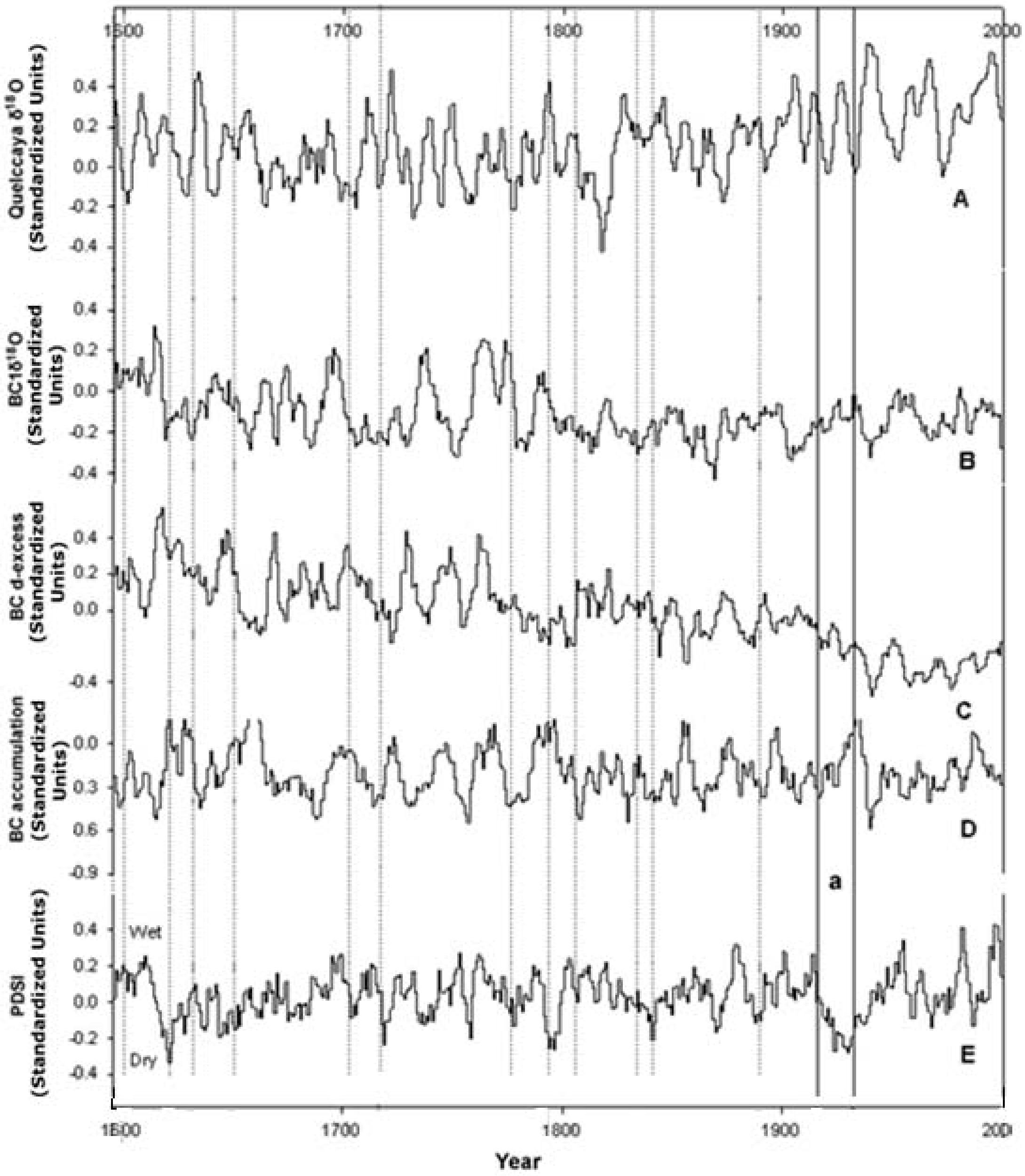

Figure 5.11 Compares the reconstructed PNW PDSI and drought events to the response in the ice core records from Quelccaya and Bona Churchill from A.D. 1600 to 2000. Dashed lines represent the largest drought events in the record of PNW PDSI, as derived from Table 5.3. (A) Quelccaya δ^{18}O, (B) BC1 δ^{18}O, (C) BC d-excess, (D) BC accumulation, (E) PNW PDSI Reconstruction. The box labeled “a” is one of the larger drought events during the last four centuries, and it is depicted for easy comparison with the ice core records. Time series are shown as 5-year averages and are scaled between -1 and 1.

Significant Step Changes in Pacific Climate: Modified from *Verdon and Franks* (2006)								
PDO	*Linsely* (2000)	*Biondi* (2001)	*D'Arrigo* (2001)	*Gedalof* (2001)	*MacDonald* (2005)	Count	Standard Deviation	Average or Historical
1975	1979+	1974+			1968+			1975
1942	1943-	1947-	1944-	1945-	1943-			1942
1922				1921+				1922
		1907+			1908+			1908?
1890*								1890?
	1875+*		1874+*		1874-			1874?
	1857-	1839-	1853-	1848-		4	7.76	1849?
	1830+	1825+	1824+	1821+	1831+	5	4.2	1826
	1805-	1806-	1805-	1805-	1805-	5	.44	1805
	1791+		1790+		1791+	3	.57	1791
	1779-		1776-		1776-	3	1.73	1777
	1764+	1765+	1758+	1759+		4	3.5	1761
		1727-	1723-	1733-		3	5	1728
		1717+		1711+	1717+	3	3.47	1715
		1703-		1696-	1696-	3	4.04	1698
		1678+		1681+	1679+	3	1.5	1679
				1661-	1662-	2	.7	1662
					1634+	1	0	1634
					1612-	1	0	1612

*Disagrees in sign with McDonald
*Minobe

Table 5.6 North Pacific Regime shifts – This table summarizes the results from multiple studies and is reproduced from *Verdon and Franks,* 2006.

study of temperature patterns along the west coast during the last 400 years based on both tree ring records and historical records of temperature. A comparison of the time series of the 5-year averages of Quelccaya $\delta^{18}O$, BC $\delta^{18}O$, BC d-excess, and BC accumulation with reconstructed temperature anomalies from *Ware* (2000) during the period A.D. 1630 to 1975 does not reveal any significant correlations or patterns (Fig. 5.12). A comparison of the ice core data with the regime shifts identified by *Verdon and Franks* (2006), as summarized in Table 5.6, shows that in several cases, positive accumulation anomalies in the BC core line up with positive PDO regimes (Fig. 5.13). For instance, four out of the 10 PDO positive regimes are marked by positive accumulation. During the other six PDO positive regimes, the response in accumulation is more difficult to define, because it is either variable or neither strongly positive nor negative.

A comparison of the ice core data sets and the reconstructed PNW PDSI failed to find any significant patterns or correlations between the data sets, even though a strong La Niña signal would be expected in the PNW PDSI. A possible cause might be a subdued tree ring response during La Niña events. Drought events invariably result in low-growth years, and wet events result in high-growth years. However, the response to increasing precipitation is limited in that very wet years don’t lead to very high growth, because once a tree has sufficient water to grow, providing additional water beyond that critical amount won’t help it grow any faster. The same reasons that make it difficult to reconstruct a record of La Niña events in the PNW may on the other hand explain why drought/La Niña events in the SW are easy to recognize in the regional tree ring records.

5.5 Conclusions

The strongest correlations between Quelccaya $\delta^{18}O$ and Pacific SSTs occur in the northern equatorial Pacific between 150°W and 160°E, where a strong relationship is noted between modern coral records from Palmyra Island (162°W, 6°N), as given by *Cobb* (2001). While modern coral records are strongly correlated with Qualccaya $\delta^{18}O$ (Fig. 5.8), the older coral records from the same location are not (Fig. 5.5 to 5.7). A review of fossil corals from other locations point to a dramatic shift in SST/salinity occurring at the end of the LIA in approximately 1880 that is also clearly demarcated in the Quelccaya record.

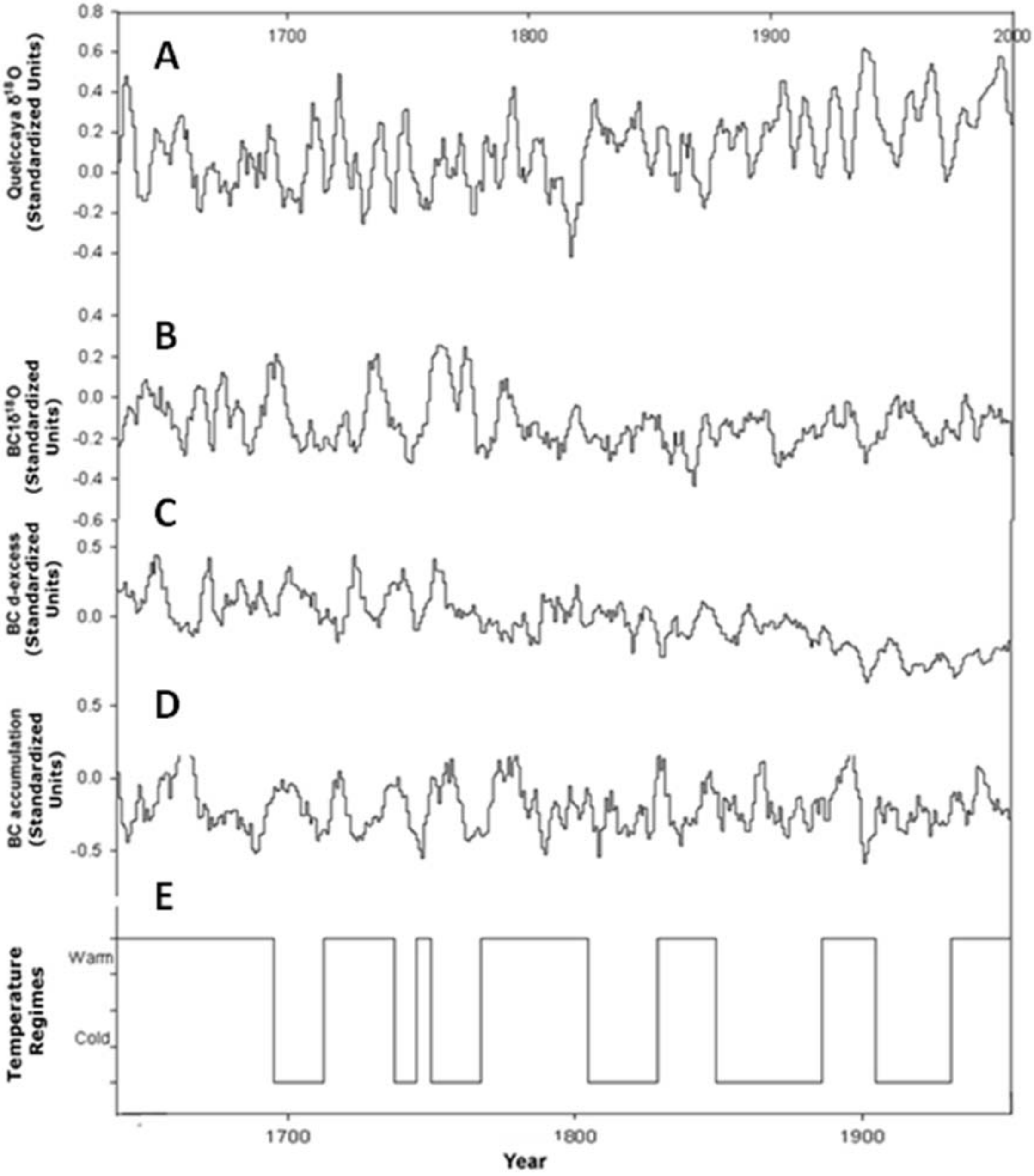

Figure 5.12 Cold and warm temperature regimes, as identified by *Ware* (2000), compared (A) Quelccaya δ^{18}O, (B) BC1 δ^{18}O, (C) BC d-excess, (D) BC accumulation from A.D. 1600 to 2000 and (E) cold and warm regimes of *Ware* (2000). *Ware* (2000) identified cold and warm regimes based on reconstructed temperatures from tree ring at different locations along the coast of the western United States (see Section 5.4.2.3). Temperature regimes are shown as being either warm or cold. All the time series are shown as 5-year averages and are scaled between -1 and 1.

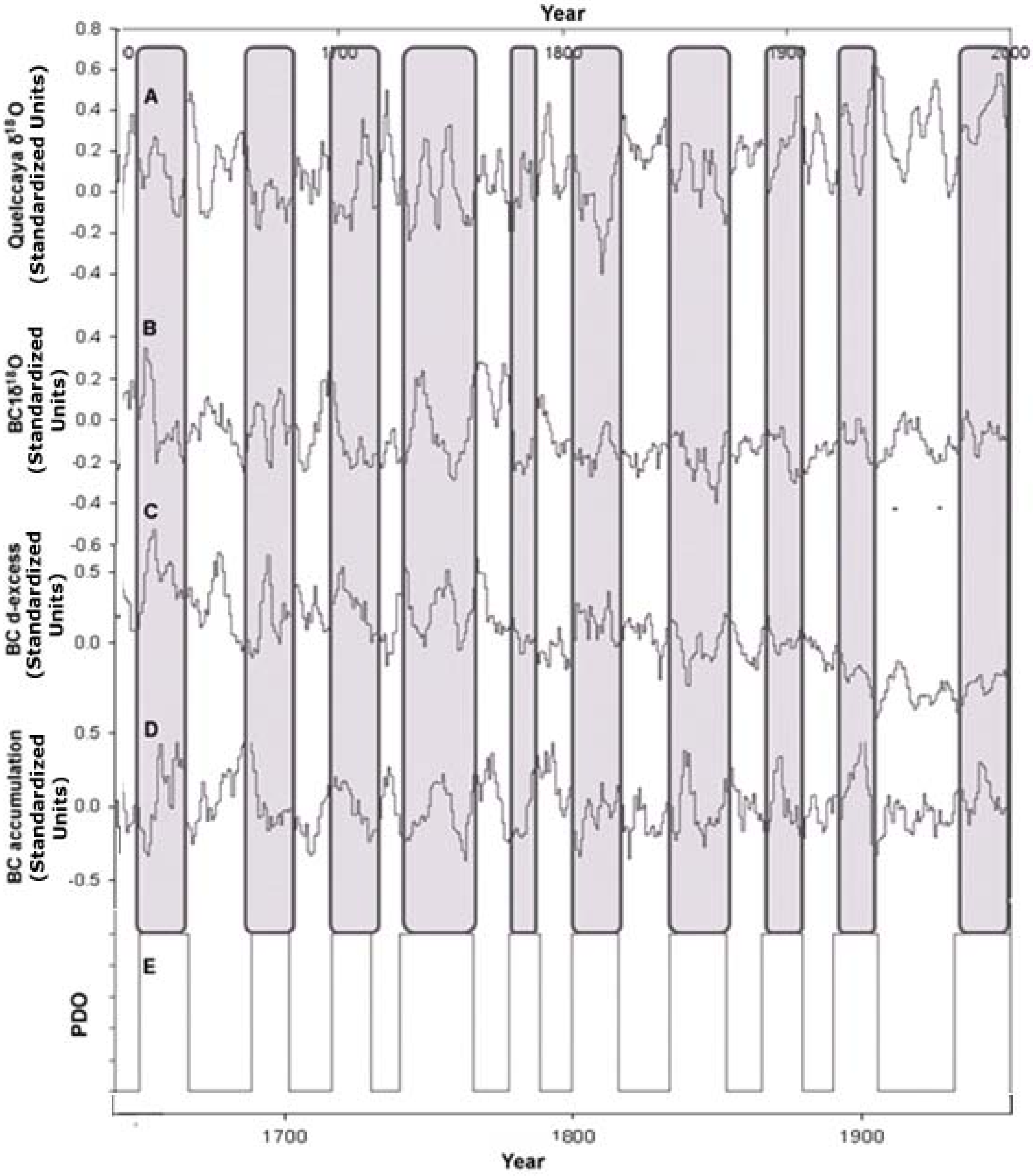

Figure 5.13 Comparison of positive and negative PDO regimes as identified by *Verdon and Franks* (2006) with (A) Quelccaya $\delta^{18}O$, (B) BC1 $\delta^{18}O$, (C) BC d-excess, (D) BC accumulation from A.D. 1600 to 2000, and (E) Positive and negative PDO regimes identified by *Verdon and Franks* (2006). Periods with a positive PDO are depicted with shaded boxes that overlie the rest of the time series. Time series are shown as 5-year averages and are scaled between -1 and 1.

A strong relationship is identified in this chapter between more negative values of Quelccaya $\delta^{18}O$ and drought events in the SW (Fig. 5.9). Previous studies have shown that the precipitation anomalies generated by ENSO in the Southwest are some of the more dependable teleconnections of ENSO (*Cole and Cook*, 1998). Furthermore, it appears that the impact of La Niña events is more consistent than that of El Niño (*Cayan et al.,* 1999). Future studies might attempt to verify the link between drought events in the SW and their correspondence to the record of Quelccaya $\delta^{18}O$.

The lack of connection between the ice core variables from Peru and Alaska during both the last 100 years and the last 1,000 years might result from the BC record of $\delta^{18}O$ being more strongly related to fluctuations in the AO than in the AL. At the same time, it might result from the fact that the Quelccaya $\delta^{18}O$ record reflects decadal NIÑO 4 variability and seems for the most part disconnected to the lower frequency regime shifts associated with the PDO, which primarily reflects North Pacific variability.

CHAPTER 6
CONCLUSIONS AND REVIEW

6.1 The Bona Churchill Ice Core

6.1.1 Climate-ice relationship

The Bona Churchill Ice Core (BC1), drilled to bedrock in the spring of 2002 in the Wrangell-St. Elias Mountains of southeast Alaska (61° 24' N, 141° 42'W; 4420 meters), is one of the only annually dateable records of extended historical duration to ever be recovered from the northeastern side of the Pacific Basin. The analysis of the ice-climate relationship shows that the records of $\delta^{18}O$ and dust from BC1 can be related to long-term shifts in atmospheric circulation, as expressed by the two primary modes of Northern Hemisphere circulation, the Aleutian Low (AL) and the Arctic Oscillation (AO). The records of dust and $\delta^{18}O$ can be considered to be recording the history of northerly flow (associated with weak AL and negative AO) versus southerly flow. Large dust events and more negative values of $\delta^{18}O$ occur in BC1 when the AL is weak and the AO is negative. These findings are supported by a study of *Bond and Harrison* (2006), which found that the effects of ENSO are weaker when the AO is positive and enhanced when the AO is negative. This is very similar to what is observed in the record of BC1, in that the AO modulates the signal of the AL in the ice core record.

The different possible phases of the AO and AL can be associated with four different climatic end members (Fig. 2.6). The pattern of flow over the drilling site generated by the occurrence of a weak AL at the same time as a negative AO is unique from the other three situations in that it brings a westerly airflow over the drilling site. This difference is depicted in Figure 2.47, which shows the 300mb vector wind anomalies that occur when the AO is negative and the AL weak. The occurrence of a weak AL and a negative AO is unusual, because these two indices usually correspond so that a positive (negative) AO is associated with a weak (strong) AL. In general, when the AO is negative, the effects of the AL are accentuated and when the AO is positive they are diminished. The rapid warming of the 1920s is a good example of how the AO modulates the response of the AL, because this period is coincident with shifts in the strength of the AL and AO, with changes in the ice-climate relationship, and in patterns of accumulation and values of d-excess at BC1 (Fig. 2.9).

Composites plots of the 15 years with the most enriched and most depleted values of δ^{18}O were compared to examine contributing meteorological differences. These composites (Fig. 2.42 and 2.43) show that when isotopes are most enriched, the AL is centered far to the west, almost over the Kamchatka Peninsula, and that when isotopes are depleted the AL is centered further eastward in the Gulf of Alaska. These composites are very similar to the composite anomaly plots of the 850mb level showing years with most and least dust, respectively.. These composites are supported by strong relationships observed between BC1$_{sp}$ δ^{18}O with the strength of the AL (r=-0.31, 1902-1992) and the longitude of the AL (r=-0.33, 1902-1992).

Higher concentrations of dust occur in years with a weak AL, and negative AO occur in A.D. 1951, 1956, 1965, 1966, 1969, and 1979 (Fig. 2.1). In the longer record depicted in Figures 2.17 and 2.18, every significant dust peak (trough) is accompanied by more positive (negative) values of δ^{18}O. The timing of the 1960s event coincides with a period during which the AL was much weaker than normal, the AO was negative, and one in which prevailing winds at the 500 mb are offshore rather than onshore, which is typical in the region. The relatively rare pattern of offshore winds during this period resulted in record cold temperatures at Yakutat during January of 1966 and 1969.

6.1.2 Timescale and seasonal patterns of BC1

The timescale for BC1 is well constrained during the last 1,000 years, and annual layering is present throughout the length of BC1. The timescale for BC1 is based upon multiple lines of evidence, including the identification of radioactivity in the ice core from open air nuclear testing in the 1950s and 1960s; peaks in sulfate and fluoride that correspond with historic volcanic eruptions; and annual peaks in dust, other measured ions, and a well-defined cycle in oxygen isotopes. In addition to the clear presence of annual layers, the dating of BC1 is well constrained by the identification of the 1963 β-peak, the 1912 eruption of Katmai, and the 1783 eruption of Laki in the ice core. Annual layers are clearly resolvable throughout the last 1,000 years of record, and a depth model based on observed thinning suggests that BC1 dates back to A.D. 265 (estimated errors are given in Table 2.1).

This study pinpoints the period A.D. 760 to 777 (according to the BC1 timeline, which is based on a simple thinning model prior to A.D. 1000) as the likely location of the White River Ash, an important regional chronostratigraphic marker, in BC1. This conclusion is supported by the following:

1. The largest dust peak in the last 1,500 years in BC1 occurs at A.D. 760 to 777 (Fig. 2.11).
2. The large dust peak is not matched by a response in δ^{18}O. This is unique in the entire ice core, and as such it appears as an outlier in the normal relationship between dust and δ^{18}O, indicating the absence of the normal weather-related relationship between these two variables (Fig. 2.10).
3. The timing of A.D. 760 to 777 matches the A.D. 803 timing of the White River Ash.
4. A general increase in background dust is evident from the difference in the ratio of Quartile1 to Quartile 3 dust concentrations in a given sample year (Section 2.3.4.2). This is unique in the ice core because the typical pattern is for the dust peak to be fairly well-defined seasonally, but the dust within this interval of the core is more disseminated (Fig. 2.13).

To define the intra-annual cycles in BC1, composites of each measured ice core parameter were developed based on the 39 annual layers deposited between 1963 and 2002. The seasonal composites (Fig. 2.15 and Section 2.4) show that enrichment of δ^{18}O, minimum values in d-excess, and maximum values in all other ice core parameters, which include dust, SO_4^{2-}, $Ca^{2+,}$ NO_3^-, NH_4^+, Na^+, Cl^-, and Mg^{2+} (but exclude K^+ and F^-), all occur at the same time in the spring. The spring timing of the dust peak is well constrained in this study by multiple lines of evidence, which include the timing of Asian dust storms and associated influx of dust into the region, the ^{3}H profile, and hypothesized changes in the rate of accumulation at the drill site.

6.1.3 The record of BC1 from A.D. 1000 to 2000

A strong correlation is evident between $BC1_{sp}$ $\delta^{18}O$ and dust (r=-0.62, A.D. 500-2000, as shown in Fig. 2.10 and Fig. 2.11) for the entire length of the time series, which could attend to the stability of the relationship between climatic factors and both of these variables. The most striking feature of the BC1 $\delta^{18}O$ record is a sustained and gradual shift from -30‰ to -26‰ between A.D. 500 and 1400. This long trend of steadily increasing values of $\delta^{18}O$ ends abruptly at A.D. 1400, as values quickly drop but then rebound and remain relatively high until 1800. The 19th- and 20th- century values of $\delta^{18}O$ have been on average more negative than during the preceding period from A.D. 1400 to 1800. Values are for the most part high during the period 1400 to 1800, but a significant shift from high to low is seen at A.D. 1618. The seasonal cycle of $\delta^{18}O$ is depicted in Figure 2.18, and lower values are associated with the spring peak in dust.

The relationships identified between $\delta^{18}O$ and dust with both the AO and AL suggest the temperature response recorded by BC1 is indefinable, because more negative values of $\delta^{18}O$ are associated with a weaker AL and/or a negative AO, and more positive values of $\delta^{18}O$ are associated with a stronger AL and/or a positive AO (Fig. 2.53). This ambiguous response can explain the lack of response in the record of $\delta^{18}O$ to recent warming. During the last 25 years, the AL has gotten stronger and the AO has been more positive. This suggests at least cooler temperatures in the upper atmosphere due to the influence of the AO and warmer temperatures at the surface, which is due to the influence of a stronger AL. These results are consistent with the accumulation record from BC1, as well as historical records of precipitation and temperature, which shows increased accumulation during this period. This might be expected given an overall increase in the regional lapse rate and increased moisture flux into the region, which is associated with a strong AL.

The record of $\delta^{18}O$ is not a standalone record of either long-term AL or AO variability, and as a result it cannot be used as a simple temperature record. The lack of any low-frequency AO signal, with the exception of the event at A.D. 1400 (Section 1.4.5.1), may suggest that the longer-term shifts in the record $\delta^{18}O$ reflect AL variability. This conclusion is supported by comparisons of the record of BC1 $\delta^{18}O$ and reconstructions of salmon productivity, which were constructed by *Finney* (2002) and that show that productivity began a gradual increase around A.D. 100 and continued gradually increasing until A.D. 1200. Overall higher levels of productivity persisted between A.D. 1200 and 1900. This general trend corresponds well with BC1 $\delta^{18}O$, where it is observed that values of $\delta^{18}O$ increase gradually in the early part of the record and are less negative in general after A.D. 1200.

The degree to which the AO, AL, and Siberian High (SH) exhibit independent variability and the amount that is shared is the subject of debate, as is the question as to whether these relationships have changed through time. One possibility is that the Pacific component of AO variability is dependent on local variability and independent of the NAO (*Huth*, 2006; *Fu*, 2001). A recent study by *Castanheira* (2003) found that a significant negative correlation only exists between north Pacific and Atlantic pressure fields when the polar vortex is strong.

6.2 The Quelccaya Ice Core

The year 2003 marked the completion of a major drilling project in which three ice cores, two of which were drilled to bedrock, were retrieved and returned frozen to Byrd Polar. This study builds on previous research in the region by Dr. Thompson and focuses on developing the record of the Summit Core (168.8m), which was retrieved as part of the 2003 expedition. Despite the differences in sampling, comparisons of the isotopic profiles of 2003 and that of the 1983 ice core over the last 500 years show that both records are nearly identical (*Thompson et al.,* 2006). This attests to the stability of the derived $\delta^{18}O$ profiles through time and serves as a verification of the original timeline that was developed in 1983. The 2003 core can be dated back to A.D. 315 by making use of both a time depth model and annual layer counting. Counting of annual layers was possible from A.D. 615 to 2003.

6.2.1 Climate-ice relationship

The analysis of the 2003 Quelccaya core identifies a strong correlation between Quelccaya $\delta^{18}O$ and NIÑO 4 Sea Surface Temperatures (SSTs) ($r=0.646$, $p<0.001$, 1856-2003). The Pierson correlation coefficient between Jan-Dec Niño 4 SST and Quelccaya $\delta^{18}O$ during the period 1856 to 1882 is 0.75 (as opposed to 0.65 for the modern period of record from 1882 to 2000), indicating that a strong relationship between $\delta^{18}O$ and SST persisted even during the Little Ice Age (LIA) despite a substantially different background climate. A comparison (shown in Fig. 3.4) of the $\delta^{18}O$ time series with NIÑO 4 and NIÑO 1+2 SST illustrates the predominantly decadal nature of the $\delta^{18}O$ signal. This finding is supported by previous studies of the 1983 Quelccaya $\delta^{18}O$ record by *Henderson* (1996) and by the record of NIÑO 4 SSTs by *Lohmann and Latif* (2005), which show that the dominant mode of climate variability in both these records is decadal rather than interannual. Although ENSO events appear to be superimposed on the $\delta^{18}O$ time series, they are certainly not the dominant feature that they are in records from the NIÑO 1+2 regions (Fig. 3.4).

In general, SST anomalies in the western Pacific are more persistent and evolve on slower timescales than those in the eastern Pacific (*Klotzbach and Gray*, 2004). A study of timescale variability of the 1983 Quelccaya core by *Melice and Roucou* (1998) found a strong 12-year oscillation in the time series of $\delta^{18}O$ that persisted throughout the period of analysis from 1485 to 1984. This study links the 12-year oscillation observed in the Quelccaya core to SST variability in the northern tropical Atlantic that occurs at the same frequency. Studies of Atlantic SSTs by *Xie and Tanimoto* (1998) identify a dominant mode of 10-14 year variability. Meanwhile, a reconstruction of trade winds based on foram productivity in the Cariaco Basin by *Black* (1999) shows that trade wind intensities vary on both decadal and centennial timescales.

Quelccaya $\delta^{18}O$ is most strongly related to SST in the easternmost margin of the Pacific Warm Pool (PWP). The marginal regions may be better recorders of warm pool contraction and expansion because they exhibit a larger degree of SST variability than the interior of the PWP, where SSTs are most consistent. Previous studies indicate that increased convection in the eastern portion of the warm pool results in weaker trade winds in the Atlantic and warmer SST in the northern tropical Atlantic (*Cobb*, 2001). Establishing a connection between decadal variability in the Pacific and Atlantic is of key importance, as the Atlantic is the primary moisture source area for Quelccaya.

6.2.2 Timeline

The timescale for the 2003 Quelccaya Summit Core is based upon multiple lines of evidence, including annual layer counting based on peaks in dust; a well-defined annual cycle in $\delta^{18}O$; the identification of ash layers in the ice core corresponding to historic volcanic eruptions; and comparisons of the Quelccaya core with other regional ice cores. A comparison with the Coropuna Core shows that individual years can be identified and matched peak for peak for the last 200 years; this serves as a valid cross-check on the derived timeline and shows that the isotope profiles are not unique to either ice core, but are rather preserved systematically across this entire region of the Andes. The 2003 summit core can be dated back to A.D. 315 by making use of both a time depth model and annual layer counting. Counting of annual layers was possible from A.D. 615 to 2003, and the estimated error at A.D. 615 is approximately 10 years (Table 3.1).

6.3 ENSO reconstructions and ice core comparisons

6.3.1 An ice core-based ENSO reconstruction

The record of Quelccaya is strongly impacted by ENSO events and has the potential to play an important role in future reconstructions of ENSO. This thesis finds strong linkages between the record of $\delta^{18}O$ from Quelccaya with the El Niño events identified by *Quinn* (1987) during the last 500 years and with a reconstruction of the Palmer Drought Severity Index (PDSI) of the Southwest, a region with strong and dependable ENSO teleconnection. Of 26 strong or very strong El Niño events identified by Quinn, 16 match with positive anomalies in $\delta^{18}O$, and in four cases the response is unclear (Fig. 4.8 and 4.9).

One of the primary purposes of this thesis was to reconstruct a multi-ice core history of El Niño events using the records from BC and Quelccaya. The results of this analysis were shown to be of limited use because of the weak overall relationship between BC and ENSO events. This analysis shows that the strongest signal in the record of BC1 is the Aleutian Low but that this signal is modulated by the AO so that it doesn’t correspond directly with records that are tropical in origin. The Quelccaya record offers a great deal of promise for future reconstructions of ENSO variability but needs to be paired with other proxy records that exhibit a strong ENSO signal, such as the record of *Quinn* (1987) or the tree ring records from the SW, as a means for cross-verification.

6.3.2 Quelccaya--Bona Churchill comparisons

The time series of $\delta^{18}O$ and d-excess from Quelccaya and BC1 exhibit different large-scale trends, and correlation analysis using a 50-year sliding window shows that strong correlations between these records don't persist for any length of time (Fig. 5.1). An event analysis examining the timing of events in the records of dust and $\delta^{18}O$ from both ice cores shows a general lack of correspondence (Table 5.1). The lack of connection between the ice core variables from Peru and Alaska during both the last 100 years and the last 1,000 years might be the result of the BC record of $\delta^{18}O$ being more strongly related to fluctuations in the AO than in the AL. At the same time, it might result from the fact that the Quelccaya $\delta^{18}O$ record reflects decadal NIÑO 4 variability and seems for the most part disconnected to the lower-frequency regime shifts associated with the Pacific Decadal Oscillation (PDO), which primarily reflects North Pacific variability.

6.3.3 Tree ring and corals

A strong relationship is identified in this chapter between more negative values of Quelccaya $\delta^{18}O$ and drought events in the SW (Fig. 5.9). This analysis shows that out of 24 large drought events during the last 1,000 years, as detailed in Table 5.3, 13 of the events match negative isotopic anomalies, three match positive anomalies, and eight are difficult to define. Previous studies have shown that the precipitation anomalies generated by ENSO in the Southwest are some of the more dependable teleconnections of ENSO (*Cole and Cook,* 1998). Future studies might attempt to verify the link between drought events in the SW and their correspondence to the record of Quelccaya $\delta^{18}O$.

The strongest correlations between Quelccaya $\delta^{18}O$ and Pacific SSTs occur in the northern equatorial Pacific between 150° W to 160° E. A strong relationship is noted between modern corals growing near Palmyra Island (162º W, 6º N) and records of SSTs (*Cobb*, 2001). These coral records are of particular interest, as they lie in the same region where SSTs are most strongly related to Quelccaya $\delta^{18}O$. The time series of modern coral

$\delta^{18}O$ is strongly correlated with Quelccaya $\delta^{18}O$ (r=.62, 1889-1995). However, although the modern coral records exhibit a match (Fig. 5.8), older coral records from the same location do not (Fig. 5.5 to 5.7). A review of fossil corals from other locations points to a dramatic shift in SST/Salinity occurring at the end of the LIA in approximately 1880; this is also clearly demarcated in the Quelccaya record.

APPENDIX A

ALASKAN WEATHER DATA

A.1 Gulkana

Gulkana is located on the east side of the Copper River Basin and to the west of the Wrangell-St. Elias Mountains. The station lies at an elevation of 479 meters and is positioned at 62º 9' N, 145º 28' W. The period of record is from 1949 to the present and is 98% complete Desert Research Institute (DRI). Monthly and daily data were obtained from the National Climate Data Center (NCDC).The temperature record shows a strong positive trend during the period of record. This trend may be due to small changes in the location of actual data collection, as colder stations have been eliminated in favor of warmer ones (climate.gi.alaska.edu/History/CopperValley/Gulkana.html).

The highest average maximum temperature, 20º C, occurs in July, and the lowest average maximum temperature, -16º C, occurs in January. Average total precipitation peaks in June with 4.6 centimeters, and a secondary peak in precipitation occurs in December with 2.2 centimeters. The lowest amount of precipitation is in April, with 0.5 centimeters, and a secondary low occurs in November, when 1.8 centimeters accumulate. The primary summer (May to October total) peak accounts for 3.7 times more precipitation that the smaller secondary winter peak (December to March total).

A.2 Chitina

The Chitina weather station is positioned at 61º 32' N, 144º 27' W. The elevation at the recording site is approximately 190 meters. The actual site of the weather station has changed in location through time. At its highest, the elevation of the recording site was 183 meters, and the lowest elevation was 174 meters (NCDC). The period of record is from August 1950 until May 1971. The record is 76% complete (DRI). The highest average maximum temperature of 19.5º C occurs in July, and the lowest average maximum temperature of –18º C occurs in January. Precipitation peaks in December, when 4.1 centimeters accumulate, and a secondary peak occurs in September, when 3.4 centimeters accumulate. Minima in precipitation occur in April, when 0.4 centimeters accumulate, and in October, when 2.8 centimeters accumulate (DRI).

A.3 McCarthy 3 SW

(Note: Two identifiers for McCarthy data: McCarthy 3 SW and McCarthy 1 NE.)

This is located at 61º 25' N, 143º 0' W, with an elevation of 381 meters. Both monthly and daily data are available during the period of record from October 1983 to August 2001 (NCDC) and are 94% complete (DRI). The highest average max temperature of 22º C occurs in July, and the lowest average maximum temperature of –14º C occurs in January. Precipitation peaks in September, when 7.6 centimeters accumulate, and a secondary peak occurs in December, when 5.1 centimeters accumulate. Minima in precipitation occur in April, when 0.6 centimeters accumulate, and in November, when 2.9 centimeters accumulate (DRI).

A.4 Mc Carthy 1 NE

This is located at 61º 26' N, 142º 54' W, with an elevation of 469 meters. The period of record is from June 1956 to March 1983 (NCDC). The climatology of McCarthy 1 NE is similar to that of McCarthy 3 SW, as both stations are in close proximity to each other.

A.5 Kennecott

This is located at 61º 29' N, 142º 53' W, with an elevation of 674 meters. The period of record is from January 1922 until December 1947 (NCDC). The climatology of Kennecott is similar to that of McCarthy 3 SW, as the stations are in close proximity to each other.

A.6 Paxson

This is located at 63º 02' N, 145º 30' W, with an elevation of 823 meters. The period of record is from January 1960 to present (NCDC). The record is approximately

80% complete. The highest average maximum temperature of 19º C occurs in July, and the lowest average maximum temperature of –13º C occurs in January. Precipitation peaks in July, when 8.1 centimeters accumulate, and a secondary peak occurs in December, when 3.6 centimeters accumulate. Minima in precipitation occur in April, when 1.5 centimeters accumulate, and in November, when 2.8 centimeters accumulate (DRI).

A.7 NCEP/NCAR data sets

NCEP-NCAR reanalysis data for total air column perceptible water (P_{wat}) and data for pressure level temperatures at 200mb, 300mb, 400mb, 500mb, 700mb, 850mb, and 925mb were obtained for calibration purposes. The monthly means of these data sets were obtained for the period 1949 to 2003 for the grid point nearest the Bona-Churchill (BC) drilling site (140º W, 60º N). Strong positive correlations are present between the 925mb temperatures and the winter temperature series from the Alaskan Long Composite (ALC) (r=0.89, 1953-2001) and from the Alaskan Short Composite (ASC) (r=0.81, 1953-2001). The similarity between the two different records both derived using different methods verifies the ability of both of the composite time series to successfully replicate interannual temperature variability in the vicinity of the drilling site. The NCEP-NCAR reanalysis time series demonstrates the varying response of precipitation to temperature with elevation. A negative correlation (r=-0.7, 1953-2001) is found between ALC winter precipitation and 200mb temperatures. A positive correlation (r=0.7, 1953-2001) is present between 925mb temperatures and ALC winter precipitation. This varying relationship is best explained by changes in lapse rate associated with Aleutian Low (AL) variability.

A.8 Construction of Composite Records

A.8.1 The Alaskan Short Composites

The Alaskan Short Composites (ASC) are based upon weather station data from McCarthy, Kennecott, Chitina, Gulkana, and Paxson. Records from the individual weather stations in this data set are of limited use for the purpose of calibration, as most are missing several data points and are of a shorter duration than might be desired. To overcome these limitations, all available station data were combined in order to reconstruct a composite time series of precipitation and temperature from 1923 to 2002. Seasonal divisions of the ASC composite time series were defined by the natural peaks and minima that occur in precipitation during the year, so that winter is defined as the period December through March and summer is defined as May through October (*Urmann*, 2003).

The following steps outline the general procedure for constructing both the ASC and the ALC (discussed in the preceding section):

1. Monthly temperature and precipitation time series for both the winter (December January February--DJF) and summer (June July August--JJA) were individually converted into standardized values (z-scores). The standardized values from the winter and summer months were averaged in order to obtain a JJA and DJF value.

2. The standardized scores for the available station were summed for each year and then divided by the number of stations from which data were available in a given year.

3. To construct 5-year averages, years with missing data (1830-1831, 1878-1880, and 1892-1893) were either extrapolated from the previous year's data or removed entirely. The only major adjustment was made for the ALC precipitation time series, where the years 1878-1880 were removed. The winter of 1877 was a record-setting winter, and all three stations in the composite exhibit the highest precipitation totals in the entire period of record. Because data are missing for the years following this precipitation extreme, it didn't make sense to extrapolate those values across a series of years.

A.8.2 The Alaska Long Composite (ALC)

The ALC is based on a subset of data from the Alaska Historical Climate Network (AHCN) (Table A.1). The AHCN consists of 47 station records extending from 1828 to 1990. This data set includes the longest record of climate for the entire west coast of the Americas, and it comes from the Sitka Magnetic Station, where records have been kept on a discontinuous basis since 1828. Almost every year between 1828 and 1990 is represented by some type of meteorological measurement from at least one of the stations in the network (some exceptions are 1830-1831, 1879-1880, and 1892-1893).

Composite time series of DJF precipitation and both DJF and JJA temperatures were constructed in order to obtain lengthy and continuous records of these time series. The winter temperature composite is based on 33 stations, and the summer temperature composite is based on 27 stations. The Pierson coefficients (r values) calculated for the correlations between the composite time series and the individual winter and summer time series averaged 0.86 and 0.735, respectively. Time series of precipitation in general display greater regional variability, and as a result this composite is based on the sum of just three station time series that showed a high degree of intercorrelation. The selection of the three individual stations was based on both the length of record available and the strength of correlation between the record and the ASC. The ALC of precipitation is based on station data from the Sitka Magnetic Station, Wrangell, and Juneau. This series is strongly correlated (r=0.68, 1924-1990) with the ASC precipitation composite described in the previous section.

Comparisons of the ALC time series with regional teleconnections indices show that ALC winter temperatures are negatively correlated (r=-0.8, 1900-1990) with the strength of the AL and that weaker but significant correlations exist with Niño 3.4 temperatures (r=0.34, 1900-1990) and the Pacific Decadal Oscillation (PDO) (r=0.65, 1923-2002). Unlike the Alaskan Short Composite (ACS), a strong negative correlation is observed between the AL and DJF precipitation (r=-0.59, 1900-1990). Regression analysis comparing the ACS time series with regional teleconnections indices shows that ASC winter temperatures are strongly negatively correlated (r=-0.7, 1923-1995) with the strength of the AL, and weaker but significant correlations are also observed with Niño 3.4 temperatures (r=0.34, 1923-2002) and the PDO (r=0.45, 1923-2002). Of note is the lack of a significant correlation between winter precipitation in the Wrangell region and the strength of the AL. This contrasts with the ALC time series, which is primarily based on data from coastal stations. One possibility is that the coastal stations (ALC) are subject to more of a direct flow from the Pacific, whereas the ASC station data are primarily derived from low-elevation sites in the interior valleys where precipitation patterns are strongly impacted by the rain shadow effect created by the Chugach Mountains.

Stations in Winter Composite	(r)	Stations in Summer Composite	(r)
Allakaket	0.66	Anchorage	0.76
Anchorage	0.94	Bethel	0.68
Annette	0.85	Bettles	0.70
Annex Creek	0.89	Big Delta	0.82
Bethel	0.71	Cordova	0.72
Bettles	0.90	Eagle	0.61
Big Delta	0.97	Fairbanks	0.69
Cordova	0.87	Gulkana	0.74
Eagle	0.87	Haines	0.75
Fairbanks	0.93	Holy Cross	0.74
Gulkana	0.85	Homer	0.81
Haines	0.89	Juneau	0.63
Holy Cross	0.81	Kenai	0.62
Homer	0.95	King Salmon	0.72
Juneau	0.86	Kodiak	0.64
Kenai	0.96	Little Port Walter	0.77
Ketchikan	0.68	Matanuska	0.82

Continued

Table A.1 A list of stations that were used in the reconstruction of the ALC. Also reported are the r values for the correlation between the composite time series and individual stations.

Table A.1 continued

Stations in Winter Composite	(r)	Stations in Summer Composite	(r)
King Salmon	0.86	McGrath	0.81
Kodiak	0.86	McKinley Park	0.74
Kotzebue	0.68	Nome	0.64
Little Port Walter	0.92	St. Paul Island	0.76
Matanuska	0.95	Seward	0.72
McGrath	0.91	Sitka Magnetic Observatory	0.85
McKinley Park	0.93	Talkeetna	0.89
Nome	0.73	Tanana	0.79
Seward	0.93	Fairbanks	0.71
Sitka Observatory	0.89	Yakutat	0.71
Talkeetna	0.94		
Tanana	0.92		
Fairbanks	0.89		
Valdez	0.74		
Wrangell	0.86		
Yakutat	0.86		

Year	VEI	Location	BC Sulfate	BC Fluoride	Dye 3	GRIP	Name of Volcano	Uncertainty associated with eruption date
1977	4	Alaska					Spurr	
1976		Alaska	x	x-			Augustine	
1975	4	Kamchatka	x	x-			Kliuchevskoi	
1973	4	Kuriles					Sarychev Peak	
1912	6	Alaska Peninsula	x	x		x-	Katmai	
1907	5	Kamchatka					SHIVELUCH	
1907	5	Kamchatka Peninsula					KSUDACH	
1906		N/A	x-	x-	x			
1883	4	Alaska					Augustine	
1883	6	Indonesia					KRAKATAU	
1882		N/A	x-?	x-?				
1877	4	Japan - Ryukyu Islands					IRIOMOTE-JIMA	
1875	5	Northeastern Iceland					ASKJA	
1872	4	Kuriles					Chikurachki	
1869		N/A		x				
1856	4	Japan - Honshu					ASAMA	
1854	5	Alaska					Hayes* (dating?)	
1854	5	Kamchatka Peninsula					SHIVELUCH	

Continued

Table A.2 Compares timing of known eruptions and those identified in BC1, Dye 3, and GRIP from 1795 to 1980. Shown are (A) years of known eruptions and in cases where the eruption was only identified in BC1, the BC1 timeline was used; (B) the VEI; (C) checked if the event is indicated in BC1 Sulfate (the magnitude of the event in the ice core records is indicated as small or large by “x- or x+”); (D) checked if the event is indicated in BC1 Sulfate; (E) checked if the event was found in Dye 3 record; (F) checked if the event is indicated in GRIP record.

(F) = Name of volcano, if known; (G) = Uncertainty with the date, if any.

Table A.2 continued

Year	VEI	Location	BC Sulfate	BC Fluoride	Dye 3	GRIP	Name of Volcano	Uncertainty associated with eruption date
1853	4	Japan - Hokkaido					KOMAGA-TAKE	
1853	5	Kamchatka					Ksudach	
1853	5	Kurile Islands					CHIKURACHKI	
1835	5	Nicaragua					COSIGUINA	
1830		N/A	x-	x				
1829	4	Kamchatka					Kliuchevskoi	
1827	4	Kamchatka					Avachinsky	
1825	4	Alaska					Anianchak	
1822	4	Japan - Hokkaido	x-	x-			KOMAGA-TAKE	
1822	5	Indonesia - Java					GALUNGGUNG	
1815	7	Indonesia - Lesser Sunda Islands	x-?		x- 1816	x- 1816	TAMBORA	
1813	4	Japan - Ryukyu Islands					SUWANOSE-JIMA	
1810		Unknown?				x-		
1800	5	US - Washington					ST. HELENS	
1797		N/A	x-	x-				
1795	4	Kuriles					Chirpoi	

Year	VEI	Location	BC Sulfate	BC Fluoride	Dye 3	GRIP	Name of Volcano	Uncertainty
1795	4	Alaska					Pavlof Sister, Westdahl	
1793	4	Kamchatka					Ksudach	
1786	4	Kuriles					TiaTia	
1783		Iceland	x+		x+	x+	Laki	
1783	4	Japan - Izu Islands					OSHIMA	
1779	4	Japan - Ryukyu Islands					SUWANOSE-JIMA	
1778	4	Kuriles					Sinarka	
1769	4	Japan - Hokkaido					USU	
1765	3	Kamchatka					Koshelev	
1763	4	Japan - Kyushu					SAKURA-JIMA	
1762	4	Alaska					Augustine	
1750	6	Alaska					Katmai	
1741	4	Japan - Hokkaido					USU	
1739	5	Japan - Honshu					FUJI	
1739	5	Japan - Hokkaido					SHIKOTSU	
1734		N/A	x-					
1713	3	Kamchatka					Kliuchevskoi	
1712	4	Kuriles					Raikoke	
1712	4	Kurile Islands					CHIRPOI	
1707	6	Alaska					Veniaminof* (dating?)	
1707	5	Japan - Honshu					FUJI	

Continued

Table A.3 Compares timing of known eruptions and those identified in BC1, Dye 3, and GRIP from 1648 to 1795. Shown are (A) Years of known eruptions, and in cases where the eruption was only identified in BC1, the BC1 timeline was used; (B) the VEI; (C) checked if the event is indicated in BC1 Sulfate (the magnitude of the event in the ice core records is indicated as small or large by “x- or x+”); (D) checked if the event is indicated in BC1 Sulfate; (E) checked if the event was found in Dye 3 record; (F) checked if the event is indicated in GRIP record.

(F) = Name of volcano, if known, (G) = Uncertainty with the date, if any.

Table A.3 continued

Year	VEI	Location	BC Sulfate	BC Fluoride	Dye 3	GRIP	Name of Volcano	Uncertainty
1705		N/A		x-				
1697	3	Alaska					Isanotski	
1694	4	Japan - Hokkaido					USU	
1691		N/A	x	x				
1690	3	Alaska					Amukta	
1690	4	Kuriles					SARYCHEV PEAK	
1685		N/A	x-	x-				1685/86
1680	5	Indonesia - Sulawesi					TONGKOKO	
1673	5	Indonesia - Halmahera					GAMKONORA	
1668		N/A	x-	x- (1670)	x-	x-		1667/68
1667	5	Japan - Honshu					ASAMA	
1667	5	Japan - Hokkaido					SHIKOTSU	
1663	5	Japan - Hokkaido					SHIKOTSU	
1663	5	Japan - Hokkaido					USU	
1655	4	Kamchatka					Avachinsky	
1648		N/A	x-	x-				

Year	VEI	Location	BC Sulfate	BC Fluoride	Dye 3	GRIP	Name of Volcano
1642		N/A			x-	x-	
1641	5	Philippines - Mindanao			PARKER		
1640	5	Japan - Hokkaido				SHIKOTSU	
1640	5	Japan - Hokkaido				KOMAGA-TAKE	
1631	5	Italy					VESUVIUS
1630	5	Azores					FURNAS
1624		N/A	x+				
1617		N/A	x+				
1607		N/A	x+	x+			
1600	4	Japan - Ryukyu Islands					SUWANOSE-JIMA
1600	6	Perú					HUAYNAPUTINA
1596		N/A	x+				
1593	5	Indonesia - Java					RAUNG
1586	5	Indonesia - Java					KELUT
1580	6	Bougainville Island					BILLY MITCHELL
1578		N/A	x				
1554		N/A			x-	x-	

Continued

Table A.4 Compares timing of known eruptions and those identified in BC1, Dye 3, and GRIP from 1648 to 1450. Shown are (A) years of known eruptions, and in cases where the eruption was only identified in BC1, the BC1 timeline was used; (B) the VEI; (C) checked if the event is indicated in BC1 Sulfate (the magnitude of the event in the ice core records is indicated as small or large by “x- or x+”); (D) checked if the event is indicated in BC1 Sulfate; (E) checked if the event was found in Dye 3 record; (F) checked if the event is indicated in GRIP record.

(F) = Name of volcano, if known.

Table A.4 continued

Year	VEI	Location	BC Sulfate	BC Fluoride	Dye 3	GRIP	Name of Volcano
1551		N/A	x-				
1552	4	Japan - Kyushu					KIRISHIMA
1550	4	Kamchatka					Tolbachik
1550	5	Japan - Hokkaido					USU
1517		Mt. Logan Core	x-	x+			
1513		N/A			x-	x+	
1510		Iceland					Hekla
1509		N/A			x-	x-	
1487			x+				
1482	5	US - Washington					ST. HELENS
1477		Iceland			x-	x	Bardarbunga
1471	6	Alaska					Aniakchak* (dating?)
1457		N/A			x+		
1450	5	Japan - Hokkaido					KOMAGA-TAKE

Year	VEI	Location	BC Sulfate	BC Fluoride	Dye 3	GRIP	Name of Volcano	Uncertainty
1441		N/A				x		
1432		N/A	x-					
1403		N/A			x+			
1386		N/A	x					
1369		N/A	x					
1362	5	Southeastern Iceland	x-	x+	x+(1360)		ORAEFAJOKULL	1362-1363
1352		N/A	x+					
1339		N/A	x					
1330		N/A	x					
1317		N/A	x	x+				
1310	5	New Zealand					OKATAINA	
1299		N/A	x					
1291		N/A	x					
1277		N/A	x					
1273		N/A	x					
1267	4	Japan - Izu Islands					OSHIMA	
1266		N/A	x					
1259		N/A			x+	x+		
1235	4	Japan - Ryukyu Islands					SUWANOSE-JIMA	

Continued

Table A.5 Compares timing of known eruptions and those identified in BC1, Dye 3, and GRIP from A.D. 1450 to 1000. Shown are (A) years of known eruptions, and in cases where the eruption was only identified in BC1, the BC1 timeline was used; (B) the VEI; (C) checked if the event is indicated in BC1 Sulfate (the magnitude of the event in the ice core records is indicated as small or large by "x- or x+"); (D) checked if the event is indicated in BC1 Sulfate; (E) checked if the event was found in Dye 3 record; (F) checked if the event is indicated in GRIP record.

(F) = Name of volcano, if known; (G) = Uncertainty with the date, if any.

Table A.5 continued

Year	VEI	Location	BC Sulfate	BC Fluoride	Dye 3	GRIP	Name of Volcano	Uncertainty
1229		N/A			x-	x+		
1205		N/A	x					
1179		N/A			x-	x+	Icelandic:Katla	1179-1180
1176		N/A	x					
1155		N/A	x					
1150	6	Ecuador					QUILOTOA	
1113		N/A	x					
1112	4	Japan - Izu Islands					OSHIMA	
1108	5	Japan - Kyushu					SAKURA-JIMA	
1108	5	Japan - Honshu					ASAMA	
1104	5	Southern Iceland			x+	x-	Icelandic: Hekla	1104-1106
1045		N/A	x					
1040	6	Eastern China					BAITOUSHAN	1040-1051
1030	5	Bougainville Island					B. MITCHELL	
1030	5	Kamchatka Peninsula					SHIVELUCH	
1029		N/A	x					

BIBLIOGRAPHY

Abbott, M. B., M. W. Binford, M. Brenner, and K. R. Kelts, A 3500 14C yr high-resolution record of water-level changes in Lake Titicaca, Bolivia/Peru, *Quat. Res.,* 47, 169–180, 1997.

Anderson, L., M. B. Abbott, B. P. Finney, and S. J. Burns, Regional atmospheric circulation change in the North Pacific during the Holocene inferred from lacustine carbonate oxygen isotopes, Yukon Territory, Canada, *Quat. Res.,* 64, 21-35, 2005.

Arendt, A. A., K. A. Echelmeyer, W. D. Harrison, C. S. Lingle, and V. B. Valentin, .Rapid wastage of Alaska glaciers and their contribution to rising sea level, *Science*, 297, 382-386, 2002.

Asami, R., T. Yamada, and Y. Iryu, Interannual and decadal variability of the Western Pacific sea surface condition for the years 1787-2000: reconstruction based on stable isotope record from a Guam coral, *J Geophys Res,* 110, doi: 10.1029/2004jc00205555, 2005.

Baumgartner, T. R., A. Soutar, and V. Ferreira-Bartrina, Reconstruction of the history of Pacific sardine and northern anchovy populations over the last two millennia from sediments of the Santa Barbara Basin, California, CalCOFI Rep. 33, 24-40, 1992.

Biondi, F., A. Gershunov, and D. R. Cayan, North Pacific decadal climate variability since 1661, *Journal of Climate,* 14, 5-10, 2001.

Bjerknes, J., Atmospheric teleconnections from the equatorial Pacific, *Monthly Weather Review*, 97, 163-172, 1969.

Black, D. E., L. C. Peterson, J. T. Overpeck, A. Kaplan, M. N. Evans, and M. Kashgarian, Eight centuries of North Atlantic ocean atmosphere variability, *Science*, 286, 1709-1713, 1999.

Bond, N. A., and D. E. Harrison, ENSO's effect on Alaska during opposite phases of the arctic oscillation, *International Journal of Climatology*, 26, 1821-1841, doi: 10.1002/joc.1339, 2006.

Bradley, R. S., M. Vuille, D. R. Hardy and L. G. Thompson, Low latitude ice cores record Pacific sea surface temperatures, *Geophys Res Lett*, 30(4), 1174-1177, doi: 10.1029/2002GL016546, 2003.

Bradley, R. S., *Paleoclimatology: reconstructing climates of the quaternary*, San Diego: Academic Press, 1999.

Buckley, B. M., P. Kritsadapan, D. Khwanchai, S. Prasong, and P. Patsi, Decadal scale droughts over northwestern Thailand over the past 448 years: links to the tropical Pacific and Indian Ocean sectors, *Clim Dyn,* 29, 63–71, 2007.

Calkin, P. E., G. C. Wiles, and D. J. Barclay, Holocene coastal glaciation of Alaska, *Quaternary Science Reviews*, 20, 449-461, 2001.

Castanheria, J. M., and H. F. Graf, North Pacific-north Atlantic relationships under stratospheric control, *J Geophys Res,* 108, 2574, 2003.

Chang, E. K. M., The impact of wave packets propagating across Asia on Pacific cyclone development, *Mon Weather Rev,* 133, 1998-2015, 2005.

Chang, P., L. Ji, and L. Hong, A decadal climate variation in the tropical Atlantic Ocean from thermodynamic air-sea interactions, *Nature*, 385, 516–518, 1997.

Chepstow-Lusty, A., M. R. Frogley, B. Bauer, M. Bush, and A. Herrera, A late Holocene record of arid events from the Cuzco region, Peru, *Journal of Quaternary Science,* 18(6), 491–502, 2003.

Chylek, P., M. K. Dubey, and G. Lesins, Greenland warming of 1920–1930 and 1995–2005, *Geophys Res Lett*, 33, L11707, doi:10.1029/2006GL026510, 2006.

Clague, J. J., S. G. Evans, V. N. Rampton, and G. J. Woodsworth, Improved age estimates for the White River and Bridge River tephras, western Canada, *Canadian Journal of Earth Sciences,* 32, 1172–1179, 1995.

Clement, A. C., R. Seager, M. A., Cane, and S. E. Ziebiak, An ocean dynamical thermostat, *Journal of Climate*, 9, 2190-2196, 1996.

Cobb, K. M., C. D. Charles,, H. Cheng, and R. L. Edwards, El Nino/Southern Oscillation and tropical Pacific climate during the last millennium, *Nature,* 424, 271-275, 2003.

Cobb, K. M., C. D. Charles, and D. E. Hunter, A central tropical Pacific coral demonstrates Pacific, Indian, and Atlantic decadal climate connections, *Geophys Res Lett,* 28(11), 2209-2212, 2001b.

Cook, E. R., R. Seager, M. A. Cane, and D. W. Stahle, North American drought reconstructions causes and consequences, *Earth-Science Reviews*,81, 93-134, 2007.

Cook, E. R., C. A. Woodhouse, C. M. Eakin, D. M. Meko, and D. W. Stahle, Long term aridity changes in the western United States, *Science*, 306, 1015-1018, 2004.

Cook, E. R., and R. D. D'Arrigo, A well verified, multiproxy reconstruction of the winter North Atlantic Index since 1400 A.D., *Journal of Climate,* 15, 1254-1264, 2001.

Cook, E. R., Nino 3 index reconstruction, in International Tree-Ring Data Bank, ftp://ftp.ngdc.noaa.gov/paleo/treering/reconstructions/nino3_recon.txt, Boulder, CO:, World Data Center-A for Paleoclimatology, 2000.

Cook, E. R., D. M. Meko, D. W. Stahle, and M. K. Cleveland, Drought reconstructions for the continental United States, *Journal of Climate,* 12, 1145-1162.

Cook, E. R., K. R. Briffa, D. M. MekoA. Greybill, and G. Funkhouser, The 'segment length curse' in long tree-ring chronology development for paloeclimate studies, *The Holocene,* 5, 229-237, 1995.

Crowley, T. J., Causes of climate change over the past 1000 years, *Science*, 289, 270-277, 2000.

Crozaz, G., C. C. Langway, and E. Picotto, Artificial radioactivityHorizons in Greenland firn. Research Report #208, Hanover, NH: U.S. Army Cold Regions Research and Engineering Laboratory, 1966.

Covey, C. and P. L. Haagenson, A model of oxygen isotope composition of precipitation: implications for paleoclimate data, *J Geophys Res,* 89(D3), 4647-4655, 1984.

Cyan, D. R., M. D. Dettinger, and H. F. Diaz, Decadal variability of precipitation over western North America, *Journal of Climate*, 11, 3148-3166, 1998.

D' Arrigo, R., R. Wilson, J. Palmer, P. Krusic, A. Curtis, J. Sakulich, S. Bijaksana, S. Zulaikah, L. Ngkoimani, and A. Tudhupe, The reconstructed Indonesian warm pool sea surface temperatures from tree rings and corals: Linkages to Asian monsoon drought and El Nino–Southern Oscillation, *Paleoceanography*, 21, PA3005, doi:10.1029/2005PA001256, 2006.

D'Arrigo, R.D., R.J. Wilson, C. Deser, G. Wiles, E.R. Cook, R. Villlalba, A. Tudhope, J. Cole, and B. Linsley, , Tropical-North Pacific climate linkages over the past four centuries, *Journal of Climate*, 18, 5253-5265, doi:10.1175/JCLI3602.1, 2005.

D'Arrigo, R., R. Wilson, F. Panagiotopoulos, and B. Wu, On the long term interannual variability of the east Asian Winter Monsoon, *Geophys Res Lett,* 32, 23235, 2005.

D'Arrigo, R., E. Cook, R. Wilson, R. Allan, and M. Mann, On the variability of ENSO over the past six centuries, *Geophys Res Lett,* 32, L03711, doi:10.1029/2004GL022055, 2005.

D'Arrigo, R.M., R. Villalba, and G. Wiles, Tree ring estimates of Pacific decadal climate variability, *Climate Dynamics*, 18, 219-224, 2001.

D’Arrigo, R. D., G. Jacony, M. Free, and A. Robock, Northern Hemisphere temperature variability for the past three-centuries: Tree-ring and model estimates, *Climate Change*, 42, 663-675, 1999.

D’Arrigo, R. D., and G. C. Jacoby, A tree ring reconstruction of New Mexico winter precipitation and its relationship to the Southern Oscillation, In: Diaz, H. F., and V. Markgraf, *El Niño: Historical and paleoclimatic aspects of the Southern Oscillation*, New York: Cambridge University Press, 1992

D'Arrigio, R. D., and G. C. Jacoby, A thousand year record of northwestern New Mexico winter precipitation reconstructed from tree rings and its relationship to El Niño and the Southern Oscillation, *Holocene*, 12, 95-102, 1991.

Dai, J., E. Mosley-Thonpson, and L.G. Thompson, Ice core evidence for an explosive tropical eruption 6 years preceding Tambora, *J Geophys Res,* 96, 17,361-17,366, 1991.

Dansgaard, W.,Stable isotopes in precipitation, *Tellus,* 16436-468, 1964.

Dargan, M. W., W. Frierson, J. Lu, G. Chen, Width of the Hadley cell in simple and comprehensive general circulation models, GRL 34, L18804, doi:10.1029/2007GL031115, 2007.

Davi, N. K., G. C. Jacoby, and G. C. Wiles, Boreal temperature variability inferred from maximum latewood density and tree ring data, Wrangell Mountain Region, Alaska, *Quaternary Research,* 60, 252-262, 2003.

deMenocal, P. B., Cultural response to climate change during the late Holocene, *Science,* 292, 668-673, 2001.

de Silva, S. L., J. Alzueta, and G. Salas, In: Heiken, G., and F. McCoy, eds., *Volcanic Disasters in Human Antiquity, Geol. Soc. Am.*, Spec. Paper, 345, 2000.

Diaz, H. F., and R. S. Pulwarty, A comparison of Southern Oscillation and El Niño signals in the tropics. In: Diaz, H. F., and V. Markgraf, *El Niño: Historical and paleoclimatic aspects of the Southern Oscillation*, New York: Cambridge University Press, 1992.

Dole, R. M., and N. M. Gordon, Persistent anomalies of the Extratropical Northern Hemisphere winter time circulation: geographical distribution and regional persistence characteristics, *Monthly Weather Review,* 111, 1567-1586, 1983.

Downes, H., Evidence of magma heterogeneity in the White River ash (Yukon Territory), *Canadian Journal of Earth Sciences,* 22, 929-934, 1985.

Dunbar, R. B., G. M. Wellington, M. W. Colgan, and P. W. Glynn, Eastern Pacific sea surface temperatures since 1600 A.D.: The δ^{18O} record of climate variability in Galapagos corals, *Paleoceanography,* 9, 291-315, 1994.

Dyke, A. S., and J. M. Savaelle, Holocene history of the Bering Sea Bowhead whale (Balaena mysticetus) in its Beaufort Sea Summer Grounds off Southwestern Victoria Island, Western Canadian Arctic, *Quaternary Research,* 55, 371-379, 2001.

Esper, J., E. R., Cook, and F. H. Schweingruber, Low frequency signals in long tree ring chronologies for reconstructing past temperatures, *Science*, 295, 2250-2253, 2002.

Evans, M. N., A. Kaplan, and M. A. Cane, Pacific sea surface temperatures from coral δ^{18}O data using reduced space objective analysis, *Paleoceanography*, 17, 710-713, 2002.

Evans, M. N., M. A. Cane, D. P. Shrag, A. Kaplan, B. K. Linsey, R. Villalba, and G. M. Wellington, Support for tropically driven Pacific decadal variability based on paleoproxy evidence, *Geophys Res Lett,* 28, 3689-3692, 2001a.

Evans, M. N., A. Kaplan, M.A. Cane, and R. Villalba, Globality and optimality in climate field reconstructions from proxy data, In: V. Markgraf, ed., *Inter-hemispheric climate linkages,* Cambridge, UK: Cambridge University Press, 2001b

Finney, B. P., I. Gregory-Evans, M. S. Douglas, and J. P. Smol, Fisheries productivity in the northeastern Pacific Ocean over the past 2200 years, *Nature*, 416, 729-733, 2002.

Finney, B. P., I. Gregory-Evans, J. Sweetman, M. S. V. Douglas, and J. P. Smol, Impacts of climate change and fishing on Pacific Salmon over the past 300 years, *Science*, 290, 795-799, 2000.

Fisher, D. A., C. Wake, K. Kreutz K. Yalcin, P. Mayewski, L. Anderson, J. Zheng, S. Rupper, C. Zdanowicz, M. Demuth, M. Waxkiewicz, D. Dahl-Jensen, K. Gobo-Azuma, J. Bourgeas, R.M. Koerner, J. Sekerka, E. Osterberg, M. Abbott, B.P. Finney, and S.J. Burns, Stable isotope records from Mount Logan and Eclipse ice cores and nearby Jellybean Lake; water cycle of the North Pacific over 2000 years and over 5 vertical kilometers; sudden shifts and tropical connections, *Geographie Physique et Quaternaire,* 58, 9033-9048, 2004.

Fu, Q., C. M. Johanson, J. M. Wallace, and T. Reichler, Enhanced mid-latitude tropospheric warming in satellite measurements, *Science*, 312, 1179, 2006.

Fu, C., H. F. Diaz, D. Dong, and J. O. Fletcher, Changes in atmospheric circulation over northern hemisphere oceans associated with the rapid warming of the 1920s, *International Journal of Climatology*, 19(6), 581-606, 1999.

Gedalof, Z., D. L. Peterson, and N. J. Mantua, Columbia River flow and drought since 1750, *Journal of the American Water Resources Association,* 40 1579-1592, 2004.

Gedalof, Z. and N. J. Mantua, A multi-century perspective of variability in the Pacific decadal oscillation: new insights from tree rings and corals, *Geophys Res Lett*, 29, 15824, 2002.

Gedalof, Z., and D. J. Smith, Interdecadal climate variability and regime-scale shifts in Pacific North America, *Geophys Res Lett,* 28(8), 1515-1518, 2001.

Garreaud, R., M. Vuille, and A. C. Clement, The climate of the Altiplano: observed current conditions and mechanisms of past changes, *Palaeogeo Palaeoclim Palaeoeco*, 194, 5-22, 2003.

Garreaud, R. D., and P. Aceituno, Interannual rainfall variability over the South American Altiplano, *J of Climate*, 14, 2779-2789, 2001.

Grissino-Mayer, H. D., C. H. Baisan, K. A. Morino, and T. W. Swetnam, Multi-century trends in past climate for the Middle Rio Grande Basin, A.D. 622–1992, Report 2002/06, Laboratory of Tree-Ring Science, USDA Forest Service, Rocky Mountain Research Station, New Mexico, 2002.

Grottoli, A. G., and M. C. Eakin, A review of modern coral δ^{18}O and Δ^{14}C proxy records, *Earth Science Reviews,* 81, 67-91, 2007.

Hage, K. D., J. Gray, and J. C. Linton, Isotopes in precipitation in northwestern North America, *Monthly Weather Review,* 103, 958-966, 1975.

Hansen, J., Mki. Sato, R. Ruedy, K. Lo, D.W. Lea, and M. Medina-Elizade, Global temperature change, *Proc Natl Acad Sci*, 103, 14288-14293, doi: 10.1073/pnas.0606291103 14288-14293, doi:10.1073/pnas.0606291103, 2006.

Henderson, K.A., *The El Niño southern oscillation and other modes of interannual tropical climate variability as recorded in ice cores from the Nevado Huascaran Col Peru*, master's thesis, Columbus: The Ohio State University, 1996.

Hendy, E. J., M. K. Gagan, C. A. Alibert, M. T. McCulloch, J. M. Lough, and P. J. Isdale, Abrupt decrease in tropical Pacific sea surface salinity at the end of the LIA, *Science,* 295, 1511-1514, 2002.

Held, I. M., and B. J. Soden, Robust responses of the hydrological cycle to global warming, *J Clim,* 19, 5686-5699, 2006.

Herron, M. M.,. Inpurity sources of F-, Cl-, NO3-, and So42- in Greenland and Antarctic precipitation, *J Geophys Res,* 87(4), 3052-3060, 1982.

Herweijer, C., R. Seager, and E. R. Cook, North American droughts of the mid to late nineteenth century: a history, simulation and implication for Mediaeval drought, *The Holocene*, 16(2), 159-171, 2006.

Herweijer, C., R. Seager, E. R. Cook, and J. Emile-geay, North American droughts of the last millennium from a gridded network of tree-ring data, *Journal of Climate,* 20, 1353-1375, 2007.

Hoerling, M. P., and A. Kumar, The perfect ocean for drought, *Science*, 299, 691–699, 2003.

Hoerling, M. P., and A. Kumar, Atmospheric response patterns associated with tropical forcing, *J. Climate,* 15**,** 2184–2203, 2002.

Hoerling, M. P., and A. Kumar, Understanding and predicting extratropical teleconnections related to ENSO, In: Diaz, H.F., and V. Markgraf, eds., *El Niño and the Southern Oscillation, Multiscale Variability and Regional Impacts*, New York: Cambridge University Press, 2000.

Honrath, R. E., and D. A. Jaffe, Seasonal cycle of nitrogen oxides in the arctic troposphere at Barrow Alaska, *J Geophys Res,* , 97(20), 615-630, 1992.

Hunt, B. G., and T. I. Elliot, Secular variability of ENSO in a 1000-yr climate simulation, *Climate Dynamics,* 20, 689-703, 2003.

Huth, R., Pacific centre of the arctic oscillation*:* product of high local variability rather than teleconnectivity*, Tellus*, 58A, 601-604, 2006.

Jones, P. D., and M. E. Mann, Climate over the past millennia, *Journal of Climate,* 17(4), 711-726, RG2002, doi: 10.1029/2003RG000143, 2004.

Jhun, J., and E. Lee, A new east Asian winter monsoon index and associated characteristics of the winter monsoon, *Journal of Climate,* 17(4), 711, 2004.

Juillet-Leclerc, A., and H. Schrader, Variations of upwelling intensity recorded in varved sediment from the Gulf of California during the past 3000 years, *Nature*, 329, 146-149, 1987.

Keen, F. P., Climatic cycles in eastern Oregon as indicated by tree rings, *Monthly Weather Review*, 65, 175-188, 1937.

Kekonen, T., J. C. Moore, R. Mulvaney, E. Isaksson, V. Pohjola, and R. S.W.Van De Wal, A 800 year record of nitrate from the Lomonosovfonna ice core, Svalbard, *Annals of Glaciology,* 35, 261-265, 2002.

Kennett, J. P., and B. L. Ingram, A 20,000-year record of ocean circulation and climate change from the Santa Barbara basin, *Nature*, 277, 510-513, 1995.

Klotzbach, P. J., and W. M. Gray,: Updated 6-11 month prediction of Atlantic basin seasonal hurricane activity, *Weather and Forecasting*, 19, 917-934, 2004.

Knapp, P. A., P. T. Soule, H. D. Grissino-Mayer, Occurrence of sustained droughts in the interior Pacific Northwest (A.D. 1733-1980) inferred from tree-ring data, *Journal of Climatology,* 17, 140-150, 2003.

Knapp, P. A., P. T. Soule, and H. D. Grissino-Mayer, Climatic regionalization and the spatio-temporal occurrence of extreme single-year drought events (100-1998) in the interior Pacific Northwest, USA, *Quat. Res.,* 58, 226-233, 2002.

Kreutz, K. J., P. A., Mayewski, L. D., Meeker, M. S., Twickler, S. I. Whitlow, and , I. I. Pittalwala, Bipolar changes in atmospheric circulation during the Little Ice Age, *Science,* 277(5330), 1294-1296, doi: 10.1126/science.277.5330.1294, 1997.

Laird, K. R., S. C. Fritz, K. A. Maasch, and B. F. Cumming, Greater drought intensity and frequency before A.D. 1200 in the Northern Great Plains, U.S.A., *Nature*, 384, 552-554, 1996.

Latif, M., R. Kleeman, and C. Eckert, Greenhouse warming, decadal variability or El Niño? An attempt to understand the anomalous 1990s, *J. Climatology,* 10, 2221-2239, 1997.

Lamoureux, S. F., and J. M. H. Cockburn, Timing and controls over neoglacial expansion in the northern coast mountains, British Columbia, Canada, *The Holocene*, 15, 619-624, 2005.

Legrand, M., and P. Mayewski, Glaciochemistry of polar ice cores: a review, *Reviews of Geophysics,* 35(3), 219-243, 1997.

Lerbekmo, J. F., and F. A. Campbell, Distribution, composition, and source of the White River ash, Yukon Territory, *Canadian Journal of Earth Sciences*, 6, 109-116, 1969.

Leonard, E. M., The relationship between glacial activity and sediment production: evidence from a 4450-year varve record of neoglacial sedimentation in Hector Lake, Albert, Canada, *Journal of Paleolimnology,* 17, 319-330, 1997.

Linsley, B. K., G. M. Wellington, D. P. Schrag, L. Ren, M. J. Salinger, and A. W. Tudhope, Geochemical evidence from corals for changes in the amplitude and spatial pattern of South Pacific interdecadal climate variability over the last 300 years, *Climate Dynamics*, 22, 1-11, 2004.

Linsley, B. K., G. M. Wellington, and D. P. Schrag, Decadal sea surface temperature variability in the sub-tropical South Pacific from 1726 to 1997, *Science*, 290, 1145-1148, 2000.

Liu, K., C. A. Reese, and L. G. Thompson, Ice-core pollen record of climatic changes in the central Andes during the last 400 yr, *Quaternary Research*, 64, 272-278, 2005.

Lohmann, K., and M. Latif, Tropical Pacific variability and the subtropical-tropical cells, *Journal of Climate,* 18, 5163-5178, 2005.

Lough, J. M., An index of the southern oscillation reconstructed from western North American tree ring chronologies,, In: Diaz, H. F., and V. Markgraf, *El Niño: Historical and paleoclimatic aspects of the Southern Oscillation*, New York: Cambridge University Press, 1992.

Lough, J. M., and H. C. Fritts, The southern oscillation and tree rings: 1600-1961, *Journal of Climate Applied Meterology,* 24, 952-966, 1985.

Luchin. V. A., I. P. Semiletov, and G. E. Weller, 2(X)2: changes in the Bering Sea region: atmosphere-ice-water system in the second half of the twentieth century, *Progress in Oceanography,* 55(1-2), 23-44, 2002.

Luckman, B. H., K. R. Briffia, P. D. Jones, and F. H. Schweingruber, Tree ring-based reconstructions of summer temperatures at the Columbia Icefield, Alberta, Canada, *The Holocene*, 7, 375-389, 1997.

Luckman, B. H.,. The Little Ice Age in the Canadian Rockies, *Geomorphology*, 32, 357-384, 2000.

Luckman, B. H.,. Neoglacial fluctuations in the Canadian Rockies, *Quaternary Research,* 39, 144-153, 1993.

Lukas, J. J., M. K. Hugher, and M. W. Salzer, Medieval drought in the upper Colorado River Basin, *Geophys Res Lett*, 34, L10705, doi: 10.1029/2007GL029988, 2007.

McCabe, G. J., and M. D. Dettinger, , Summary: Primary modes and predictability of year-to-year snowpack variations in the western United States from teleconnections with Pacific Ocean climate, *Journal of Hydrometeorology,* 3, 13-25, 2002.

MacDonald, G. M., and R. A. Case, Variations in the Pacific Decadal Oscillation over the past millennium, *Geophys Res Lett,* 32, L08703, doi: 10.1029/2005GL022478, 2005.

Mann, M. E., M. A. Cane, S. E. Zeibak, and A. Clement, Volcanic and solar forcing of the tropical Pacific over the past 1000 years, *Journal of Climate,* 18, 447-456, 2005.

Mann, M. E., R. S. Bradley, and M. K. Hughes, Global-scale temperature patterns and climate forcing over the past six centuries, *Nature*, 392, 779-787, 1998.

Mann, M. E., E. Gille, R. S. Bradley, M. K. Hughes, J. Overpeck, F. T. Keimig, and W. Cross, Global temperature patterns in past centuries: An interactive presentation, *Earth Interact.,* 4, 1-29, 2000.

McGimsey, R. G., D. H. Richter, G. D. DuBois, and T. P. Miller,A postulated new source of the White River ash, Alaska, In: Bradley, D. C., and A. C. Ford, eds., *Geological Studies in Alaska*, United States Geological Survey, Bulletin 1999, 212-218, 1992.

Mantua, N. J., Pacific-Decadal Oscillation (PDO), In: McCracken, M. C., and J. S. Perry, eds., *The Encyclopedia of Global Environmental Change, Volume 1, The Earth System: Physical and Chemical Dimension of Global Environmental Change*,, Winchester, England: John Wiley and Sons, Ltd.,, 2002.

Mantua, N. J., and S. R. Hare, The Pacific Decadal Oscillation, *J. Oceanogr.,* 58, 35-44, 2002.

Mantua, N. J., S. R. Hare, Y. Zhang, J. M. Wallace, and R. C. Francis, A Pacific interdecadal climate oscillation with impacts on salmon production, *Bull. Am. Meteorol. Soc.,* 78(6), 1069-1079, 1997.

Meeker, L. D., and P. A. Mayewski, A 1400-year high-resolution record of atmospheric circulation over the North Atlantic and Asia, *The Holocene,* 12, 257-266, 2002.

Meko, D. M., and C. A. Woodhouse, Tree-ring footprint of joint hydrologic drought in Sacramento and Upper Colorado River basins, western USA, *Journal of Hydrology,* 308, 196-213, 2005.

Melice, J. L., and P. Roucou, Decadal time scale variability recorded in the Quelccaya Summit Ice Core δ^{18}O isotopic ratio series and its relation with sea surface temperatures, *Climate Dynamics*, 14, 117-132, 1998.

Mestas-Nunex, A. M., and D. B. Enfield, Rotated global modes of non-ENSO sea surface temperature variability, *J. Climate*, 12, 2734, 1999c.

Michaelsen, J., and L. G. Thompson, A comparison of proxy records of El Niño/Southern Oscillation, In: Diaz, H. F., and V. Markgraf, *El Niño: Historical and paleoclimatic aspects of the Southern Oscillation,* New York: Cambridge University Press, 1992.

Minobe, S., A 50-70 year climatic oscillation over the North Pacific and North America, *Geophys Res Lett,* 24, 683-686, 1997.

Mock, C. J., P. J. Bartlein, and P. M. Anderson, Atmospheric circulation patterns and spatial climatic variations in Beringia, *Int J Climatol*, 10, 1085-1104, 1998.

Molnia, B. F., Late nineteenth to early twenty-first century behavior of Alaskan glaciers as indicators of changing regional climate, *Global and Planetary Change*, 56, 23-56, 2008.

Moore, G. W. K., G. Holdsworth, and K. Alverson, The impact that elevation has on the ENSO signal in precipitation records from the Gulf of Alaska Region, *Climate Change*, 59, 101-121, 2003.

Moore, G. W. K., G. Holdsworth, and K. Alverson, Climate change in the North Pacific region over the past three centuries, *Nature*, 420, 401-403, 2002.

Moore, G. W. K., G. Holdsworth, and K. Alverson, Extra-tropical response to ENSO as expressed in an ice core from the Saint Elias Mountain Range, *Geophys Res Lett*, 28, 3457-3460, 2001.

Monaghan, M. C., and G. Holdsworth, The origin of non-sea-salt sulfate in the Mt. Logan ice core, *Nature*, 343, 245-248, 1990.

Nakamura, H., G. Lin, and T. Yamagata, Decadal climate variability in the North Pacific during the recent decades, *Bull. Amer. Meteor. Soc.,* 78, 2215-2225, 1997.

Nash, J. M., *El Niño unlocking the secrets of the master weather-maker*, New York: Warner Books, , 2002.

Ortlieb, L., The documented historical record of El Niño events in Peru: An update of the Quinn record (sixteenth through nineteenth centuries), In: Diaz, H., and V. Markgraf, eds., *El Niño and the southern oscillation: multiscale variability and global and regional impacts*, New York: Cambridge Univ. Press, 2000.

Overland, J. E., J. M. Adams, and N. A. Bond, Decadal variability of the Aleutian Low and its relation to high-latitude circulation, *J. Climate*, 12, 1542-1548, 1999.

Panagiotopoulos, F., M. Shahgedanova, A. Hannach, and D. B. Stephenson, Observed trends and teleconnections of the Siberian High: A recently declining center of action, *Journal of Climate*, 18, 1411-1422, 2005.

Papineau J. M., Wintertime temperature anomalies in Alaska correlated with ENSO and PDO, *International Journal of Climatology,* 21, 1577-1592, 2001.

Pederson, G.T., Long-term perspectives on northern Rockies climatic variability from tree rings in Glacier National Park, Montana, M.S. thesis, Montana State University, Bozeman, 2004.

Pohl, K. A., K. S. Hadley, and K. B. Arabas, A 545-year drought reconstruction for central Oregon, *Physical Geography,* 23(4), 302-320, 2002.

Quinn, W. H., V. T. Neal, and S. E. Antunez de Mayolo, El Niño occurrences over the past four and a half centuries, *J Geophys Res*, 92, 14,449-14,461, 1987.

Quinn, W. H., The study of Southern oscillation-related climate activity from A.D. 622-1900 incorporating Nile River Flood data, In: Diaz, H. F., and V. Markgrat, eds., El Nino, Historical and Paleoclimatic Aspects of the Southern Oscillation, Cambridge: Cambridge University Press, 1992.

Rahn, K., R. D. Borys, and G. E. Shaw, The Asian source of arctic haze, *Nature*, 268, 713-715, 1977.

Rasmusson, E. M. and T. H. Carpenter,: Variations in tropical sea-surface temperature and surface wind fields associated with the Southern Oscillation/El Niño. *Monthly Weather Review*, 110, 354-384, 1982.

Renwick. J. A., and J. M. Wallace, Relationships between North Pacific wintertime blocking, El Niño, and the PNA pattern, *Mon. Wea. Rev.,* 124, 2071-2076, 1996.

Richter, D. H., S. J. Preece, R. G. McGIMSEY, and J. A. Westgate, Mount Churchill, Alaska: The source of the late Holocene White River ash, *Canadian Journal of Earth Sciences*, 32, 741-748, 1995.

Rind, D., The sun's role in climate variability, *Science*, 296, 673-676, 2002.

Robertson, A. W., and M. Ghil, Large-scale weather regimes and local climate over the western United States, *Journal of Climate*, 12, 1796-1813, 1999.

Robinson, D, P., R. X. Black, and B. A. McDaniel, A Siberian precursor to midwinter intraseasonal variability in the North Pacific storm track, *J Geophys Res*, 33, 26458, 2006,

Rodionov S. N., J. E. Overland, and N. A. Bond, The Aleutian Low and winter climatic conditions of the Bering Sea, Part I: Classification, *Journal of Climate,* 18, 160-177, 2005.

Rogers, J. C., The North Pacific oscillation, *Journal of Climatology*, 1, 39-57, 1981.

Rossby, C. G., Relations between variations in the intensity of the zonal circulation of the atmosphere and the displacements of the semipermanent centers of action, *J. Mar. Res.*, 3, 38-55, 1939.

Ruper, S., E. J. Steig, and G. Roe, The relationship between snow accumulation at Mt. Logan, Yukon, Canada and climate variability in the North Pacific, *Journal of Climate*, 17, 4724-4739, 2004.

Salinger, M. J., B. B. Fitzharris, J. E. Hay, P. D. Jones, J. P. MacViegh, and I. Schmidley-Leleu,. Climate trends in the southwest Pacific, *International Journal of Climatology*, 21, 1705-1721, 1995.

Salzer, M. W., and K. F. Kipfmueller, Reconstructed temperature and precipitation on a millennial timescale from tree rings in the southern Colorado Plateau, *Climatic Change*, 70, 465-487, 2005.

Seager, R., M. Ting, I. Held, Y. Kushnir, J. Lu, G. Vecchi, H. Huang, N. Harnik, A. Leetma, N. Lau, C. Li, J. Velez, and N. Naik, Model projections of an imminent transition to a more arid climate in southwestern North America, *Science*, 316, 1181-1184, 2007.

Shiraiwa, T., S. Kanamori, C. Benson, D. Solie, and Y. D. Muravyev, Shallow ice-core drilling at Mount Wrangell, Alaska, *Bulletin of Glaciological Research*, 21, 71-77, 2004.

Siegenthaler, U., H. Oeschger, U. Schotterer, and K. Hänni, Conversion of water to a counting gas for low-level tritium measurements by means of aluminium carbide, *International Journal of Applied Radiation and Isotopes*, 26, 459-464, 1975.

Simkin, T., and L. Siebert, *Volcanoes of the World*, 2nd ed.,Tucson, AZ: Geoscience Press (in association with the Smithsonian Institution Global Volcanism Program), 1994.

Spooner, I. S., S. Barnes, K. B. Baltzer, R. Raeside, G. D. Osborn, and D. Mazzucchi, The impact of air mass circulation dynamics on Late Holocene paleoclimate in northwestern North America, *Quaternary International*, 108, 77-83, 2002.

Stabeno, P. J., D. K. Kachel, N. A. Kachel, and M. A. Sullivan, Observations from moorings in the Aleutian passes: Temperature, salinity, and transport, *Fish. Oceanogr.*, 14(suppl. 1), 39-54, 2004.

Stahle, D. W., E. R. Cook, M. K. Cleaveland, M. D. Therrell, D. M. Meko, H. D. Grissino-Mayer, E. Watson, and B. H. Luckman, Tree-ring data document 16th century megadrought over North America, EOS, *Transactions of the American Geophysical Union*, 81(12), 121 and 125, 2000.

Stahle, D. W., M. K. Cleaveland, M. D. Therrell, D. A. Gay, R. D. D'Arrigo, P. J. Krusic, E. R. Cook, R. J. Allan, J. E. Cole, R. B. Dunbar, M. D. Moore, M. A. Stokes, B. T. Burns, J. Villanueva-Diaz, and L. G. Thompson, Experimental dendroclimatic reconstruction of the Southern Oscillation, *Bull. Am. Meteorol. Soc.,* 79, 2137-2152, 1998.

Steffensen, J. P., Analysis of the seasonal variation in dust, CL-, NO3- and SO42- in two central Greenland firn cores, *Annals of Glaciology*, 10, 171-177, 1988.

Stine, S., Extreme and persistent drought in California and Patagonia during medieval time, *Nature*, 369, 546-549, 1994.

Szeicz, J. M., and G. M. MacDonald, Dendroclimatic reconstructions of summer temperature in northwestern Canada since A.D. 1638 based on age-dependent modeling, *Quaternary Research*, 44, 257-266, 1995.

Thompson, D. W., and J. M. Wallace, The Arctic oscillation signature in the wintertime geopotential height and temperature fields, *GeophysRes Lett,* 25, 1297-1300, 1998.

Thompson, D. W. J., and J. M. Wallace, Regional impacts of the Northern Hemisphere annular mode, *Science*, 293, 85-89, 2001.

Thompson, L. G., E. Mosley-Thompson, and B. M. Arnao, El Niño-Southern oscillation events recorded in the stratigraphy of the tropical Quelccaya Ice Cap, Peru, *Science*, 226, 50-53, 1984.

Thompson, L. G., E. Mosley-Thompson, J. F. Bolzan, and B.R. Koci, A 1500-year record of climate variability recorded in ice cores from the tropical Quelccaya Ice Cap, *Science*, 229(471), 971-973, 1985.

Thompson, L. G., E. Mosley-Thompson, W. Dansgaard, and P. M. Grootes, The "Little Ice Age" as recorded in the stratigraphy of the tropical Quelccaya ice cap, *Science*, 234, 361-364, 1986.

Thompson, L. G., Ice core evidence for climate change in the Tropics: implications for our future, *Quaternary Science Reviews*, 19, 19-35, 2000.

Thompson, L. G., E. Mosley-Thompson, H. Brecher, M. E. Davis, B. León, D. Les, P. Lin, T. Mashiotta, and K. Mountain, Abrupt tropical climate change: past and present, *Proc. Natl. Acad. Sci.,* 103, 10536-10543, 2006.

Thompson, L. G., E. Mosley-Thompson, M. E. Davis, K. A. Henderson, H. H. Brecher, V. S. Zagorodnov, T. A. Mashiotta, P.-N. Lin, V. N. Mikhalenko, D. R. Hardy, and J. Beer, Kilimanjaro ice core records: Evidence of Holocene climate change in tropical Africa, *Science*, 298, 589-593, 2002.

Thompson, L. G., E. Mosley-Thompson, and P. A. Thompson, Reconstructing interannual climate variability from tropical and subtropical ice-core records, In: Diaz, H. F., and V. Markgraf, *El Niño: Historical and paleoclimatic aspects of the Southern Oscillation,* New York: Cambridge University Press, 1992.

Timmermann, A., J. Oberhuber, A. Bacher, M. Esch, L. Latif, and E. Roeckner, Increased El Niño frequency in a climate model forced by future greenhouse warming, *Nature*, 398, 694-668, 1997.

Tsonis, A. A., J. B. Elsner, A. G. Hunt, and T. H. Jagger, Unfolding the relation between global temperature and ENSO, *Geophys Res Lett,* 32, L09701, doi: 10.1029/2005GL022875, 2005.

Tunicliffe, V., J. M. O'Connell, and M. R. McQuoid, A Holocene record of marine fish remains from the northeastern Pacific, *Mar. Geol.*, 174, 197-210, 2001.

Urban, F. E., J. E. Cole, and J. T. Overpeck, Influence of mean climate change on climate variability from a 155-year tropical Pacific coral record, *Nature*, 407 989-993, 2000.

Urmann, D., ENSO and PDO variability in ice core and lake level records over the past century, master's thesis, The Ohio State University, 196, 2004.

VanCuren, R. A., and T. A. Cahill, Asian aerosols in North America: Frequency and concentration of fine dust, *J Geophys Res*, 107(D24), 4804, 2002.

Veniaminoc, I., *Notes on the Islands of the Unalashka District*, Kingstone, Ontario: Limestone Press, 1984.

Verdon, D., and S. W. Franks, Long-term behaviour of ENSO: Interactions with the PDO over the past 400 years inferred from paleoclimate records, *Geophys Res Lett*, 33, L06712, doi: 10.1029/2005GL025052, 2006.

Vuille, M., R. S. Bradley, M. Werner, and F. Keimig, 20th century climate change in the tropical Andes--observations and model results, *Climatic Change*, 59(1-2), 75-99, 2003.

Vuille, M., Atmospheric circulation over the Bolivian Altiplano during dry and wet periods and extreme phases of the Southern Oscillation, *International Journal of Climatology,* 19, 1579-1600, 1999.

Wake, C. P., K. Yalcin, and N. S. Gundersrup, The climate signals recorded in the oxygen-isotope accumulation and major-ion time series from the Eclipse ice core, Yukon Territor, Canada. *Annals of Glaciology*, 35, 416-422, 2002.

Wang, B., Interdecadal changes in El Niño onset in the last four decades, *J. Climate*, 8, 267-285, 1995.

Ware, D. M., and R. E. Thomson, Interannual to multidecadal timescale climate variations in the northeast Pacific, *Journal of Climate*, 13, 3209-3220, 2000.

Whitlow, S., P. A. Mayewski, and J. E. Dibb, A comparison of major chemical species input timing and accumulation at South Pole and Summit Greenland, *Atmos. Environ.,* 26, 2045-2054, 1992.

Wiles, G. C., G. C. Jacoby, N. K. Davi, and R. P. McAllister, Late Holocene glacier fluctuations in the Wrangell Mountains, Alaska, *GSA Bulletin*, 114 (7), 896-908, 2002.

Wiles, G. C., R. D. D'Arrigo, and G. C. Jacoby, Gulf of Alaska atmosphere-ocean variability over recent centuries inferred from coastal tree-ring records, *Clim. Change*, 38, 159-205, 1998.

R. Wilson1, R. D'Arrigo, B. Buckley, U. Büntgen, J. Esper, D. Frank, B. Luckman, S. Payette, R. Vose, and D. Youngblut, A matter of divergence--tracking recent warming at hemispheric scales using tree ring data, *J Geophys Res--Atmospheres*, 112, D17103, doi: 10.1029/2006JD008318 2007.

Wilson, R., G. Wiles, R. D'Arrigo, and C. Zweck, Cycles and shifts: 1,300 years of multidecadal temperature variability in the Gulf of Alaska, *Climate Dynamics*, 28, 425-440, doi: 10.1007s00382-006-0194-9, 2007.

Woodhouse, C. A., A 431-year reconstruction of western Colorado snowpack, *Journal of Climate*, 16, 1551-1561, 2003.

Woodhouse, C. A., A Paleo perspective on hydroclimatic variability in the western United States, *Aquatic Sciences*, 66, 346-356, 2004.

Woodhouse, C. A., and P.A. Kay, The use of tree-ring chronologies to show spatial and temporal changes in an air mass boundary, *Physical Geography*, 11, 172-190, 1990.

Wyrtki, K., El Niño--the dynamic response of the equatorial Pacific Ocean to atmospheric forcing, *Journal of Physical Oceanography*, 5, 572-584, 1975.

Xie, S-P, and Y. Tanimoto, A Pan-Atlantic decadal climate oscillation, *Geophys Res Lett*, 25, 2185-2188, 1998.

Yang, Q., P. A. Mayewski, S. Whitlow, M. Twickler, M. Morrision, R. Talbot, J. Dibb, and E.,Linder, Global perspective of nitrate flux in ice cores, *J Geophys Res*, 100(d3), 5113-5121, 1995.

Yarnal, B. and H. F. Diaz, Relationships between extremes of the Southern Oscillation and the winter climate of the Anglo-American Pacific Coast, *Journal of Climatology*, 6, 197-215, 1986.

Yasunari, T. J., T. Shiraiwa, S. Kanamori, J. Fujii, M. Igarashi, K. Yamazaki, C. S. Benson, and T. Hondoh, Intra-annual variations in atmospheric dust and tritium in the North Pacific region detected from an ice core from Mount Wrangell, Alaska, *J Geophys Res*, 112(d10), D10208, 2007.

Zhu, X., J. Sun, Z. Liu, Q. Liu, and J. E. Martin, A synoptic analysis of the interannual variability of winter cyclone activity in the Aleutian Low region, *J Clim*, 20(8), 1523, 2007